CHARACTERIZING THE ENTRY RESISTANCE OF SMOKE DETECTORS

by

James Arthur Ierardi

A Dissertation

Submitted to the Faculty

of the

WORCESTER POLYTECHNIC INSTITUTE

in partial fulfillment of the requirements for the

Degree of Doctor of Philosophy

in

Fire Protection Engineering

_____

May 2005

APPROVED:

_____
Professor Jonathan R. Barnett, Ph.D., Major Advisor

_____
Professor Nicholas A. Dembsey, Ph.D., P.E., Co-Advisor

_____
Craig L. Beyler, Ph.D., Co-Advisor
Hughes Associates, Inc.

_____
Professor Kathy A. Notarianni, Ph.D., P.E., Head of Department

ABSTRACT

Entry resistance in smoke detectors was investigated using experimental and analytical approaches. The experimental work consisted of measuring velocity inside the sensing chamber of smoke detectors with a two-component Laser Doppler Velocimeter and exposing addressable smoke detectors to four different aerosol sources. The velocity measurements and exposure tests were performed in NIST's Fire Emulator / Detector Evaluator under steady state flow conditions in the range of 0.08 to 0.52 m/s. The addressable detectors were a photoelectric and an ionization detector. A specially constructed rectangular detector model was also used for the interior velocity measurements in order to have geometry compatible with numerical approaches, such as computational fluid dynamics modeling or a two-dimensional analytical solution. The experimental data was used to investigate the fluid mechanics and mass transport processes in the entry resistance problem.

An inlet velocity boundary condition was developed for the smoke detectors evaluated in this study by relating the external velocity and detector geometry to the internal velocity by way of a *resistance factor*. Data from the exposure tests was then used to characterize the nature of aerosol entry lag and sensor response. The time to alarm for specific alarm points was determined in addition to performing an exponential curve fit to obtain a characteristic response time. A mass transport model for smoke detector response was developed and solved numerically. The mass transport model was used to simulate the response time data collected in the experimental portion of this study and was found, in general, to underestimate the measured response time by up to 20 seconds. However, in the context of wastebasket fire scenario the amount of underprediction in the model is 5 seconds or less which is within the typically polling interval time of 5 to 10 seconds for an addressable system. Therefore, the mass transport model results developed using this proposed engineering framework show promise and are within the expected uncertainty of practical fire protection engineering design situations.

ACKNOWLEDGEMENTS

Table of Contents

List of Figures

List of Tables

1 Introduction

The accurate prediction of smoke detector response is an important consideration in the performance of a detection system. As occupant and fire department notification can be dependent upon smoke detector response, more realistic objectives in terms of occupant evacuation times and fire department operations may be possible with more accurate predictions of detector response.

Aerosol entry resistance in smoke detectors remains an unresolved issue in fire protection engineering. The mechanisms of aerosol entry resistance are not well understood and impacts predictive methods as well as approval testing. Methods commonly used by fire protection engineers to predict smoke detector response do not fully incorporate characteristics of both the detector and the aerosol. This shortcoming makes it difficult to predict performance characteristics for different hazard scenarios or distinguish the advantages of a particular smoke detector relative to another. The knowledge gap with respect to aerosol entry resistance in approval standards makes it difficult to set the proper metrics for assessing smoke detector performance.

An analogy could be drawn to the sprinkler industry where the development of the response time index (RTI) concept from lumped mass heat transfer analysis provided fundamental insight into the activation of fusible links. A variety of innovative sprinkler technologies emerged from this fundamental understanding such as Early Suppression Fast Response (ESFR) sprinklers.

Aerosol entry in smoke detectors has been investigated with experimental and analytical techniques. The experimental work consisted of measuring velocity inside the sensing chamber of smoke detectors with a two-component Laser Doppler Velocimeter and exposing addressable smoke detectors to four different aerosol sources. The experimental data was used to investigate the fluid mechanics and mass transport processes in the entry resistance problem.

Velocity measurements were made inside the sensing chambers of smoke detectors using a two-component Laser Doppler Velocimeter for a range of steady state external flow conditions in NIST's Fire Emulator / Detector Evaluator. The detectors used in this study were a photoelectric and an ionization smoke detector as well as a specially constructed rectangular detector model with geometric features similar to those of the ionization smoke detector. The detectors were modified to provide optical access to the sensing chamber. The external bulk flow velocities ranged from 0.08 to 0.52 m/s. The internal flow conditions of the detectors used in this study were found to be laminar despite the turbulent nature of the external bulk flow. This finding is based on Reynolds number calculations as well as a comparison of velocity profiles between the LDV measurements in the rectangular model detector and an analytical solution for viscous flow between fixed parallel plates. The velocity data set from the rectangular model could be used to verify computational fluid dynamics models of aerosol entry phenomena.

The internal and external velocity was used to develop an inlet boundary condition for smoke detectors. Existing correlations for incompressible flow past insect screens was used as the basis for developing a semi-empirical correlation relating external velocity and detector geometry to the internal velocity in the sensing chamber of the detector. A sensitivity analysis was conducted and indicated that the external velocity and insect screen hydraulic diameter as the most influential input parameters in terms of propagation of uncertainty into the predicted internal velocity values. However, it was found that the typical estimated uncertainties in the external velocity and insect screen hydraulic diameter propagated an uncertainty into the predicted internal velocity that was less than the range of uncertainties in the measured values of the internal velocity which were on the order of 10 to 30%.

An addressable photoelectric and ionization smoke detector were exposed to four different aerosol sources for a range of steady state external flow conditions in NIST's Fire Emulator / Detector Evaluator. The aerosol sources included smoldering cotton wicks, soot from a laminar propylene flame, and vegetable oil delivered using two different devices. The four aerosol sources were delivered as a step input exposure to the detector. Additionally, a limited number of ramp input exposures using nebulized vegetable oil were also performed. The external bulk flow velocities ranged from 0.08 to 0.52 m/s. A modified fire alarm panel was used to collect the signal output from the detectors during the exposure tests. The detector output data was then used to characterize the nature of aerosol entry lag and sensor response. The response data was

reduced by considering the time to alarm for specific alarm points as well as by performing an exponential curve fit to obtain a characteristic response time.

The explanations offered by various researchers on the low velocity behavior of smoke detectors reveals that there is a clear need for a theoretical framework for smoke detector response. For example, Bjorkman *et al* report that Heskestad's formulation of characteristic lag time (characteristic length divided by external velocity) appears to behave as characteristic length divided by external velocity squared for low velocities. Strictly speaking the units for characteristic lag time would have units of seconds squared per unit length under this observation. This is not to imply that Bjorkman *et al* proposed to modify Heskestad's model in this manner. However, this observation of data trends at low velocity illustrates the difficulty in providing a suitable explanation of the mechanisms responsible for the agreement or disagreement between smoke detector response experiments and models without a theoretical framework describing the relevant phenomena in smoke detector response.

A theoretical basis has been developed from conservation equations and applied to the smoke detector mass transport problem. The conservation equations were nondimensionalized and simplified into a one-dimensional form. The one-dimensional form was solved via finite differencing. The one-dimensional equation was further simplified into a lumped form. The lumped form of the model was compare to commonly used smoke detector response models. A comparison to Heskestad's model constant of characteristic response time indicated that this value is a lumped parameter.

This lumped parameter was found to be consistent with the physical length scale of the detector (diameter) divided by the product of the nondimensional resistance factor and the internal velocity. This was shown by a mathematical comparison of Heskestad's formulation of characteristic time to the characteristic time developed in the lumped analysis of the current approach. This was further demonstrated by substituting the experimental values for physical length scale, resistance factor, and internal velocity from the current study and compared to the characteristic length for the detectors used in this study in accordance with Heskestad's model formulation.

In order to address this issue, a mass transport model was developed for a gas phase control volume for fully developed flow conditions inside the sensing chamber of a smoke detector. Conservation equations for mass, species, momentum, and energy were derived for the three-dimensional situation and were subsequently simplified using appropriate boundary conditions, scaling arguments, and experimental data collected in this study that were confirmed with findings from the research literature. The governing equations were simplified to a one-dimensional form and nondimensionalized using appropriate characteristic quantities. The simplified nondimensional equations for the mass transport model were solved numerically using finite differencing. The inlet velocity boundary condition, or resistance factor, developed from the velocity measurements was used in the mass transport model to relate external flow conditions and detector geometry to the internal velocity in the sensing chamber control volume. The mass transport model was used to simulate the smoke detector response data collected in this study. In general, the magnitude of the residual between the predicted

and measured response times was nominally -10 seconds (under-predicted) for all aerosol types at 0.2%Ob/ft and at steady state for external flows 0.15 m/s and greater. In the context of a 50 kW wastebasket fire under a typical ceiling height of 2.44m located at the maximum distance from smoke detectors spaced 10m (30 ft) on center, the residuals are on the order of -5 seconds or less which is within the uncertainty of a typical addressable smoke detection system with a polling interval on the order of 5 to 10 seconds.

1.1 Guide to the Dissertation

The dissertation is primarily based on three papers that are focused on specific aspects of the research. The first paper entitled, "Measurements of Smoke Detector Internal Velocity Using Laser Doppler Velocimetry," describes the experimental and analytical work related to the interior flow fields of smoke detectors under steady state external flow conditions. The result of this paper is an inlet velocity boundary condition that incorporates external flow conditions and detector geometry into a prediction of the velocity inside the sensing chamber of a smoke detector. This inlet boundary condition was used in the mass transport model developed as part of this study. The second paper is entitled, "An Experimental Study of Aerosol Entry Lag and Smoke Detector Response," and presents the experimental and analytical investigation of detector response characteristics. The experimental portion of the research program was used in conjunction with findings from the literature to develop a mass transport model for smoke detectors. This effort is documented in the third paper, "Development of a Mass Transport Model for Smoke Detectors."

The three papers are preceded by a background chapter providing information relevant to the investigation of the entry resistance problem. The background provides a summary of smoke detector response modeling techniques typically used by fire protection engineers and practitioners. The experimental apparatus used in this study are presented and includes the detectors, NIST's Fire Emulator / Detector Evaluator, and Laser Doppler Velocimeter.

A summation of conclusions is presented in the chapter following the three papers. Although these conclusions are drawn from those presented in the individual papers, the summation allows for them to be put into an overall context. The summation of conclusions is followed by suggestions for future work. While the three papers highlight the major aspects of the research program, the detailed presentation of specific aspects such as derivations, calculations, and data compilations are presented in the various Appendices following the body of the dissertation.

2 Background

The background information related to characterizing aerosol entry in smoke detectors begins with a discussion of existing methods for smoke detector response modeling. The experimental apparatus used in the study are described. The impact that the FE/DE Plexiglass viewing windows have on the optical properties of the LDV system is presented.

2.1 Smoke Detector Response Modeling

Methods for predicting spot-type smoke detector response available from the research literature have been presented and reviewed. The predictive methods of smoke detector response have been classified into two categories – lag time and surrogate methods.

Newman(1987) suggests a residual time as a general description of a fire detection response system that introduces some useful concepts. The residual time is defined as

$$t_{residual} = t_{hazard} - \left(t_{transit} + t_{growth} + t_{response} + t_{effective} \right)$$

(1)

where

$t_{residual}$ – residual time [s]

t_{hazard} – fire hazard exposure time to people and buildings [s]

$t_{transit}$ – transit time to the detector location [s]

t_{growth} – fire growth time to reach detectable levels of fire products [s]

$t_{response}$ – detector response time [s]

$t_{effective}$ – effective response time once fire has been detected [s]

Upon closer inspection this general description reveals a very complex scenario for smoke detection. The process of smoke generation and transport involves transient particle size and concentration changes as a result of agglomeration, deposition, and sedimentation. The phenomena associated with and the methods for predicting these quantities are beyond the scope of the current effort. The primary focus is on the issue of detector response time in relation to the applicable sensor technology. A generic smoke detector response model is presented. This framework addresses some of the physical processes that a fire protection engineer or practitioner would attempt to address with the aid of predictive methods.

2.2 Discussion of Predictive Methods

Smoke detector response modeling is typically based on activation criteria. The activation criteria associated with predictive methods vary in terms of complexity as well as the correspondence to the physical phenomena that influence the particular detection mechanism. The methods for predicting spot-type smoke detector response are discussed in terms of lag time and of surrogate methods. A description of each category is given in general terms with the details of some specific approaches.

2.2.1 Lag Time Methods

Lag time methods are based on the concept that an amount of time exists between when a condition is present outside the detector and when the detector responds (or an alarm condition is attained). Environmental conditions outside the detector are often easier to measure than inside the detector itself. Therefore, the concept of lag time has utility from an experimental standpoint. However, the definition of lag time can be defined from different points of view. Lag time can be, and most often is, described as the difference between the time when the detector responds (or when the alarm threshold is achieved at the sensor) and the time when an alarm threshold value achieved outside the detector.

$$\Delta t_{lag} = t_{th,sen} - t_{th,ext}$$

(2)

Where

Δt_{lag} - detector response lag time [s]

$t_{th,sen}$ - time for sensor to reach threshold condition [s]

$t_{th,ext}$ - time for external environment to reach threshold condition [s]

It should be noted that although a detailed description of their response mechanisms is beyond the scope of this work, the concept of lag time in this context is applicable to gaseous products detectors, such as CO detectors. Gaseous product detectors are typically housed in enclosures similar to those of ionization and photoelectric spot-type smoke detectors.

An expression of lag time was originally proposed by Heskestad (1975) where the time rate of change of optical density inside the detector is equal to the difference between the optical density outside the detector, D_u, and the optical density inside the detector, D_{ui}, divided by the detector time constant, τ.

$$\frac{dD_{ui}}{dt} = \frac{1}{\tau}\left(D_u - D_{ui}\right)$$

(3)

Assuming the rate of change of optical density and the detector time constant are constant quantities, Equation 3 can be solved with the substitution of optical density at response outside the detector, D_{ur}, and the optical density at response inside the detector, D_{uo}.

$$D_{ur} = D_{uo} + \tau\left(\frac{dD_u}{dt}\right)\left[1 - \exp\left(-D_{ur}\frac{1}{\tau}\left(\frac{dD_u}{dt}\right)\right)\right]$$

(4)

If the exponential term can be considered small relative to the rate of change term, it can be ignored and Equation 4 simplifies to

$$D_{ur} = D_{uo} + \tau\left(\frac{dD_u}{dt}\right)$$

(5)

The detector time constant was defined by Heskestad as

$$\tau = \frac{L}{v}$$

(6)

Where

L - characteristic length of detector [m]

v - velocity of ceiling jet [m/s]

The lag time is expressed in a linear relationship as the characteristic length of a smoke detector divided by the local ceiling jet velocity. The lag time at the sensor for this particular approach is relative to environmental conditions that are local to the detector. The detector characteristic length incorporates the geometric features of the particular smoke detector. Characteristic length values are determined experimentally and have been demonstrated by Heskestad (1977), Marrion (1989), Oldweiler (1995), and Bjorkman *et al* (1992). Example characteristic length values for both ionization and photoelectric smoke detectors are summarized in Table 1.

Table 1 -- Experimentally determined characteristic length values for both ionization and photoelectric smoke detectors (Schifiliti,1996).

Source	L(m) -- Ionization	L(m) – Photoelectric
Bjorkman (1992)	3.2 +/- 0.2	5.3 +/- 2.7
Heskestad (1977)	1.8	15
Marrion (1989)	Not studied	7.2, 11.0-13.0, 18.4
Oldweiler (1995)	4.0-9.5, 4.3-14.2	Not studied

While there is utility in quantifying characteristic length, aspects of the geometry corresponding to the specific detector are seldom given. Therefore, from an engineering standpoint, the practical application of this research is difficult as it is not possible to select an appropriate characteristic length without performing an experimental determination. Additionally, the characteristic lengths summarized in Table 1 do not correspond to a physical length scale such as detector diameter, which is typically on the order of 10 to 20 cm. The characteristic length values for Heskestad's method are approximately 1 to 2 orders of magnitude larger than the physical length scale of a typical smoke detector.

Bjorkman *et al* found Heskestad's description of lag time in agreement for local flow velocities greater than 0.2 m/s (Bjorkman,1992). For flow velocities less than 0.2 m/s, however, the increase in optical density was faster than the stated linear relationship to local velocity (Bjorkman,1992).

Heskestad's description of lag time has been augmented with a mixing term (Cleary,1998). For constant velocity, this mixing model equation is expressed as:

$$\kappa Y(t - \delta t) = \tau \frac{dx(t)}{dt} + x(t)$$

(7)

with

$$a_i = \alpha_i \, \mathrm{Re}^{\beta i}$$

(8)

13

where a$_i$ can represent either δt or τ

The variables used in the mixing model are

κ - constant for converting optical density to detector output

Y - smoke optical density

t - time

δt - transport time

τ - mixing time constant

$x(t)$ - detector output as a function of time

α_i - pre-exponent to be determined

β_i - exponent to be determined

Re - Reynolds number

This mixing term can represent a diffusion process occurring within the detector itself and, with further investigation, could explain the observations of Bjorkman *et al* for detectors responding to local flow velocities less than 0.2 m/s. These low velocity scenarios could represent a situation where there is sufficient convective momentum to transport fire signatures from the ceiling jet into the housing of the smoke detector, however, in encountering the geometry of the detector there is insufficient convective momentum to transport to the sensor itself. Therefore, a diffusive or mixing process might be transporting fire signatures to the sensor in these cases of low or negligible convective momentum internal to the detector.

Brozovsky *et. al.* (1995) made experimental measurements of lag time for a photoelectric-type smoke detector and an artificial aerosol using a range of velocities up to 0.2 m/s in a wind tunnel. The analysis of the data demonstrated an exponential decay-type relationship between lag time, Δt_{lag}, and local flow velocity, u, for the specific photoelectric detector and aerosol combination in the following form (Brozovsky,1995):

$$\Delta t_{lag} = \exp\left[-1527u^3 + 918.1u^2 - 187.7u + 14.84\right] \quad 0.07 \le u \le 0.2 m/s$$

(9)

A plot of the data curve fit is reproduced in Figure 1.
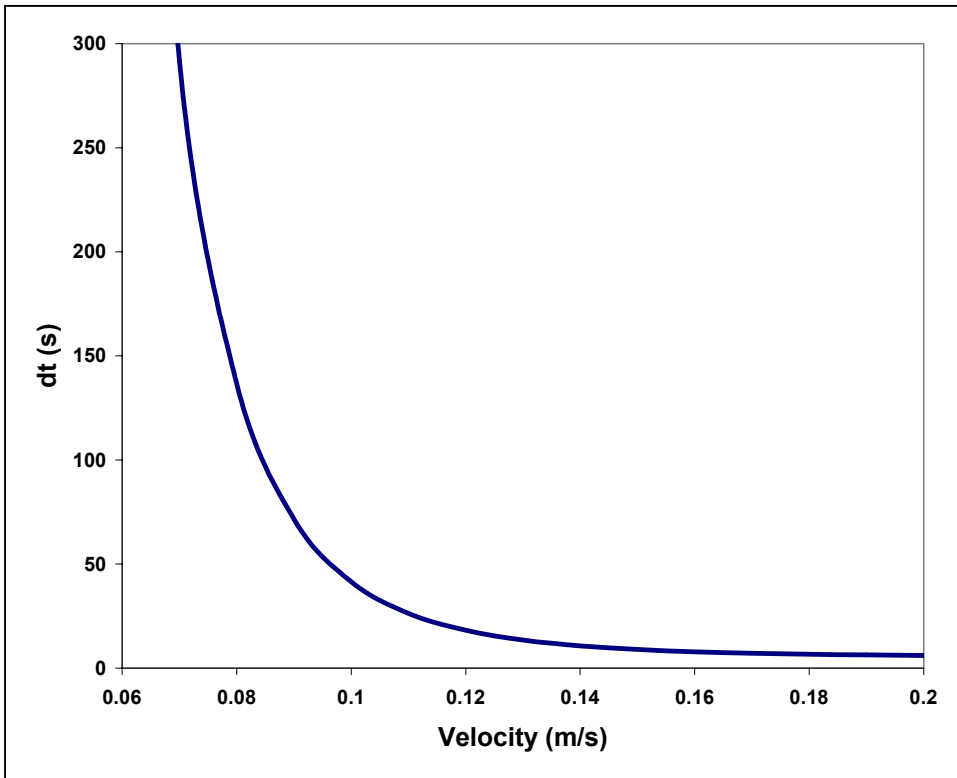
Figure 1 -- Representative plot of lag time versus velocity from Brozovsky et al (1995).

15

The work of Brozovsky *et. al.* (1995) has spawned the concept of critical velocity where the lag time in detector response for ceiling jet velocities less than this critical value were determined to be unacceptable. Unfortunately, despite the insistence that the particular critical velocity value arrived at in the study represents a detector/aerosol specific relationship, a value of 0.15 m/s has propagated through the literature as a guiding value for detector design. What has been lost in the process is the insight that Figure 1 provides. As admitted in the original paper, the method for calculating the critical velocity value, u_{cr}, was arbitrary in nature (Brozovsky,1995). The specific value of was arrived at by taking the average value of the maximum flow velocity tested, u_{max}, and the flow velocity associated with a lag time that is twice that of the maximum flow velocity (Brozovsky,1995):

$$u_{cr} = \frac{u_{max} + u\left(\Delta t_{lag} = 2\Delta t_{lag}\big|_{u_{max}}\right)}{2}$$

(10)

In the Brozovsky *et al* paper, the maximum flow velocity tested was 0.2 m/s and the velocity that had a lag time twice that of the 0.2 m/s case was 0.12 m/s. Therefore, the average of these velocities was 0.16 m/s. However, the core issue in interpreting their results is selecting an acceptable amount of lag time for a particular design situation. From Figure 1 it can be seen that a horizontal asymptote is reached for large enough flow velocities, and therefore, selecting the largest flow velocity tested may be inappropriate as the associated lag time would show negligible differences between 0.18 m/s, 0.20 m/s, or even 0.5 or 1.0 m/s. However, the availability of a plot of lag time versus velocity for

16

a specific detector and specific aerosol could be very useful for design purposes where an acceptable amount of lag time could be left to the designer's discretion.

2.2.2 Surrogate Methods

Surrogate methods are predictions based upon an incomplete account of physics relevant to the particular sensing technology without a direct accounting for lag time. Often only a single parameter, such as optical density or temperature rise, is used for response criterion. Arguably the most commonly used method in detector response modeling is the temperature rise analogy. In particular, a value of 13 $^{\circ}$C has essentially become common practice. The origin of this particular value can be traced to the work of Evans and Stroup (1986) that developed a specific value of 13 $^{\circ}$C using Heskestad's data for wood cribs and the optical density at alarm of an ionization smoke detector responding to wood fires.

The temperature rise analogy was proposed by Heskestad (1977) based on a series of full-scale smoke detector tests conducted by FM Global (then known as Factory Mutual) and the National Institute of Standards and Technology (then known as the National Bureau of Standards) in the late 1970s. The testing involved ceiling heights of 2.44, 4.57, and 8.84 m for ambient temperatures in the range of 18 to 29 $^{\circ}$C and relative humidities between 5 and 87%. The analysis portion of the data included a set assumptions leading to a method of using temperature rise as a means of predicting smoke detector response. The assumptions of this method are:

17

- Mass production rate of smoke is proportional to mass burning rate of fuel

- Smoke is transported by turbulent convection and is not affected by molecular motion, gravity, and particle-fluid inertial effects

- Radiation heat transfer is not accounted for

- Heat transfer between the fluid and enclosing surfaces is not accounted for

- Particle size distribution remains unchanged

- Ratio of optical density to temperature rise is constant in time and space

The activation temperature rise, ΔT_{act}, is determined by the optical density at response, $(OD_r)_d$, for the detector divided by the ratio of optical density to temperature rise for the fuel, $\left(\dfrac{OD}{\Delta T}\right)$.

$$\Delta T_{act} = \frac{(OD_r)_d}{\left(\dfrac{OD}{\Delta T}\right)_f}$$

(11)

Where ratios of optical density to temperature rise (Heskestad, 1977) were estimated from a data set for the flaming combustion of fuels shown in Table 2.

Table 2 -- Ratios of optical density to temperature rise for flaming combustion.

Material	$10^2 D_u \big/ \Delta T \quad \left[ft^{-1} \cdot {}^{o}F^{-1} \right]$
Wood (sugar pine, 5% moisture content)	0.02
Cotton fabric (unbleached muslin)	0.01/0.02
Paper wastebasket	0.03
Polyurethane foam	0.4
Polyester fiber (in bed pillow)	0.3
PVC insulation	0.5/1.0
Foam rubber/polyurethane (sofa cushion)	1.3

Bukowski and Averill (1998) as well as Schifiliti and Pucci (1996) provide a detailed critique of the assumptions used in developing the temperature rise analogy.

The temperature rise method can be applied to both ionization and photoelectric smoke detectors as long as the optical density at response for the particular detector and the ratio of optical density to temperature rise for the particular fuel are known.

2.3 Experimental Apparatus

2.3.1 Fire Emulator / Detector Evaluator

The Fire Emulator / Detector Evaluator is a single-pass wind tunnel that simulates ceiling jet conditions and was developed at NIST for the purpose of testing smoke and gaseous products detectors (Cleary, 2001).   Environmental conditions such as velocity,

temperature, and humidity as well as delivery of specific aerosol or gaseous products can be controlled. For the series of tests considered in this work velocity and aerosol delivery were the only input parameters of interest.

A schematic diagram of the FE/DE is shown in Figure 2. Velocity in the FE/DE is controlled by a variable speed fan at the beginning of the FE/DE system and was set to a constant value during each test. The aerosol delivered in this series of tests was used to seed the flow for Laser Doppler Velocimetry measurements and is described in greater detail in Section 2.3. A section of ducting measuring approximately 4m in length connects the aerosol injection location to a flow straightening honeycomb screen and includes a 90° elbow. The flow straightening honeycomb screen is connected to the FE/DE test section by a 1m section of ducting. The test section is constructed out of Plexiglass and measures 1m in length by 0.67m in width by 0.33m in height. Detectors are mounted to the top of the test section at a distance of approximately 1.2m from the flow straightening honeycomb screen. Instrumentation for characterizing the environmental conditions is present in the test section. The LDV had optical access to the test section via a Plexiglass cover at the bottom of the test section. This allowed for the measurement of the streamwise component of velocity.
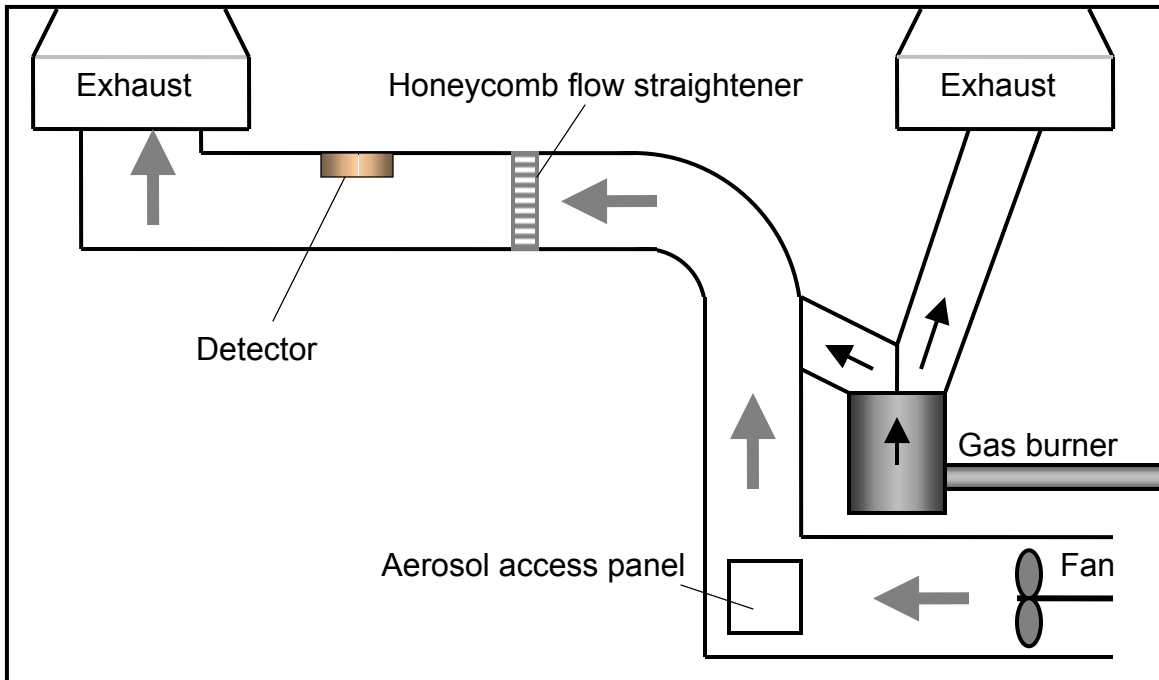
Figure 2 -- Schematic diagram of FE/DE.

A laser transmittance measurement is made to assess smoke obscuration in the test section. A section view of the laser path is shown in Figure 3 and a plan view is shown in Figure 4. A HeNe laser passes through a power filter in order to ensure a steady output. The laser passes through a beam splitter which directs 50% of the beam into the middle of the test section and the remaining 50% to a mirror which directs the beam into the upper portion of the test section. Mirrors inside the test section create 3 legs of the overall pathlength and the laser beam terminates at the photodiodes. The overall pathlength is approximately 1.5m.
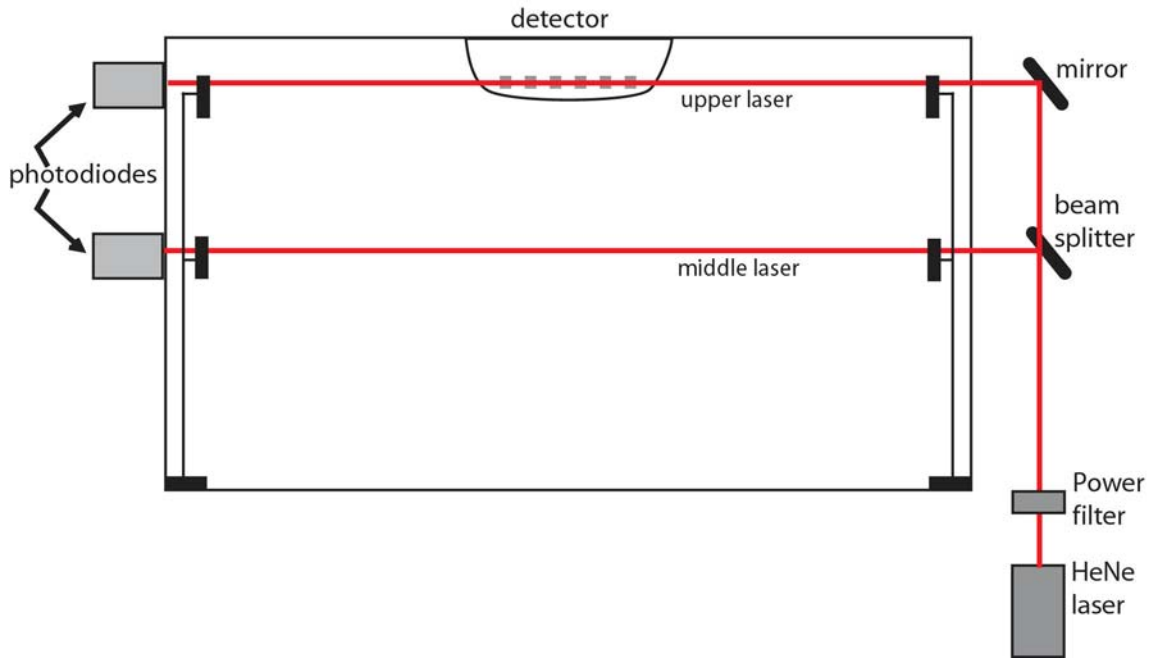
Figure 3 -- Section view of FE/DE laser transmittance measurement.
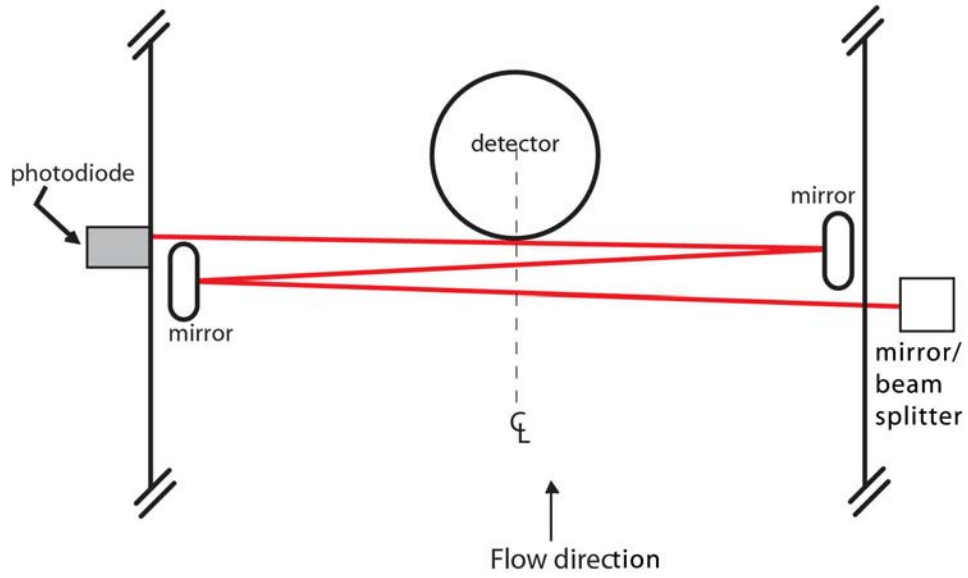
Figure 4 -- Plan view of FE/DE laser transmittance measurement.

2.3.2   Rectangular Detector Model

A specially constructed rectangular detector model was used to represent the geometric features of a typical smoke detector while lending itself to analysis techniques such as computational fluid dynamics modeling with structured rectilinear grids. The geometry for the rectangular detector model was based on features of the ionization smoke detector used in this study and is shown with relevant dimensions in Figure 5, Figure 6, and Figure 7.

The rectangular smoke detector model was evaluated with and without the insect screen in place. The insect screen was removed in consideration that the data set could be easily evaluated using CFD codes that are not capable of representing the geometry of the insect screen.

The interior and exterior baffles were constructed out of ABS plastic and attached to a bakelite base with epoxy. The insect screen was attached directly to the interior surfaces of the interior baffles of the detector model. A section of plate glass, 174mm by 70mm and 4mm thick, formed the bottom of the detector and provided optical access to the interior space of the model. This interior space was consistent with a sensing chamber of a typical smoke detector, however, there was no sensing element present.
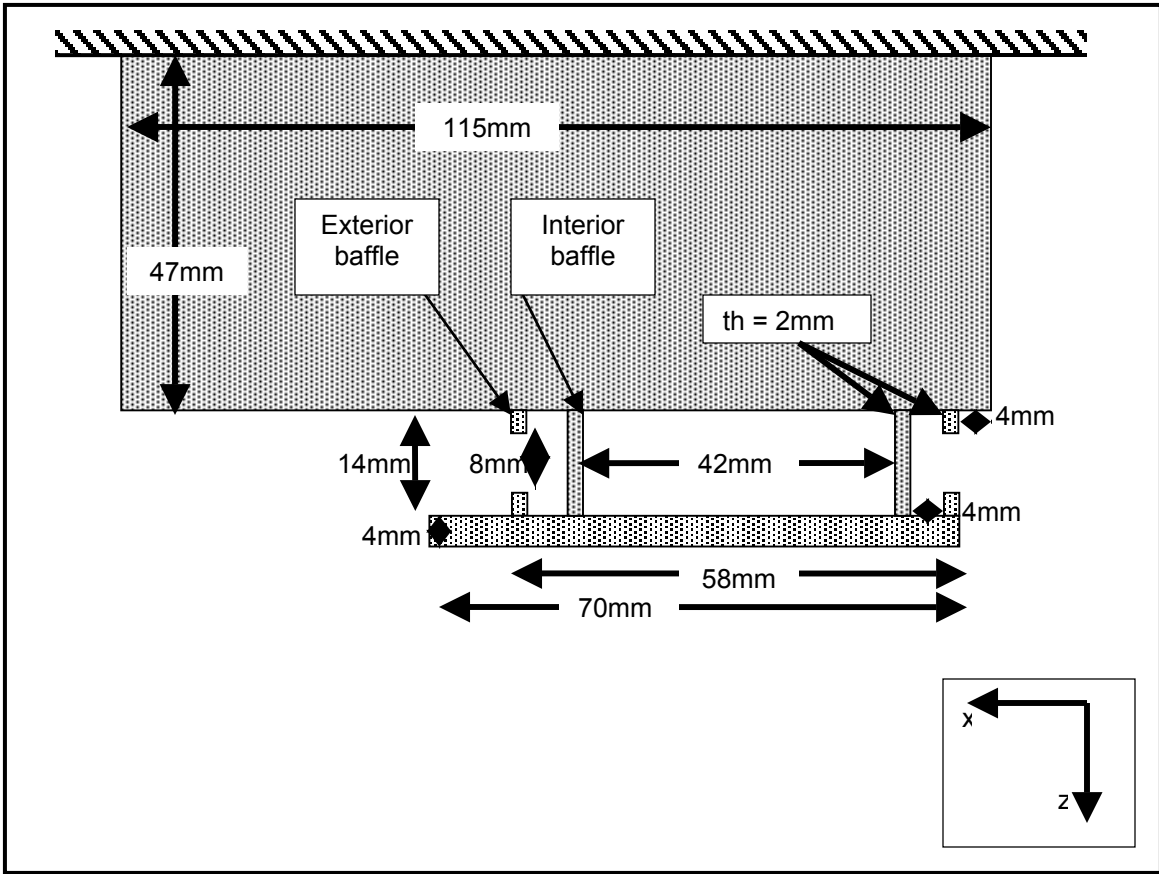
Figure 5 -- Elevation side view of rectangular model detector with dimensions. Streamwise flow is in positive x-direction.
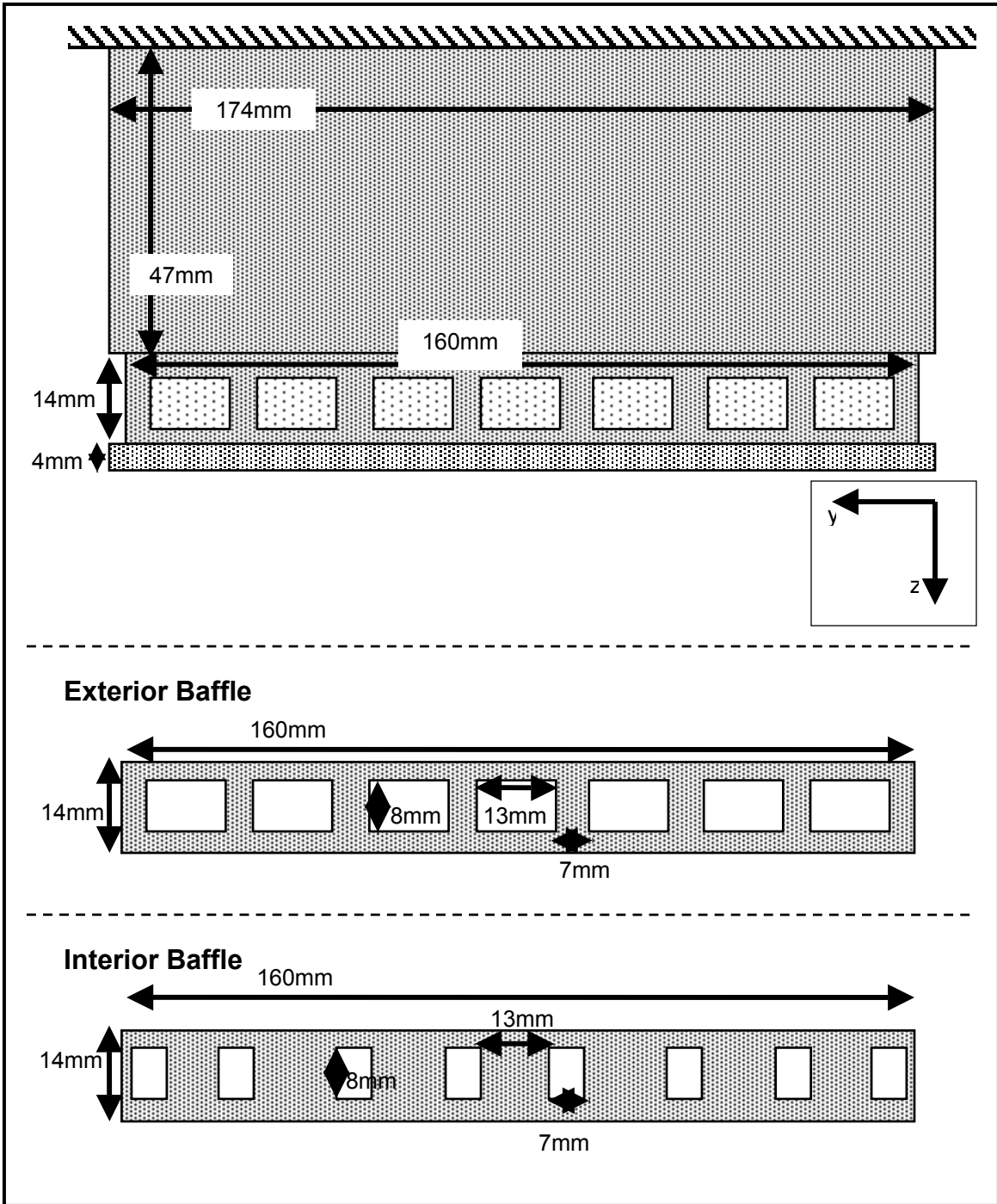
Figure 6 -- Elevation front view of rectangular model detector and details of external and internal baffle sections with dimensions. Streamwise flow is into the page.

174mm

4mm
4mm

58mm

Interior
baffles
(th = 2mm)

Exterior
baffles
(th = 2mm)

70mm

4mm

160mm

Solid sides
(th = 2mm)

115mm

y

x
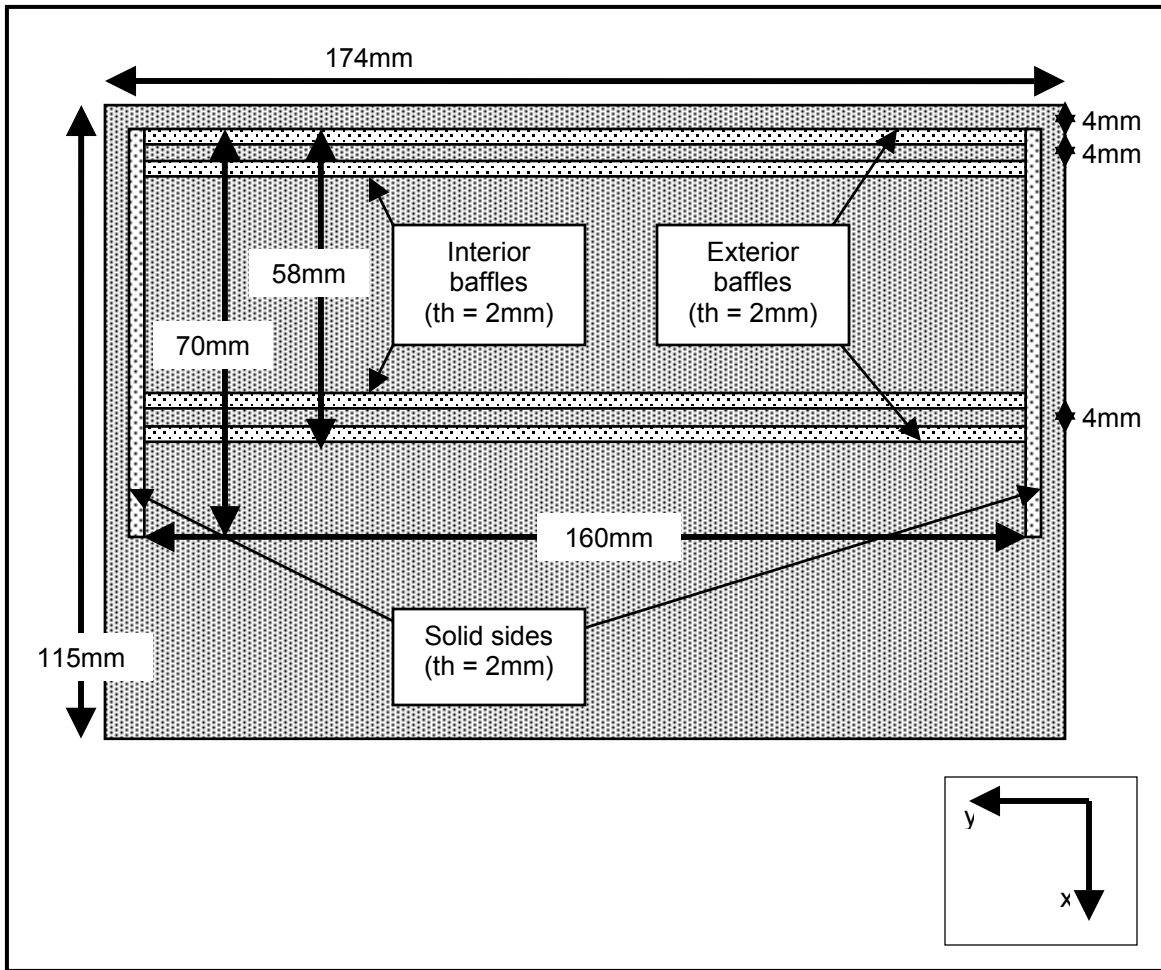
Figure 7 -- Plan view looking up into bottom of rectangular model detector with dimensions. Streamwise flow is in the positive x-direction.

2.3.3   Photoelectric Detector

The addressable photoelectric detector used in this study is shown below in Figure 8.
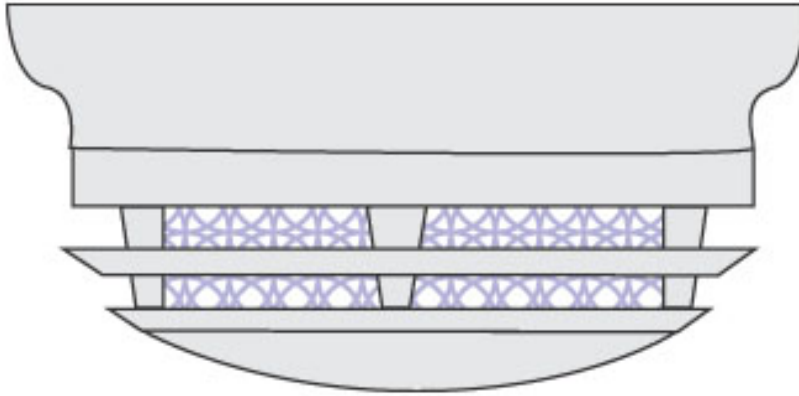
Figure 8 -- Photoelectric detector profile.

The photoelectric sensor was 124mm in diameter at the base and 55mm in height. The aerosol entry location was from 34 to 45mm measured vertically from the bottom of the base. The nominal diameter at the aerosol entry location was 102mm. The sensing chamber was 48mm in diameter and 13mm in height. An insect screen 13mm in height encompassed the diameter of the sensing chamber. A series of light obstructing louvers also surrounded the circumference of the sensing chamber and resulted in a nominal entrance area of $5.72 \times 10^{-4} m^2$ to the sensing chamber. The volume of the sensing chamber was approximately $2.35 \times 10^{-5} m^3$.

A circular piece of glass was added to the sensing chamber to provide optical access to the inner portion of the sensing chamber. Figure 9 shows a photoelectric detector with optical access in comparison to the same detector model.

Figure 9 -- Photoelectric smoke detectors with (l), and without (r) optical access.

Figure 10 shows the modifications in more detail.
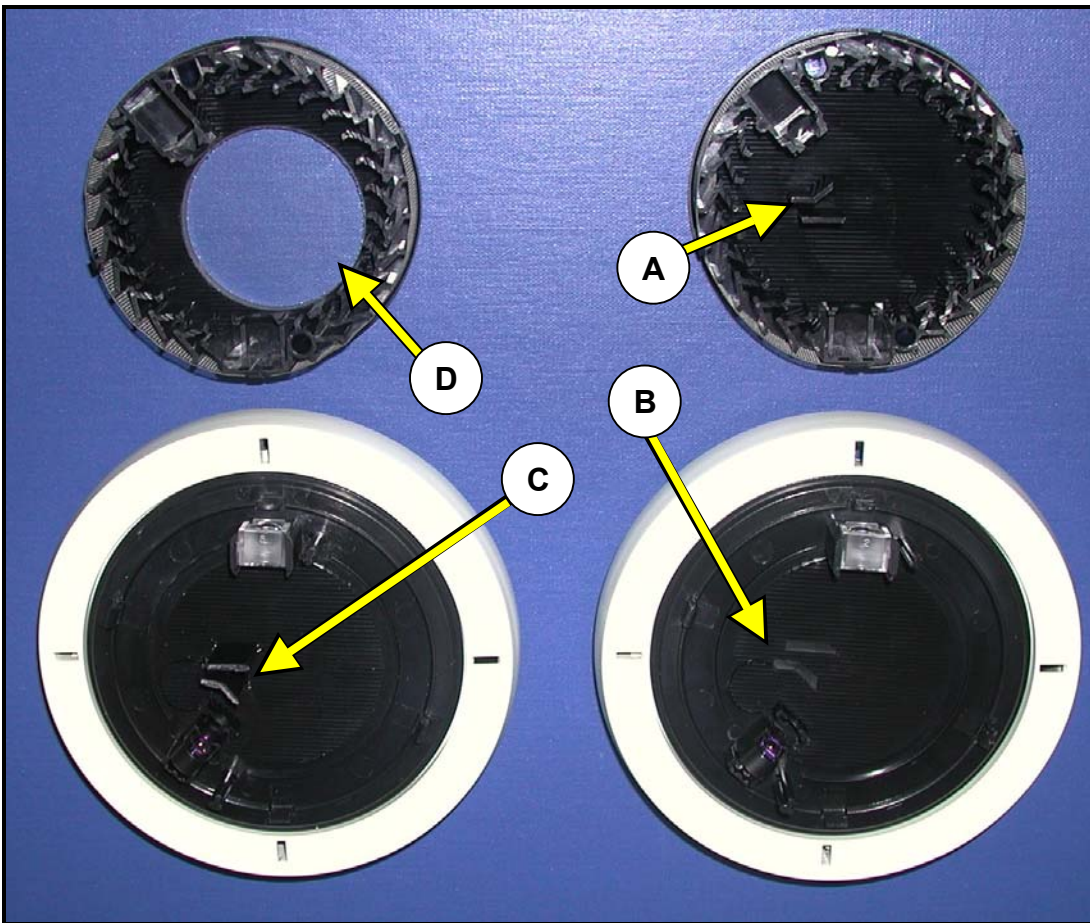
Figure 10 -- Main features of adding optical access to photoelectric detectors. Optical partitions (A), optical partition recess (B), optical partitions moved to recess (C), and glass disk (D) shown.

The right-hand side of Figure 10 shows a typical unmodified photoelectric smoke detector. The left-hand side shows the modified photoelectric smoke detector. The main features of interest in adding optical access were the optical partitions for the photoelectric light/receiver pair (A) and the associated recess (B). The partitions normally rest within the recess when the chamber is assembled. The goal of adding optical access required removing a circular section of the photoelectric chamber. The optical partitions were also part of the section to be removed. Therefore, the optical partitions were broken off from the chamber using a pair of pliers and glued into the recesses. The result of this process is shown in (C) of Figure 10. A 38mm diameter opening in the chamber was created. A 38mm diameter disk of silica glass (D) was inserted into the opening. A circular opening 40mm in diameter was added to the external cover of the smoke detector, as shown in Figure 15, to provide optical access to the glass disk. This feature did not significantly alter the geometry of the detector and, therefore, was not expected to significantly alter the aerosol flow patterns.

2.3.4   Ionization Detector

The addressable ionization detector used in this study is shown below in Figure 11.

29

Figure 11 -- Ionization detector profile.

The ionization sensor was 120mm in diameter at the base and 65mm in height. The aerosol entry location was from 55 to 62mm measured vertically from the bottom of the base. The nominal diameter at the aerosol entry location was 50mm. The sensing chamber was 35mm in diameter and 13mm in height. An insect screen 13mm in height encompassed the diameter of the sensing chamber. The entrance area to the sensing chamber was approximately $3.92 \times 10^{-4} m^2$. The volume of the sensing chamber was approximately $1.25 \times 10^5 m^3$.

Optical access to the sensing chamber was provided in a manner similar to that described for the photoelectric detector. A 38mm diameter piece of silica glass was added by creating a 38mm diameter concentric opening in the external cover of the ionization detector. A 25mm diameter concentric opening was made into the sensing chamber. This opening was made air tight by the optical glass from the external cover resting upon it. Therefore, the geometry of the ionization detector was not significantly altered from an aerodynamic standpoint.

2.3.5 Laser Doppler Velocimetery

Laser Doppler Velocimetry is a direct point measurement of velocity in which two laser beams of the same wavelength are crossed to form an interference pattern at the point of intersection.
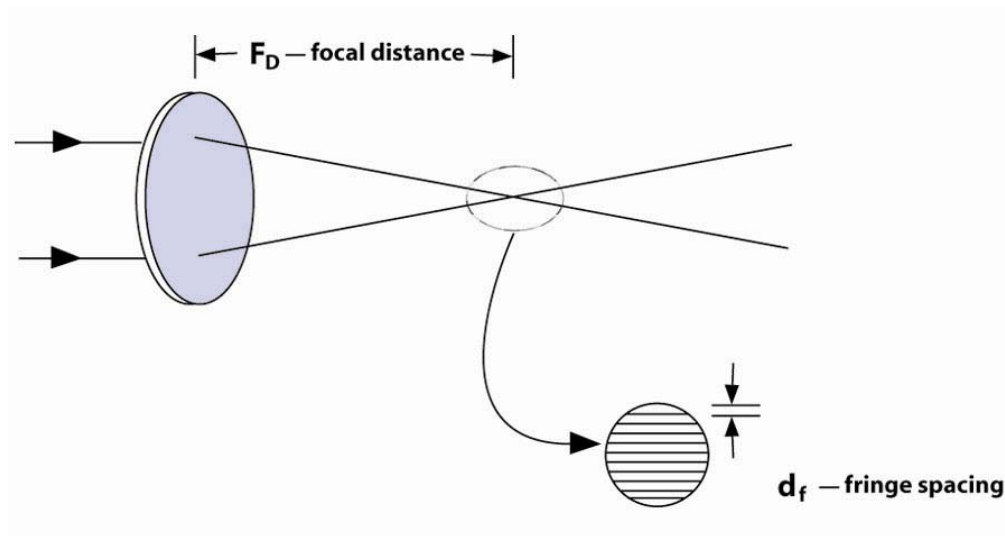
Figure 12 -- LDV focal distance, intersection point, and fringe spacing.

The interference pattern consists of light and dark bands spaced at even intervals, also known as the fringe spacing. The fringe spacing depends upon the laser wavelength, λ, and the half-angle, κ, subtended by the two laser beams. The fringe spacing, d_f, is computed from the following relationship (TSI, 1997)

$$d_f = \frac{\lambda}{2\sin\kappa}$$

(12)

Particles passing through this interference pattern scatter light at a frequency that depends upon the particle velocity and fringe pattern spacing. The particle velocity, u, is determined from the frequency of scattered light measured at the photodetector, f_m, and the known spacing of the fringe pattern (TSI, 1997).

$$u = f_m d_f$$

(13)

A TSI[1] two-component Laser Doppler Velocimeter operating in direct backscatter mode was used to measure velocity. The LDV consisted of a Spectra-Physics Stabilite 2017 Argon-Ion laser with a maximum power output of 5W. The multimode laser beam was separated into green (514.5nm), blue (488.0nm), and violet (476.5nm) wavelengths by a Colorbust beam separator. Only the green and blue wavelengths were used in this study. Fiberoptic couplers transmitted the laser light to the fiber optic probe. The photodiode receiver was integral to the fiberoptic probe, therefore, the system operated in the direct backscatter mode.

The beam half angles out of the probe were 3.95° and the focal distance to the measurement point was nominally 350mm (TSI, 1998). The ellipsoid measurement volumes formed by each pair of laser beams were coincident and had nominal

---

[1] Specific commercial products are identified in this paper for the purpose of adequately describing the research methodology. In no case does such identification imply recommendation or endorsement by the authors and sponsors, nor does it imply that the commercial products identified are the best available for the purpose.

dimensions of 90µm wide by 1.3mm long (TSI, 1998). The flow was seeded with

atomized vegetable oil using a TSI six-jet atomizer with 15 psi of dilution air.

2.4 Impact of Viewing Windows on LDV Focal Distance

The experimental work conducted in this study used Laser Doppler Velocimetry to

measure flow field velocity. These measurements were made through optical viewing

windows in NIST's FE/DE and viewing windows added to smoke detectors. This section

of the Background presents the theory of the LDV technique and specifically addresses

the impact that glass and Plexiglass viewing windows have on the optical properties of

the LDV measurement.

Laser Doppler Velocimetry is a direct point measurement of velocity in which two laser

beams of the same wavelength are crossed to form an interference pattern at the point of

intersection. The interference pattern consists of light and dark bands spaced at even

intervals, also known as the fringe spacing. A schematic diagram of this measurement

technique is shown below in Figure 13 demonstrating the focal distance from the lens to

the intersection point as well as the fringe spacing of the intersection point.
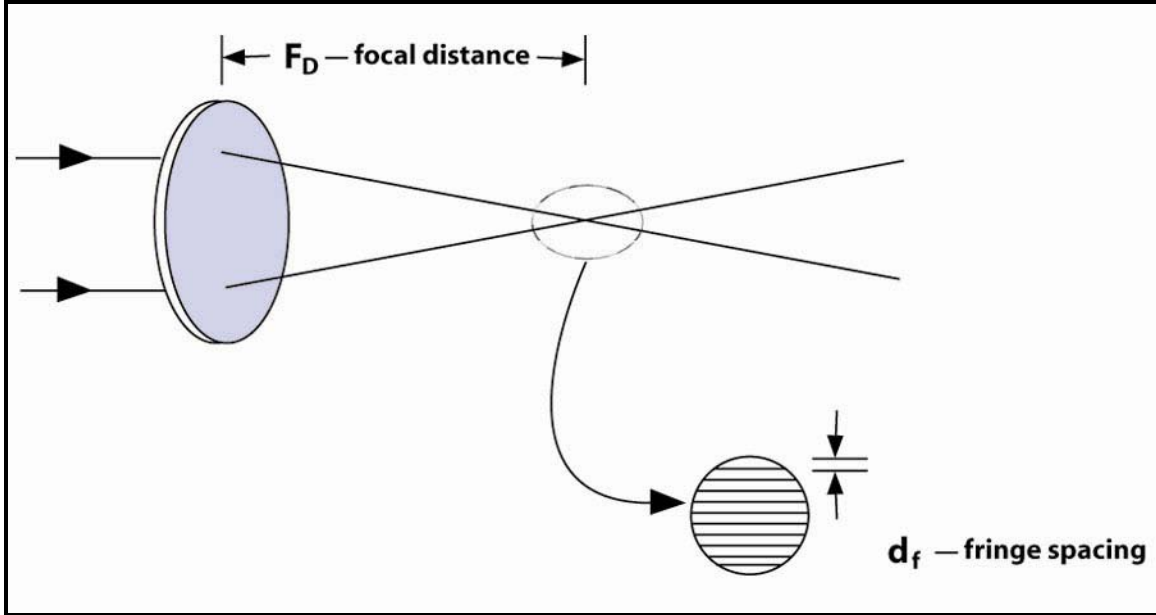
Figure 13 -- Schematic of Laser Doppler Velocimetry measurement technique.

The fringe spacing depends upon the laser wavelength, λ, and the half-angle, κ, subtended by the two laser beams. The fringe spacing, d_f, is computed from the following relationship (TSI, 1997)

$$d_f = \frac{\lambda}{2\sin\kappa}$$

(14)

Particles passing through this interference pattern scatter light at a frequency that depends upon the particle velocity and fringe pattern spacing. The particle velocity, u, is determined from the frequency of scattered light measured at the photodetector, f_m, and the known spacing of the fringe pattern (TSI, 1997).

$$u = f_m d_f$$

(15)

The LDV measurements in the experimental portion of this study were made through optical windows. The FE/DE test section was constructed of Plexiglass, which is used in the following sections to illustrate the resulting impact of optical viewing windows on the LDV system. The effect of a Plexiglass viewing window on the optical properties of the LDV system is addressed by starting with Snell's Law, where N is the index of refraction for a specific material.

$$N_1 \sin \kappa_1 = N_2 \sin \kappa_2$$

(16)

For the specific situation addressed in this study of an air-Plexiglass-air arrangement, Snell's Law yields:

$$N_1 \sin \kappa_1 = N_2 \sin \kappa_2 = N_3 \sin \kappa_3$$

(17)

Where the subscripts 1 and 3 correspond to air and the subscript 2 corresponds to the Plexiglass viewing window. Since the index of refraction is the same for both terms related to air, the half angles are the same. The half angle formed when the laser travels through the Plexiglass window can be calculated from equation 16 by solving for κ_2:

$$\kappa_2 = \sin^{-1}\left[\frac{N_1}{N_2}\left(\sin\kappa_1\right)\right]$$

<div align="right">(18)</div>

The index of fraction for air and Plexiglass are 1 and 1.49, respectively. The half-angle of the laser in air is known from the specifications of the TSI Model 9253-350 fiberoptic probe and is given as 3.95°. Therefore, substituting these known values into equation 18 yields:

$$\kappa_2 = \sin^{-1}\left[\frac{1}{1.49}\left(\sin\left(3.95\right)\right)\right] = \sin^{-1}\left[\frac{1}{1.49}\left(0.0689\right)\right] = 2.65^{o}$$

<div align="right">(19)</div>

The following proof shows that fringe spacing is independent of the refractive index of the Plexiglass in this air-Plexiglass-air configuration.

The fringe spacing is described as

$$d_f = \frac{\lambda}{2\sin\kappa}$$

<div align="right">(20)</div>

The index of fraction is defined as the ratio of the wavelength of light in a vacuum, λ_o, relative to the wavelength of light in the medium, λ,:

$$N = \frac{\lambda_o}{\lambda}$$

<div align="right">(21)</div>

Using the subscripts 1 and 2 to denote air and Plexiglass, respectively, the indices of refraction can be written as:

$$N_1 = \frac{\lambda_o}{\lambda_1}; \quad N_2 = \frac{\lambda_o}{\lambda_2}$$

<div align="right">(22)</div>

The terms from equation 22 can be brought together by the λ_o term and produces:

$$N_1 \lambda_1 = N_2 \lambda_2$$

<div align="right">(23)</div>

From the definition of fringe spacing shown in equation 20, the identities shown in equations 16 and 23 can be applied to show the following where N_1 is known to be 1:

$$d_f = \frac{\lambda_1}{2\sin\kappa_1} = \frac{(\lambda_2 N_2 / N_1)}{2(N_2/N_1)(\sin\kappa_2)} = \frac{\lambda_2}{2\sin\kappa_2}$$

<div align="right">(24)</div>

Therefore, it is shown that according to Snell's Law and the definition of refractive index that the fringe spacing is independent of the window's index of refraction.

However, due to the change in half angle experienced by the laser beam as it moves through the Plexiglass viewing window, the focal distance will be affected. The general equation for computing the resultant focal distance, F, for the air-Plexiglass-air scenario is:

$$F = F_D \frac{\tan \kappa_1}{\tan \kappa_3} + th \left[1 - \frac{\tan \kappa_2}{\tan \kappa_3} \right] + d_1 \left[1 - \frac{\tan \kappa_1}{\tan \kappa_3} \right]$$

(25)

Where F_D is the focal distance in air, th is the window thickness and d_1 is the distance from the exterior of the lens to the window. All dimensions are in mm. However, as proved previously the half angles are the same for subscripts 1 and 3, so equation 25 simplifies to:

$$F = F_D + th \left[1 - \frac{\tan \kappa_2}{\tan \kappa_3} \right]$$

(26)

A schematic LDV measurements being made without and with a Plexiglass optical window are shown in .

38
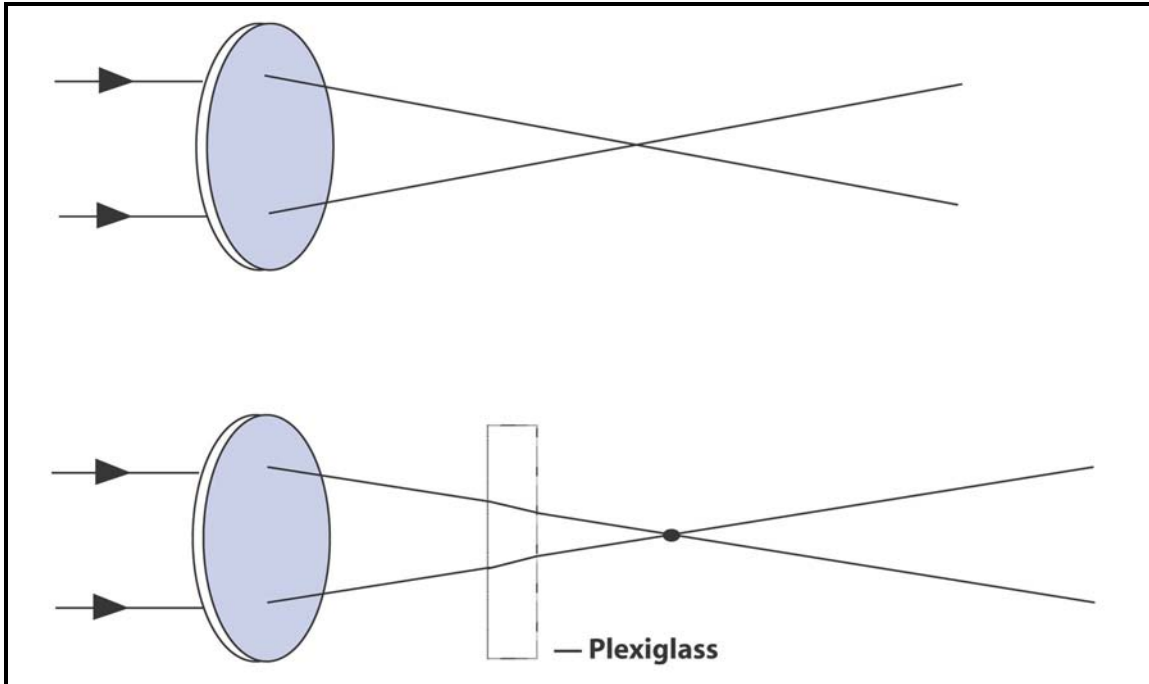
Figure 14 -- Schematic showing LDV measurements made (top) without and (bottom) with an optical window.

The top scenario is representative of an LDV measurement being made without an optical window. The bottom scenario is representative of an LDV measurement being made through a Plexiglass optical window. It can be seen that the half angles of the laser in air are unchanged and the focal distance is increased slightly due to the change in half angle occurring only within the thickness of the Plexiglass.

For the specific arrangement used in this study with nominally 6.35mm thick Plexiglass in the test section of the FE/DE and a standard focal distance of 349.7mm for the TSI Model 9253-350 fiber optic probe, the focal distance accounting for the influence of the Plexiglass window is:

$$F = 349.7 + 6.35\left[1 - \frac{\tan 2.65}{\tan 3.95}\right] = 349.7 + 6.35\left[1 - \frac{0.0463}{0.0690}\right] = 351.8mm$$

(27)

For each detector evaluated a preliminary series of vertical measurements were made within the sensing chamber to ensure that the focal distance of the LDV was properly calibrated in the vertical direction. A visual observation was made initially to locate the measurement volume of the LDV within the approximate midpoint of the sensing chamber height. The flow was seeded under steady state flow conditions at a nominal external velocity of 0.80 m/s. LDV data was collected to verify that valid internal velocity measurements were being made. The LDV probe was translated vertically in set increments until no valid data points or non-physical velocity values were observed. Non-physical velocities were characterized as values exceeding the external velocity nominal value of 0.80 m/s. However, non-physical velocity values were typically 32 m/s and thus easily identified. This established an initial upper bound for the sensing chamber. The LDV probe was then translated vertically in an amount equal to the measured internal height of the sensing chamber in an attempt to locate the LDV measurement volume on or within the surface of the optical access glass. This condition was characterized by either no valid data points or non-physical velocity data points measured by the LDV. This procedure served as a double-check to verify that the LDV was properly calibrated within the upper and lower bounds of the sensing chamber for a particular detector.

Nomenclature

d_f fringe spacing [μm]

Δt_{lag} lag time [s]

D optical density [1/m]

f focal length of lens [mm]

F focal distance of optical system [mm]

L characteristic length [m]

N index of refraction [dimensionless]

OD optical density [1/m]

t time [s]

ΔT temperature rise [C]

u velocity [m/s]

Greek letters

κ half-angle [deg]; extinction [m^{-1}]

λ wavelength [nm]

π value of pi [dimensionless]

τ characteristic time [s]

References

Bjorkman, J., M.A. Kokkola, H. Ahola. "Measurements of the Characteristic Lengths of Smoke Detectors," *Fire Technology*, **28(2)**, pp. 99-109, (1992).

Brozovsky, E., V. Motevalli, and R. Custer, "A First Approximation Method for Smoke Detector Placement Based on Design Fire Size, Critical Velocity, and Detector Aerosol Entry Lag Time," *Fire Technology*, **31(4)**, pp. 336-354, (1995).

Bukowski, R.W. and J.D. Averill, "Methods for predicting smoke detector activation," Fire Suppression and Detection Research Application Symposium, Research and Practice: Bridging the Gap. February 25-27, 1998, Orlando, FL. Proceedings. National Fire Protection Research Foundation, Quincy, MA, pp. 64-72, (1998).

Cleary, T., A. Chernovsky, W. Grosshandler, and M. Anderson, "Particulate Entry Lag in Smoke Detectors," Annual Conference on Fire Research. Book of Abstracts. K.A. Beall, Ed. Building and Fire Research Laboratory, National Institute of Standards and Technology, Gaithersburg, MD. October, 1998, NISTIR 6242, pp. 11-12, (1998).

Evans, D.D. and D.W. Stroup, "Methods to Calculate the Response Time of Heat and Smoke Detectors Installed Below Large Unobstructed Ceilings," Building and Fire Research Laboratory, National Institute of Standards and Technology, NBSIR 85-3167, July 1985 and *Fire Technology*, **22(1)**, pp. 54-65, (1986).

Heskestad, G., "Generalized Characterization of Smoke Entry and Response for Products-of-Combustion Detectors," International Conference on Automatic Fire Detection, 7th. (Probleme der Automatischen Brandentdeckung), March 5-6, 1975, Germany, pp. 267-310 and National Research Council. Fire Detection for Life Safety. March 31-April 1, 1975, pp. 93-127, (1975).

Heskestad, G and M.A. Delichatsios, "Environments of Fire Detectors. Phase 1. Effect of Fire Size, Ceiling Height and Materials. Volume 2. Analysis," Factory Mutual Research Corp., Norwood, MA, National Bureau of Standards, Gaithersburg, MD, FMRC Serial 22427 and NBS GCR 77-95, (1977).

Marrion, C.E. "Lag Time Modeling and Effects of Ceiling Jet Velocity on the Placement of Optical Smoke Detectors," M.S. Thesis, Center for Firesafety Studies, Worcester Polytechnic Institute, Worcester, MA, (1989).

Newman, J.S., "Prediction of Fire Detector Response," *Fire Safety Journal*, **12**, pp. 205-211, (1987).

Oldweiler, A.J. "Investigation of the Smoke Detector L-Number in the UL Smoke Box," M.S. Thesis, Center for Firesafety Studies, Worcester Polytechnic Institute, Worcester, MA, (1995).

Schifiliti, R.P. and W.E. Pucci, *Fire Detection Modeling, State of the Art*, Fire Detection Institute, Bloomfield, CT, (1996).

3 Paper 1: "Measurements of Smoke Detector Internal Velocity Using Laser Doppler Velocimetry"

Measurements of Smoke Detector Internal Velocity

Using Laser Doppler Velocimetry

Abstract

Velocity measurements were made inside the sensing chambers of smoke detectors using a two-component Laser Doppler Velocimeter for a range of steady state external flow conditions in NIST's Fire Emulator / Detector Evaluator. The detectors used in this study were a photoelectric and an ionization smoke detector as well as a specially constructed rectangular detector model with geometric features similar to those of the ionization smoke detector. The detectors were modified to provide optical access to the sensing chamber. The external bulk flow velocities ranged from 0.08 to 0.52 m/s. The internal flow conditions of the detectors used in this study were found to have laminar characteristics with the external bulk flow exhibiting turbulent characteristics. These findings are based on Reynolds number calculations as well as a comparison of velocity profiles between the LDV measurements in the rectangular model detector and an analytical solution for viscous flow between fixed parallel plates. The velocity data set from the rectangular model could be used to verify computational fluid dynamics models of aerosol entry phenomena. For the rectangular model detector used in this study the internal velocity values at steady state were found to be on the order of 8 to 60 times smaller than the external velocity. The photoelectric and ionization detectors used in this study were found to have internal velocity values at steady state on the order of 8 to 36 times smaller than the external velocity. The experimental data collected in this study were used to formulate an inlet velocity boundary condition for smoke detectors that relates external velocity and detector geometry to internal velocity with the use a *resistance factor*. This inlet boundary condition was used in the development of a mass transport model for smoke detector response.

Keywords: smoke detection, resistance factor, entry resistance, entry lag, Laser Doppler Velocimetry

Nomenclature

A area [m^2]

d_{screen} insect screen hydraulic diameter [m]

h half-height between fixed parallel plates [m]

K incompressible resistance coefficient [dimensionless]

$\dot{m}$ mass flow rate [kg/s]

R smoke detector resistance factor [dimensionless]

Re_d Reynolds number based on insect screen diameter [dimensionless]

V velocity [m/s]

$\bar{V}$ average velocity (velocity profile integrated over height of interest) [m/s]

V^* nondimensional velocity (internal velocity scaled to external velocity) [m/s]

x streamwise distance [m]

y transverse distance [m]

z vertical distance [m]

Greek letters

α screen porosity [dimensionless]

ν kinematic fluid viscosity [m^2/s]

ρ density [kg/m^3]

Subscripts

int   insect screen

ext   rectangular detector model without insect screen

max   rectangular detector model with insect screen

1. Introduction

Internal velocity measurements for a photoelectric, ionization, and a specially constructed

rectangular detector model were made with a two-component Laser Doppler Velocimeter

(LDV) under steady state flow conditions. The LDV measurements were made for the

purpose of assessing aerosol entry resistance for steady state forced flow conditions in

NIST's Fire Emulator / Detector Evaluator (FE/DE). The data collected in this study was

used to develop an inlet velocity boundary condition for a mass transport model of smoke

detector response (see Model Paper). The concept of a smoke detector resistance factor

is introduced as a means of relating external flow velocity and detector geometry to

internal velocity for use in smoke detector response modeling.

2. Experimental Apparatus

The velocity inside three detector types was measured using a Laser Doppler

Velocimeter. The three detector types were; a specially constructed rectangular model, a

photoelectric-type, and an ionization-type detector. All three detectors had optical access to the sensing chamber area. The detectors were placed in NIST Fire Emulator / Detector Evaluator and subjected to a range of steady state velocities. The FE/DE, detectors, and LDV apparatus used in this study are described in the sections below.

2.1 Fire Emulator / Detector Evaluator

The Fire Emulator / Detector Evaluator is a single-pass wind tunnel that simulates ceiling jet conditions and was developed at NIST for the purpose of testing smoke and gaseous products detectors (Cleary, 2001). Environmental conditions such as velocity, temperature, and humidity as well as delivery of specific aerosol or gaseous products can be controlled. For the series of tests considered in this work velocity and aerosol delivery were the only input parameters of interest.

2.2 Detectors

A specially constructed rectangular detector model was used to represent the geometric features of a typical smoke detector while lending itself to analysis techniques such as computational fluid dynamics modeling with structured rectilinear grids. The geometry for the rectangular detector model was based on features of the ionization smoke detector used in this study.

The interior and exterior baffles were constructed out of ABS plastic and attached to a bakelite base with epoxy. The insect screen was attached directly to the interior surfaces of the interior baffles of the detector model. A section of plate glass, 174mm by 70mm

47

and 4mm thick, formed the bottom of the detector and provided optical access to the interior space of the model. This interior space was consistent with a sensing chamber of a typical smoke detector, however, there was no sensing element present.

The relevant geometric features of all three detectors are summarized in Table 3.

Table 3 -- Detector profiles and relevant dimensions.

Detector	Rectangular	Photoelectric	Ionization
Profile			
OD/X_o (mm)	58	102	50
ID/X_i (mm)	42	48	35
Z_{entry} (mm)	50-58	35-45	55-62
$Z_{chamber}$ (mm)	14	13	13
A_{entry} (m^2)	4.48E-04	5.72E-04	3.92E-04
$V_{chamber}$ (m^3)	9.17E-05	2.35E-05	1.25E-05

The arrow in Table 3 indicates the streamwise flow direction relative to the detector profile. The range of values cited for the aerosol entry height, z_{entry}, represent the upper and lower bounds of this dimension relative to the ceiling. The internal height of the sensing chamber is denoted as $z_{chamber}$. The entry area of the detector was determined from measurements of the openings in the exterior housing of the detector perpendicular to the bulk flow direction (180 degrees). The interior volume of the sensing chamber is denoted as $V_{chamber}$.

A piece of silica glass with nominal dimensions of 38mm in diameter and 3mm thick was added to the sensing chamber of the photoelectric and ionization detectors to provide optical access to the inner portion of the sensing chamber. Figure 15 shows a photoelectric detector with optical access in comparison to the same detector model.

Figure 15 -- Photoelectric smoke detectors with (l), and without (r) optical access.

2.3 Laser Doppler Velocimetry

A TSI[2] two-component Laser Doppler Velocimeter operating in direct backscatter mode was used to measure velocity. The LDV consisted of a Spectra-Physics Stabilite 2017 Argon-Ion laser with a maximum power output of 5W. The multimode laser beam was separated into green (514.5nm), blue (488.0nm), and violet (476.5nm) wavelengths by a Colorbust beam separator. Only the green and blue wavelengths were used in this study. Fiberoptic couplers transmitted the laser light to the fiber optic probe. The photodiode receiver was integral to the fiberoptic probe, therefore, the system operated in the direct backscatter mode.

---

[2] Specific commercial products are identified in this paper for the purpose of adequately describing the research methodology. In no case does such identification imply recommendation or endorsement by the authors and sponsors, nor does it imply that the commercial products identified are the best available for the purpose.

The beam half angles out of the probe were 3.95° and the focal distance to the measurement point was nominally 350mm (TSI, 1998). The ellipsoid measurement volumes formed by each pair of laser beams were coincident and had nominal dimensions of 90μm wide by 1.3mm long (TSI, 1998). The flow was seeded with atomized vegetable oil using a TSI six-jet atomizer with 15psi of dilution air.

3. Procedure
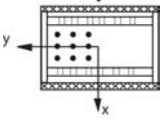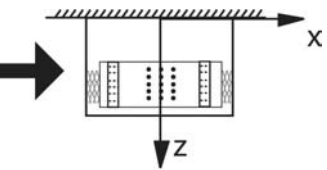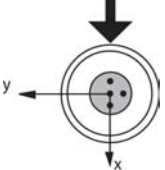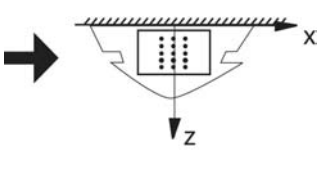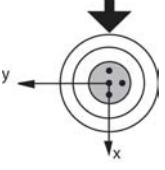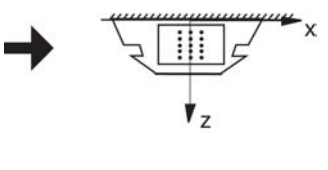
The streamwise velocity profiles in the FE/DE for different fan speeds were characterized with the LDV (Appendix A.2). The suitability of the LDV was verified with a comparison to velocity measurements made by a thermal anemometer (Appendix A.2). Two prototype experiments were conducted to assess the capability of measuring velocity inside the sensing chamber through an optical window with the LDV (Appendix A.2). The internal velocity measurements made for the rectangular, photoelectric, and ionization detectors were used to develop an inlet velocity boundary condition for a smoke detector mass transport model.

33.3 Internal Velocity Measurements

Internal velocity measurements were made using the LDV for a rectangular smoke detector model as well as actual photoelectric and ionization-type smoke detectors under steady state flow conditions in the FE/DE. Each planar measurement location for the rectangular model detector was aligned along the centerline in the streamwise direction of an interior baffle opening and were chosen due to the availability of seed particles along

these streamwise locations. Attempts to measure velocity profiles behind the baffle obstructions were unsuccessful and was attributed to insufficient seed particles present in the shadow of the obstruction. The photoelectric and ionization detectors were oriented in the least favorable position for aerosol entry. Plan and section views of the measurement locations for all three detector types are shown in Table 4. The arrow indicates the direction of the flow relative to the plan or section view of the respective detector. The figures shown in Table 4 are intended to provide a general indication of the locations used for the LDV measurements of internal velocity. These measurement locations were generally symmetric with respect to the optical access window and the internal height of the sensing chamber.

Table 4 -- Plan and section views of detector measurement locations with x, y, and z values.

Detector	Plan View	X,Y (mm)	Section View	Z (mm)
Rectangular		(-10,5), (0, 5), (10, 5), (-10,15), (0,15), (10, 15), (-10,25), (0,25), (10,25)		50, 52, 54, 56, 58
Photo		(0,0), (-10,0), (0,-10), (10,0)		38, 40, 41, 42, 44
Ion		(0,0), (-10,0), (0,-10), (10,0)		56, 57, 57.5, 58, 59

4. Results and Discussion

The results of internal velocity measurements using Laser Doppler Velocimetry are presented. These results include the rectangular model with and without the insect screen in place as well as for the photoelectric and ionization detectors. The velocity data sets were used to develop and inlet velocity boundary condition for use in a mass transport model for smoke detector response (see Model Paper).

4.1 Internal Velocity

4.1.1 Screening Criteria for LDV Data Points

4.1.4 Internal Velocity Results

The screening method described in Appendix A.3 was applied to the internal velocity measurements for all detector types in order to identify and remove anomalous data points. The screening process required a minimum number of 10 valid data points and a turbulence intensity (standard deviation expressed as a percentage of time averaged velocity measurement) of less than 100%. The time averaged velocity values for the insect screen used in the prototype experiments as well as the rectangular model, photoelectric, and ionization detectors are plotted as a function of the average external velocity is shown in Figure 16. The y error bars represent one statistical standard deviation in the measurement and were used as an estimate of the measurement uncertainty. The uncertainty in the LDV measurements was characterized as the statistical standard deviation at each measurement point. The standard deviation was typically displayed as error bars in the data plots and also described in terms of the percentage of the corresponding mean velocity value
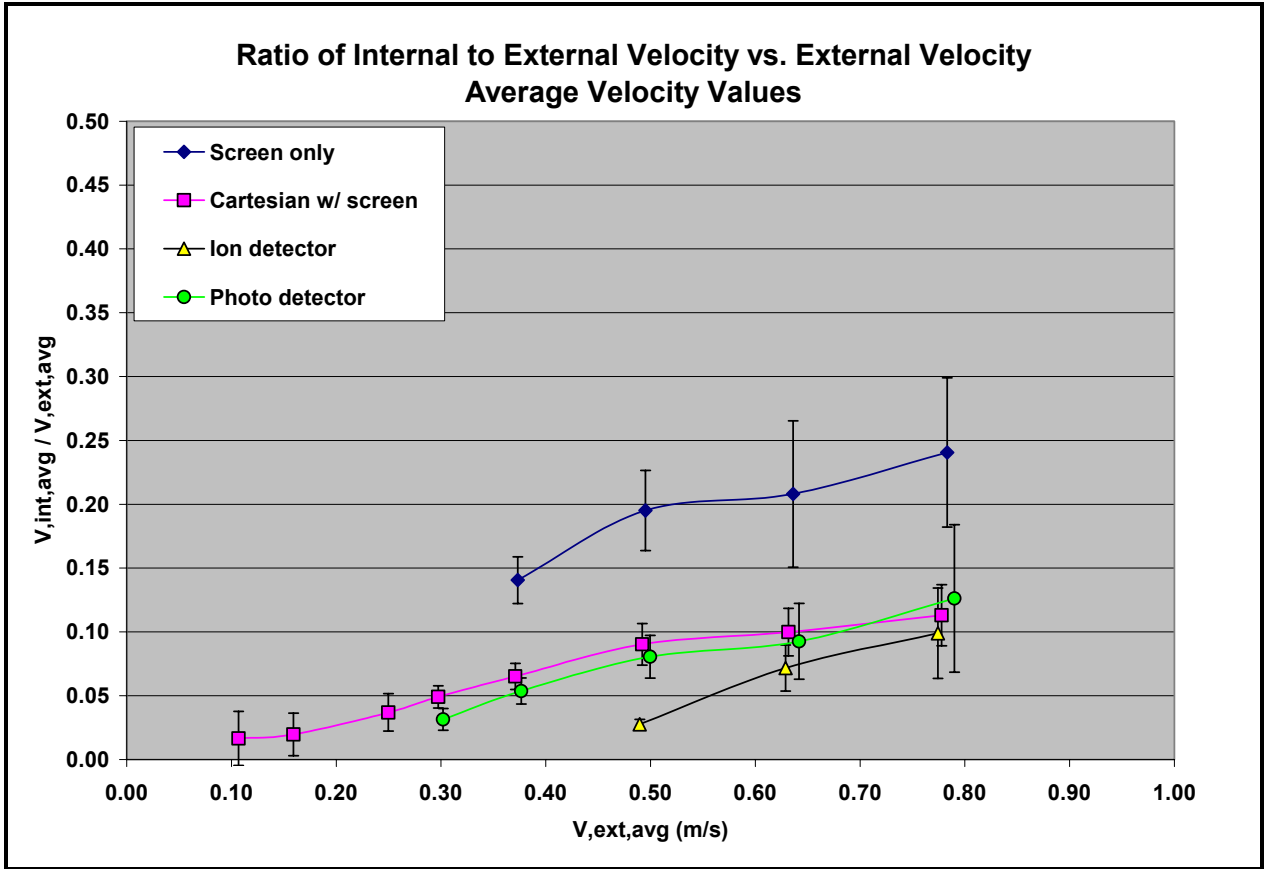
Figure 16 – Ratio of internal to external velocity vs external velocity for screen, model detector, as well as photo and ion detectors.

The comparison of internal velocities as a function of external velocity indicates that the insect screen in isolation has a lower degree of resistance to the flow compared to the rectangular, ionization, and photoelectric detectors. The screen in isolation has internal velocities that are nominally 4 to 7 times smaller than the external velocity. The rectangular detector has internal velocities that are nominally 8 to 60 times smaller than the external velocity. The photoelectric and ionization detectors have internal velocities that are nominally 8 to 36 times smaller than the external velocity. These trends indicate a consistent pattern where more restrictive elements in the photo and ion detectors

experience a larger degree of entry resistance as reflected in the significantly larger reduction in velocity relative to the external velocity.

4.3 Viscous Flow Analysis

4.4 Inlet Velocity Boundary Condition

An inlet velocity boundary condition was developed using the velocity measurements made in this study in order to relate external flow conditions and detector geometry to the internal velocity in smoke detectors. In this study it has been demonstrated that the insect screen introduces a significant amount of resistance to the external flow (Appendix A.4). The development of the inlet velocity boundary condition is summarized and a more detailed explanation is provided in Appendix C.3.

Existing incompressible pressure drop correlations for flow through an insect screen were identified from various sources in the fluid mechanics literature (Brundrett, 1993, Baines and Peterson, 1951, Munson, 1988). These correlations share the same general form in relating the upstream velocity and geometric characteristics of the insect screen to the pressure drop. These correlations were examined but were found to be inappropriate for the smoke detector mass transport problem. The existing incompressible pressure drop correlations for insect screens were developed for pipe flow situations where the insect screen occupied the entire cross section of the flow region. Therefore, the entire mass flow rate of fluid upstream of the screen would pass through the screen. For the smoke detector mass transport problem, the insect screen and detector profile occupy a fraction of the flow field. This situation applies to detectors in the FE/DE as well as ceiling

mounted smoke detectors exposed to a ceiling jet from a fire. In these situations a portion of the upstream flow is diverted underneath the detector and a portion passes through the insect screen. In this situation mass is conserved over the entire cross sectional area of the duct or ceiling jet region.

Therefore, a method was devised to account for this flow situation for an insect screen occupying only a portion of the entire flow field. This approach is semi-empirical as it uses elements from fluid mechanics theory and empirical data from research literature as well as data from this study. Therefore, this approach cannot be considered a rigorous treatment of the physics involved in fluid flow through the insect screen for the smoke detector mass transport problem. Developing a general form of the resistance coefficient that is dependent upon both geometry and Reynolds number is beyond this scope of this work. Rather, an engineering relationship has been developed that expresses the ratio of internal to external velocity as a function of the Reynolds number. The particular expressions that have been developed are valid for the specific detector geometries and flow conditions used in this study. These expressions should not be used beyond the experimental conditions presented in this work nor should they be applied to different detector geometries. The development of a general smoke detector resistant correlation that is a function of both geometry and flow conditions would require detailed measurements of velocity for a wide range of Reynolds numbers and detector geometries.

The principle of conservation of mass forms the basis for this analysis. Observations from the fluids mechanics literature, and where appropriate, confirmation from the

experiments conducted in this study are applied to characterize the flow field. Portions of the flow field approaching the detector profile are assumed to be deflected underneath the detector. For the purposes of this analysis, the mass flow associated any part of the flow field perpendicular to a solid area of the detector is assumed to be deflected underneath the detector. The mass flow associated with any part perpendicular to the insect screen is assumed to have a portion deflected underneath the detector and the remaining portion is transported across the insect screen.

Concepts from previous studies of incompressible fluid flow for insect screens occupying the entire cross section of a pipe or duct are used as the foundation for developing a resistance factor for smoke detectors. This resistance factor is a function of screen porosity and wire Reynolds number of the screen. A screen porosity function commonly used in insect screen resistance correlations for incompressible flow and screens occupying the entire cross section has been applied in developing the resistance factor for smoke detectors. Velocity measurements up and downstream of an insect screen from this study are used to determine the functional dependence of the resistance factor on the wire Reynolds number.

4.4.1 Control Volume

The control volume is chosen to be slightly upstream and downstream of the detector's leading edge as shown in Figure 17. It has been assumed that the boundaries of the control volume are in regions of fully developed flow conditions and do not account for

the mixing processes expected to occur at the leading edge of the detector as well as in the developing flow region downstream of the insect screen within the detector.
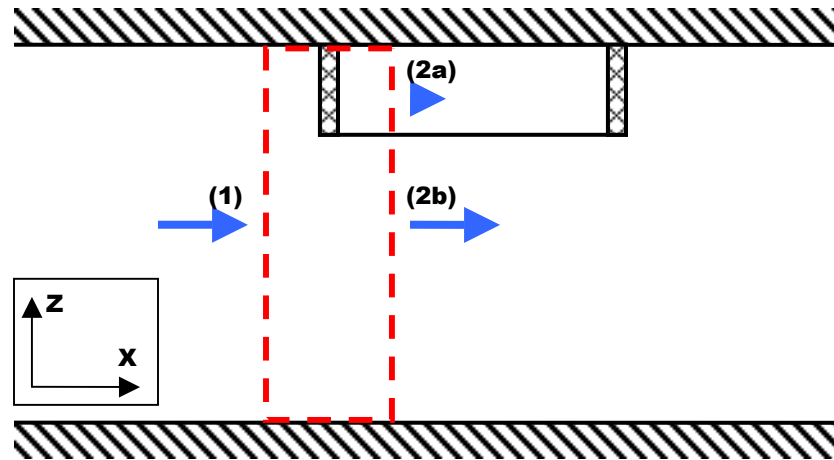
Figure 17 -- Mass conservation across FE/DE duct cross section.

The flow conditions have been assumed to be two-dimensional with the flow variation occurring in the x and z directions only. The width of the detector is assumed to be large with respect to the duct width and located far from the boundary layer on the sides of the duct.

The velocity profiles in each region are assumed to have the following characteristics as shown in Figure 18.
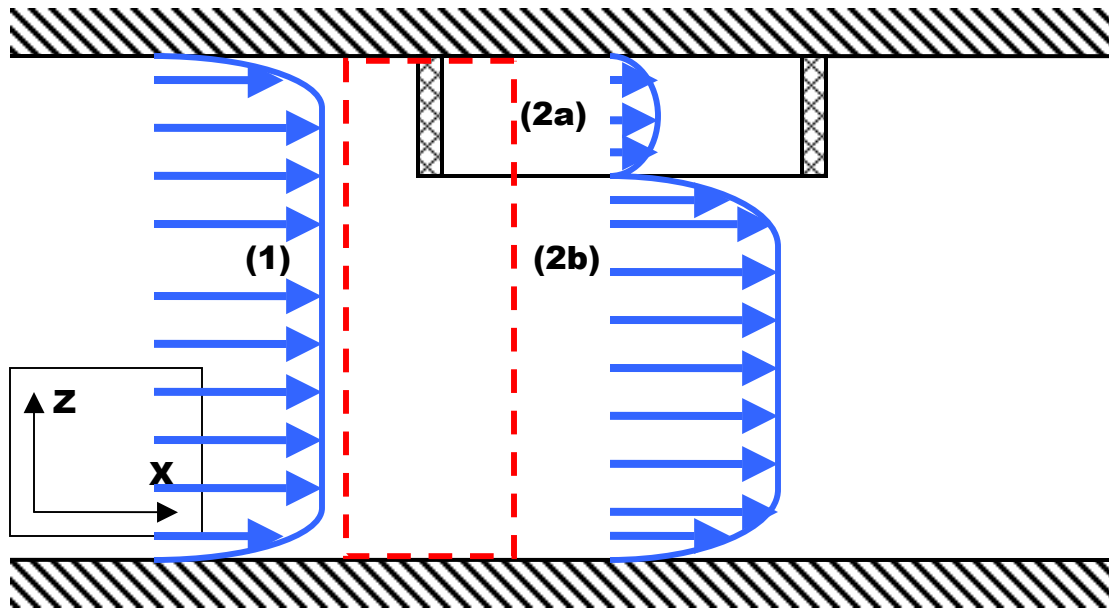
Figure 18 -- Assumed velocity profiles upstream and downstream of control volume.

In regions (1) and (2b) the velocity profile is assumed to be turbulent. This is based partially on a Reynolds number calculation for a rectangular duct and range of velocities examined in this study and shown in Appendix A.5. This calculation was confirmed with LDV measurements of the velocity profile in this region as shown in Appendix A.5. The velocity profile in region (2a) is assumed to be laminar based on previous work on flows through insect screens (Baines and Peterson, 1951) and was confirmed in this study with LDV measurements of internal velocity profiles for the rectangular detector as shown in Appendix A.5.

This approach uses a one-dimensional approximation of the external and internal velocity fields. The LDV velocity measurements and subsequent analysis demonstrated that the external flow field had turbulent characteristics and the internal flow field had laminar

characteristics. Therefore, a turbulent velocity profile was assumed for the external flow field and a laminar velocity profile for flow between two parallel plates was assumed for the internal flow field. The one-dimensional velocity values for the external and internal flow fields were determined by integrating the assumed velocity profile over the vertical height of interest. For the external flow field the vertical height of interest was the entrance height of the detector. For the internal flow field the vertical height of interest was the height of the sensing chamber. The integration process resulted in an average one-dimensional velocity that characterizes the external and internal velocity in the areas of interest to the inlet boundary condition. The relationship between the measured values, assumed velocity profiles, and the integrated one-dimensional average velocity values is illustrated in Figure 19.
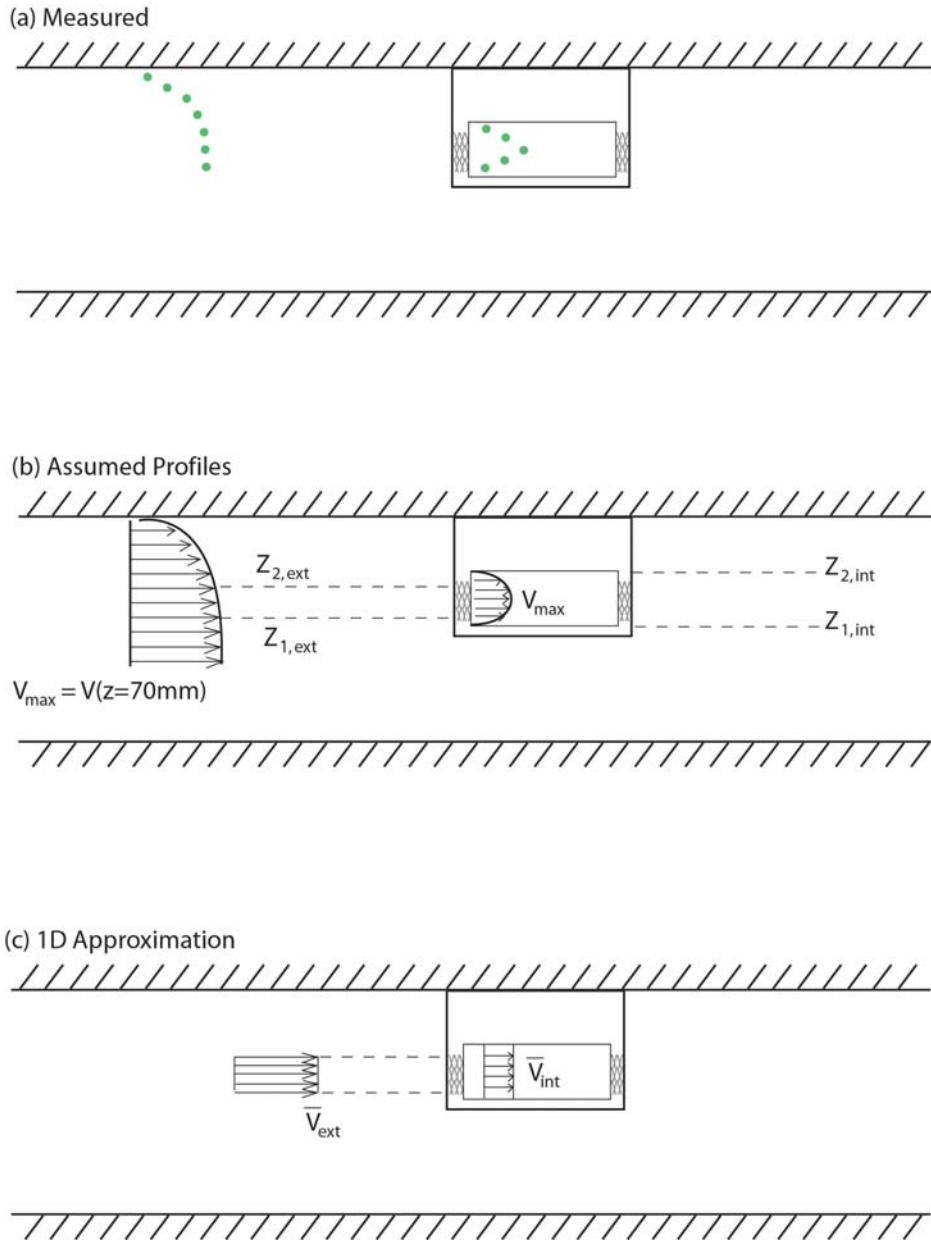
Figure 19-- Streamwise velocity profiles (a) typical LDV measurements, (b) assumed velocity profiles, and (c) and 1-D approximation used in inlet boundary condition.

4.4.2 Conservation of Mass

Mass is conserved on each boundary of the gas phase control volume for each region.

$$\dot{m}_{(1)} = \dot{m}_{(2a)} + \dot{m}_{(2b)}$$

(28)

The mass flux of fluid can be expressed as the product of fluid density, area perpendicular to the flow direction, and the average one-dimensional velocity.

$$\rho A_{(1)} \bar{V}_{(1)} = \rho A_{(2a)} \bar{V}_{(2a)} + \rho A_{(2b)} \bar{V}_{(2b)}$$

(29)

The perpendicular area for each region can be specified in the following manner, assuming that the width of the region is much larger relative to the height.

$$\rho y z_{(1)} \bar{V}_{(1)} = \rho y z_{(2a)} \bar{V}_{(2a)} + \rho y z_{(2b)} \bar{V}_{(2b)}$$

(30)

The values of fluid density and width are the same in all three terms and can be eliminated.

$$z_{(1)} \bar{V}_{(1)} = z_{(2a)} \bar{V}_{(2a)} + z_{(2b)} \bar{V}_{(2b)}$$

(31)

The mass flow rates at each of the three regions identified in Figure 18 were determined from the average one-dimensional velocity. The average one-dimensional velocity in each region was determined by integrating over the velocity profile. As mentioned

61

previously, the velocity profiles were assumed to be turbulent in regions (1) as well as (2b) and assumed to be laminar within the detector in region (2a).

4.4.3 Average Velocity for Laminar Velocity Profile

The average one-dimensional velocity within the detector was developed by integrating over the laminar velocity profile for incompressible flow between parallel plates and dividing by the height (Appendix C.3).

$$\bar{u} = \frac{2}{3} u_{max}$$

(32)

4.4.4 Average Velocity for Turbulent Velocity Profile

The average external velocity was determined by integrating the turbulent velocity profile over the height of interest and dividing by the associated distance (Appendix C.3).

$$\bar{u} = \frac{-\dfrac{7Uh}{8}\left[\left(1-\dfrac{z_2}{h}\right)^{8/7}-\left(1-\dfrac{z_1}{h}\right)^{8/7}\right]}{\left(z_2-z_1\right)}$$

(33)

4.4.5 Screen Resistance

The screen resistance for a smoke detector can be developed by considering the impact of the solid and open portions of the detector on the flow field. The flow is assumed to be two-dimensional as shown in Figure 20.
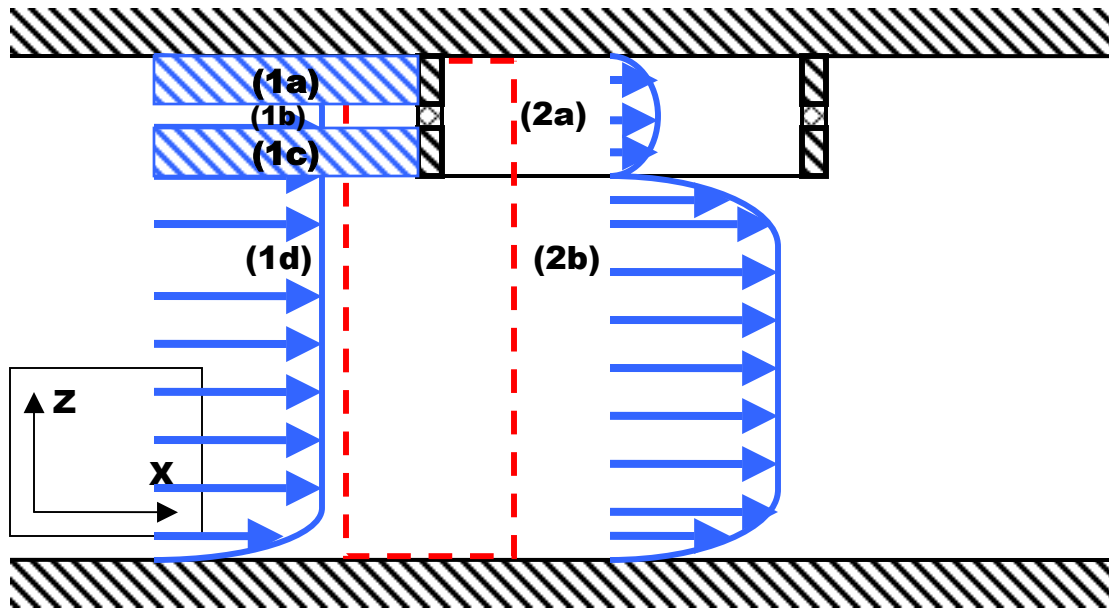
Figure 20 -- Assumed two-dimensional velocity profiles where shaded portions are assumed to be deflected.

The mass flow associated with the solid portions of the detector, indicated as areas (1a) and (1c), are assumed to be deflected below the detector. In the case of a detector with no openings, the entire mass flow perpendicular to the solid profile would be deflected underneath the detector, conserving the total mass flow. The mass flow associated with the detector opening is assumed to have a portion deflected underneath the detector and the remaining portion transported across the insect screen.

A resistance factor, R, is introduced to relate the resistance to the screen geometry and wire Reynolds number. The resistance coefficient, K, developed for insect screens occupying the entire cross section for incompressible pipe flow conditions was used as an example in the development of the resistance factor. The term *resistance factor* and the associated variable R will be used to distinguish it from the resistance coefficient

developed for incompressible pipe flow through insect screens. For incompressible pipe flow, the resistance coefficient of the screen is typically expressed as a function of the screen porosity and Reynolds number (based on wire diameter) (Munson, 1988).

$$K = K(\alpha, \mathrm{Re}_d)$$

(34)

One particular function for screen porosity, α, that has shown widespread agreement in the development of incompressible screen resistance correlations is (Brundrett, 1993)

$$f(\alpha) = \frac{\left(1 - \alpha^2\right)}{\alpha^2}$$

(35)

The wire Reynolds number, Re_d, is based on the external flow velocity and hydraulic diameter of the insect screen openings. In this formulation the average external velocity was used and was determined by integrating the velocity profile over the aerosol entry height of a given detector.

$$\mathrm{Re}_d = \frac{\bar{V}_{ext} d_{screen}}{\nu}$$

(36)

The porosity function and wire Reynolds number will be applied in the development of the resistance factor for smoke detectors. Therefore, the resistance factor for smoke detector insect screens can be expressed in general as

64

$$R = \left(\frac{1-\alpha^2}{\alpha^2} \right) f\left(\mathrm{Re}_d\right)$$

The functional dependence upon the wire Reynolds number was determined by applying the internal velocity data sets collected in the experimental portion of this study.

The assumed velocity profiles at the entrance region of the detector are shown in Figure 21.
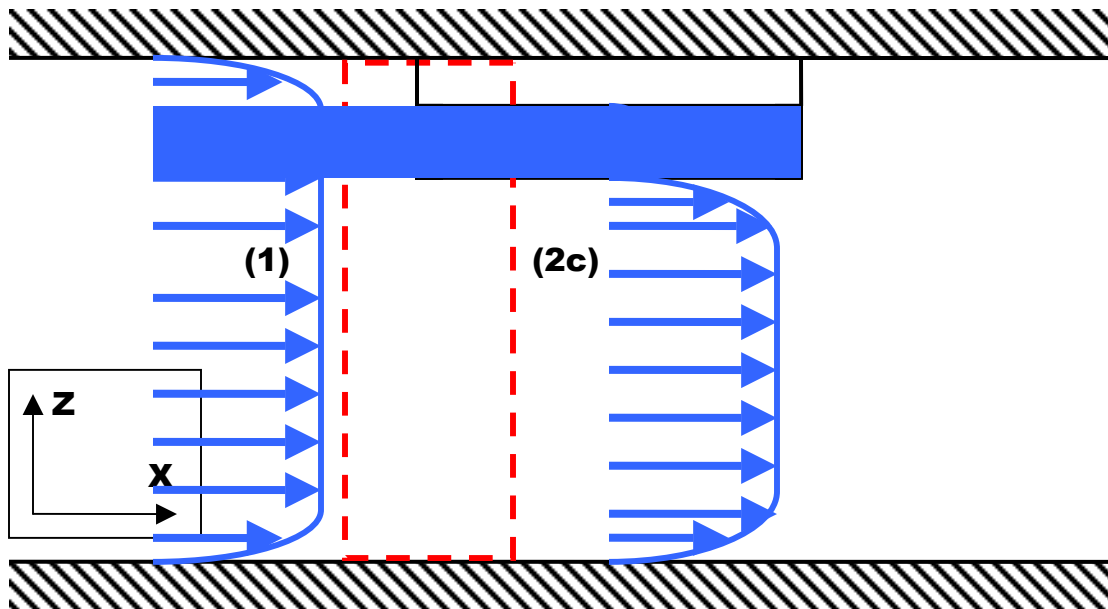
Figure 21 -- Assumed velocity profiles for arbitrary detector where shaded portion is area of interest.

Mass is conserved across the entire cross section. It is assumed that mass is conserved across the insect screen (indicated as the shaded portion in Figure 21 above) in the

following manner; a portion of the upstream mass is deflected underneath the detector and the remaining portion of the upstream mass passes through the screen. The control volume for mass conservation at the detector entrance area is shown in Figure 22.
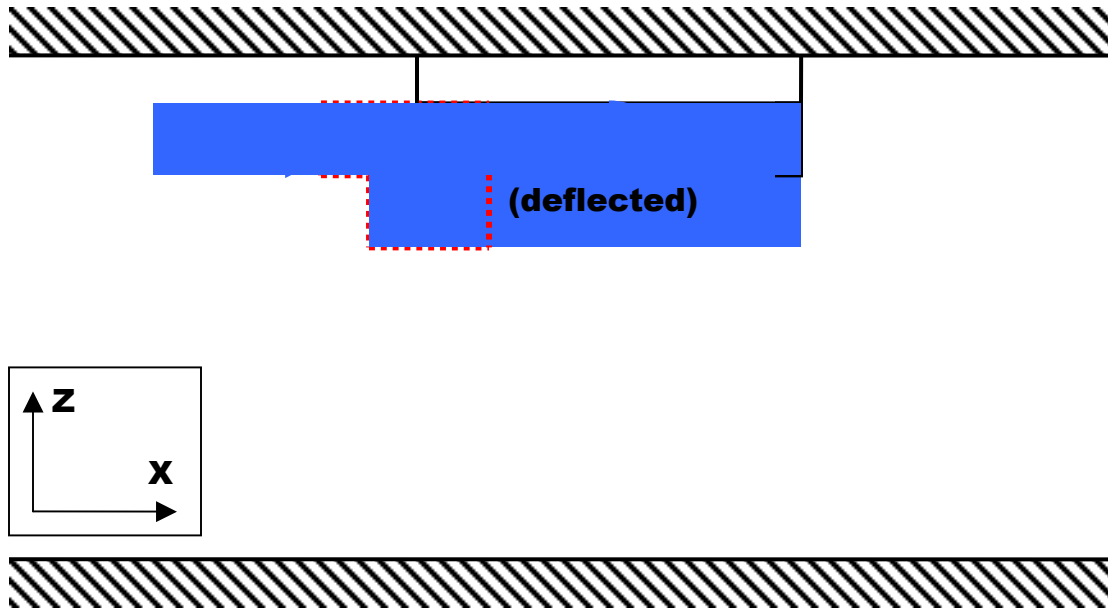
Figure 22 – Control volume at detector entrance region indicating portions of upstream flow that are deflected and transported across screen.

The mass conservation for this situation is expressed as

$$\dot{m}_{(1b)} = \dot{m}_{(2b)} + \dot{m}_{(deflected)}$$

(38)

Expanding the mass flow rate terms on each side yields

$$\rho A_{(1b)} \overline{V}_{(1b)} = \rho A_{(2b)} \overline{V}_{(2b)} + \rho A_{(deflected)} \overline{V}_{(deflected)}$$

$$(39)$$

The density for each area is constant and leads to the following simplification.

$$A_{(1b)} \overline{V}_{(1b)} = A_{(2b)} \overline{V}_{(2b)} + A_{(deflected)} \overline{V}_{(deflected)}$$

$$(40)$$

However, the area and velocity of the deflected portion of the flow were not measured as part of this study. Instead, the mass conservation equation was reformulated to express the deflected mass flow as a fraction, X, of the upstream mass flow in the following manner.

$$\dot{m}_{(1b)} = \dot{m}_{(2b)} + X\dot{m}_{(1b)}$$

$$(41)$$

Equating the upstream mass flows from the mass conservation equation at the insect screen leads to

$$(1 - X)\dot{m}_{(1b)} = \dot{m}_{(2b)}$$

$$(42)$$

Dividing the internal mass flow by the external mass flow

$$\frac{\dot{m}_{(2b)}}{\dot{m}_{(1b)}} = (1 - X)$$

$$(43)$$

The mass flow terms can be expanded to yield

$$\frac{\rho A_{(2b)} \bar{V}_{(2b)}}{\rho A_{(1b)} \bar{V}_{(1b)}} = (1 - X)$$

$$(44)$$

The density and areas for regions 1b and 2b are the same and the quantity *(1-X)* can be expressed as the resistance factor, *R*. These simplifications lead to the following result.

$$\frac{\bar{V}_{(2b)}}{\bar{V}_{(1b)}} = R$$

$$(45)$$

This expression for the resistance factor is consistent with experimental measurements conducted as part of this study as the two velocities are not expected to be the same due to the resistance of the insect screen. The resistance factor is used to relate the external to the internal average velocity. This specific formulation relates the nondimensional velocity (average internal velocity scaled to average external velocity) to the resistance factor. At this point the subscripts for the internal and external velocity values are

changed from *(1b)* and *(2b)* to the more descriptive *int* and *ext* for the remainder of this development.

$$V* = \frac{\overline{V}_{(1b)}}{\overline{V}_{(2b)}} = \frac{\overline{V}_{int}}{\overline{V}_{ext}} = R$$

(46)

The general form of the resistance factor can be substituted to expand this expression to

$$\frac{\overline{V}_{int}}{\overline{V}_{ext}} = f\left(\frac{1-\alpha^2}{\alpha^2}\right)(\mathrm{Re}_d)$$

(47)

The average external velocity was determined by integrating the turbulent approach velocity profile between the aerosol entry locations and dividing by the height of the opening for the range of velocities. The average velocity for the external turbulent profile was determined to be within the region where the power law velocity profile is valid. The literature indicates that this region exists at a *y/h* distance greater than 0.19 from the wall surface. For the FE/DE, *h* would be equal to 0.167m (half height of duct test section) and results in a distance of *y* greater than 32mm from the wall being within the region governed by the power law velocity profile. This distance is less than the highest aerosol entry location of 38mm on the photoelectric detector. Therefore, integrating the approach velocities with the turbulent velocity profile is appropriate for the range of detectors examined in this study.

69

The average internal velocity was determined from the previous development for laminar velocity profiles. The maximum internal velocity value was multiplied by 2/3 in order to obtain the average velocity. The sections that follow summarize the external average velocity and the corresponding average internal velocity values for the insect screen in isolation as well as the detectors examined in this study.

4.4.6 Insect Screen in Isolation

The integration points for determining the average external velocity were from 42 to 55 mm in the z direction. The following results provide the time averaged (mean) velocity, statistical standard deviation of the velocity measurement, and the turbulence intensity (V TI%) which is the standard deviation expressed as a percentage of the time averaged velocity value.

Table 5 – Time averaged and integrated velocity values for screen in isolation.

	FE/DE Time Avg Velocity Profiles			Screen in Isolation				
Fan (Hz)	V,mean (m/s)	Std dev	V TI%	V,ext,avg	V,int,max	V,int,avg	Std dev	V TI%
30	0.822	0.048	5.85	0.783	0.283	0.188	0.044	15.70
25	0.668	0.045	6.71	0.636	0.198	0.132	0.035	17.78
20	0.520	0.035	6.81	0.495	0.145	0.097	0.014	9.60
15	0.392	0.028	7.20	0.373	0.079	0.052	0.006	7.09

4.4.7 Rectangular Model Detector with Insect Screen

The integration points for determining the average external velocity were from 50 to 58 mm in the z direction.

Table 6 – Time averaged and integrated velocity values for rectangular detector with screen.

Fan (Hz)	FE/DE Time Avg Velocity Profiles			Cartesian Detector W/Screen				
	V,mean (m/s)	Std dev	V TI%	V,ext,avg	V,int,max	V,int,avg	Std dev	V TI%
30	0.822	0.048	5.85	0.778	0.132	0.088	0.018	13.53
25	0.668	0.045	6.71	0.632	0.095	0.063	0.011	11.45
20	0.520	0.035	6.81	0.492	0.067	0.044	0.007	11.04
15	0.392	0.028	7.20	0.371	0.036	0.024	0.003	9.17
12	0.314	0.027	8.70	0.297	0.022	0.015	0.002	10.29
10	0.264	0.026	9.84	0.250	0.014	0.009	0.004	25.66
7	0.168	0.027	16.07	0.159	0.005	0.003	0.003	55.54
5	0.113	0.025	22.07	0.107	0.003	0.002	0.002	84.31

4.4.8 Photoelectric Detector

The integration points for determining the average external velocity were from 38 to 44

mm in the z direction.

Table 7 – Time averaged and integrated velocity values for rectangular detector with screen.

Fan (Hz)	FE/DE Time Avg Velocity Profiles			Photoelectric Detector				
	V,mean (m/s)	Std dev	V TI%	V,ext,avg	V,int,max	V,int,avg	Std dev	V TI%
30	0.822	0.048	5.85	0.790	0.149	0.100	0.045	30.26
25	0.668	0.045	6.71	0.642	0.089	0.059	0.019	20.91
20	0.520	0.035	6.81	0.500	0.060	0.040	0.008	13.04
15	0.392	0.028	7.20	0.377	0.030	0.020	0.004	11.74
12	0.314	0.027	8.70	0.302	0.014	0.010	0.002	17.00

4.4.9 Ionization Detector

The integration points for determining the average external velocity were from 56 to 59

mm in the z direction. It should be noted that only a limited number of velocity sets at

relatively high external velocities were found to be suitable. The ionization detector

features two sets of offset baffles and an insect screen. It is likely that these geometric

features limited the amount of seed particles entering the detection chamber for the

purposes of taking LDV measurements.

Table 8 – Time averaged and integrated velocity values for ionization detector.

Fan (Hz)	FE/DE Time Avg Velocity Profiles			Ionization Detector				
	V,mean (m/s)	Std dev	V TI%	V,ext,avg	V,int,max	V,int,avg	Std dev	V TI%
30	0.822	0.048	5.85	0.774	0.115	0.077	0.027	23.52
25	0.668	0.045	6.71	0.629	0.068	0.045	0.011	16.14
20	0.520	0.035	6.81	0.490	0.020	0.013	0.002	8.13

The average internal velocity was plotted against the average external velocity for the screen in isolation, the rectangular detector, ionization detector, and photoelectric detector.

Figure 23 -- Average internal velocity plotted against average external velocity.

It is interesting to note that the general trend indicates that the ratio of internal to external velocity decreases as the object's resistance to flow increases. The screen in isolation has a higher degree of resistance to the flow relative to the rectangular detector without the insect screen. This is demonstrated by the relatively lower ratio of internal to external velocity. The group consisting of the rectangular detector with the insect screen and the photoelectric and ionization detectors has the highest degree of resistance relative to the screen in isolation. This is demonstrated by the relatively low ratios of internal to external velocity.

The functional relationship between the nondimensional velocity to resistance factor terms for geometry and Reynolds number is developed in the discussion that follows.

The screen porosity, α, is the ratio of open area to the total area and was determined to be 0.664 for the insect screens used in all detectors tested in this study (Appendix C.3).

$$R = 1.268 f\left(\text{Re}_d\right)$$

(48)

Substituting this expression into the relationship between the nondimensional velocity and resistance factor leads to the following

$$\frac{\overline{V}_{int}}{\overline{V}_{ext}} = 1.268 f\left(\text{Re}_d\right)$$

(49)

The functional dependence upon the Reynolds number was determined by plotting the nondimensional velocity against the resistance factor terms. This plot, shown in Figure 24, indicated a linear relationship. A linear curve fit was applied with the constraint that the y intercept being equal to zero. This constraint satisfies the condition that as the Reynolds number approaches zero, the nondimensional velocity ratio goes to zero.
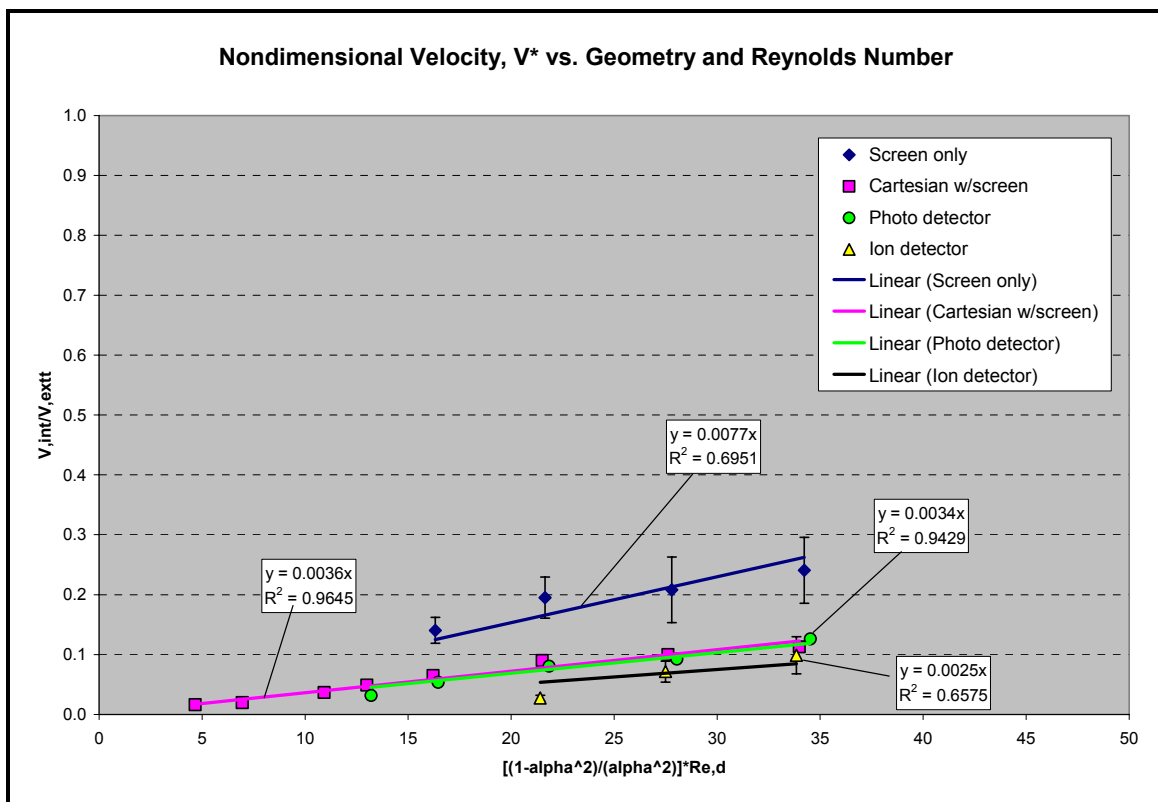
Figure 24 -- Nondimensional velocity plotted against the product of the porosity function and wire Reynolds number.

The error bars shown for the insect screen in isolation represents one statistical standard deviation in the associated velocity measurement and is used as estimate of the measurement uncertainty. The error bars indicate that the linear curve fit is within the

measurement uncertainty despite the relatively poor correlation coefficient. However, this poor degree of correlation can be partially attributed to the limited number of data points collected. Likewise, the limited number of data points collected for the ionization detector can be partially attributed to the poor degree of correlation as indicated by the R^2 value for the linear curve fit.

The following functional relationships resulted from the linear curve fitting procedure as shown above. The corresponding screen porosity and range of screen Reynolds numbers are indicated for each relationship.

Table 9 – Summary of resistance factors for insect screen and detectors.

Detector	Resistance Factor	Conditions
Isolated Screen	$\dfrac{\bar{V}_{int}}{\bar{V}_{ext}} = 0.0077\left[\left(\dfrac{1-\alpha^2}{\alpha^2}\right)\mathrm{Re}_d\right]$	$\alpha = 0.664 \ and \ 16 < \mathrm{Re}_d < 27$
Rectangular	$\dfrac{\bar{V}_{int}}{\bar{V}_{ext}} = 0.0036\left[\left(\dfrac{1-\alpha^2}{\alpha^2}\right)\mathrm{Re}_d\right]$	$\alpha = 0.664 \ and \ 5 < \mathrm{Re}_d < 34$
Photoelectric	$\dfrac{\bar{V}_{int}}{\bar{V}_{ext}} = 0.0034\left[\left(\dfrac{1-\alpha^2}{\alpha^2}\right)\mathrm{Re}_d\right]$	$\alpha = 0.664 \ and \ 10 < \mathrm{Re}_d < 27$
Ionization	$\dfrac{\bar{V}_{int}}{\bar{V}_{ext}} = 0.0025\left[\left(\dfrac{1-\alpha^2}{\alpha^2}\right)\mathrm{Re}_d\right]$	$\alpha = 0.664 \ and \ 17 < \mathrm{Re}_d < 27$

4.5 Uncertainty Analysis

The resistance factor correlations presented in the previous section can be used to predict the internal velocity of a smoke detector based on the external flow conditions and

geometric characteristics. This internal velocity from the resistance factor correlation could then used in a mass transport model to predict smoke detector response such as the mass transport model developed in Paper 3.

The resistance factor developed in Appendix C.3 is a function of the screen porosity and screen Reynolds number. The resistance factor for the photoelectric detector used to demonstrate various aspects of the analysis in the current study is

$$R = 0.0034 \left[\left(\frac{1-\alpha^2}{\alpha^2} \right) \mathrm{Re}_d \right]$$

(50)

The corresponding partial derivatives for the resistance factor are as follows:

$$\frac{\partial R}{\partial \left(\frac{1-\alpha^2}{\alpha^2} \right)} = 0.0034 \left[\mathrm{Re}_d \right]$$

(51)

$$\frac{\partial R}{\partial \mathrm{Re}_d} = 0.0034 \left[\left(\frac{1-\alpha^2}{\alpha^2} \right) \right]$$

(52)

The standard error propagation equation for the resistance factor is

$$s_R = \sqrt{\left(0.0034\left[\mathrm{Re}_d\right]\right)^2 s_{f(\alpha)}^2 + \left(0.0034\left[\left(\frac{1-\alpha^2}{\alpha^2}\right)\right]\right)^2 s_{\mathrm{Re}}^2}$$

<div align="right">(53)</div>

Where *s* represents the standard error (or estimated uncertainty) in the particular variable indicated in the subscript. For example, the estimated uncertainty in the resistance factor, *R*, is denoted as s_R. The determination of the estimated uncertainty in the screen porosity function *f(α)* and Reynolds number, *Re*, variables is provided in Appendix C.13. The analysis for determining the estimated uncertainty in the resistance factor, *s,R*, shows the nominal screen porosity value and the range of nominal external velocities as well as the associated uncertainty estimates on the left hand columns. These values were used as inputs to the standard error propagation equation. The nominal resistance factor value and estimated uncertainty – expressed in terms of the magnitude as well as a percentage of the nominal value – are indicated on the right hand side of the summary table that follows.

Table 10 – Summary of resistance factor uncertainty analysis.

Resistance Factor (Photo Detector)

Variable	Value	Uncertainty		R	s,R	%(s,R)
f(alpha)	1.268	0.213				
Re	21.14	1.90	==>	0.0911	0.0174	19.08
	15.93	1.48	==>	0.0687	0.0132	19.23
	12.78	1.34	==>	0.0551	0.0109	19.84
	10.74	1.23	==>	0.0463	0.0094	20.37
	6.84	1.17	==>	0.0295	0.0071	24.00
	4.59	1.05	==>	0.0198	0.0056	28.37
	3.11	0.99	==>	0.0134	0.0048	36.00

As shown in terms of a percentage of the nominal values above, the estimated uncertainty in the resistance factor is a function of screen Reynolds number and varies from 20 to 36% of the nominal value. This Reynolds number dependence will be used in determining the estimated uncertainty in subsequent variables that are a function of the resistance factor.

The standard error propagation equation was also used to determine the uncertainty in the interior velocity value calculated with the resistance factor. The details of this analysis are provided in Appendix C.13, however, a summary of the uncertainty estimate is discussed. The internal velocity is expressed as

$$v_{int} = R v_{ext}$$

(54)

The corresponding partial derivatives for the interior velocity are as follows:

$$\frac{\partial v_{int}}{\partial R} = v_{ext}$$

(55)

$$\frac{\partial v_{int}}{\partial v_{ext}} = R$$

(56)

The standard error propagation equation for the interior velocity is

$$s_{v_{int}} = \sqrt{\left(v_{ext}\right)^2 s_R^2 + \left(R\right)^2 s_{v_{ext}}^2}$$

(57)

The nominal values for external velocity and resistance factor as well as the associated uncertainty estimates are provided in the left hand side of the table that follows. These values were used as inputs to the standard error propagation equation. The nominal value of the internal velocity as well as the associated uncertainty (expressed as a magnitude and a percentage of the nominal value) are summarized on the right hand side.

Table 11 – Summary of internal velocity uncertainty analysis for photo detector.

Internal Velocity (Photo Detector)

V,ext (m/s)	s,V,ext (m/s)	R	s,R		v,int	s,v,int	%(s,v,int)
0.500	0.034	0.091	0.017	==>	0.04554	0.00923	20.26
0.377	0.027	0.069	0.013	==>	0.02587	0.00531	20.53
0.302	0.026	0.055	0.011	==>	0.01664	0.00361	21.67
0.254	0.025	0.046	0.009	==>	0.01175	0.00266	22.62
0.162	0.026	0.029	0.007	==>	0.00477	0.00138	28.89
0.108	0.024	0.020	0.006	==>	0.00214	0.00077	35.94
0.074	0.023	0.013	0.005	==>	0.00099	0.00047	47.69

As shown in the percentages above, the estimated uncertainty in the internal velocity is a function of external velocity and resistance factor. The estimated uncertainty values vary from 20 to 48% of the nominal value. This velocity dependence will be used in determining the estimated uncertainty in subsequent variables that are a function of the internal velocity such as the mass transport model described in Paper 3.

5. Conclusions

Velocity profiles inside a photoelectric, ionization, and a specially constructed rectangular detector model were measured with a two-component Laser Doppler Velocimeter. A series of prototype experiments confirmed the suitability of the using the LDV in the bulk external flow field as well as inside the sensing chamber where the effects of the optical glass and insect screen were accounted for.

The LDV measurements in the bulk flow region were used to determine that the external flow exhibited turbulent characteristics for the range of velocities considered in this study, 0.08 to 0.52 m/s. The LDV velocity measurements made inside the detectors revealed that the internal flow exhibited laminar characteristics based on both Reynolds number and a comparison to the analytic solution for laminar flow between fixed parallel plates. Previous studies of incompressible flow past insect screens (Baines and Patterson, 1951) also confirmed this finding.

The data sets collected in this study were used to develop an inlet velocity boundary condition that relates the external flow conditions and detector geometry to the internal velocity of the detector sensing chamber with the use of a *resistance factor*. Existing correlations for incompressible flow past insect screens presented in the fluid mechanics literature were used as a template for establishing the semi-empirical expressions for the detectors examined in this study.

The standard error propagation equation was used to estimate the uncertainty in the resistance factor as well as for the interior velocity calculated with the resistance factor. For external velocities ranging from 0.07 to 0.50 m/s, the resistance factor was determined to have nominal values in the range of 0.013 to 0.091 with an estimated uncertainty of 20 to 36%. The interior velocity calculated with the resistance factor was determined to have nominal values in the range of 0.001 to 0.045 m/s with an estimated uncertainty of 20 to 48%.

This approach characterized the detector geometry by the insect screen which is the most restrictive flow element. The influence of detector housing opening geometry in conjunction with the insect screen as a combined resistive element was beyond the scope of this study. Additional research is needed to adequately address the appropriate geometric characteristics to be used in developing a general form of the resistance factor correlation for smoke detectors. However, this initial investigation has shown that the typical uncertainty in the input variables results in an uncertainty propagation that is within the range of the uncertainty for the measured internal velocity values of the detectors examined in this study.

References

Adrian, R.J., "Laser Velocimetry," *Fluid Mechanics Measurements*, R.J. Goldstein (Ed.), Hemisphere, p. 155-240 (1983).

Baines, W.D., E.G. Peterson, "An Investigation of Flow Through Screens," *Transactions of the ASME*, vol. 73, pp.467-480, (1951).

Brundrett, E., "Prediction of pressure drop for incompressible flow through screens," *Journal of Fluids Engineering*, 155(2), pp. 239-242, (1993).

Cleary, T., M. Donnelly, W. Grosshandler, "The Fire Emulator / Detector Evaluator: Design, Operation, and Performance," AUBE '01 Conference Proceedings, (2001).

Munson, B.R., "Very Low Reynolds Number Flow Through Screens," *Journal of Fluids Engineering*, Vol. 110, pp. 462-463, (1988).

Munson, B.R., D.F. Young, T.H. Okiishi, *Fundamentals of Fluid Mechanics, 2nd Edition*, John Wiley & Sons, New York, NY, (1994).

Schetz, J.A., A.E. Fuhs, *Fundamentals of Fluid Mechanics*, John Wiley & Sons, New York, NY, (1999).

TSI Inc., "TSI System Training Workshop on Laser Doppler Velocimetry Manual," TSI, Inc., St. Paul, MN (1997).

TSI Inc., "Model 9800 Series Fiberoptic Probes Manual," TSI, Inc., St. Paul, MN (1998).

4 Paper 2: "An Experimental Study of Aerosol Entry Lag and Smoke Detector Response"

An Experimental Study of Aerosol Entry Lag and Smoke Detector Response

Abstract

An addressable photoelectric and ionization smoke detector were exposed to four different aerosol sources for a range of steady state external flow conditions in NIST's Fire Emulator / Detector Evaluator. The aerosol sources included smoldering cotton wicks, soot from a laminar propylene flame, and vegetable oil delivered using two different devices. The four aerosol sources were delivered as a step input exposure to the detector. Additionally, a limited number of ramp input exposures using nebulized vegetable oil were also performed. The external bulk flow velocities ranged from 0.08 to 0.52 m/s. A modified fire alarm panel was used to collect the signal output from the detectors during the exposure tests. The detector output data was then used to characterize the nature of aerosol entry lag and sensor response. The response data was reduced by considering the time to alarm for specific alarm points as well as by performing an exponential curve fit to obtain a characteristic response time. The data collected in this study was used to evaluate a mass transport model developed for smoke detectors.

Keywords: smoke detector response, entry resistance, Fire Emulator / Detector Evaluator

Nomenclature

A area normal to diffusion path [m^3]

c_m mass concentration [kg/m^3]

$D_{C,air}$ binary diffusion coefficient of carbon into air [cm^2/s]

L pathlength [m]

$m_{1,e}$ mass fraction of species 1 in medium e [dimensionless]

$\dot{m}_1$ mass flowrate of species 1 [kg/s]

M_i molecular weight of species i [g/m^3]

Ou percent obscuration of aerosol per unit length [%Ob/m]

P absolute pressure [kPa]

t time [s]

t_{ch} characteristic response time [s]

T temperature [K]

V_i molecular volume of species i [cm^3]

y_n normalized value [dimensionless]

Greek letters

λ wavelength [nm]

κ_λ extinction coefficient [m^{-1}]

ρ density [kg/m^3]

σ_s specific extinction area [m^2/g]

τ transmittance [dimensionless]

1. Introduction

A series of aerosol exposure tests were conducted using addressable photoelectric and ionization smoke detectors under steady state flow conditions in NIST's Fire Emulator / Detector Evaluator. Measurements of detector output as a function of time were made for the purpose of assessing the entry lag and response characteristics.

The photoelectric and ionization smoke detectors used in this study were addressable. The detector output was extracted as a function of time using a modified fire alarm panel. Four different aerosol sources were used in the exposure tests and included smoldering cotton wicks, soot from a laminar propylene flame, and vegetable oil delivered by two different devices. The geometric features of the detectors as well as additional details of the aerosol sources and FE/DE are described in the "Experimental Apparatus" section.

The procedures used in the ramp and step input exposure tests are found in Section 3. The results of the exposure tests and data reduction is presented in Section 4. Time to alarm was tabulated for different detector sensitivity settings. The detector output from the ramp exposure tests was normalized to itself and an exponential curve-fitting

procedure was used. This analysis led to the development of a characteristic response time and a detector response lag time.

The conclusions from this work are summarized in Section 5.

2. Experimental Apparatus

The exposure tests conducted in this study subjected addressable photoelectric and ionization-type smoke detectors to four different aerosol sources in the Fire Emulator / Detector Evaluator. The capabilities of the Fire Emulator / Detector Evaluator are presented, the four aerosol sources are described, and the addressable smoke detectors are discussed in the sections that follow.

2.1 Fire Emulator / Detector Evaluator

The Fire Emulator / Detector Evaluator is a single-pass wind tunnel that simulates ceiling jet conditions developed at NIST for the purpose of testing smoke and gaseous products detectors (Cleary, 2001). Environmental conditions such as velocity, temperature, and humidity as well as delivery of specific aerosol or gaseous products can be controlled. For the series of tests considered in this work velocity and aerosol delivery were the only input parameters of interest.

A schematic diagram of the FE/DE is shown in Figure 25. Velocity in the FE/DE is controlled by a variable speed fan at the beginning of the FE/DE system and was set to a

constant value during each test. Four different aerosol types were delivered in this series

of tests and are described in greater detail in Section 2.2. A section of ducting measuring

approximately 4m in length connects the aerosol injection location to a flow straightening

honeycomb screen and includes a 90° elbow. The flow straightening honeycomb screen

is connected to the FE/DE test section by a 1m section of ducting. The test section is

constructed out of Plexiglass and measures 1m in length by 0.67m in width by 0.33m in

height. Detectors are mounted to the top of the test section at a distance of approximately

1.2m from the flow straightening honeycomb screen. Instrumentation for characterizing

the environmental conditions is present in the test section, however, the only

measurements of interest in this study were laser transmittance of the aerosol and the

output signal from addressable smoke detectors.
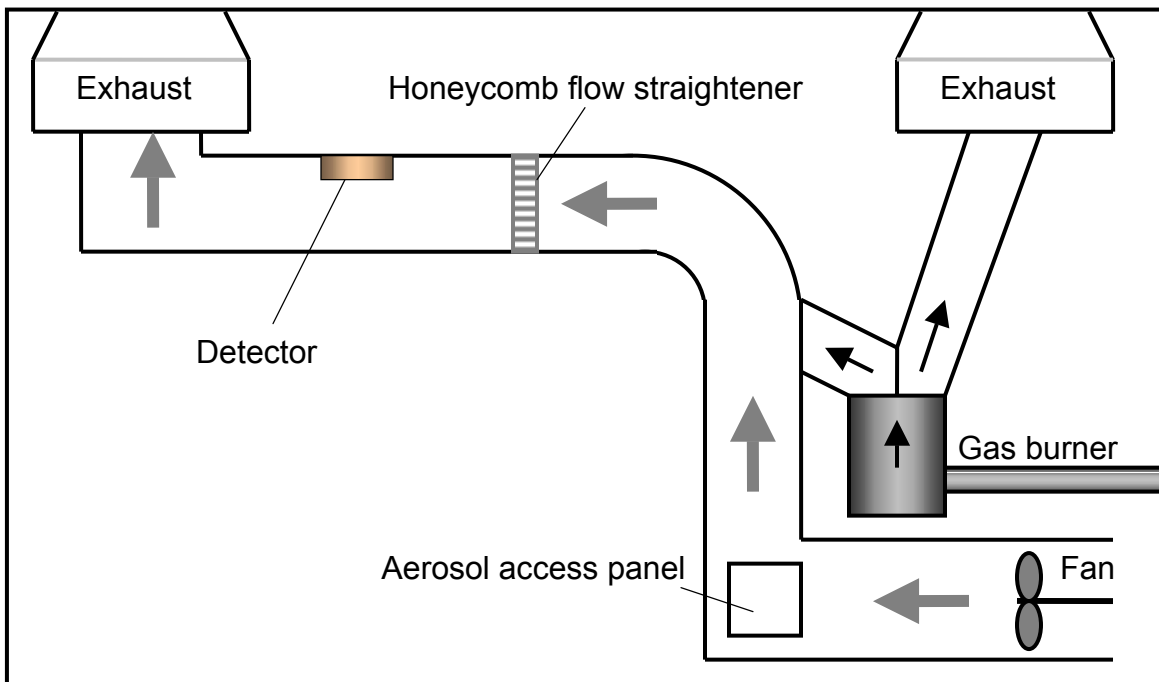
Figure 25 -- Schematic diagram of FE/DE.

2.1.1 Laser Transmittance

The laser transmittance measurement in the FE/DE test section uses a 500mW Helium-Neon laser source. The beam passes though a power filter that provides a constant power level out of the filter, despite fluctuations in input laser power. The beam passes though a 45° beam splitter that directs half the beam into the lower test section area at a 90° angle, while the other half continues in the vertical direction. The vertical half of the laser beam hits a 45° prism that directs the beam into the upper test section area at a 90° angle.

Each beam travels across the width of the test section and is redirected by a pair of mirrors. The redirected beams travel across the width of the test section to a second set of mirrors. The beams are redirected across the width of the test section a third time and terminate at photodiode receivers. The overall pathlength of the laser in the medium is 1.5m and each leg of the laser beam was approximately 1, 3 and 5cm from the edge of the detector base.
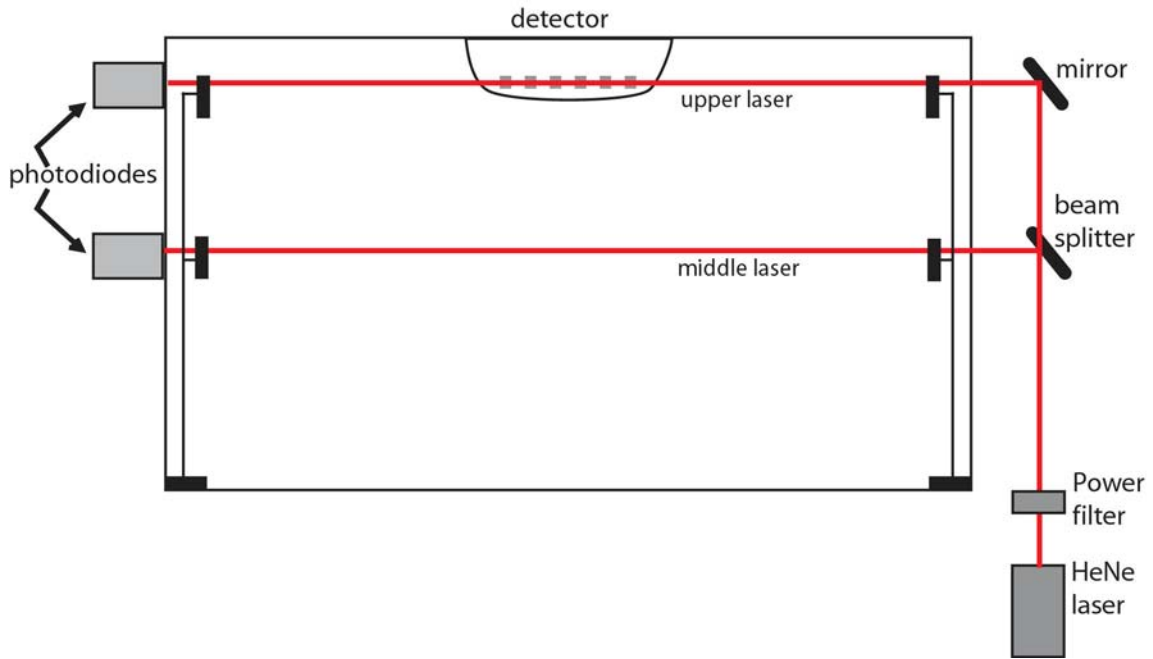
Figure 26 -- Section view of FE/DE laser transmittance measurement.
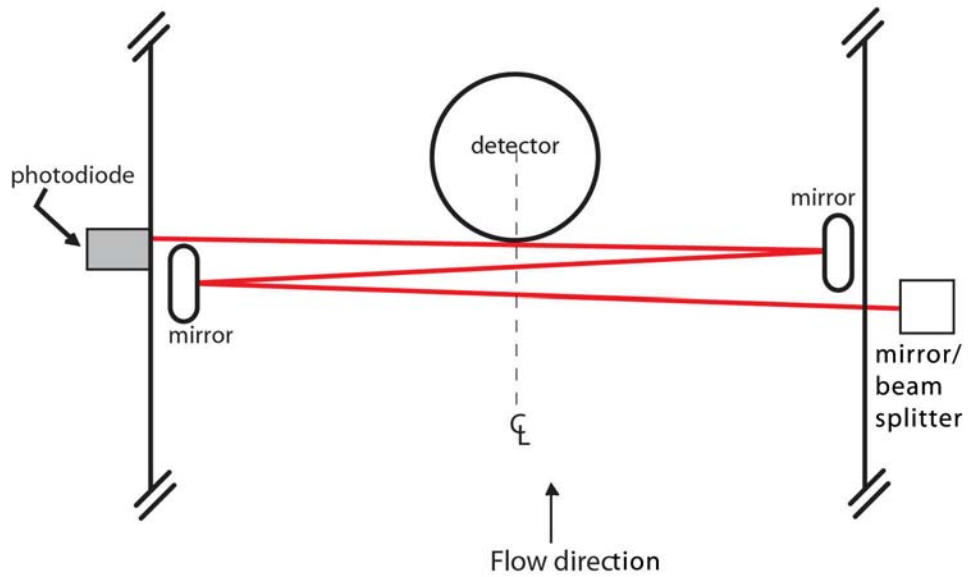
Figure 27 -- Plan view of FE/DE laser transmittance measurement.

89

2.2 Aerosol

Four types of aerosol were used; vegetable oil from a six-jet atomizer, vegetable oil from a nebulizer with an in-line impactor, smoldering cotton wicks, and soot from a laminar propylene flame. The details of each are provided in the sections that follow.

2.2.1 Vegetable Oil from Six-Jet Atomizer

Vegetable oil was atomized by operating a single jet of a TSI[3] six-jet atomizer to produce an aerosol source for the exposure tests. The atomizer air pressure was varied to produce nominally constant transmittance values for the range of external velocities. The appropriate air pressure setting was determined by keeping the external velocity constant and adjusting the air pressure until a nominally steady laser transmittance value was attained. This process was performed for all external velocities. Table 12 summarizes the atomizer air pressure settings for the photoelectric and ionization detectors at each external velocity used in the exposure testing. A higher concentration of particles was used for the ionization detector.

Table 12 -- Air pressure settings for single nozzle of six-jet atomizer.

V,ext (m/s)	Air (psi) Photo	Air (psi) Ion
0.52	16	38
0.39	14	30
0.31	13	26
0.26	12	23
0.17	11	20

[3] Specific commercial products are identified in this paper for the purpose of adequately describing the research methodology. In no case does such identification imply recommendation or endorsement by the authors and sponsors, nor does it imply that the commercial products identified are the best available for the purpose.

0.11	10	17
0.08	10	15

2.2.2 Vegetable Oil from Nebulizer with In-line Impactor

A second vegetable oil aerosol source with different particle size characteristics was generated using a nebulizer with an in-line impactor. The device was developed at NIST for the purpose of producing an aerosol source suitable for the field testing of smoke detectors (Lee, 1978). The impactor plate contains five holes that are 0.53mm in diameter (Lee, 1978). The aerosol output from the device was fixed, therefore, the aerosol concentration decreased for increasing external velocity because of dilution.

2.2.3 Smoldering Cotton Wicks

A smoldering fire source of cotton wicks was used to account for a more realistic aerosol source. Smoldering cotton wicks are a source considered in the UL and EN approvals testing. Pieces of cotton rope in 20cm lengths were suspended vertically with heating coils at the bottom end. The heating coils were turned on to initiate the smoldering of the cotton wicks. The number of cotton wicks used for each external velocity was varied in order to produce a nominally consistent value of transmittance at the test section. The cotton wicks used at each external velocity were the same for photoelectric and ionization detectors and are summarized in Table 13.

Table 13 -- Number of cotton wicks for range of external velocities.

V,ext (m/s)	# Wicks
0.52	16
0.39	12
0.31	10

0.26	8
0.17	6
0.11	4
0.08	3

2.2.4 Propylene Soot from Laminar Flame

A laminar propylene flame was used to produce soot to account for a combustion aerosol.

The exhaust system above the gas burner had two branches with one end connecting to

the FE/DE and the other end connecting to a separate exhaust hood (see Figure 25). Each

branch contained an adjustable damper. With the FE/DE supply damper fully closed and

the exhaust damper fully open, all the soot from the burner would be sent to the exhaust

hood. The FE/DE supply damper could be opened fully or partially to introduce soot into

the FE/DE. As with the cotton wicks and atomized vegetable oil sources, the amount of

propylene soot was adjusted at each external velocity to account for dilution and to

ensure a nominally consistent value of transmittance in the test section. In addition to

adjusting the dampers for the FE/DE supply and exhaust hood, the fuel and air supply

could be adjusted to change the fire size. The ratio of fuel to air was held constant. The

conditions for the dampers and the flowrates of propylene and air were the same for both

the photoelectric and ionization detectors and are summarized in Table 14.

Table 14 -- Settings for propylene soot over range of external velocities.

V,ext (m/s)	Supply (cm open)	Exhaust (cm open)	C_3H_6 (slm)	Air (slm)
0.31	3.60	4.7	0.4	40
0.26	2.85	4.7	0.4	40
0.17	2.70	4.7	0.4	40
0.11	2.60	4.7	0.4	40
0.08	2.50	4.7	0.4	40

2.3 Detectors

A photoelectric and an ionization smoke detector were evaluated in the aerosol exposure tests. Both were addressable detectors that were compatible with the same fire alarm panel.

2.3.3 Fire Alarm Panel

A modified fire alarm panel was used in conjunction with terminal communications software to extract the output signal for the addressable smoke detectors. The detector output signal is an 8-bit representation of the analog signal. The data collection interval for the detector output signal was approximately 0.5 seconds.

3. Procedure

Two types of exposure tests, ramp-type and step-type, were conducted under steady state flow conditions. The methods used for each type of aerosol exposure are described below. The photoelectric detector was evaluated at the least favorable orientation for aerosol entry and was also rotated 90 degrees. The ionization detector was evaluated in only a single orientation due to the symmetry of the detector.

3.1 Ramp Exposure Tests

An analog photoelectric smoke detector was exposed to atomized vegetable oil in the FE/DE for steady external velocities in the range of 0.11 to 0.52 m/s. A laser transmittance measurement was made at 45mm below the top of the FE/DE test section near the approximate aerosol entry location of the detector. The pathlength is 1.5m and

involves mirrors that create three passes through the width of the test section. The approximate locations of the three beams comprising the total pathlength were at 10, 20, and 30mm from the leading edge of the base of the detector.

The test began with 60 seconds of clean air at the fan speed of interest. The vegetable oil aerosol was delivered by a nebulizer with 20psi of dilution air and an impactor that limited the maximum particle size.

The aerosol was delivered after 60 seconds of clean air. The typical aerosol exposure lasted for 180 seconds and was shut off at 240 seconds. The output from the nebulizer was fixed and, therefore, the aerosol buildup phase was nominally linear until steady state conditions were achieved. The three phases of the ramp exposure tests are shown in Figure 28. The laser transmittance measurement was made by the FE/DE. The detector's analog output came from a modified fire alarm panel with it's own separate data acquisition. The system clocks for computers connected to the FE/DE and modified fire alarm panel were synchronized. The data acquisition process was also begun at the same time for each device to insure coincidence. The data acquisition file from both the FE/DE and the fire alarm panel were time-stamped. The time stamps were taken into account for any possible time shifting of data sets that were found not to commence at the same time.
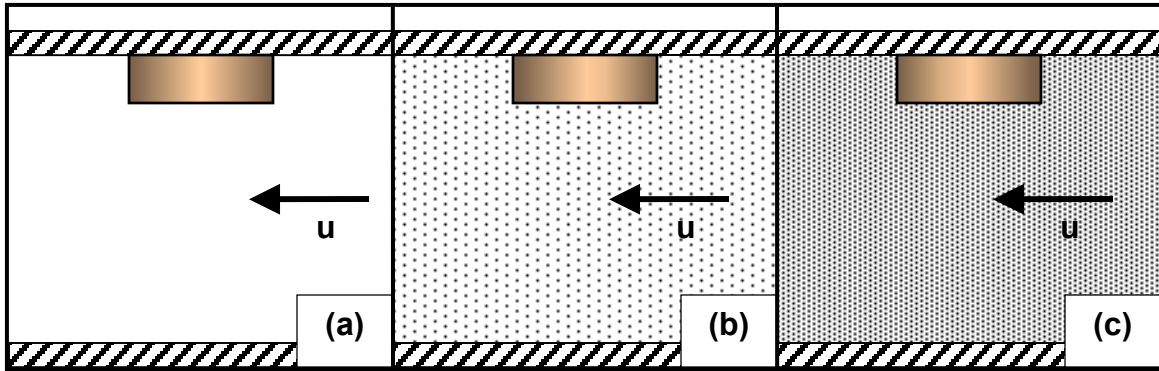
Figure 28 -- Ramp exposure test phases (a) clean air stage, (b) aerosol buildup, and (c) steady state aerosol conditions.

3.2 Step Exposure Tests

The photoelectric and ionization detectors were also exposed to a step input of aerosol from four different sources. The four aerosol sources were vegetable oil from a six-jet atomizer, vegetable oil from a nebulizer with an inline impactor, smoldering cotton wicks, and soot from a laminar propylene flame. Each test was performed in triplicate.

The step input of aerosol was achieved by using a can to enclose the detector during the aerosol filling stage as shown in Figure 29. The can was approximately 15cm in diameter and 9.5cm in height with a rubber gasket around the top to form a seal with the top of the FE/DE test section. Purge air was supplied at approximately 10psi through the top of the FE/DE test section to create positive pressure inside the can during the aerosol filling stage until the aerosol concentration had stabilized. The aerosol concentration was deemed stable based on observations of the real-time output of laser light transmittance through the medium. The aerosol exposure phase involved turning off the purge air and lowering the can. This provided a reasonable step-input of aerosol to the detector under steady state flow conditions.
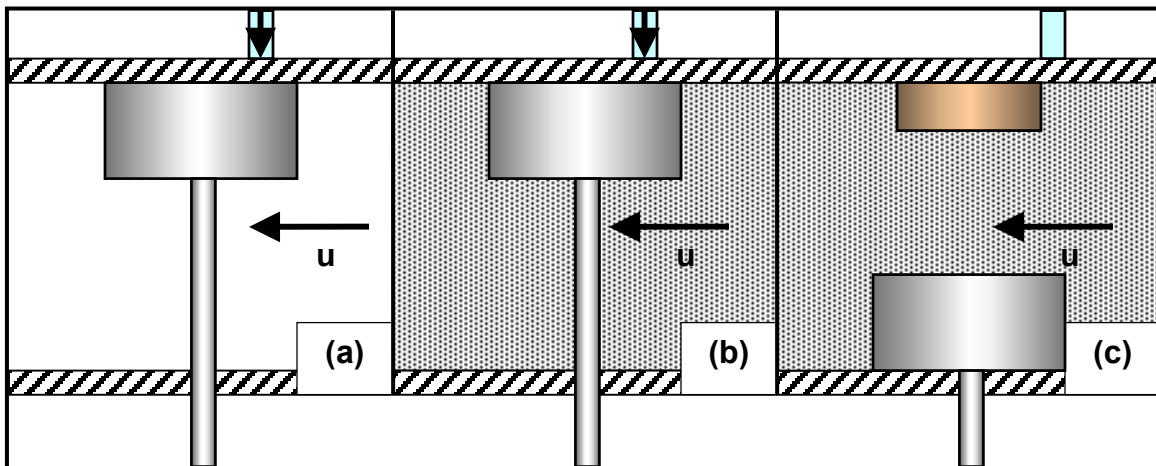
Figure 29 -- Step exposure stages (a) can covering detector with purge air on, (b) aerosol reaching steady state conditions with can covering detector and purge air on, and (c) exposure of detector to aerosol with can dropped and purge air off.

4. Results and Analysis

4.1 Aerosol particle size distributions

An ELPI 12 stage cascading impactor was used to characterize the particle size distribution for the vegetable oil and cotton wick sources over a range of fan speed settings. The cascading impactor is not a suitable method for characterizing propylene soot. Two 10-second samples were collected at external velocities of 0.08 and 0.52 m/s and provided the number and mass concentration at each stage. The geometric mean number size and geometric mean volume diameter were calculated from the number concentration data. These two methods were used because the output of photoelectric smoke detectors is more dependent upon geometric mean volume size, while an ionization smoke detector is more dependent upon geometric mean number size (Mulholland, 1995). The geometric mean mass size was also computed from the mass concentration data sets.

The geometric mean number size is defined as

$$\log d_{gn} = \sum_{i=1}^{n} \frac{N_i \log d_i}{N}$$

<div align="right">(58)</div>

Where d_{gn} is the geometric mean number size, d_i is the mean size of stage I, N_i is the number concentration at stage i, and N is the total number concentration.

The geometric standard deviation is

$$\log \sigma_{gn} = \left[\sum_{i=1}^{n} \frac{\left(\log d_i - \log d_{gn}\right)^2 N_i}{N} \right]^{1/2}$$

<div align="right">(59)</div>

The geometric mean mass size is similar to Equation 58 with the mass concentration replacing number concentration.

$$\log d_{gm} = \sum_{i=1}^{n} \frac{m_i \log d_i}{m}$$

<div align="right">(60)</div>

The geometric standard deviation for the mean mass size is similar to Equation 59 with the mass concentration replacing number concentration.

$$\log \sigma_{gm} = \left[\sum_{i=1}^{n} \frac{\left(\log d_i - \log d_{gm} \right)^2 m_i}{m} \right]^{1/2}$$

(61)

The geometric mean volume size for number concentration is

$$\log d_{gvn} = \frac{\sum_{i=1}^{n} V_i \log d_i}{V_T}$$

(62)

Where V_T is the total volume resulting from the summation of V_i, which is defined as

$$V_i = N_i \frac{1}{6} \pi d_i^3$$

(63)

Again, the geometric mean volume size for mass concentration is obtained by replacing the number concentration with mass concentration. Therefore, Equation 63 becomes

$$V_i = m_i \frac{1}{6} \pi d_i^3$$

98

The volume data can then be used in Equation 62 to compute the geometric mean volume size for mass concentration.

It was observed during the real time display during the data collection that the particle size distribution did not change significantly over the range of fan speeds. Therefore, the average values for the geometric mean size and geometric mean volume size and the associated standard deviations using both number and mass concentration data for each fan   speed   setting   are   summarized   in

Table 15. The bracketed values in bold is the percent variation with respect to the mean value based on measurements made at four different flow velocities. This provides an indication of the degree to which the particle size varies between the upper and lower bounds of FE/DE flow velocities.

Table 15 -- Summary of geometric mean size and geometric volume size using number and mass concentration data for three selected aerosols.

Aerosol	Atomized veg. oil	Nebulized veg. oil	Cotton wicks
d_{gn} (μm) [%variation]	0.31 **[0.4 - 10.5%]**	0.18 **[1.5 - 2.5%]**	0.06 **[0.09 - 2.0%]**
σ_{gn}	2.05	1.91	1.80
d_{vn} (μm) [%variation]	0.71 **[0.3 - 1.1%]**	0.35 **[0.2 - 1.2%]**	0.17 **[0.7 - 8.1%]**
σ_{vn}	1.18	1.13	1.28
d_{gm} (μm) [%variation]	1.01 **[0.4 - 3.3%]**	0.47 **[0.3 - 2.5%]**	0.31 **[3.2 - 16%]**
σ_{gm}	1.74	1.83	2.14
d_{vm} (μm) [%variation]	1.55 **[0.05 - 2.0%]**	1.13 **[1.1 - 2.6%]**	1.03 **[11 - 20%]**
σ_{vm}	1.06	1.18	1.20

The geometric mean mass size for the smoldering cotton wicks was nominally 0.31 μm and is consistent with the previous findings (Weinert, 2001). The propylene soot particles were not characterized with the cascading impactor. However, a value of 0.05 μm for the mean particle size of a laminar propylene flame has been reported (Lamprecht, 1999). As was observed with the three other aerosol sources, it was assumed that the mean particle size distribution did not significantly vary with fan speed.

4.3 Determining Lag Time in Ramp Exposure Tests

The delay between external flow conditions at the detector's leading edge and the sensor output was determined from the ramp type exposure tests. The lag time during the ramp test provides an indication of the sensor response lag, such as signal processing and alarm verification.

The analog output from the detector and the laser transmittance measurement were normalized and plotted as a function of time. The detector output signal had a nominal clean air value of 87 for the photoelectric detector and 94 for the ionization detector. The

clean air values were the minimum expected output and would be zero on the normalized scale. The detector output would increase to a nominally steady value above the clean air value and would be the expected maximum value. This value would become unity on the normalized scale. However, the transmittance value was nominally unity for clean air conditions and decreased to a steady state value once the aerosol stabilized. Therefore, the transmittance values were adjusted by subtracting the transmittance value from unity in order to ensure that the clean air value was zero and the maximum value would be unity on the normalized scale. This is consistent with the definition of absorption of light in a medium (*i.e.,* absporption = 1 – transmittance).

The minimum and maximum values from the detector output and the adjusted transmittance values were normalized using the following relationship.

$$y_n = \frac{Y(t) - Y_{min}}{Y_{max} - Y_{min}}$$

(65)

A typical plot of the normalized output data is shown in Figure 30.
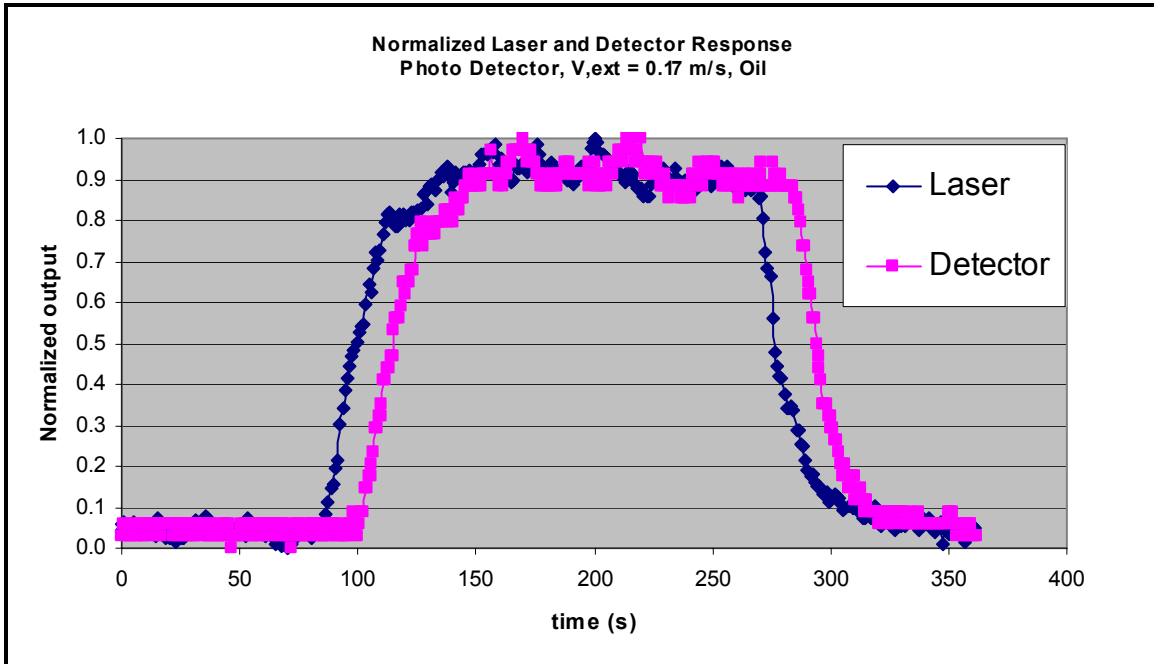
Figure 30 -- Typical normalized plot of laser transmittance and detector output values.

The linear portion of the response phase was identified and the slopes and intercepts for the laser transmittance and detector output were determined by a linear least-squares fit approach. The linear portion of the response phase was typically between 0.2 and 0.7 on the normalized curves. Using the equations for the respective lines, the time values associated with 0.2 to 0.7 in 0.05 increments were computed. The lag time was computed by subtracting the laser transmittance time from detector response time.

The lag time value had to be corrected for the distance between where the laser transmittance measurement was made and the leading edge of the detector's aerosol entry location. This distance was nominally 3cm. The approach velocity measured with the LDV at approximately 1.5cm from the detector's aerosol entry location was used, as

103

opposed to the bulk freestream velocity. The approach velocity was more indicative of the flow conditions at the aerosol entry location. The time adjustment associated with moving the 3cm distance at the approach velocity was also computed. The approach velocities and resultant time adjustments are summarized in Table 16.

Table 16 -- Freestream and approach velocities with time adjustment from transmittance measurement location to leading edge of aerosol entry location.

Fan (Hz)	$V_{freestream}$(m/s)	$V_{approach}$(m/s)	t_{adjust} (s)
20	0.52	0.34	0.08
10	0.26	0.16	0.19
7	0.17	0.08	0.38
5	0.11	0.06	0.50

The mean value of the lag time for 5 repeated tests with the proper time adjustments from Table 1 were calculated and are summarized in Figure 31 for both the worst and best orientation for aerosol entry.
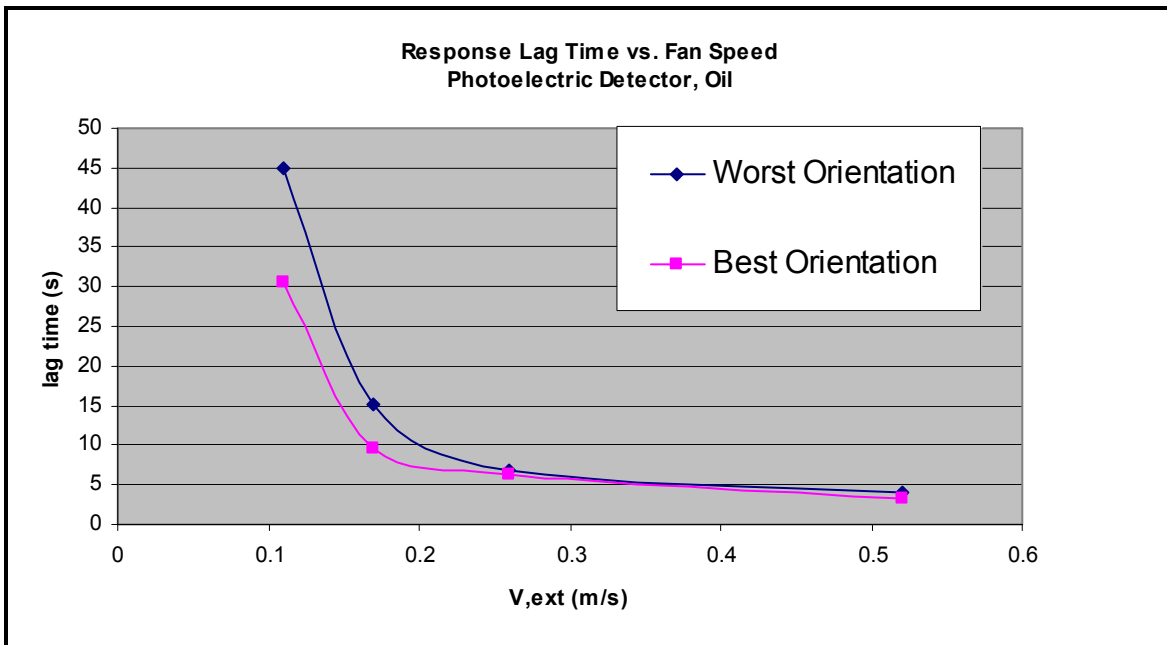
Figure 31 -- Response lag time for photoelectric detector.

From the lag time results and using a nominal distance of 3.5cm from the leading edge of the detector aerosol entry location to the center of the sensing chamber, the equivalent internal velocity value was computed. This equivalent internal velocity could be helpful in interpreting the results of the LDV velocity measurements made inside the sensing chamber. The equivalent velocity values are summarized in Table 17.

Table 17 -- Equivalent internal velocities for worst and best aerosol entry orientations.

Fan (Hz)	$V_{freestream}$(m/s)	$V_{approach}$(m/s)	$V_{int,worst}$(m/s)	$V_{int,best}$(m/s)
20	0.52	0.34	0.0080	0.0102
10	0.26	0.16	0.0048	0.0052
7	0.17	0.08	0.0021	0.0034
5	0.11	0.06	0.0007	0.0011

4.4 Time to Alarm from Step Exposure Tests

The time to alarm was determined from the step exposure tests for the photoelectric and ionization detectors. Both detectors were addressable with the ability to set the sensitivity at the fire alarm panel. The sensitivity settings were 0.2, 0.5, 1.0, 1.5, 2.0, 2.5, 3.0, and 3.7%/ft for the photoelectric detector and 0.5, 0.9, 1.3 and 1.7%/ft for the ionization detector. Each sensitivity setting corresponded to a specific output value, in terms of an 8-bit value, from the modified fire alarm panel.

The steady state aerosol exposure was determined from the steady state output of each smoke detector sensor in relation to the UL 217/268 smoke box calibration data provided by the manufacturer. The sensor output is expressed as an 8-bit value with a possible range of 0 to 255. The UL 217/268 smoke box data is reported in %Ob/ft and is based on

the rise in sensor output relative to the clean air background level. The 8-bit sensor values for clean the clean air background readings were 87 for photoelectric and 94 for the ionization detectors. The UL 217/268 alarm points varied for each addressable sensor type and are summarized in the Table that follows.

Table 18 -- UL 217/268 alarm points for addressable photo and ion detectors.

Photoelectric Clean Air = 87		Ionization Clean Air = 94	
%Ob/ft (UL 217/268)	Δ=output - 87	%Ob/ft (UL 217/268)	Δ=output - 94
0.2	6	0.5	50
0.5	15	0.9	65
1.0	28	1.3	80
1.5	42	1.7	100
2.0	55		
2.5	68		
3.0	82		
3.7	100		

The range of alarm points is different for each sensor with only the 0.5%Ob/ft alarm point in common. For a given external exposure it was possible for one test to trigger more than one alarm point for measurement purposes. It should be noted that in practice only one alarm point would be set at the fire alarm control panel. However, in the aerosol exposure tests where the 8-bit representation of the sensor output was recorded, it was possible to monitor when the various alarm points were exceeded in a single given test. An example of this is shown in the Figure that follows.
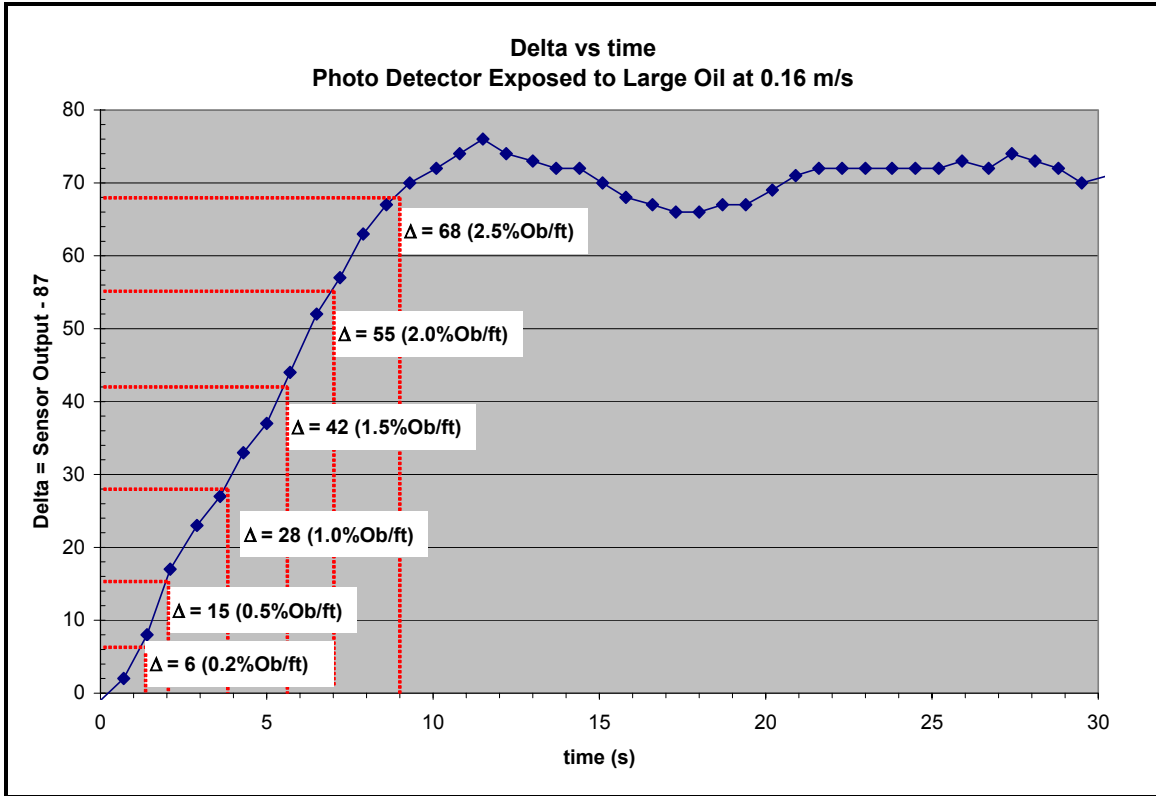
Figure 32 -- Sensor output delta vs time with multiple alarm points being exceeded in a single test.

It has been assumed that at the steady state condition the internal aerosol concentration is equal to the external concentration. The steady state aerosol exposure as a function of external velocity is shown for the four aerosol sources used in this study for both the photoelectric and ionization smoke detectors. The data shown are based on three repeated tests under nominally the same conditions. The data points are the mean value and the y error bars represent one standard deviation as a combined estimate of the measurement uncertainty and experimental variability.
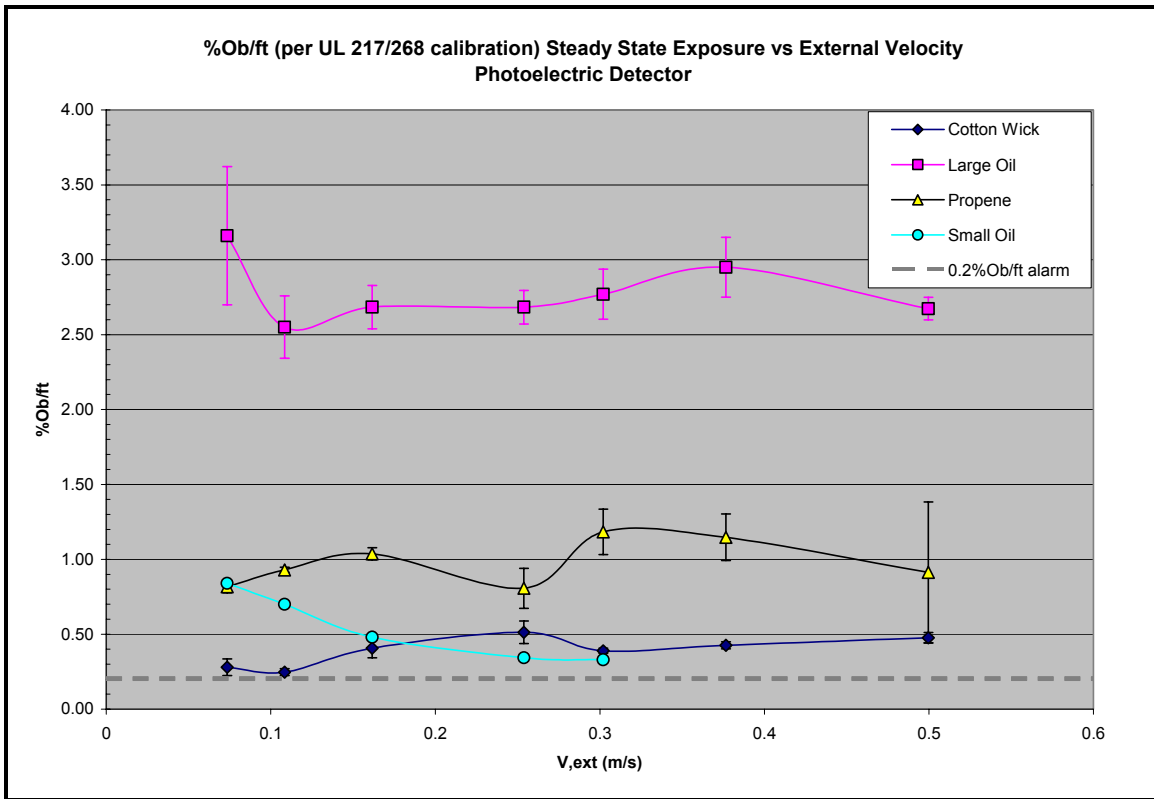
Figure 33 -- Steady state aerosol exposure per the UL 217/268 smoke box calibration data for the photo detector.

The aerosol output from three of the four sources (cotton wick, large oil, and propene) was adjusted at each external velocity in order to provide a nominally consistent exposure concentration. The nominal aerosol exposures were 0.4%Ob/ft for the cotton wick, 2.75%Ob/ft for the large oil, and 1%Ob/ft for the propene soot. The small oil source had a fixed output of aerosol. Therefore, the aerosol concentration decreased as external velocity increased due to the increased dilution of aerosol in air. This general trend is indicated in the Figure as the small oil varies from 0.25 to 0.80%Ob/ft over the range of velocities. The photoelectric detector's minimum sensitivity setting was 0.2%Ob/ft which is indicated in Figure 33.
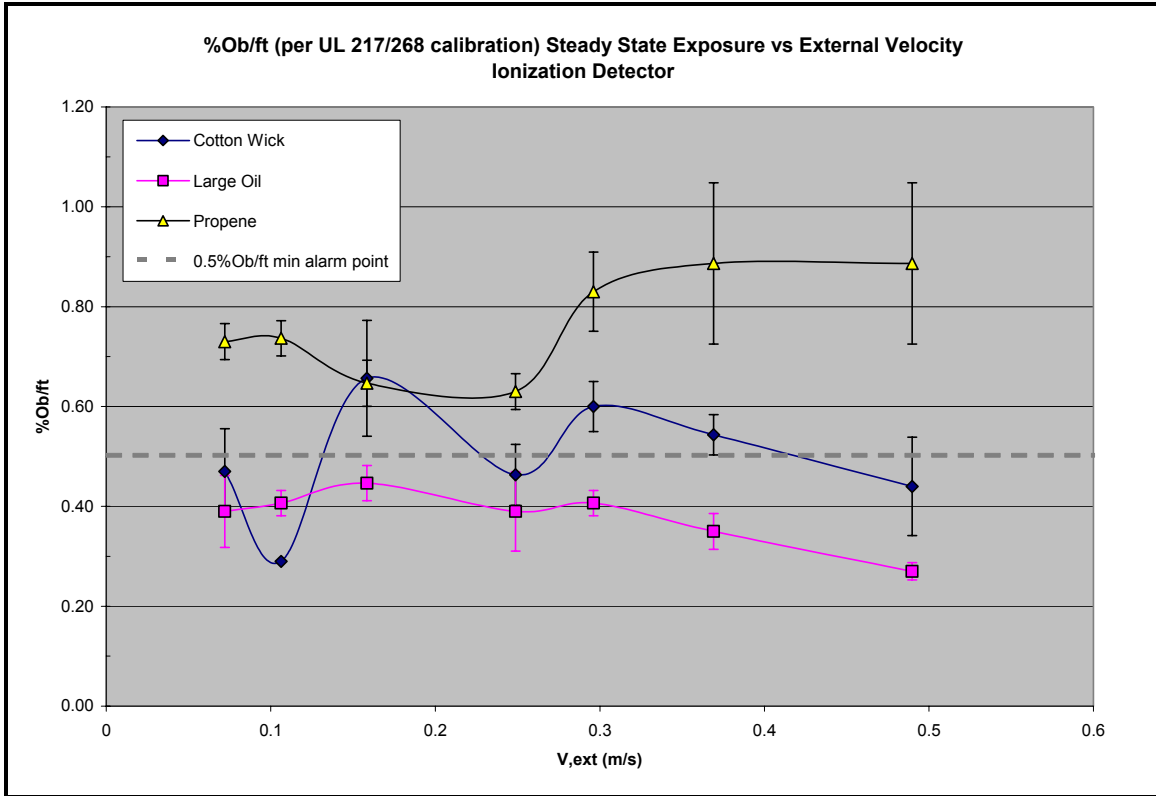
Figure 34 -- Steady state aerosol exposure per the UL 217/268 smoke box calibration data for the ion detector.

The cotton wick and propene sources for both the photoelectric and ionization detectors were the same. The steady state sensor output from both the photoelectric and ionization sensors were similar for the cotton wick and propene sources. However, the large oil exposure for the photoelectric detector was larger relative to that for the ionization detector. The ionization detector steady state response to the large oil droplets was at a saturated level (i.e., the maximum output value of 255) when it was exposed to the same aerosol level as was used in comparable photoelectric detector tests. The small oil droplet exposure for the ionization detector is not plotted as this particular exposure did not exceed the minimum 0.5%/ft alarm point. The small oil droplet exposure was a fixed source and, therefore, it was not possible to increase the aerosol exposure concentration.

109

Additionally, as shown in Table 18, the alarm points for the ion detector were more limited relative to the photo detector and were in the range of 0.5 to 1.9%Ob/ft. This was a contributing factor in the rather limited response time data reported for the ionization detector.

It can be seen in Figure 34 that only the propene soot provided a consistent concentration within the 0.5%/ft alarm point for the ionization detector. It should be noted that the 0.5%/ft alarm point was the most sensitive setting available from the manufacturer of the ion detector. In contrast, the photoelectric detector was capable of a 0.2%/ft alarm point and, therefore, was able to respond to all the aerosol sources.

The average times to alarm for the applicable sensitivity settings are shown in Table 19, Table 20, and Table 21 that follow for the ionization detector as well as the photoelectric detector at the least favorable orientation and rotated 90 degrees.

Table 19 -- Average time to alarm for ionization detector step exposure tests.

Ionization Detector		Time to alarm (s)	
Aerosol Source	V,ext(m/s)	0.5%/ft	1.0%/ft
Cotton Wick	0.08	29.9	
	0.11		
	0.17	15.2	
	0.26	11.2	
	0.31	8.4	
	0.39	10.8	
	0.52	14.8	
Atomized Oil	0.08	48.3	
	0.11	39.0	
	0.17	26.4	
	0.26	19.9	
	0.31	20.9	
	0.39	9.4	
	0.52		
Propylene	0.08	34.8	
	0.11	25.3	
	0.17	16.3	
	0.26	10.1	
	0.31	7.7	20.7
	0.39	4.3	6.5
	0.52	2.9	5.1
Nebulized Oil	0.08		
	0.11		
	0.17		
	0.26		
	0.31		

Table 20 -- Time to alarm summary for photoelectric detector at worst orientation step exposure tests.

Photoelectric Detector @worst	Time to alarm (s)					
Aerosol Source	V,ext(m/s)	0.2%/ft	0.5%/ft	1.0%/ft	1.5%/ft	2%/ft	2.5%/ft
Cotton Wick	0.08	34.8					
	0.11	25.9					
	0.17	9.1					
	0.26	5.2					
	0.31	3.6					
	0.39	2.7					
	0.52	1.5					
Atomized Oil	0.08	14.2	17.8	21.4	27.2	33.1	39.9
	0.11	9.1	10.8	13.2	17.5	23.8	39.9
	0.17	4.3	5.2	6.7	8.6	10.1	13.2
	0.26	1.4	3.3			4.6	7.7
	0.31	1.4	2.1		2.4	3.1	5.0
	0.39	1.1		2.1	2.2		2.9
	0.52		1.5		1.8	2.9	
Propylene	0.08	15.9	23.1				
	0.11	12.5	17.8				
	0.17	6.0	8.2	17.8			
	0.26	4.6	6.3	15.1			
	0.31	3.6	4.1	6.3	14.7		
	0.39	2.2	2.9	10.8			
	0.52	2.9	10.8				
Nebulized Oil	0.08	24.2	34.1				
	0.11	19.2	27.4				
	0.17	12.2					
	0.26	5.0					
	0.31	4.1					

Table 21 -- Average time to alarm for photoelectric detector rotated 90 degrees step exposure tests.

Photoelectric Detector @90deg	Time to alarm (s)					
V,ext(m/s)	0.2%/ft	0.5%/ft	1.0%/ft	1.5%/ft	2%/ft	2.5%/ft
Cotton Wick 0.08	20.2					
0.11	13.9					
0.17	6.0					
0.26	3.1					
0.31	2.6					
0.39	1.7					
0.52	1.2					
Atomized Oil 0.08	8.9	10.8	14.7	17.5	20.7	25.2
0.11	8.6	10.5	12.2	13.7	15.1	16.2
0.17	5.1	5.8	7.0	8.0	8.9	10.1
0.26	1.8	2.1				3.6
0.31				2.1		2.9
0.39	1.4					2.6
0.52				1.4	1.7	
Propylene 0.08	16.3	20.9				
0.11	9.9	12.3				
0.17	6.0	7.7	13.7			
0.26	2.9	3.6	15.9			
0.31	2.4	3.1	6.7			
Nebulized Oil 0.08	20.7	26.2				
0.11	10.1	21.7				
0.17	7.5					
0.26	4.1					
0.31	3.4					

4.5 Determining Lag and Characteristic Response Times from Step Exposure Tests

The output data from the detector during the step input of aerosol was analyzed by examining the nature of the response signal. Typical response signals from three repeated tests are shown in Figure 35 where the 8-bit representation of the detector output signal was plotted as a function of time.
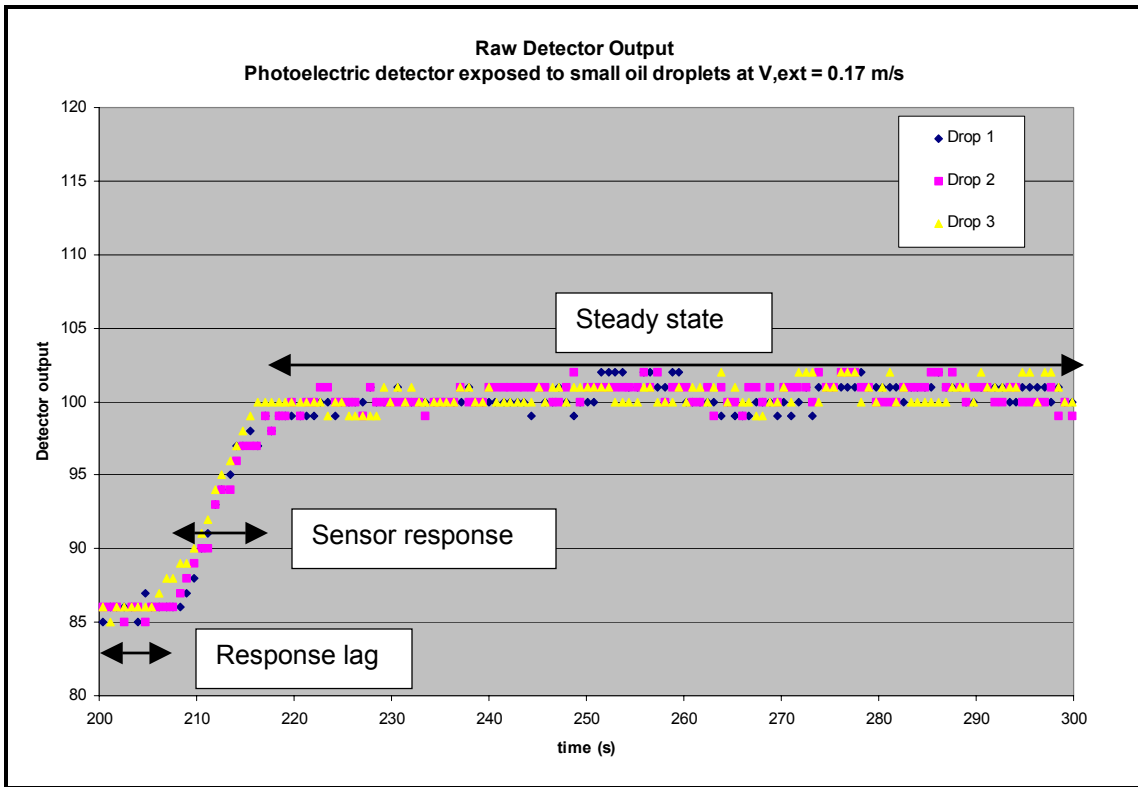
Figure 35 -- Detector output signals from three tests of a photoelectric detector exposed to nebulized vegetable oil at 0.17 m/s.

The exposure phase for this particular set of tests, shown in Figure 35, began at 200s. It can be seen that the output signal remains at the clean air value of approximately 87 until the range of 206 to 208 seconds for this particular set of tests. This period of time where the output signal did not significantly deviate from the clean air range was defined as the *detector response lag time*. The response portion was typically seen occur when the output value exceeded 88, as the clean air value was nominally 87 with a range of 85 to 88.

The response portion of the detector output signal was fitted using an exponential curve fitting procedure which would yield a characteristic response time for the specific

114

detector exposed to specific flow conditions. Exponential curve fitting is typically employed to characterize the response of instruments exposed to a step input signal. The detector output signal was first normalized to itself so that the clean air value was 0 and the steady state response value was 1. Therefore, the detector output signal was normalized using Equation 65.

The time values were adjusted by subtracting off the time corresponding to the last clean air value before the detector response began. An example of this determination is given in Table.

Table 22 -- Example detector output for determining start of sensor response.

Time (s)	Detector Output
200.0	87
200.5	87
201.0	86
201.5	87
202.0	87
202.5	89
203.0	90
203.5	93

From the table above the response exceeds the clean air value threshold of 88 at 202.5s, therefore, the time scale for the normalized detector output plot is adjusted by subtracting off 202.0s, corresponding to the time associated the last clean air value before the sensor response begins. This results in the time values beginning with a value of zero during the sensor response phase of the normalized output curve.

The normalized detector output plotted on the adjusted time scale for the scenario in Figure 35 is shown in Figure 36.
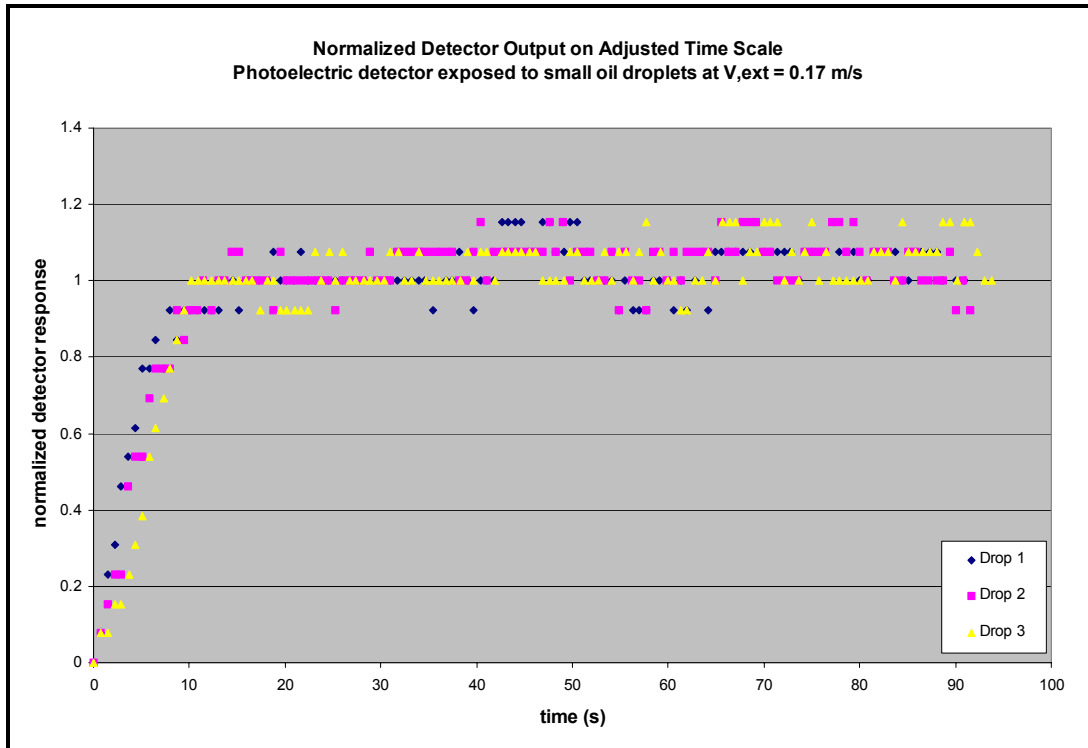
Figure 36 -- Normalized detector output for photoelectric detector exposed to nebulized vegetable oil at 0.17 m/s.

The characteristic response time was determined from an exponential curve-fit of the normalized output data in the following format.

$$y(t)_{fit} = 1 - e^{-t/t_{ch}}$$

(66)

where t is the time value on the adjusted time scale and t_{ch} is the characteristic time constant for the specific detector exposed to the specific flow condition. The quality of the curve fit was determined by computing the R^2 value for the fitted data set relative to the normalized data set. The characteristic time constant was adjusted until the R^2 was maximized.

The average response lag time values were plotted as a function of fan speed for the four aerosol types used in the step exposure tests. Figure 37, Figure 38, and Figure 39 summarize the average response time values for the photoelectric detector at both orientations as well as the ionization detector.
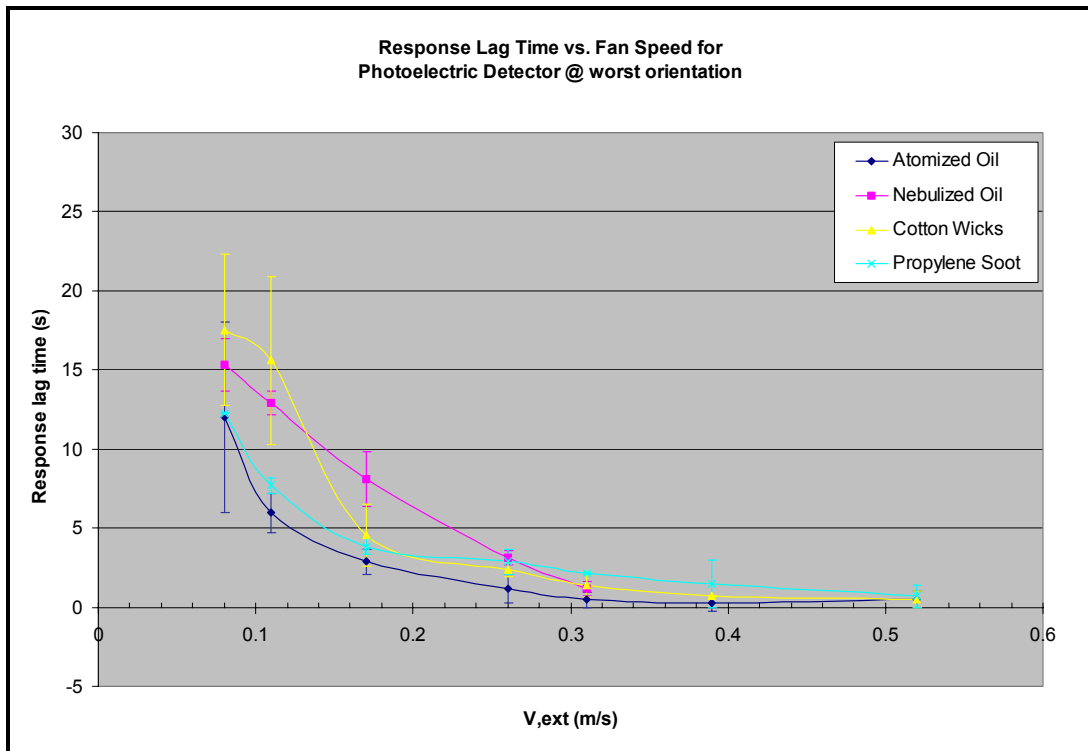
Figure 37 -- Average response lag times from step exposure tests for photoelectric detector at worst orientation.
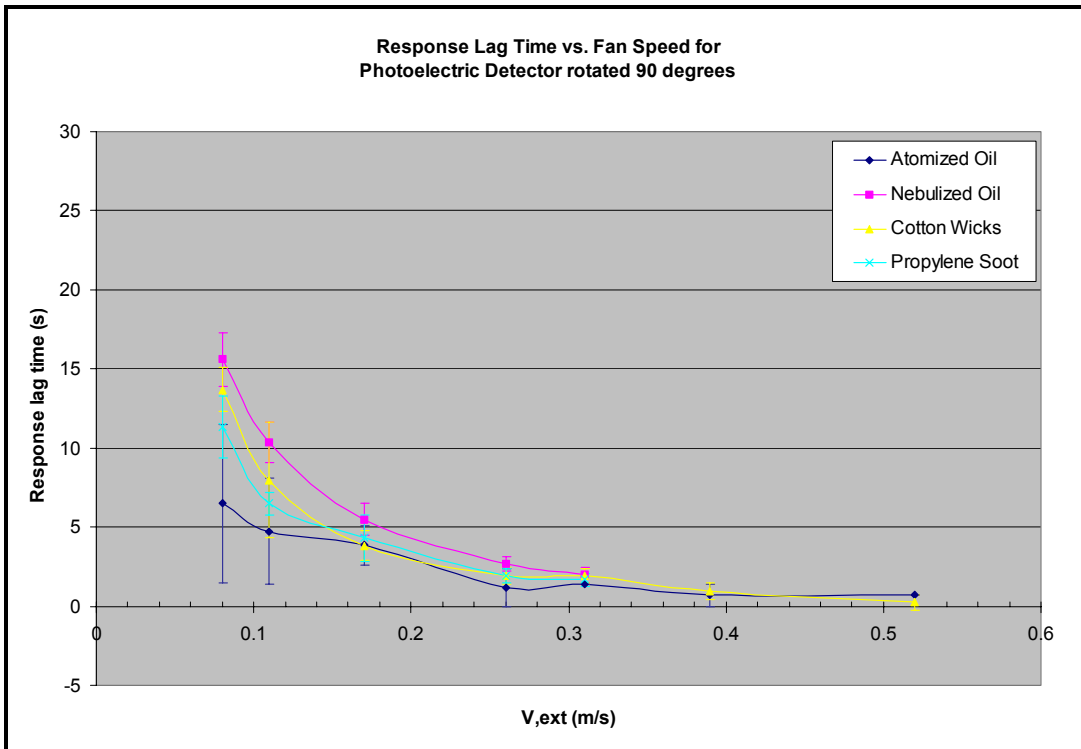
Figure 38 -- Average response lag times from step exposure tests for photoelectric detector rotated 90 degrees.
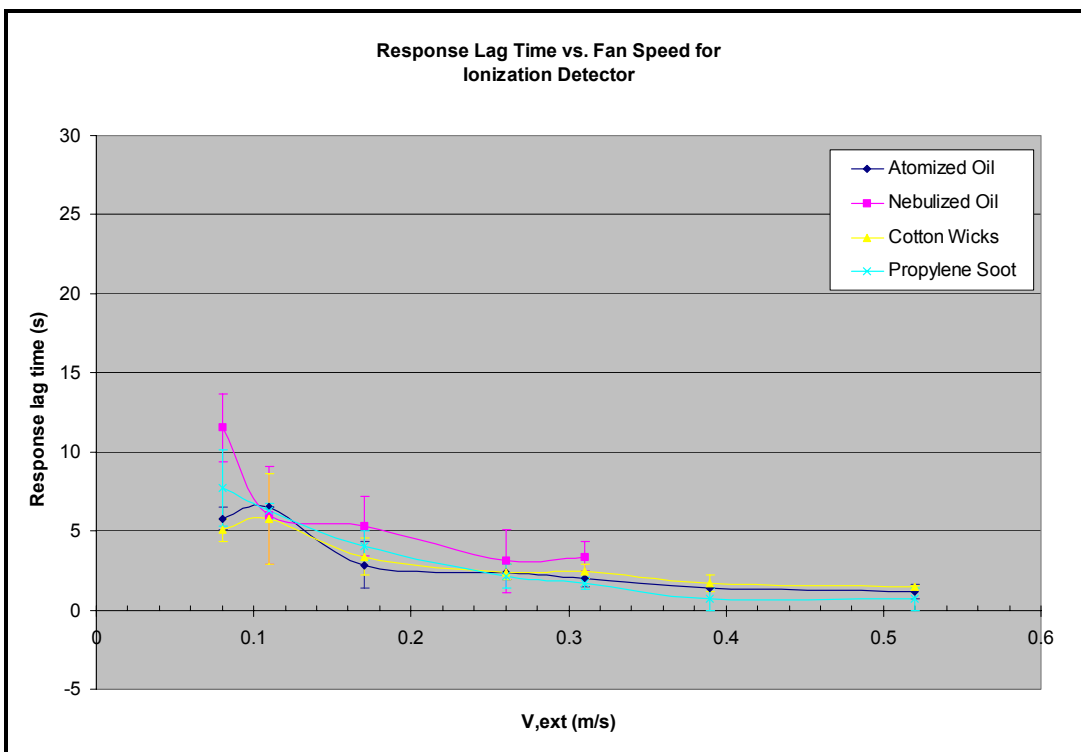
Figure 39 -- Average response lag times from step exposure tests for ionization detector.

118

The average characteristic response time values were plotted as a function of fan speed for the four aerosol types used in the step exposure tests. Figure 40, Figure 41, and Figure 42 summarize the average response time values for the photoelectric detector at both orientations as well as the ionization detector.
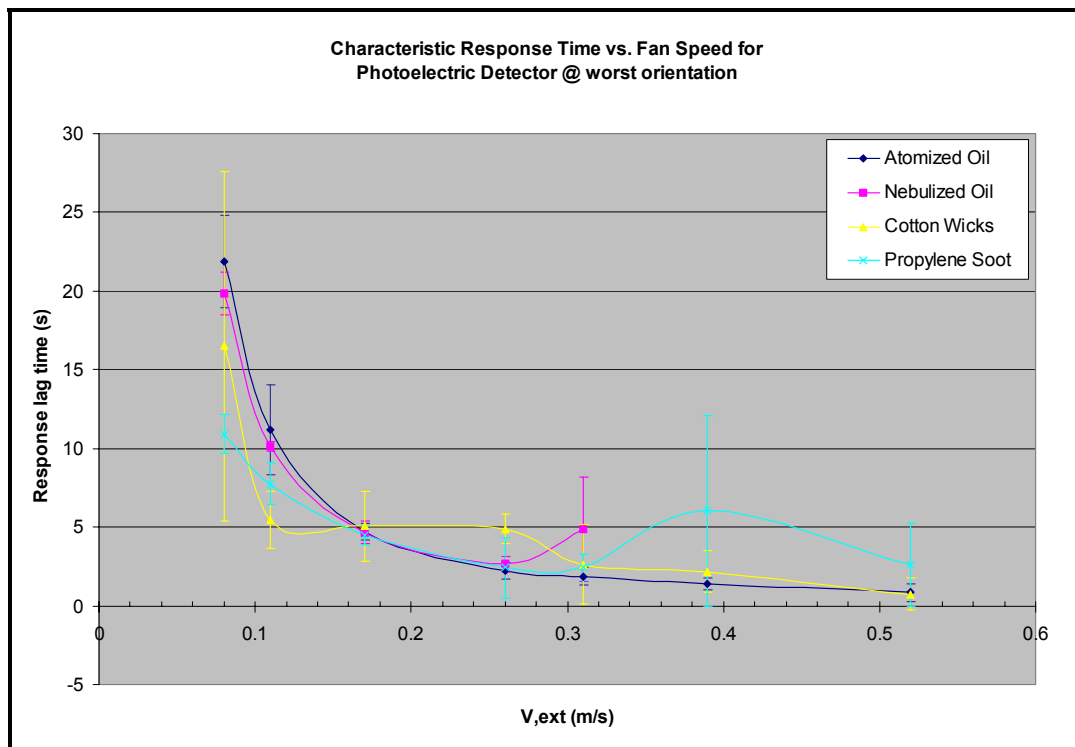
Figure 40 -- Average characteristic response times from step exposure tests for photoelectric detector at worst orientation.
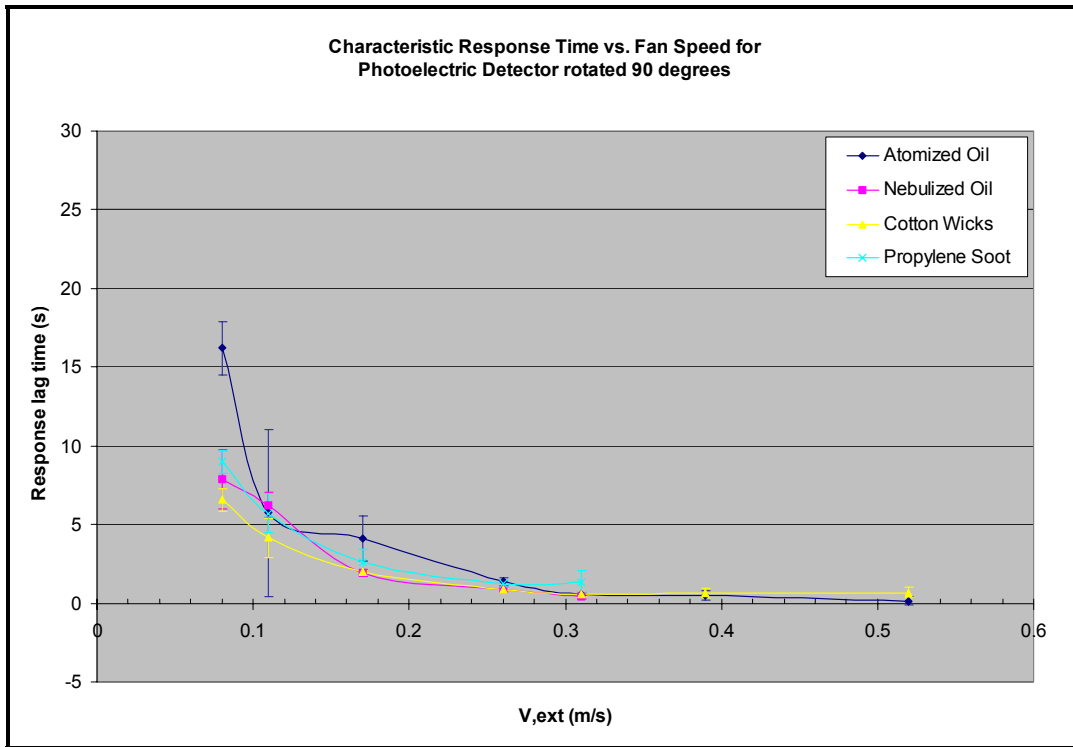
Figure 41 -- Average characteristic response times from step exposure tests for photoelectric detector rotated 90 degrees.
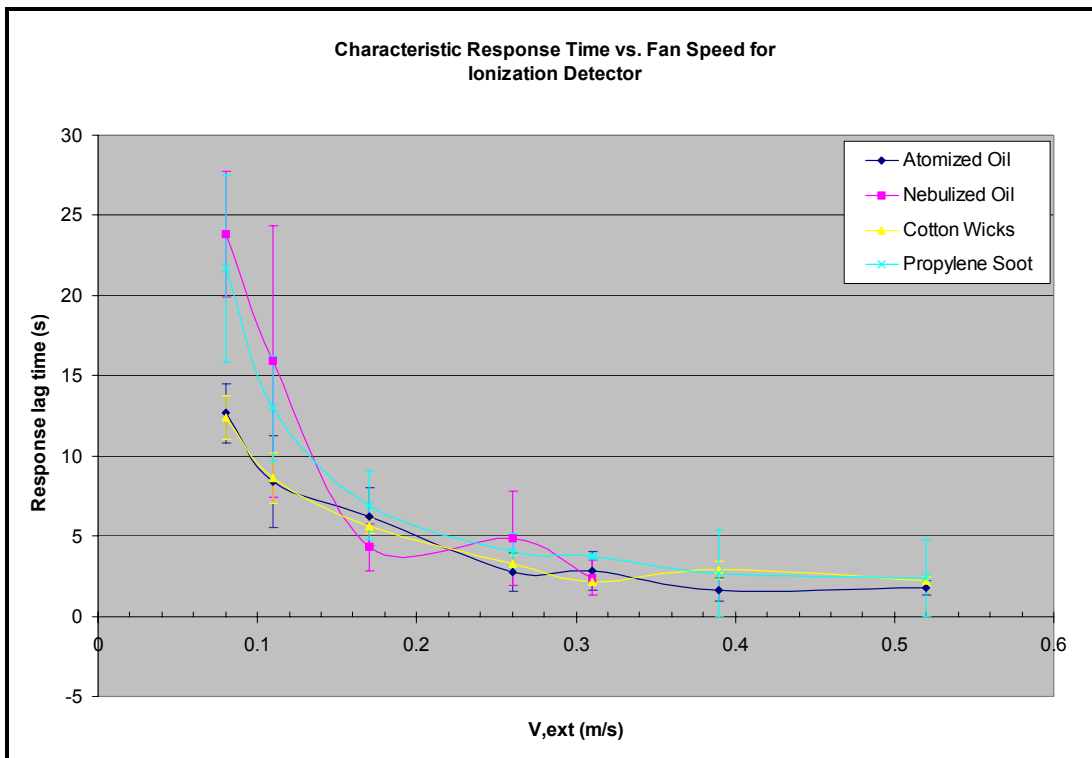
Figure 42 -- Average characteristic response times from step exposure tests for ionization detector.

120

5. Conclusions

An addressable photoelectric and ionization smoke detector were exposed to four different aerosol sources for a range of steady state external flow conditions in NIST's Fire Emulator / Detector Evaluator. The aerosol sources were delivered as a step input exposure to the detector and included smoldering cotton wicks, soot from a laminar propylene flame, and vegetable oil delivered using two different devices. Additionally, a limited number of ramp input exposures using nebulized vegetable oil were also performed.

The data set was used to characterize the nature of aerosol entry lag and sensor response. The time to alarm for specific alarm points was considered. Additionally, the detector output data set was normalized to itself and an exponential curve fitting procedure was performed to obtain a characteristic response time as well as the response lag time. The data collected in this study was used to evaluate a mass transport model developed for smoke detector response. The steady state detector output was used to characterize the external aerosol concentration in the mass transport model. The measured times to alarm and steady state conditions were used to make comparisons to the values predicted with the mass transport model.

References

Choi, M.Y., G.W. Mulholland, A. Hamins, T. Kashiwagi, "Comparisons of the Soot Volume Fraction Using Gravimetric and Light Extinction Techniques," *Combustion and Flame*, v102, n1-2, p. 161-169, (1995).

Cleary, T., M. Donnelly, W. Grosshandler, "The Fire Emulator / Detector Evaluator: Design, Operation, and Performance," AUBE '01 Conference Proceedings, (2001).

Dobbins, R.A., G.W. Mulholland, N.P. Bryner, "Comparison of a Fractal Smoke Optics Model with Light Extinction Measurements," *Atmospheric Environment*, v28, n5, p. 889-897, (1994).

Lamprecht, A., W. Einer, K. Kohse-Hoinghaus, "Dynamic Light Scattering in Sooting Premixed Atmospheric Pressure Methane-, Propane-, Ethene-, and Propene-Oxygen Flames," *Combustion and Flame*, v118, n1-2, p. 140-150, (1999).

Lee, T.G.K., "An Instrument to Evaluate Installed Smoke Detectors," National Institute of Standards and Technology, Gaithersburg, MD, NBSIR 78-1430, (1978).

Mulholland, G.W., R.D. Mountain, "Coupled Dipole Calculation of Extinction Coefficient and Polarization Ratio for Smoke Agglomerates," *Combustion and Flame*, v119, p. 56-68 (1999).

Mulholland, G.W., "Smoke Production and Properties," *SFPE Handbook of Fire Protection Engineering, 2nd Edition*, National Fire Protection Association, Quincy, MA, (1995).

Olson, A.T., K.A. Shelstad, *Introduction to Fluid Flow and the Transfer of Heat and Mass*, Prentice-Hall, Englewood Cliffs, NJ, (1987).

Weinert, D.W., T.G. Cleary, G.W. Mulholland, "Size Distribution and Light Scattering Properties of Test Smokes," AUBE '01 Conference Proceedings, (2001).

5 Paper 3: "Development of a Mass Transport Model for Smoke Detectors"

Development of a Mass Transport Model for Smoke Detectors

Abstract

A mass transport model for predicting smoke detector response has been developed that relates detector response time to the external flow conditions and detector geometry. The mass transport model is based on a set of three dimensional governing equations for the conservation of mass, species, and momentum in partial differential form. A gas phase control volume within the sensing chamber of a smoke detector was used for fully developed flow conditions. An inlet velocity boundary condition was developed to express the internal detector velocity as a function of external flow conditions and the detector geometry. The three dimensional governing equations were simplified by applying the relevant boundary conditions as well as previous findings from the fluid mechanics literature confirmed with measurements made in the experimental portion of this study. The simplified governing equations and associated boundary and initial conditions were expressed in nondimensional form. The mass transport model was solved numerically using the Lax-Wendroff explicit finite difference scheme. The one-dimensional form of the mass transport model was further simplified by integrating out the x direction in a lumped analysis. In general, the model predictions were found to underestimate the measured response times at 0.2%Ob/ft and the time to steady state conditions for external flow conditions in the range of 0.08 to 0.52 m/s. The characteristic response time for the mass transport model was shown to have an estimated uncertainty of 20 to 46% using the standard error propagation equation. The mass transport model was used to demonstrate that Heskestad's characteristic length is a lumped parameter that can be explained in terms of physical quantities related to the smoke detector mass transport problem.

Keywords: smoke detectors, entry resistance, detector response model, detection time, mass transport

Nomenclature

d screen diameter [m]

d_s particle spherical diameter [m]

D_A binary diffusion coefficient of species A

Eu Euler number [dimensionless]

h height of control volume [m]

g acceleration due to gravity [m/s^2]

K_0 incompressible pressure drop coefficient [dimensionless]

L length of control volume [m]

m screen width [m]

n screen height [m]

N_f particle concentration in flame zone [particles/m^3]

p pressure [Pa]

p_{stag} stagnation point pressure [Pa]

$p*$ nondimensional pressure [dimensionless]

Pe Peclet number [dimensionless]

Re_d Reynolds number based on screen diameter [dimensionless]

Re_h Reynolds number based on control volume height [dimensionless]

t time [s]

t_c characteristic time [s]

t_{ss} time to steady state [s]

$t*$ nondimensional time [dimensionless]

u_j^n numerical value in finite difference solution at position j at time step n

u_t shorthand notation for partial differential of variable u with respect to time

u_x shorthand notation for partial differential of variable u with respect to position

U velocity [m/s]

v_{ext} external velocity [m/s]

v_{int} internal velocity [m/s]

v_{sed} sedimentation velocity [m/s]

v_{ss} steady state velocity [m/s]

v_x x component of velocity [m/s]

125

v_y y component of velocity [m/s]

v_z z component of velocity [m/s]

$v*$ nondimensional velocity [dimensionless]

$\overline{V}_{ext}$ average external velocity [m/s]

$\overline{V}_{int}$ average internal velocity [m/s]

w width of control volume [m]

x position in x direction [m]

$x*$ nondimensional distance in x direction [dimensionless]

y position in y direction [m]

z position in z direction [m]

$z*$ nondimensional distance in z direction [dimensionless]

Greek Letters

α screen porosity, diffusivity in finite differencing [dimensionless, m^2/s]

Γ coagulation coefficient [dimensionless]

Δt time step [s]

Δx spatial discretization [m]

μ dynamic viscosity [Ns/m^2]

ν kinematic viscosity [m^2/s]

θ angle of fluid flow direction with respect to surface normal [radians]

ρ density [kg/m^3]

ρ_A concentration of species A [kg/m^3]

ρ_A^* nondimensional concentration of species A [dimensionless]

ρ_f density of fluid medium in sedimentation calculation [kg/m^3]

ρ_s density of solid particles in sedimentation calculation [kg/m^3]

σ_{KE} kinetic energy in screen flow calculation [kJ]

σ_M momentum in screen flow calculation [kg-m/s]

1. Introduction

A mass transport model for smoke detector response was developed from a set of three-dimensional governing partial differential equations for the conservation of mass, species, momentum, and energy. The fluid was assumed to be non-reacting, isothermal, incompressible and Newtonian with constant properties. The fluid was assumed to be a dilute binary mixture of aerosol and air. The three-dimensional governing equations were applied to a gas phase control volume within the sensing chamber of the smoke detector. The gas phase control volume was assumed to have fully developed flow conditions with negligible aerosol deposition. An inlet velocity boundary condition was developed to relate the internal velocity to the external flow conditions and detector geometry. This inlet velocity boundary condition was developed from previous research of incompressible fluid flow past insect screens as well as the velocity measurements made during the experimental portion of this study.

Results from the fluid mechanics literature and findings from the experimental portion of this study were used to simplify the problem. The simplified governing equations were recast in nondimensional form and further simplified using typical dimensional quantities

on an order of magnitude basis. The nondimensional form of the simplified species equation was solved using the Lax-Wendroff finite differencing scheme. The numerical solution was used to simulate the detector response time data collected in the experimental portion of this study. The nondimensional species equation was further simplified into a lumped form which resulted in a linear first-order differential equation. This lumped form of the mass transport model was solved and examined by comparisons to experimental data collected in the current study as well as existing methods of predicting smoke detector response.

2. Model Development

The model considers the mass transport process of a ceiling jet-driven aerosol stream into a conventional spot-type smoke detector. The aspect of detector response such as signal processing or alarm verification is not considered in this approach.

2.1. General Form of Governing Equations

The general governing equations for the aerosol entry problem in smoke detectors were derived using the principles of conservation of mass, species, momentum, and energy (Appendix C.1). The equations were developed for a non-reacting, isothermal, and incompressible Newtonian fluid with constant properties in three dimensional Cartesian coordinates. The fluid was treated as a dilute binary mixture of air and aerosol with negligible aerosol deposition on surfaces.

2.2. Control Volume

A gas phase control volume with fully developed flow conditions inside the sensing chamber of an idealized Cartesian representation of a smoke detector was used to formulate the model, as shown in Figure 43.
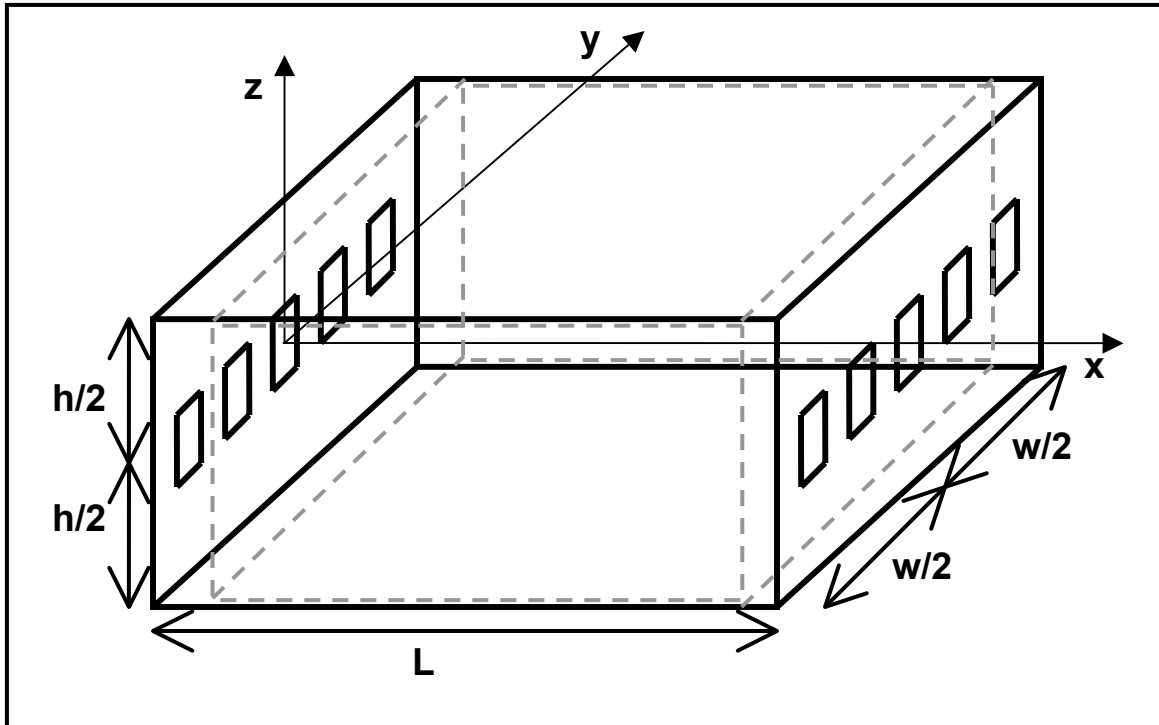
Figure 43 -- Generalized smoke detector with coordinate system and control volume (dashed lines).

Flow conditions were considered fully developed at a distance 5-10 screen diameters downstream of the insect screen [Baines and Peterson, 1951]. The insect screens in this study had openings approximately 0.58mm in diameter which would correspond to fully developed flow conditions existing at a distance between 2.9 and 5.8mm downstream from the screen. This range of distances represents 7 to 14% of the nominal 42mm length of the sensing chambers examined in this study in the streamwise direction. Experimental data collected at distances of 14, 24, and 34mm downstream from insect

screen in another part of this study indicates fully established velocity profiles at these locations [Ierardi, 2003]. These experimental observations were made within the defined region for fully developed flow conditions and are consistent with the findings of previous studies [Baines and Peterson (1951)].

2.3. Simplifying the Governing Equations

The three dimensional governing equations for conservation of momentum and species were simplified with the general procedures outlined in this section. The components of the momentum equation were considered for fully developed flow conditions within an infinitely long channel. The developing flow conditions at the entrance region were ignored in accordance with the fully developed flow assumption discussed in Section 3.2. The species equation considered mass transport in a channel with insulated boundaries at y and z surfaces. The partial differential equations were integrated and the known boundary conditions were applied to further simplify the governing equations (Appendix C.2) into the following form:

Continuity

$$\frac{\partial v_x}{\partial x} = 0 \tag{67}$$

Species

$$\frac{\partial \rho_A}{\partial t} + v_x \frac{\partial \rho_A}{\partial x} - D_A \left(\frac{\partial^2 \rho_A}{\partial x^2} \right) = 0 \tag{68}$$

Momentum

$$\frac{\partial v_x}{\partial t} + \frac{1}{\rho}\frac{\partial p}{\partial x} - v\left(\frac{\partial^2 v_x}{\partial z^2}\right) = 0 \qquad (69)$$

Energy:

The energy equation was shown to not apply to an isothermal incompressible Newtonian fluid (Appendix C.1) and therefore is not included in the discussion that follows.

2.4 Boundary Conditions

1. No slip boundary at walls

$$v_x\big|_{z=-\frac{h}{2},\frac{h}{2}} = 0 \qquad (70)$$

2. Inlet velocity

    Photoelectric Detector

$$\bar{V}_{\text{int}} = \bar{V}_{\text{ext}} 0.0034\left[\left(\frac{1-\alpha^2}{\alpha^2}\right)\text{Re}_d\right] \text{ for } \alpha=0.664 \text{ and } 10 < \text{Re}_d < 27 \qquad (71)$$

    Ionization Detector

$$\bar{V}_{\text{int}} = \bar{V}_{\text{ext}} 0.0025\left[\left(\frac{1-\alpha^2}{\alpha^2}\right)\text{Re}_d\right] \text{ for } \alpha=0.664 \text{ and } 17 < \text{Re}_d < 27 \qquad (72)$$

2.5 Initial Conditions

1. No aerosol inside sensing chamber control volume

$$\rho_A\big|_{x>0} = 0 \text{ at } t = 0 \tag{73}$$

2.6 Nondimensionalization

The following characteristic quantities were used to define the nondimensional variables

for the governing equations as well as boundary and initial conditions for the problem:

v_{ext} external velocity

L length of sensing chamber

h height of sensing chamber

$\rho_{A,max}$ maximum (steady state) aerosol concentration (see Appendix C.7)

$$\rho_{A,max} = C_{ss} = \frac{-\ln\left(1 - \frac{(\%Ob/ft_{ss})}{100}\right)}{k}$$

k extinction coefficient

p_{stag} stagnation point pressure

t_c characteristic time (to be determined in analysis)

The nondimensional variables were

$$v_x^* = \frac{v_{int}}{v_{ext}}$$

$$x^* = \frac{x}{L}$$

$$z^* = \frac{z}{h}$$

$$p^* = \frac{p}{p_{stag}}$$

$$\rho_A^* = \frac{\rho_A}{\rho_{A,max}} = \frac{C}{C_{ss}} \frac{-\ln\left(1 - \frac{(\%Ob/ft)}{100}\right)}{-\ln\left(1 - \frac{(\%Ob/ft_{ss})}{100}\right)}$$

$$t^* = \frac{t}{t_c}$$

The nondimensional variables were substituted into the simplified governing equations (Appendix C.4) and the resulting nondimensional form of the governing equations are as follows:

Continuity

$$\frac{\partial v_x^*}{\partial x^*} = 0 \tag{74}$$

Species

$$\left[\frac{1}{t_c}\right]\frac{\partial \rho_A^*}{\partial t^*} + \left[\frac{v_{ext}}{L}\right]v_x^*\frac{\partial \rho_A^*}{\partial x^*} - \left[\frac{v_{ext}}{PeL}\right]\left(\frac{\partial^2 \rho_A^*}{\partial x^{*2}}\right) = 0 \tag{75}$$

Momentum

$$\left[\frac{1}{t_c}\right]\frac{\partial v_x^*}{\partial t^*} + \left[\frac{Euv_{ext}}{L}\right]\frac{\partial p^*}{\partial x^*} - \left[\frac{v_{ext}}{Re_h\,h}\right]\left(\frac{\partial^2 v_x^*}{\partial z^{*2}}\right) = 0 \tag{76}$$

2.7. Analysis of Nondimensional Governing Equations

133

Continuity

The nondimensional continuity equation shown in Equation 74 assumes an incompressible Newtonian fluid with constant properties and indicates that the change in nondimensional velocity with respect to nondimensional distance is neglible. Therefore, it can be assumed that the velocity within the sensing chamber control volume is constant.

Species

The characteristic time for the nondimensional species equation shown in Equation 75 was assumed to be

$$t_c = \frac{L}{v_{ext}} \tag{77}$$

Substituting this value of characteristic time into the nondimensional species equation results in

$$[1]\frac{\partial \rho_A^*}{\partial t^*} + [1]v_x^* \frac{\partial \rho_A^*}{\partial x^*} - \left[\frac{1}{Pe}\right]\left(\frac{\partial^2 \rho_A^*}{\partial x^{*2}}\right) = 0 \tag{78}$$

For the experimental portion of this study the internal velocity, v_{ext}, ranged from 0.05 to 0.10 m/s. The characteristic length, L, was 0.042m and the binary diffusion coefficient, D_A, of carbon particles into air was calculated to be 2.46 x10^{-5} m^2/s. The corresponding range of Peclet numbers for the experimental conditions was 85 to 170. Therefore, the nondimensional form of the species equation covers the following range for the experimental conditions

$$[1]\frac{\partial \rho_A^*}{\partial t^*} + [1]v_x^*\frac{\partial \rho_A^*}{\partial x^*} - [0.006 \leftrightarrow 0.012]\left(\frac{\partial^2 \rho_A^*}{\partial x^{*2}}\right) = 0 \qquad (79)$$

Cleary *et al* (2000) report a diffusion coefficient on the order of 3 x 10^{-9} m^2/s for a 40 nm soot particle, which is approximately 4 orders of magnitude smaller than the calculated value for carbon particles. The Peclet numbers for the experimental conditions and the diffusion coefficient reported by Cleary *et al* range from 700,000 to 1,400,000. Substituting the inverse of these Peclet numbers into Equation 78 results in a coefficient for the diffusive term that ranges from 1.43 x 10^{-6} to 7.14 x 10^{-7}.

The above form of the species equation shows that the coefficients associated with the storage and convective terms are of order 1 whereas the coefficient for the diffusive term is approximately two orders of magnitude smaller based on a calculated value of the diffusion coefficient and is approximately 6 orders of magnitude smaller based value of diffusion coefficient for 40 nm soot particles (Cleary *et al*, 2000). Therefore, the diffusive term in the species equation can be ignored for the given experimental conditions. The nondimensional form of the species equation can be written as

$$\frac{\partial \rho_A^*}{\partial t^*} + v_x^*\frac{\partial \rho_A^*}{\partial x^*} = 0 \qquad (80)$$

The species equation assumes a dilute binary mixture of an incompressible Newtonian fluid with constant properties and insulated mass transport boundaries at the solid portions of the sensing chamber control volume (xz plane at y = +/- w/2 and xy plane at z

= +/- h/2) with no sources or sinks of species. The species equation is for a one-dimensional transient process.

The characteristic time for the species equation can be calculated for the given characteristic length of the detector and the range of characteristic internal velocities for the experiments

$$t_{c(1)} = \frac{L}{U} = \frac{0.042m}{0.05m/s} = 0.84s \tag{81a}$$

$$t_{c(2)} = \frac{L}{U} = \frac{0.042m}{0.10m/s} = 0.42s \tag{81b}$$

The range of characteristic times for the species equation is 0.42 to 0.84s.

Momentum

The characteristic time for the nondimensional momentum equation shown in Equation 76 was assumed to be

$$t_c = \frac{L}{EuU} \tag{82}$$

The following dimensional quantities were applicable to the experimental portion of this study:

$v_{int} = 0.05 - 0.10 \text{m/s}$

$v_{ext} = 0.08 - 0.50 \text{m/s}$

$h = 0.014 \text{m}$

$$v = 1.684 \times 10^{-5} \, \text{m}^2/\text{s}$$

$$\rho = 1.23 \, \text{kg/m}^3$$

$$L = 0.042 \, \text{m}$$

$$p_{stag} = \frac{1}{2} \rho v_{ext}^2 = 0.00394 \leftrightarrow 0.154 \, Pa$$

The range of Reynolds and Euler numbers for the experiments are 42-83 and 1.28-12.5, respectively. Substituting the range of Reynolds and Euler numbers along with the known height and length values into the momentum equation yields

$$[1]\frac{\partial v_x^*}{\partial t^*} + [1]\frac{\partial p^*}{\partial x^*} - [0.056 \leftrightarrow 0.0029]\left(\frac{\partial^2 v_x^*}{\partial z^{*2}}\right) = 0 \tag{83}$$

The coefficients associated with the storage and pressure terms are of order 1 while the coefficient for the viscous term is approximately 2 to 3 orders of magnitude smaller. Therefore, the viscous term in the momentum equation can be ignored for the given experimental conditions. The nondimensional form of the momentum equation can be written as

$$\frac{\partial v_x^*}{\partial t^*} + \frac{\partial p^*}{\partial x^*} = 0 \tag{84}$$

The momentum equation represents a one-dimensional transient process for an incompressible Newtonian fluid with constant properties and no sources or sinks of momentum. For steady state problems the change in velocity with respect to time is zero

and, therefore, the change in nondimensional pressure with respect to nondimensional distance is also zero. The nondimensional pressure drop is small and, therefore, can be ignored due to the relatively short length of the control volume. The viscous forces that would cause such a pressure drop are also negligible over the relatively short distance of the control volume.

The characteristic time for the momentum equation can be calculated for the given characteristic length of the detector and the range of characteristic internal velocities for the experiments

$$t_{c(1)} = \frac{L}{Euv_{int}} = \frac{0.042m}{(1.28)(0.05m/s)} = 0.66s \tag{85a}$$

$$t_{c(2)} = \frac{L}{Euv_{int}} = \frac{0.042m}{(12.5)(0.10m/s)} = 0.03s \tag{85b}$$

The range of characteristic times for the momentum equation is 0.03 to 0.66s. The range of characteristic times for the momentum equation and the species equation (0.42 to 0.84s) are approximately of the same order of magnitude.

The nondimensional governing equations for the given experimental conditions are

Continuity

$$\frac{\partial v_x^*}{\partial x^*} = 0 \tag{86}$$

138

Species

$$\frac{\partial \rho_A^*}{\partial t^*} + v_x^* \frac{\partial \rho_A^*}{\partial x^*} = 0 \tag{87}$$

Momentum (transient flow conditions)

$$\frac{\partial v_x^*}{\partial t^*} + \frac{\partial p^*}{\partial x^*} = 0 \tag{88}$$

Momentum (steady state flow conditions)

$$\frac{\partial p^*}{\partial x^*} = 0 \tag{89}$$

3. Numerical Solution

The one-dimensional transient species equation shown in Equation 87 is a linear first-order hyperbolic partial differential equation and is commonly referred to as the *linear advection equation*. The nondimensional velocity, v*, has been established as a boundary condition based on a semi-empirical resistance factor correlation that relates the external velocity and insect screen geometry to the internal velocity (Velocity Paper). The particular velocity values are average values obtained by integrating external turbulent velocity profile over the detector entrance height and integrating the internal laminar velocity profile over the detector sensing chamber height. The nondimensional continuity equation indicates that the nondimensional velocity is constant within the control volume. Therefore, the constant nondimensional velocity for use in solving the species equation is determined from the inlet velocity boundary condition correlation for the resistance factor.

Photoelectric Detector

$$v* = \frac{\overline{V}_{int}}{\overline{V}_{ext}} = 0.0034\left[\left(\frac{1-\alpha^2}{\alpha^2}\right)\text{Re}_d\right] \quad for \ \alpha = 0.664 \ and \ 10 < \text{Re}_d < 27$$

(90)

Ionization Detector

$$v* = \frac{\overline{V}_{int}}{\overline{V}_{ext}} = 0.0025\left[\left(\frac{1-\alpha^2}{\alpha^2}\right)\text{Re}_d\right] \quad for \ \alpha = 0.664 \ and \ 17 < \text{Re}_d < 27$$

(91)

The linear advection equation is typically expressed in the following general format.

$$u_t = \alpha u_x \qquad\qquad (92)$$

Where u_t is the partial derivative of the quantity u with respect to time, u_x is the partial derivative of the quantity u with respect to the x direction, and α is the velocity.

3.1. Transport Delays Outside of Control Volume

The mass transport model considers a gas phase control volume inside the sensing chamber where fully developed flow conditions exist. The model predicts the time for the sensing chamber to exceed the alarm threshold for a given external velocity and external aerosol concentration. The experimentally determined detector response times from the step exposure tests involves additional transport delays that are not accounted for in the model. Therefore, it was necessary to account for these additional transport

140

delays and adjust the response time predicted with the mass transport model accordingly. The additional delays account for the time for the aerosol to be transported from the laser transmittance measurement location to the leading edge of the detector and the time for the aerosol to be transported from the leading edge of the detector to the leading boundary of the gas phase control volume as depicted in Figure 44.
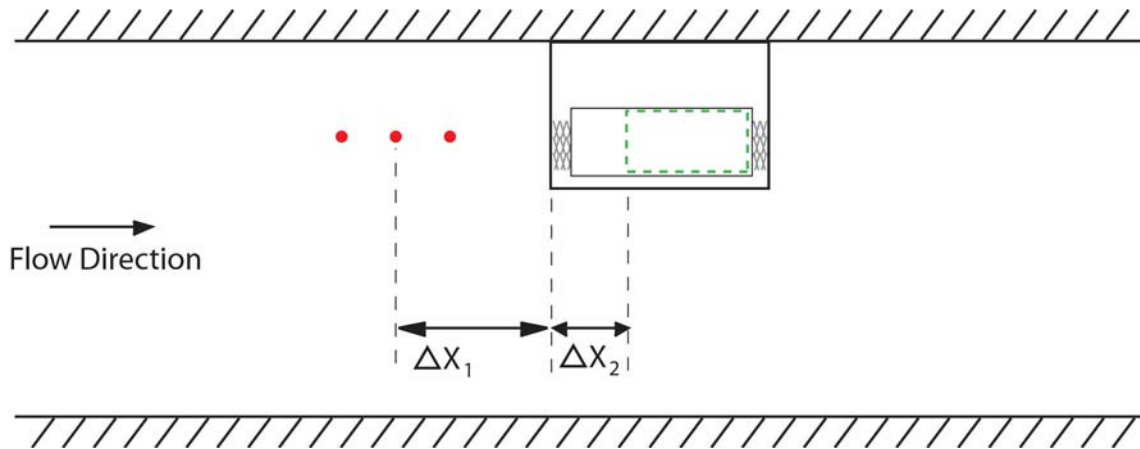
Figure 44 -- Transport delays outside of sensing chamber control volume.

The transport delay to reach the control volume for the photoelectric and ionization detectors were calculated using:

$$t_{transport} = \frac{\Delta x_1}{\overline{V}_{ext}} + \frac{\Delta x_2}{\overline{V}_{int}}$$

(93)

The resulting transport delay times are summarized in Table 23 and Table 24.

Table 23 – Photo detector transport delay times outside of sensing chamber control volume.

Photoelectric Detector		
$V_{avg,ext}$ (m/s)	$V_{avg,int}$ (m/s)	$t_{transport}$ (s)
0.500	0.037	0.217
0.377	0.021	0.355
0.302	0.014	0.527
0.254	0.010	0.725
0.162	0.004	1.681
0.108	0.002	3.601
0.074	0.001	7.637

Table 24 -- Ion detector transport delay times outside of sensing chamber control volume.

Ionization Detector		
$V_{avg,ext}$ (m/s)	$V_{avg,int}$ (m/s)	$t_{transport}$ (s)
0.490	0.026	0.283
0.369	0.015	0.471
0.296	0.010	0.707
0.249	0.007	0.979
0.158	0.003	2.306
0.106	0.001	4.988
0.072	0.001	10.649

4. Finite Difference Method

The linear advection equation was solved using the Lax-Wendroff finite differencing scheme which is an explicit method with second order accuracy (Iserles, 1996)

$$\rho*_{j}^{n+1} = \rho*_{j}^{n} - v*\Delta t \frac{\rho*_{j+1}^{n} - \rho*_{j-1}^{n}}{2\Delta x} + \frac{1}{2}(v*\Delta t)^2 \frac{\rho*_{j-1}^{n} - 2\rho*_{j}^{n} + \rho*_{j+1}^{n}}{(\Delta x)^2} \qquad (94)$$

The superscripts refer to the current time step, *n+1*, and the previous time step, *n*, while the subscripts refer to computational nodes before, *j-1*, and after, *j+1*, the current node, *j*. The CFL condition for the Lax-Wendroff finite difference scheme is (Iserles, 1996)

$$\left| v* \right| \frac{\Delta t}{\Delta x} \leq 1 \qquad (95)$$

The CFL condition was used to select an appropriate time step for the known velocity and spatial discretization.

A grid independent solution for the mass transport model was determined to exist for a spatial discretization of 25 computational nodes (Appendix C.5). The exit species concentration boundary condition was determined to have no impact on the numerical solution (Appendix C.5). Additional preliminary considerations for the mass transport included sensitivity analyses of the inlet species concentration boundary condition and interior velocity (Appendix C.5).

5. Modeling Detector Response Tests

The finite difference model was used to simulate the smoke detector response test data collected in the experimental portion of this study. The Lax-Wendroff finite difference scheme was used with a spatial discretization of 25 computational nodes. The response time was estimated by calculating the time for the average species concentration in the control volume to reach the alarm threshold. The 23 interior nodes in the control volume were used to determine the average species concentration.

The nondimensional velocity and internal velocity were determined from the inlet velocity boundary conditions for the photoelectric and ionization detector. The values in Table 25 and Table 26 correspond to the photoelectric and ionization detectors, respectively.

Table 25 -- Nondimensional and average internal velocity for photo detector.

Photoelectric Detector				
Fan (Hz)	$V_{avg,ext}$ (m/s)	Re,d	v*	$V_{avg,int}$ (m/s)
20	0.500	17.21	0.074	0.037
15	0.377	12.97	0.056	0.021
12	0.302	10.40	0.045	0.014
10	0.254	8.74	0.038	0.010
7	0.162	5.57	0.024	0.004
5	0.108	3.73	0.016	0.002
3	0.074	2.53	0.011	0.001

Table 26 -- Nondimensional and average internal velocity for ion detector.

Ionization Detector				
Fan (Hz)	$V_{avg,ext}$ (m/s)	Re,d	v*	$V_{avg,int}$ (m/s)
20	0.490	16.87	0.053	0.026
15	0.369	12.71	0.040	0.015
12	0.296	10.20	0.032	0.010
10	0.249	8.57	0.027	0.007
7	0.158	5.46	0.017	0.003
5	0.106	3.66	0.012	0.001
3	0.072	2.48	0.008	0.001

The detector response time based on average species concentration in the sensing chamber was predicted with the mass transport model and the results were plotted against the response time measured in the aerosol exposure tests.

The steady state aerosol exposure was determined from the steady state output of each smoke detector sensor in relation to the UL 217/268 smoke box calibration data provided by the manufacturer. The sensor output is expressed as an 8-bit value with a possible range of 0 to 255. The UL 217/268 smoke box data is reported in %Ob/ft and is based on the rise in sensor output relative to the clean air background level. The 8-bit sensor values for clean the clean air background readings were 87 for photoelectric and 94 for the ionization detectors. The UL 217/268 alarm points varied for each addressable sensor type and are summarized in Table 27.

144

Table 27 -- UL 217/268 alarm points for addressable photo and ion detectors.

Photoelectric	Clean Air = 87	Ionization	Clean Air = 94
%Ob/ft (UL 217/268)	Δ=output - 87	%Ob/ft (UL 217/268)	Δ=output - 94
0.2	6	0.5	50
0.5	15	0.9	65
1.0	28	1.3	80
1.5	42	1.7	100
2.0	55		
2.5	68		
3.0	82		
3.7	100		

The range of alarm points is different for each sensor with only the 0.5%Ob/ft alarm point in common. For a given external exposure it was possible for one test to trigger more than one alarm point for measurement purposes. It should be noted that in practice only one alarm point would be set at the fire alarm control panel. However, in the aerosol exposure tests where the 8-bit representation of the sensor output was recorded, it was possible to monitor when the various alarm points were exceeded in a single given test. An example of this is shown in Figure 45.
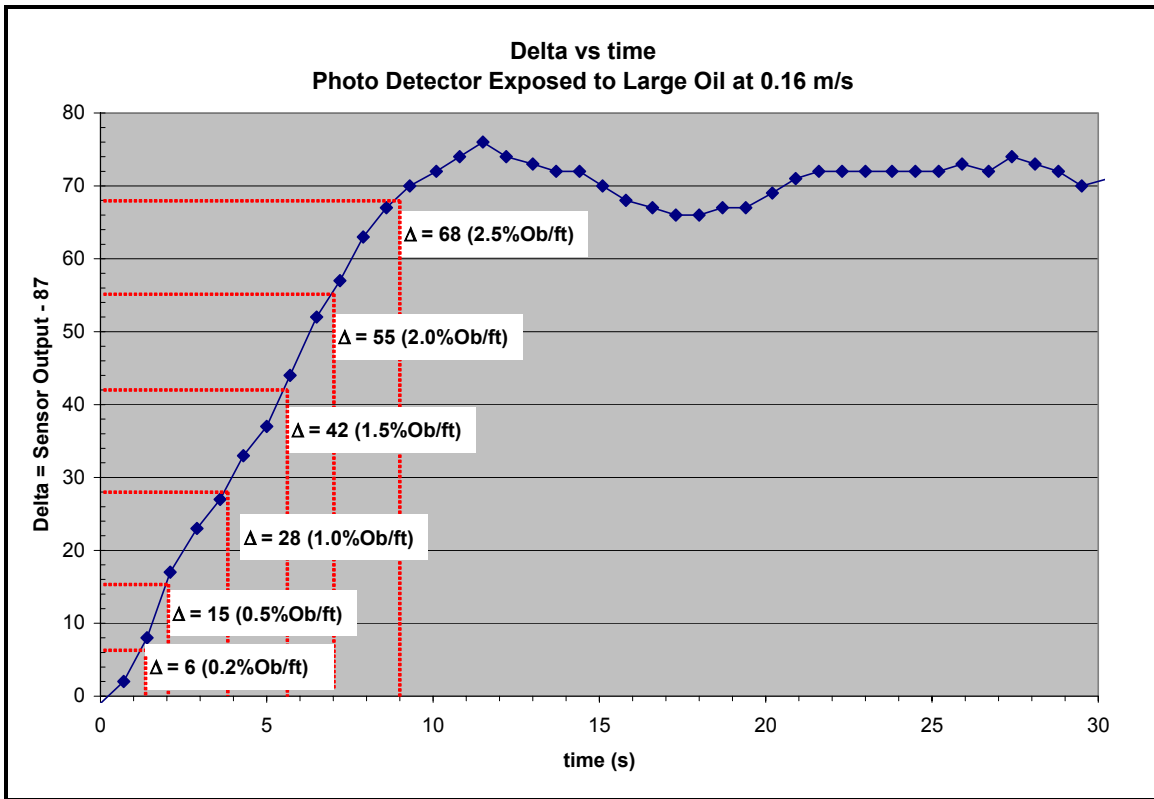
Figure 45 -- Sensor output delta vs time with multiple alarm points being exceeded in a single test.

It has been assumed that at the steady state condition the internal aerosol concentration is equal to the external concentration. The steady state aerosol exposure as a function of external velocity is shown for the four aerosol sources used in this study for both the photoelectric and ionization smoke detectors. The data shown are based on three repeated tests under nominally the same conditions. The data points are the mean value and the y error bars represent one standard deviation as a combined estimate of the measurement uncertainty and experimental variability.
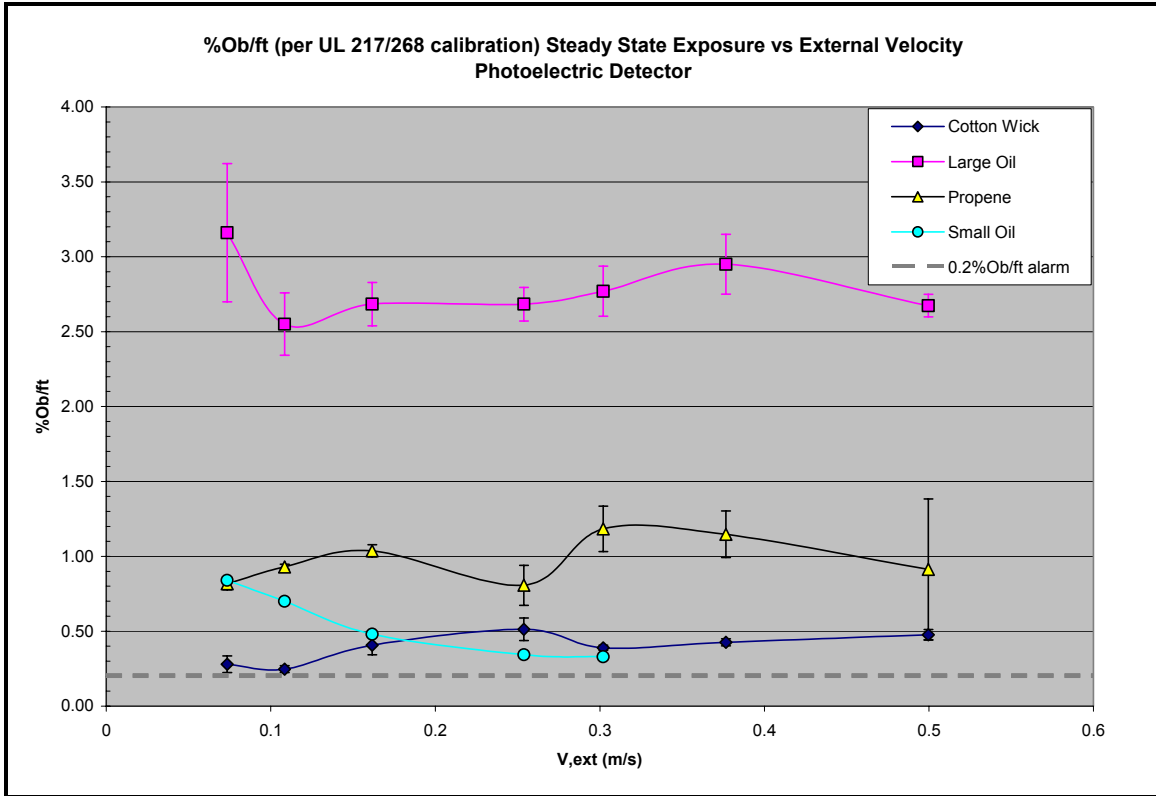
Figure 46 -- Steady state aerosol exposure per the UL 217/268 smoke box calibration data for the photo detector.

The aerosol output from three of the four sources (cotton wick, large oil, and propene) was adjusted at each external velocity in order to provide a nominally consistent exposure concentration. The nominal aerosol exposures were 0.4%Ob/ft for the cotton wick, 2.75%Ob/ft for the large oil, and 1%Ob/ft for the propene soot. The small oil source had a fixed output of aerosol. Therefore, the aerosol concentration decreased as external velocity increased due to the increased dilution of aerosol in air. This general trend is indicated in the Figure as the small oil varies from 0.25 to 0.80%Ob/ft over the range of velocities. The photoelectric detector's minimum sensitivity setting was 0.2%Ob/ft which is indicated in the Figure.

Figure 47 -- Steady state aerosol exposure per the UL 217/268 smoke box calibration data for the ion detector.

The cotton wick and propene sources for both the photoelectric and ionization detectors were the same. The steady state sensor output from both the photoelectric and ionization sensors are similar for the cotton wick and propene sources. However, the large oil exposure for the photoelectric detector was larger relative to that for the ionization detector. The ionization detector steady state response to the large oil droplets was at a saturated level (i.e., the maximum output value of 255) when it was exposed to the same aerosol level as was used in comparable photoelectric detector tests. The small oil droplet exposure for the ionization detector is not plotted as this particular exposure did not exceed the minimum 0.5%/ft alarm point. The small oil droplet exposure was a fixed source and, therefore, it was not possible to increase the aerosol exposure concentration.

148

Additionally, as shown in Table 18, the alarm points for the ion detector were more limited relative to the photo detector and were in the range of 0.5 to 1.9%Ob/ft. This was a contributing factor in the rather limited response time data reported for the ionization detector.

The species concentration was normalized according the steady state external concentration. This value was determined from the steady state output value from the addressable smoke detectors. The alarm point species concentrations were nondimensionalized using the steady state external concentration based on %Ob/ft. For example, an alarm point of 0.5%/ft would have a nondimensional value of 0.25 for a steady state external concentration of 2.0%/ft. The scaling was performed in accordance with Equation 96.

$$\rho_A^* = \frac{-\ln\left(1 - \frac{(\%Ob/ft)}{100}\right)}{-\ln\left(1 - \frac{(\%Ob/ft_{ss})}{100}\right)}$$

(96)

The nondimensional species concentration for the 0.2% alarm point threshold as a function of external velocity is shown in Figure 48 for the photoelectric and ionization detectors. These nondimensional species concentrations were used in mass transport model to predict the time as the alarm point for the 0.2%/ft threshold.

149
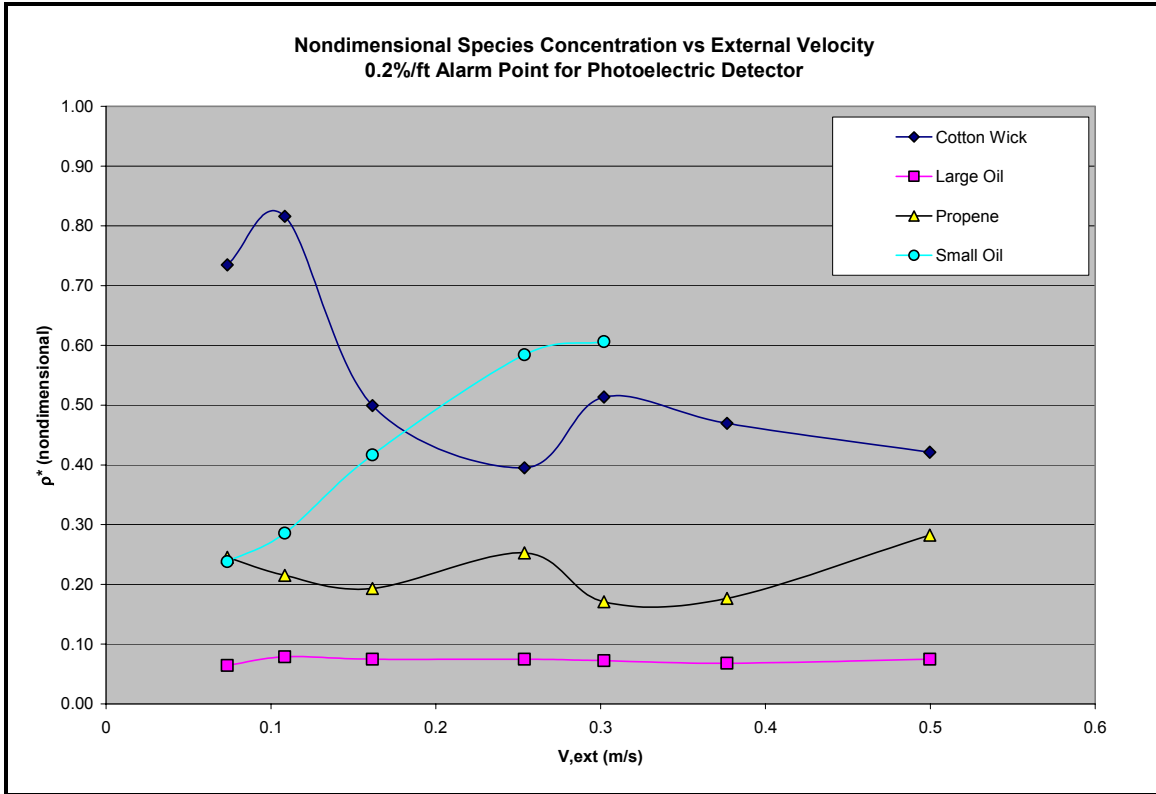
Figure 48 -- Nondimensional species concentration (alarm point normalized to exterior concentration) vs external velocity for photo detector at 0.2%/ft.
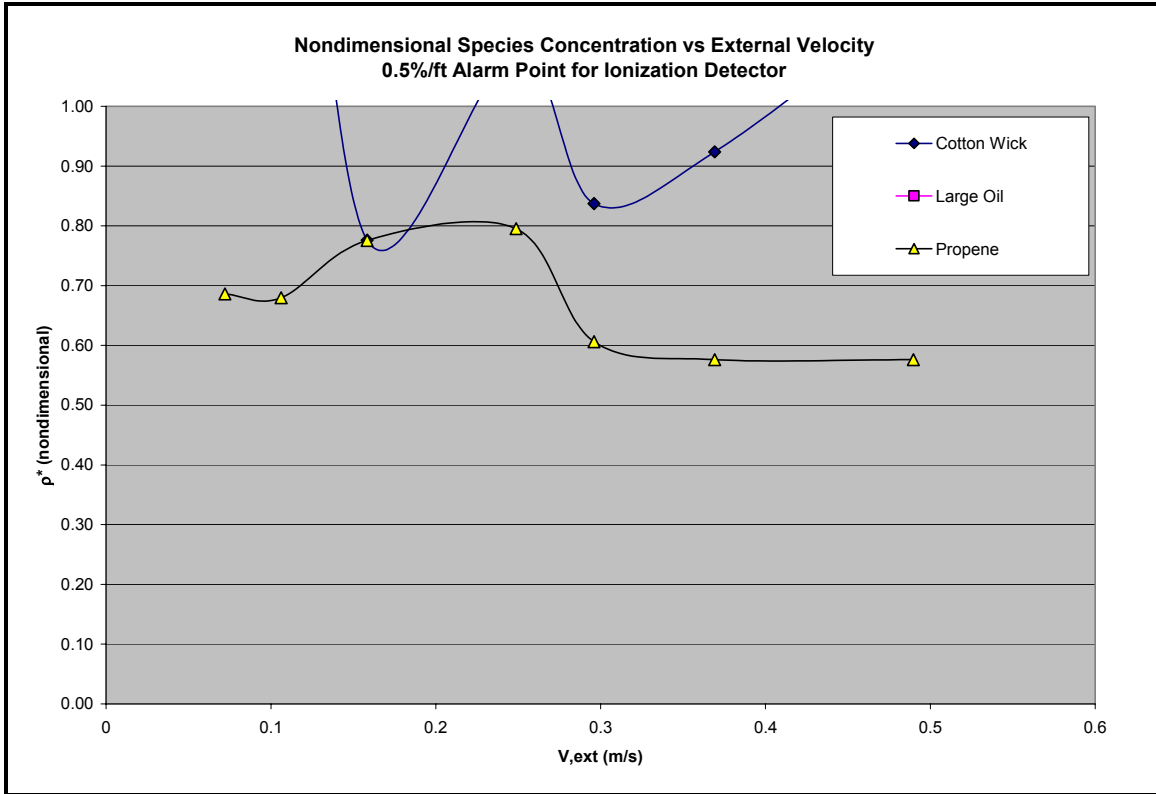
Figure 49 -- Nondimensional species concentration (alarm point normalized to exterior concentration) vs exterior velocity for ion detector at 0.5%/ft.

It can be seen that only the propene soot provided a consistent concentration within the 0.5%/ft alarm point for the ionization detector. This was previously shown in Figure 33. It should be noted that the 0.5%/ft alarm point was the most sensitive setting available from the manufacturer of the ion detector. In contrast, the photoelectric detector was capable of a 0.2%/ft alarm point and, therefore, was able to respond to all the aerosol sources.

The predicted response time was based on the average nondimensional species concentration for all interior nodes of the control volume. The interior nodes were monitored for when the average nondimensional concentration exceeded the

151

nondimensional alarm point. The time to steady state was also predicted by monitoring when the average nondimensional species concentration for all interior nodes was equal to unity which was assumed to be when the interior concentration is equal to the exterior concentration.

The Figures that follow show mass transport model prediction of response time (adjusted for transport delays outside the control volume) and the associated measured detector response times plotted as a function of external velocity. The mean values for response time represent the average value for three repeated experiments. The y error bars represent the statistical standard deviation in response time for the three repeated tests.
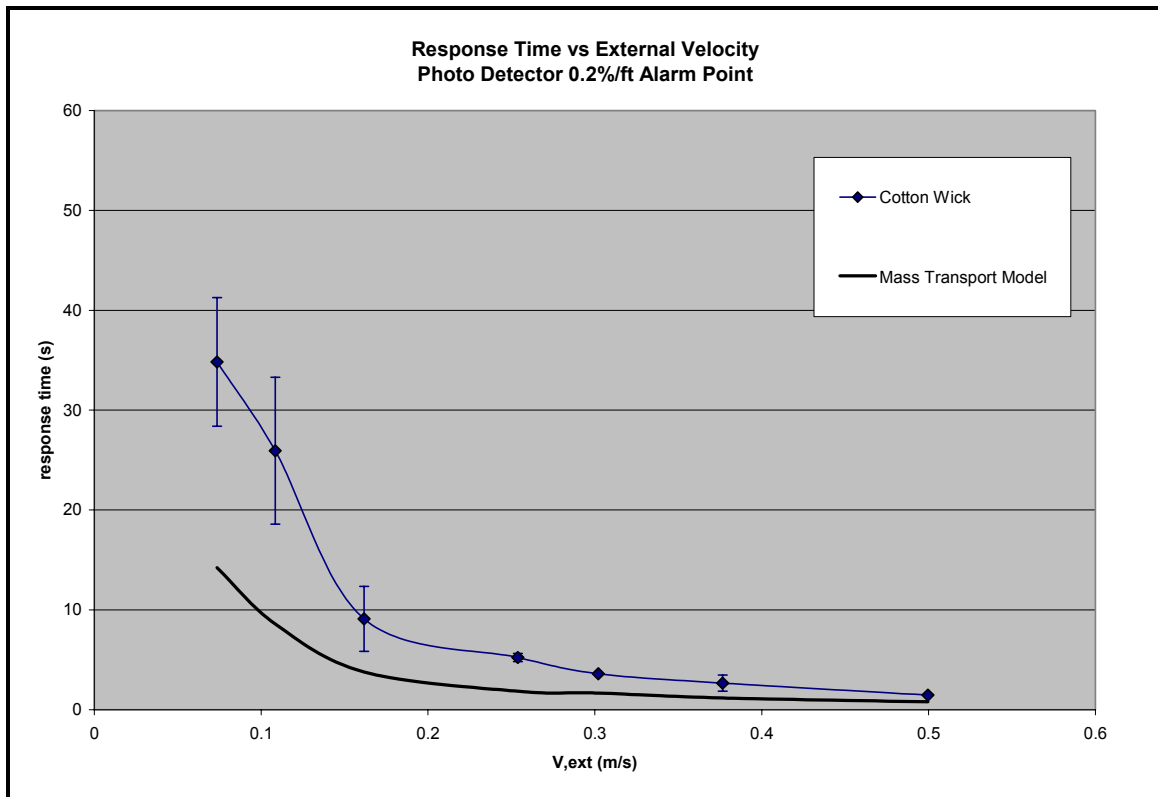
Figure 50 -- Predicted and measured response times for photo detector and cotton wick at 0.2%Ob/ft.
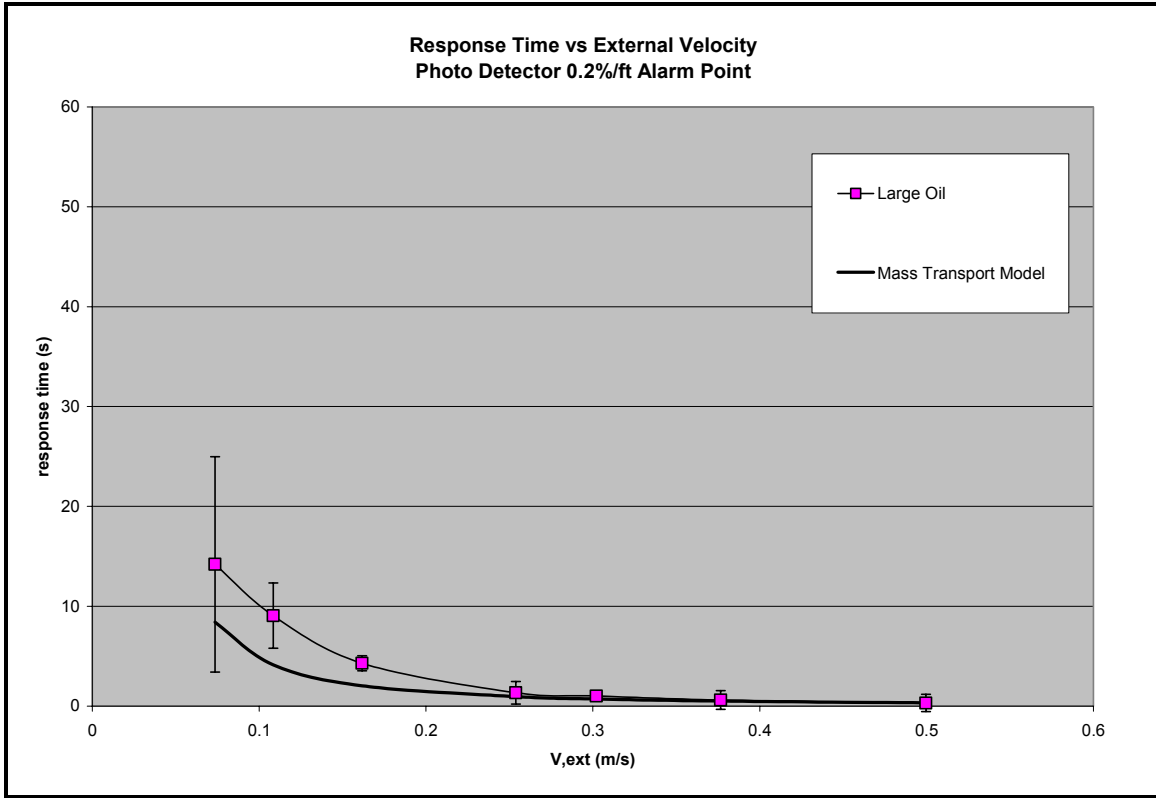
Figure 51 -- Predicted and measured response times for photo detector and large oil at 0.2%Ob/ft.
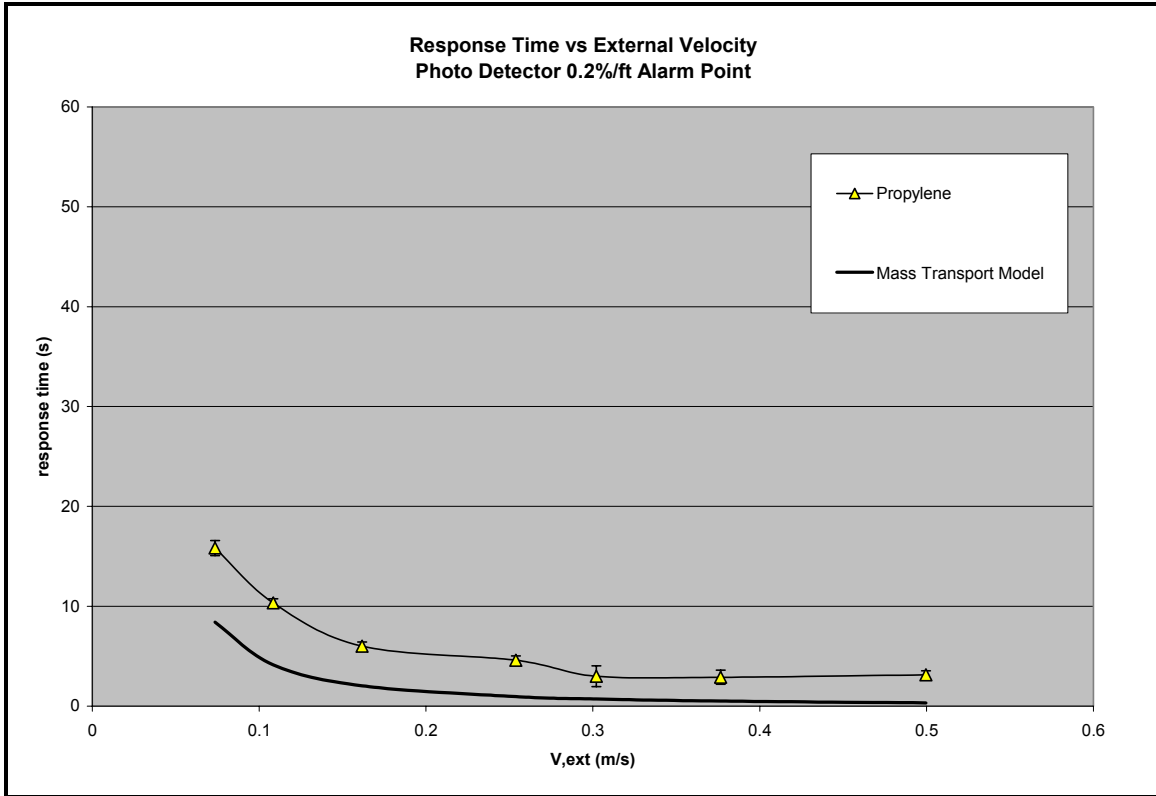
Figure 52 -- Predicted and measured response times for photo detector and propylene at 0.2%Ob/ft.
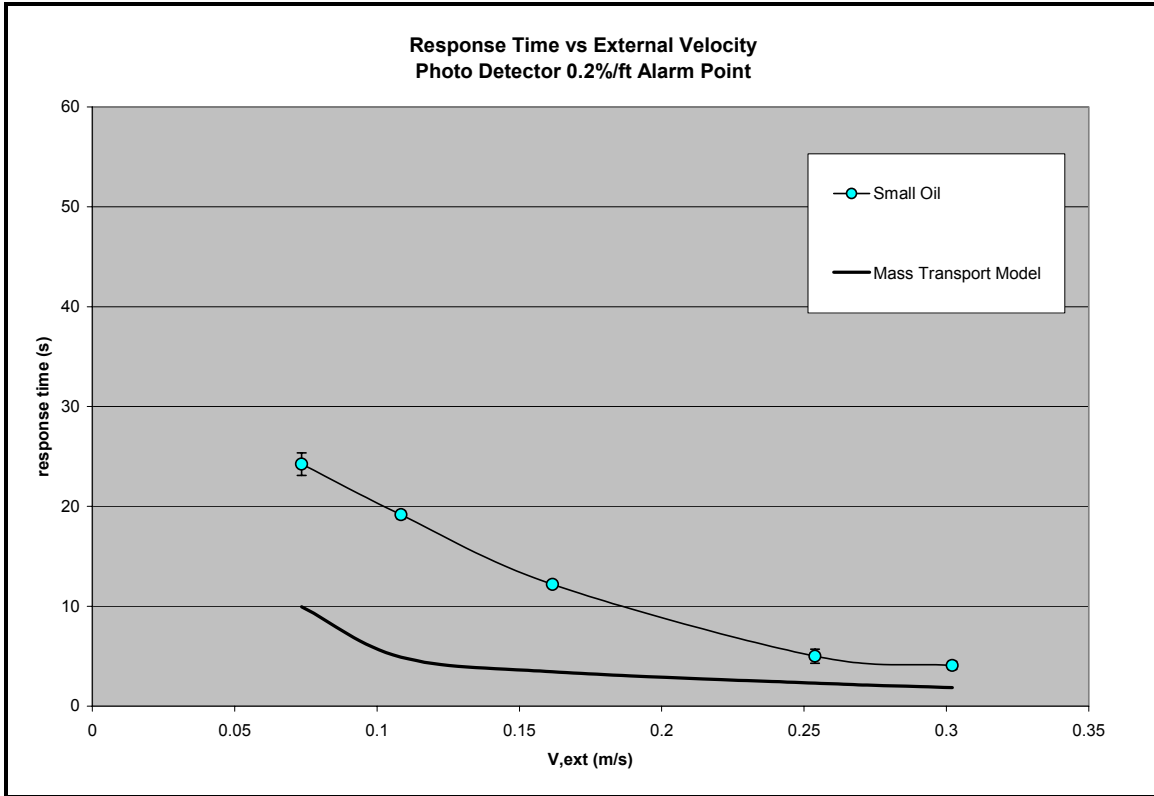
Figure 53 -- Predicted and measured response times for photo detector and small oil at 0.2%Ob/ft.

The residual between the predicted and measured response times for each aerosol source was calculated in the following manner.

$$residual = t_{response,model} - t_{response,measured}$$

(97)

The magnitude of the residual is plotted as function of time for the photoelectric detector exposed to the four aerosol sources at the 0.2%/ft alarm point are shown in the Figure below. A negative number indicates the model underestimates the measured response

155

time whereas a positive number indicates that the model overestimates the measured response time.
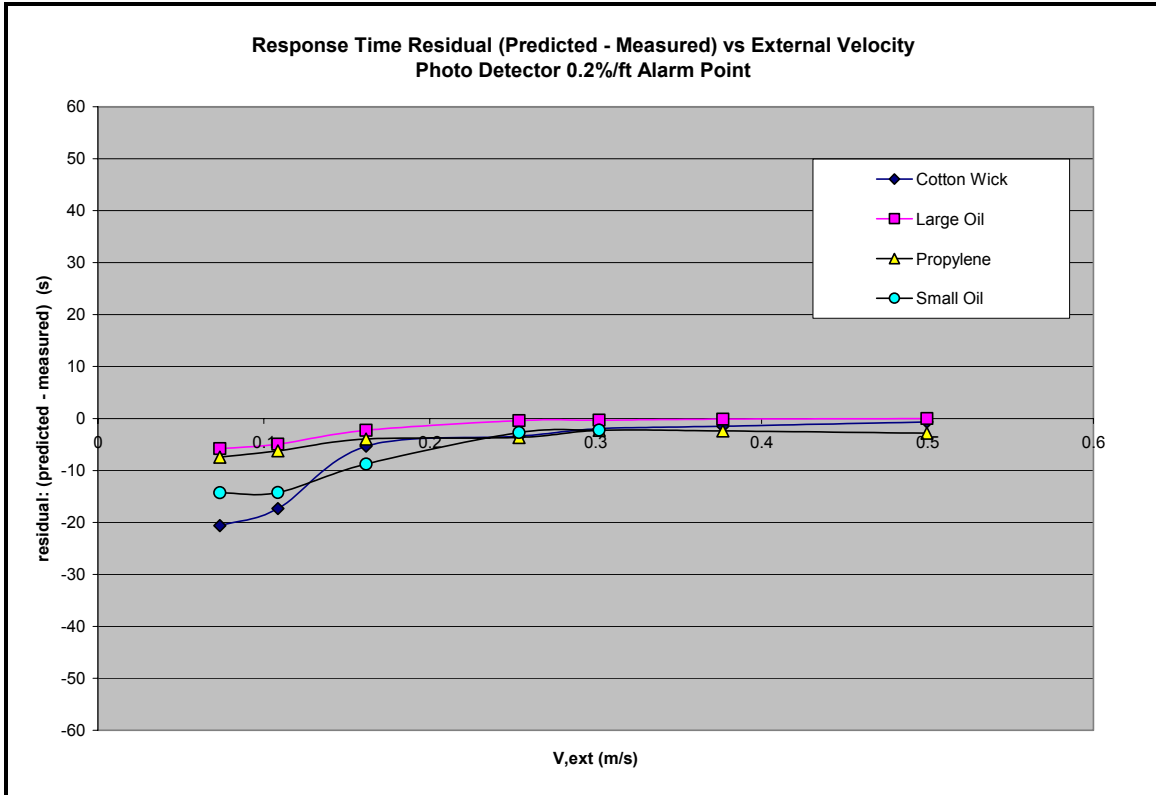
Figure 54 -- Magnitude of residual between predicted and measured response times for photo detector and all four aerosol sources.

At the 0.2%Ob/ft alarm point, the residual is -5 seconds or less for all four aerosol types when the external flow velocity is 0.25 m/s or greater. The residual for the large oil and propene sources are consistently -7 seconds or less for all velocities. The residuals for the cotton wick and small oil aerosols increases at lower velocities to -10 seconds or less for an external flow of 0.15 m/s. The maximum residuals for the cotton wick and small oil aerosols are -20 and -15 seconds respectively at the lower range of external velocities which are less than 0.15 m/s. This trend of underpredicting the response time at low

156

velocity could be the impact of neglecting ordinary diffusion in the mass transport model. The percent residual will be used to investigate this aspect as the dimensional scaling arguments used to develop the species equation clearly indicated that convective mass transport is the dominant phenomena over the experimental conditions and that diffusive transport was 4 to 7 orders of magnitude smaller. However, it is also important to put the magnitude of these residuals into a practical context of addressable smoke detection systems. Considering that a polling interval for smoke detectors in an addressable system could be on the order of 5 to 10 seconds, the predicted response time residuals for all aerosol types are within the uncertainty of the polling interval from a practical standpoint.

It is also helpful to put these results into context by considering a reasonable smoke detection scenario such as a wastebasket fire. Assuming a steady state wastebasket fire of 50 kW located under a 2.44m high ceiling at a radial distance of 6.5 m (the maximum distance from 4 smoke detectors spaced 10m (30 ft) on center), the resulting maximum ceiling jet velocity would be in the range of 0.22 m/s (using Motevalli and Marks correlation (Motevalli and Marks, 1991)) and 0.24 m/s (using Alpert's correlation (Evans, 1995). In light of this flaming fire scenario which could be considered a reasonable design situation, the residual in the predicted response time for 0.2%Ob/ft alarm is on the order of -5 seconds or less. The residuals in this context are within the typical polling interval in an addressable smoke detection system of 5 to 10 seconds.

The residuals shown above were also expressed as a percentage of the measured value and plotted as a function of the external velocity.

$$\%residual = \left(\frac{t_{response,model} - t_{response,measured}}{t_{response,measured}} \right) 100\%$$

(98)

The residual as a percentage of the measured response time for the photoelectric detector exposed to all four aerosol sources at the 0.2%/ft alarm point are shown in the following Figure. A negative percentage indicates the model underestimates the measured response time and a positive percentage indicates the model overestimates the measure response time. For the ideal situation of the predicted values being in agreement with the measured values, the percent residual would be zero.
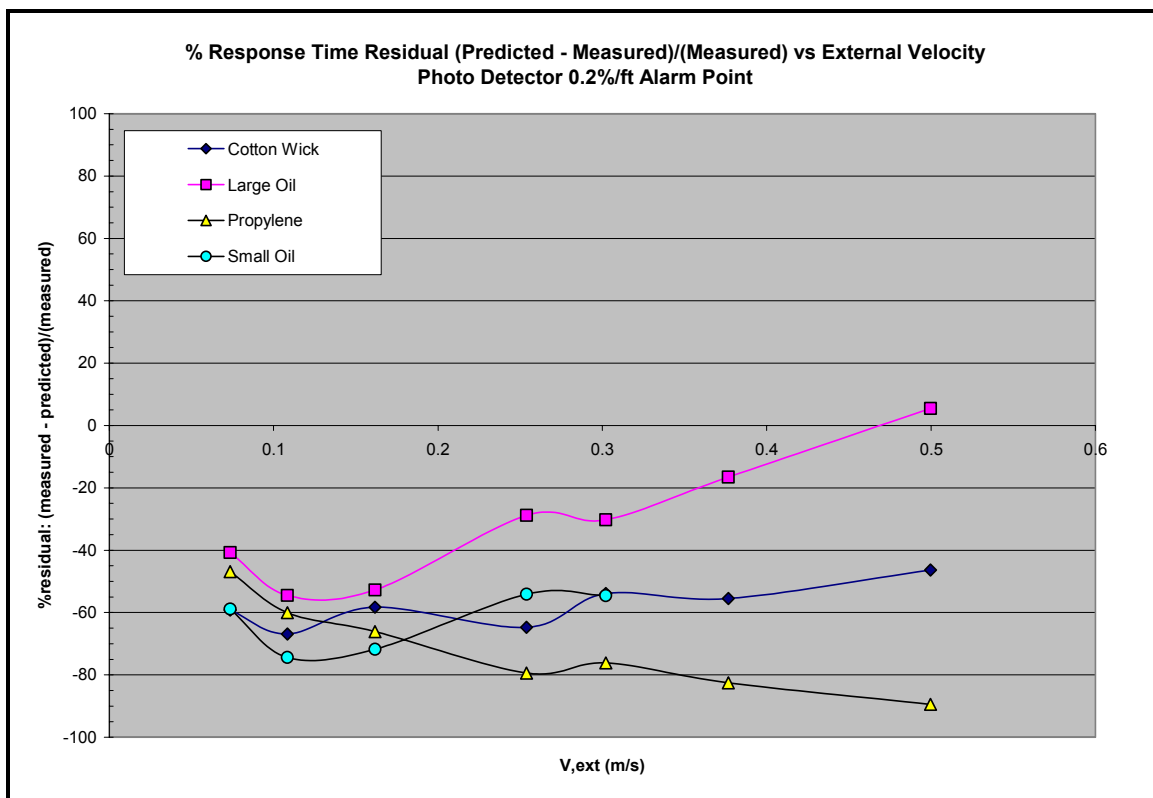
Figure 55 -- Percent residual between predicted and measured response times for photo detector and all four aerosol sources.

In general, the mass transport model underestimates the response time for all aerosol sources by as much as 40 to 80%. It should be noted that the percent residuals for the predicting response times are nominally constant over the range of velocities. This general trend indicates that ordinary diffusion does not have a significant effect, particularly at low velocities. If ordinary diffusion was a significant factor, the percent residual would be expect to increase in magnitude for low velocities. The uncertainty in the characteristic response time of the mass transport model will be evaluated in the section that follows in order to more clearly address this aspect. It should be pointed out that from a practical standpoint the magnitude of the residuals are within the uncertainty in response time for a wastebasket fire in an addressable smoke detection system.

The time to steady state for the four aerosol types was also examined with the mass transport model. The time to steady state was when the average interior species concentration was equal to unity which is when the interior species concentration is assumed to be equal to the exterior concentration. The mean values for response time represent the average value for three repeated experiments. The y error bars represent the statistical standard deviation in the response time for the three repeated tests.
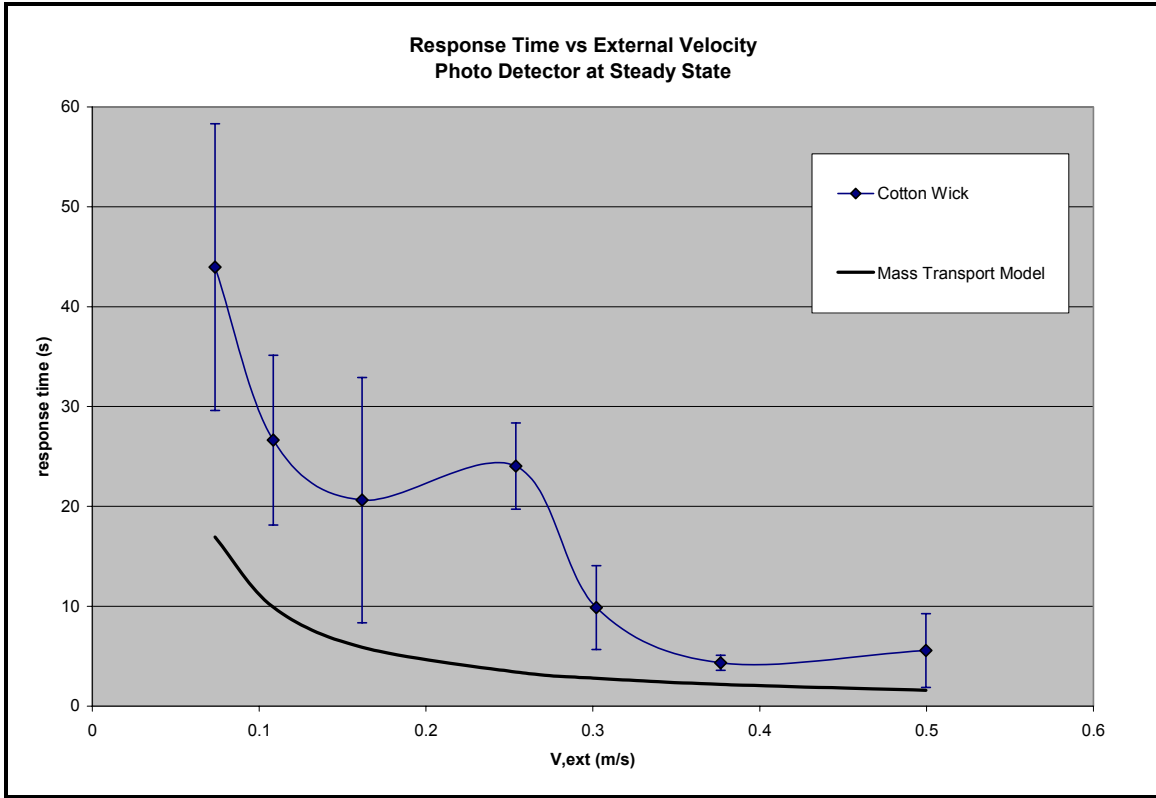
Figure 56 -- Predicted and measured time to steady state for photo detector and cotton wick.
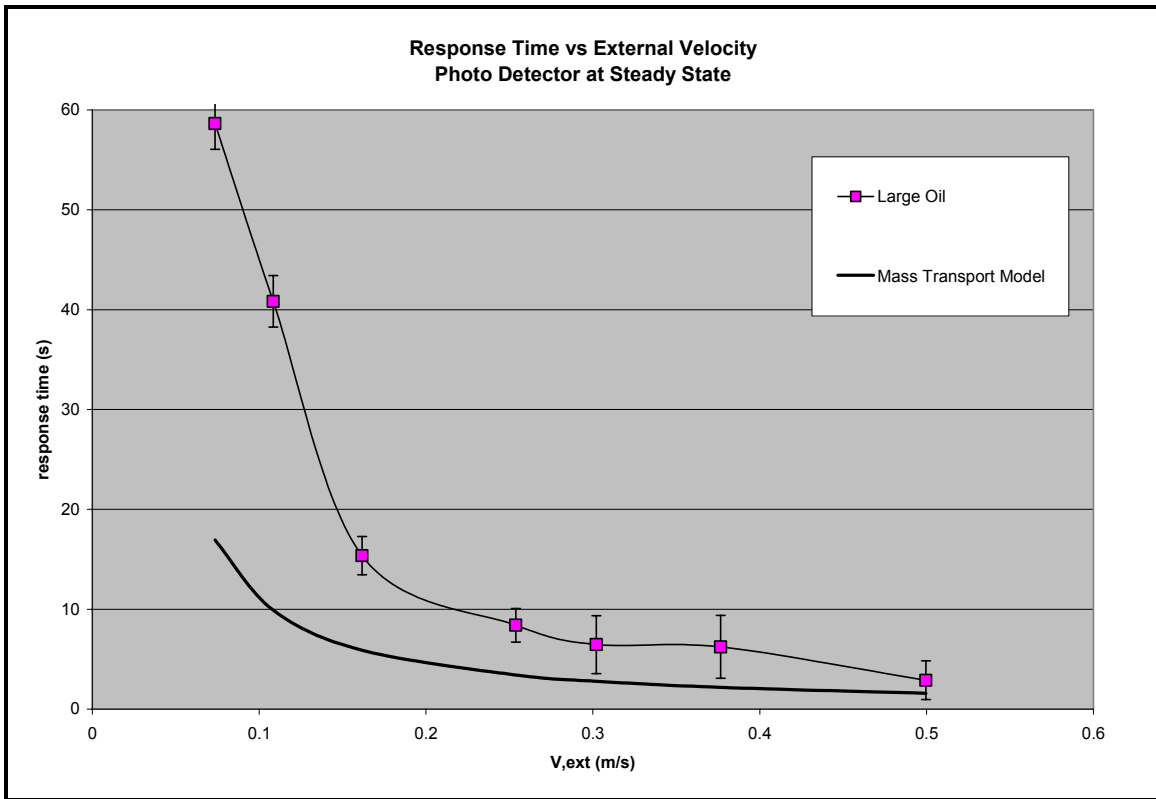
Figure 57 -- Predicted and measured time to steady state for photo detector and large oil.
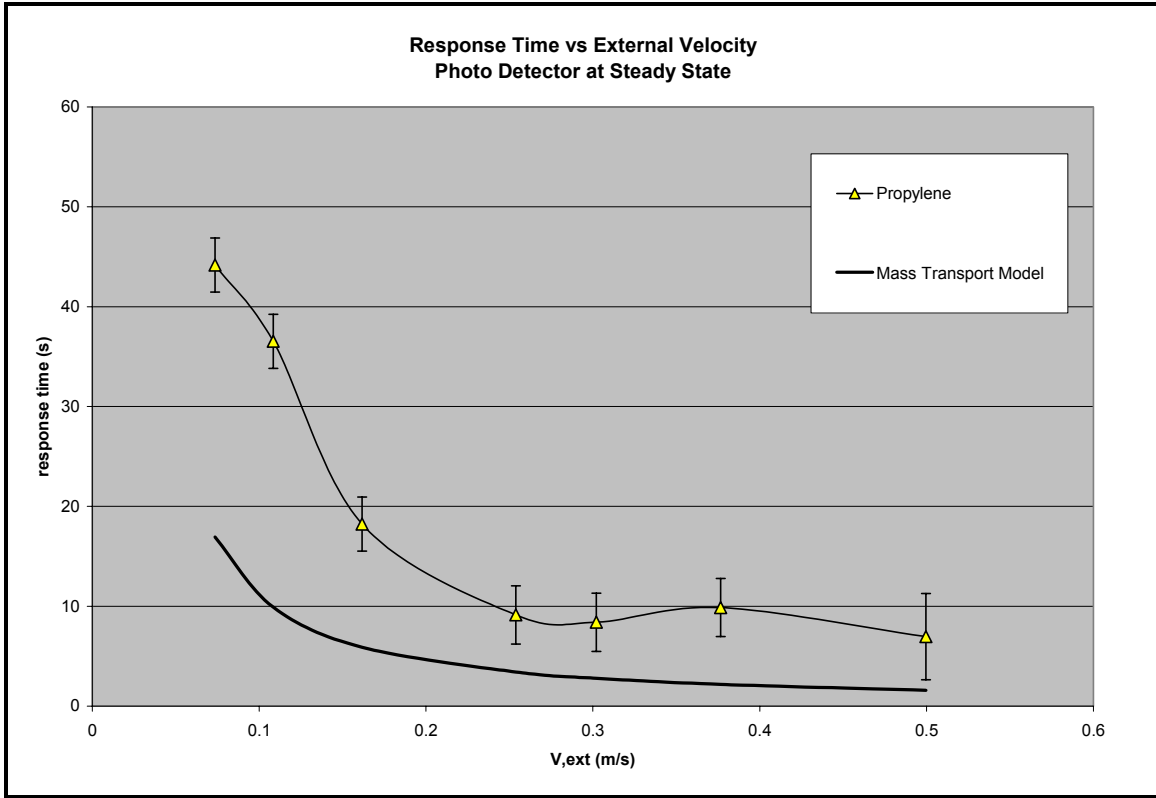
Figure 58 -- Predicted and measured time to steady state for photo detector and propylene.
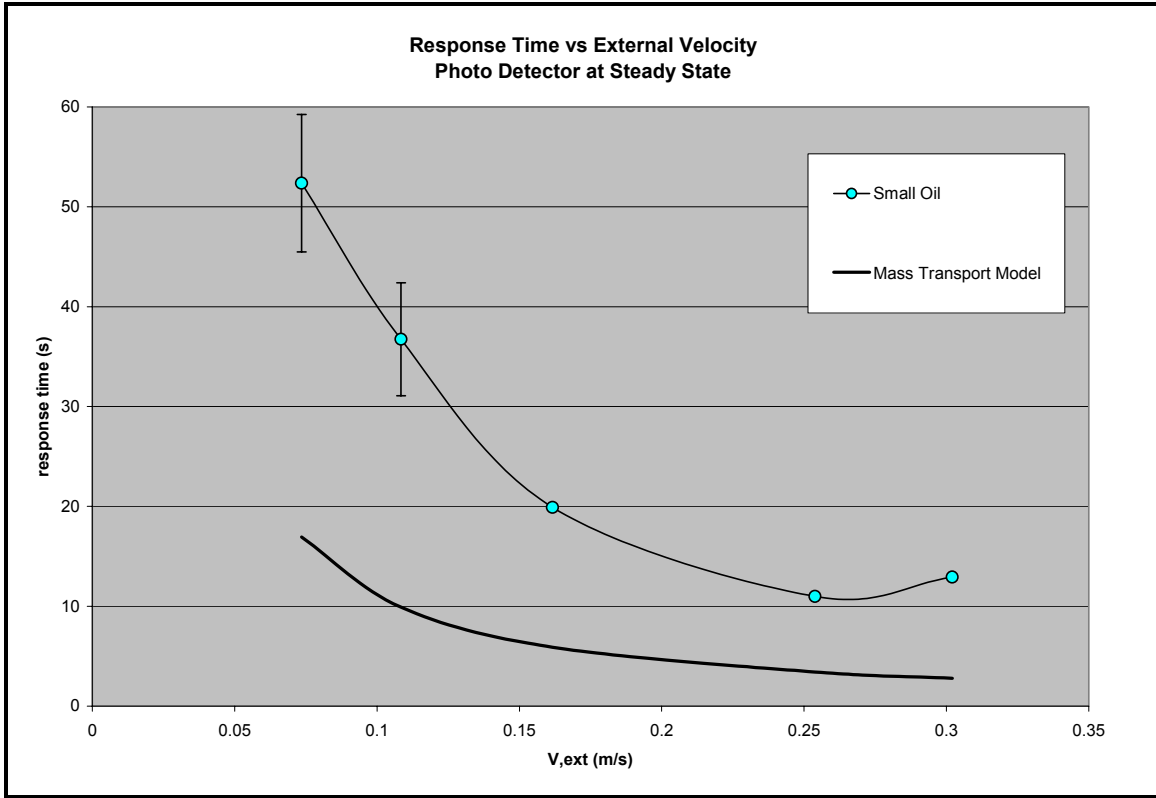
Figure 59 -- Predicted and measured time to steady state for photo detector and small oil.,

Again the residual between the predicted and measured value was computed on a magnitude and percentage basis for the steady state condition. The results are plotted in the Figures that follow.
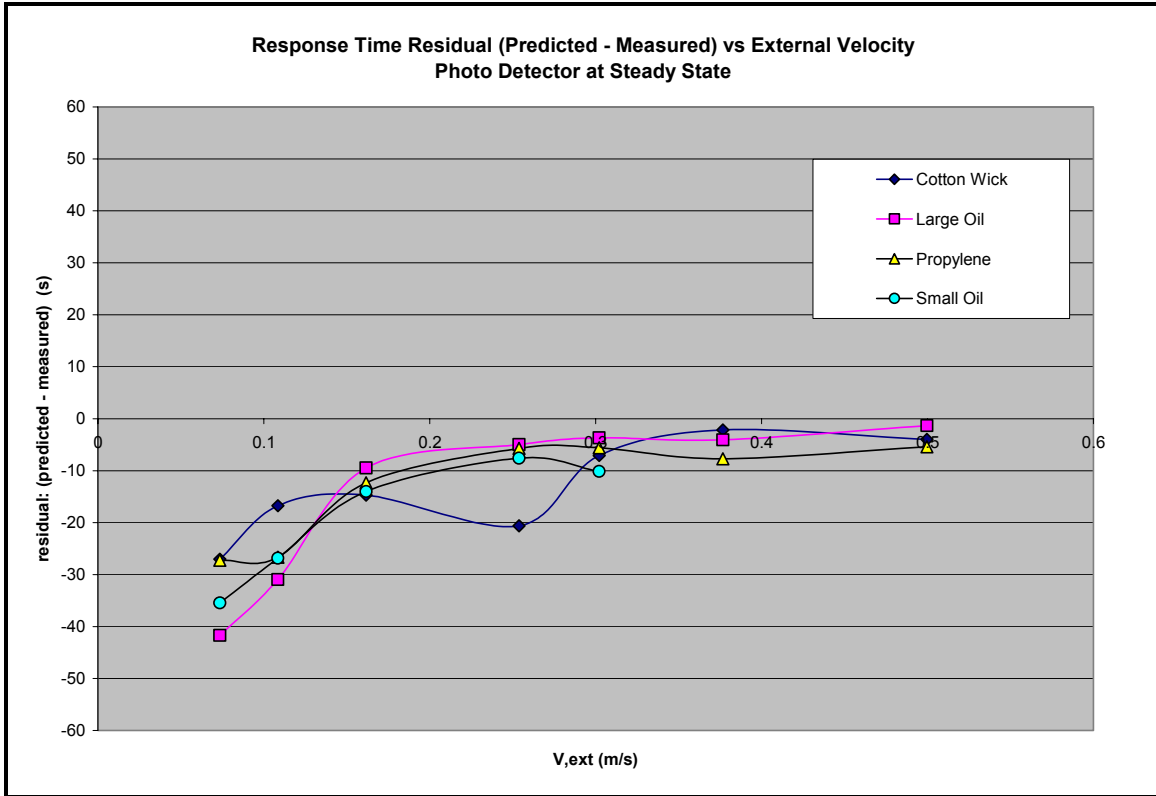
Figure 60 -- Magnitude of residual between predicted and measured time to steady state for photo detector and all four aerosol sources.

At steady state, the residual is -10 seconds or less for all four aerosol types when the external flow velocity is 0.25 m/s or greater. The residual for all four aerosol types is between -10 and -15 seconds at an external velocity of 0.15 m/s. The maximum residuals for all four aerosol types are between -25 and -40 seconds at the lower range of external velocities which are less than 0.15 m/s. For external velocities of 0.15 m/s and greater, the residuals for predicting the time to steady state are consistent with the residuals for the predicted time to 0.2%Ob/ft. For velocities, of 0.10 m/s and less, the predicted residuals for time to steady state of -25 to -40 seconds are larger than the residuals for the predicted time to 0.2%Ob/ft of -5 to -20 seconds. As was shown for the predicted time to the 0.2%/ft alarm point, the time to steady state conditions also indicate a residual that

164

increases in magnitude at low velocity. This could be the impact of neglecting ordinary diffusion in the mass transport model, despite the dimensional scaling arguments used to the contrary. Again the percent residual will be used to investigate this aspect. However, from a practical standpoint the predicted time to an alarm point is of much greater significance in a design situation that predicting the time to steady state. Additionally, it has also been demonstrated that the magnitude of the residuals are within the uncertainty in response time for a wastebasket fire in an addressable smoke detection system. .
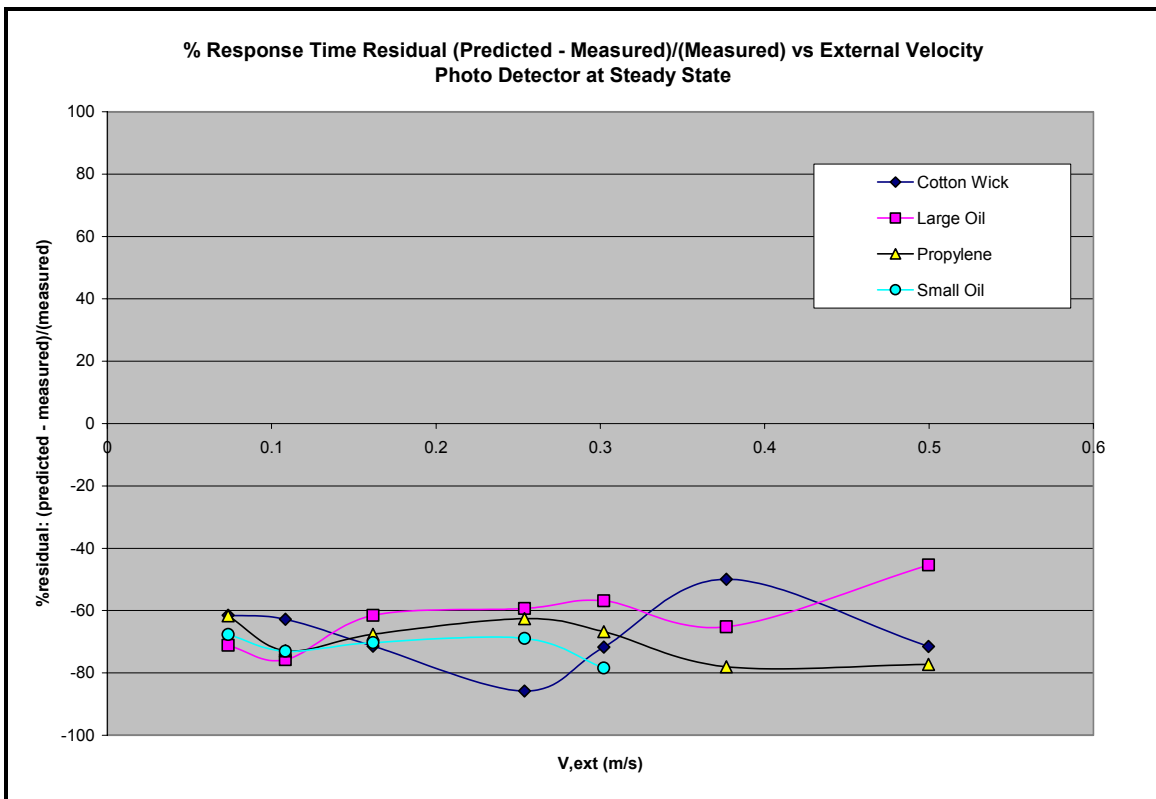
Figure 61 -- Percent residual between predicted and measured time to steady state for photo detector and all four aerosol sources.

In general, the percent residual for the time to steady state is within 60% to 80% for all four aerosol sources and are consistent with the percent residuals for predicted time to

0.2%Ob/ft alarm point. Again, the magnitude of these residuals are within the uncertainty of wastebasket fire scenario in a typical addressable smoke detection system. The nominally constant value for the percent residual indicates that ordinary diffusion does not have a signifant impact at low velocities. This result is consistent with the dimensional scaling arguments used to develop the mass transport model and is also consistent with the results for the 0.2%/ft alarm point condition. Furthermore, this nominally constant percent residual indicates that the basic physics used in the mass transport model are accounted for. The error in the model could be due to the relatively simple approach used in developing the mass transport model as well as the uncertainty propagation in the predicted response time from the input variables. The lumped analysis and associated uncertainty analysis described in the following sections were used to investigate the behavior of the model further.

6. Lumped Analysis

The one-dimensional form of the nondimensional species equation (Equation 87) was further simplified by integrating out the x-direction in a lumped analysis (see Appendix C.9). The limits of integration in the x direction spanned from the inlet boundary ($x^* = 0$) to inside portion of the gas phase control volume ($x^* = 1^{(-)}$) where the interior species concentration was assumed to have a single averaged, or lumped, value. The lumped species concentration is denoted as $\bar{\rho}^*$. It should be noted that the upper limit of integration at $x^* = 1^{(-)}$ captures the interior concentration within the control volume as opposed to the outlet boundary value at $x^* = 1$.

166

$$\int_{x^*=0}^{x^*=1^{(-)}} \frac{\partial \rho^*}{\partial t^*} dx = -v^* \int_{x^*=0}^{x^*=1^{(-)}} \frac{\partial \rho^*}{\partial x^*} dx$$

(100)

The integration results in the following

$$\frac{d\rho^*}{dt^*} = v^*\left(1 - \bar{\rho}^*\right)$$

(101)

Equation 101 is a linear first-order differential equation and resulted in the following solution

$$\boxed{\bar{\rho}^* = 1 - e^{-v^* t^*}}$$

(102)

Equation 102 was recast in dimensional form as

$$\boxed{\frac{\bar{\rho}_A}{\rho_{A,o}} = 1 - e^{-\left(\frac{v_{int} t}{L}\right)}}$$

(103)

The characteristic response time developed in the lumped mass transport model analysis is a function of physical length of the detector and internal velocity.

$$t_c = \frac{L_p}{v_{int}}$$

(104)

The estimated uncertainty in the characteristic time was determined from the standard error propagation equation. The partial derivatives for the characteristic response time are as follows:

$$\frac{\partial t_c}{\partial L_p} = \frac{1}{v_{\text{int}}}$$

(105)

$$\frac{\partial t_c}{\partial v_{\text{int}} L_p} = \frac{-L_p}{v_{\text{int}}^2}$$

(106)

The standard error propagation equation for the characteristic response time is

$$s_{t_c} = \sqrt{\left(\frac{1}{v_{\text{int}}}\right)^2 s_{L_p}^2 + \left(\frac{-L_p}{v_{\text{int}}^2}\right)^2 s_{v_{\text{int}}}^2}$$

(107)

The physical length of the detector used to determine the characteristic response time is the diameter of the sensing chamber which is consistent with the development of the mass transport model in the current study. The sensing chamber diameter of the photoelectric detector was 48 mm and was measured with a ruler with gradations to the nearest millimeter. Therefore, the uncertainty in this measurement was estimated to be 0.5 mm. The internal velocity value for the characteristic time is calculated from the product of the resistance factor and the external velocity. The estimated uncertainty in this calculated internal velocity value was determined in the Velocity Paper and is also shown in Appenidix C.13. The analysis for determining the estimated uncertainty in the characteristic response time over the range of applicable internal velocities is summarized in the table that follows. The nominal values of the physical length and calculated

internal velocity values as well as the corresponding estimated uncertainties are provided on the left hand side. The nominal characteristic response time is shown on the right hand side along with the estimated uncertainty expressed in terms of a magnitude and as a percentage of the nominal value.

Table 28 – Summary of uncertainty analysis for photo detector characteristic response time.

Characteristic Response Time (Photo Detector)

Variable	Value	Uncertainty		t,c	s,t,c	%(s,t,c)
L,p (m)	0.0480	0.0005				
v,int (m/s)	0.04554	0.00923	==>	1.054086	0.213871	20.29
	0.02587	0.00531	==>	1.8552218	0.381421	20.56
	0.01664	0.00361	==>	2.8840467	0.62557	21.69
	0.01175	0.00266	==>	4.0850865	0.925008	22.64
	0.00477	0.00138	==>	10.072779	2.911414	28.90
	0.00214	0.00077	==>	22.393939	8.052286	35.96
	0.00099	0.00047	==>	48.698178	23.22762	47.70

The values summarized in the preceding table indicate that the uncertainty in the characteristic response time range from 20 to 48% of the mean value. The uncertainty in the characteristic response time is primarily due to the uncertainty in the internal velocity which was shown in the Velocity Paper to also have a range from 20 to 48%. The 20 to 48% uncertainty in the characteristic response time can be partially attributed to the 60 to 80% residual in the 1D mass transport model results shown in Figure 55 and Figure 61.

The characteristic response time developed in the current study was also compared to existing methods of smoke detector response based on the works of Heskestad (1977), Cleary *et al* (2000) and Brozovksy *et al* (1995). The experimental data collected in the current study was used to develop the relevant model parameters for each method. The details of this process are provided in Appendices C.10, C.11, and C.12. A comparison

between the current study and the three existing methods for the photoelectric detector exposed to cotton wick is shown in the figure that follows.
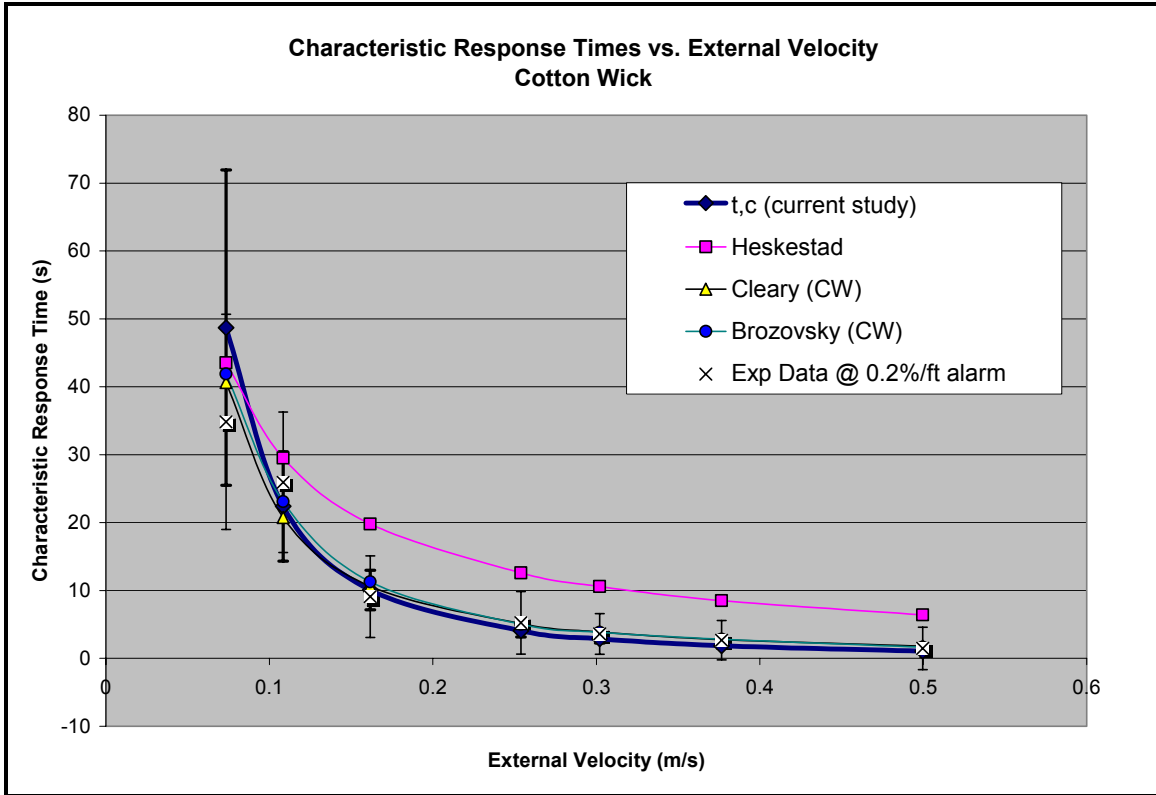
Figure 62 -- Comparison of current study and existing methods for photo detector and cotton wick.

As shown in Figure 62, the methods of Cleary and Brozovsky exhibit favorable comparison with the experimental data as well as with the characteristic response time developed in the current study. The y axis error bars for the experimental data represent the variation in response time with respect to the mean value determined from three repeated tests. The y axis error bars for the characteristic time developed in the current study is based on the estimated uncertainty in this quantity as documented in Appendix C.13.

170

The model parameters for the methods of Cleary and Brozovksy are based on curve fits to experimental data that are dependent upon aerosol type. In particular these methods rely upon the sensor output in determining the model parameters. Brozovksy's method uses the response time and Cleary's method monitors the sensor output for the purposes of determining the dwell time and mixing time. However, the characteristic time for the current study is similar to that developed by Heskestad in concept. In both cases the characteristic time is based on a length scale and a velocity. The main distinction, however, is that the method proposed in the current study utilizes the physical length of the detector and the interior velocity of the smoke detector to determine characteristic response time. Both of these quantities are independent of the aerosol. Heskestad's method relies upon a curve fitting procedure applied to a data set of external velocity and detector response values in order to determine the characteristic length. The favorable comparison of the characteristic response time for the lumped mass transport model to the curve fitting methods and experimental data is an additional indication that the relevant physics of the problem have been addressed and that ordinary diffusion is not a significant factor at low velocities. This is consistent with the analysis conducted for the 1D form of the model and is also consistent with the dimensional scaling arguments made in developing the mass transport model.

Considering the characteristic time expression used by Heskestad, it is possible that the characteristic length could actually be a lumped parameter that is the physical length scale of the detector divided by the resistance factor. This could possibly explain why experimentally determined values of Heskestad's characteristic length reported in the

171

literature are typically 1 to 2 orders of magnitude larger than the physical length scale of the detector. In order to assess this possibility, the nomenclature used in the expressions for characteristic time is made more specific to differentiate the current approach from that used in Heskestad's model. Therefore, the variable L_c is used for Heskestad's characteristic length and the variable L_p is used for the physical length of the detector used in the current approach.

The characteristic times for the two methods are examined in the following manner. The characteristic time for Heskestad's model, $t_{c,H}$, is set equal to the characteristic time for the current approach, $t_{c,I}$

$$t_{c,H} = t_{c,I}$$

(108)

Substituting the characteristic quantities that correspond to each method yields

$$\frac{L_c}{v_{ext}} = \frac{L_p}{Rv_{ext}}$$

(109)

The external velocity is common to both terms and cancels out. Heskestad's characteristic length can be solved for in terms of the current approach as

$$L_c = \frac{L_p}{R}$$

<div align="right">(110)</div>

Therefore, this analysis indicates that Heskestad's characteristic length could be a lumped parameter that consists of the physical length of the detector divided by the detector's resistance factor. The characteristic length for the photoelectric detector used in this study was determined in accordance with Heskestad's model and was found to have an average value of 3.2m (10.5 ft). The details of determining the characteristic length of this detector are provided in Appendix C.10. The characteristic length of the photoelectric detector used in the current study and the resistance factors developed from the subsequent experimental program were used to evaluate if Heskestad's characteristic length is a lumped parameter as indicated by the previous analysis. Equation 110 was rearranged in terms of the detector physical length as follows:

$$L_p = L_c R$$

<div align="right">(111)</div>

$$L_p = \left(L_c\right)\left[f * \left(\frac{1-\alpha^2}{\alpha^2}\right) * \left(\text{Re}_d\right)\right]$$

<div align="right">(112)</div>

The known values for characteristic length and resistance factor were substituted into Equation 112 in order to calculate the physical length of the detector. The resistance

factor is a function of velocity via the screen Reynolds number and therefore, was evaluated at the lower and upper bounds of velocity. The screen Reynolds numbers ranged from approximately 5 to 20 in this study. The resistance factor is also a function of screen porosity and a curve fit coefficient, however, these are fixed quantities.

The physical length at the lower bound of velocity was determined in the following manner:

$$L_{p,1} = (3.25m)(1.268*0.0034*5) = 0.07m$$

(113)

The physical length at the upper bound of velocity was determined in the following manner:

$$L_{p,2} = (3.25m)(1.268*0.0034*20) = 0.28m$$

(114)

The calculated physical length for the photoelectric detector ranges from 7cm (3 in) to 28cm (11 in), which is consistent with the measured diameter dimensions of 4.8 cm (2 in) at the sensing chamber, 10.2 cm (4 in) at the aerosol entry location of the external housing, and 12.4 cm (5 in) at the detector base. Therefore, this comparison indicates that Heskestad's characteristic length could be a lumped parameter of physical length divided by the resistance factor.

The alternative form of the characteristic time for the lumped model shown in Equation 438 of Appendix C.9 can be expanded upon by recalling that the general expression for the resistance factor is a function of the screen porosity and screen Reynolds number. Therefore, the alternative form of the characteristic time for the lumped model becomes

$$t_c = \frac{L}{\left(\dfrac{1-\alpha^2}{\alpha^2}\right) f\left(\mathrm{Re}_d\right) v_{ext}} = \frac{L}{\left(\dfrac{1-\alpha^2}{\alpha^2}\right) f\left(\dfrac{v_{ext} d}{\upsilon}\right) v_{ext}}$$

(115)

This can be further simplified to

$$t_c = \frac{L}{\left(\dfrac{1-\alpha^2}{\alpha^2}\right) f\left(\dfrac{[v_{ext}]^2 d}{\upsilon}\right)}$$

(116)

It is interesting to note that examining this expanded form of the characteristic time for the lumped model indicates an inverse relationship to external velocity squared. This form of the characteristic time where external velocity appears as a square is similar to the observation made by researchers at VTT that for velocities below 0.20 m/s the characteristic time appeared to behave as velocity squared.

175

In order to assess this observation with regards to the inverse square dependency on external velocity in the characteristic time, several external velocities were examined to observe the relative impact. The results are summarized in the table that follows where the left hand side is the external velocity and the right hand side is the external velocity squared.

Table 29 – Comparison of external velocity and external velocity squared.

V,ext	(V,ext)^2
1.50	2.25
1.25	1.56
1.00	1.00
0.75	0.56
0.50	0.25
0.30	0.09
0.20	0.04
0.15	0.02
0.10	0.01

The preceding table shows that the external velocity and the external velocity squared are of the same order of magnitude for velocities of approximately 0.30 m/s and larger. This would explain the relative agreement in characteristic time that would be observed between Heskestad's model and a similar approach where characteristic time is a function of external velocity squared for relative large velocities (*i.e.*, greater than 0.20 m/s). However, as originally pointed out by Bjorkman *et al* and confirmed with the results in the previous table, that for velocities of approximately 0.20 m/s and below the external velocity is one order of magnitude larger than the external velocity squared. This would explain the observations made by Bjorkman *et al* where an increased degree of resistance was seen relative to Heskestad's form of the characteristic time. This increased resistance at low velocities can be explained by the order of magnitude difference between the describing characteristic time as the inverse of velocity and describing the

characteristic time as the inverse of velocity squared. The hypothesis of characteristic time being inversely proportional to external velocity squared proposed by Bjorkman *et al* was based on experimental measurements, however, could not be physically justified within the confines of Heskestad's model because the resulting characteristic time would have inconsistent units of s^2/m. However, the characteristic time developed by the current approach is based on the physical length scale of the detector divided by the product of the nondimensional resistance factor and the external velocity, which has units of time. The expanded form of the characteristic time used in the lumped form of the current approach indicates an inverse dependency on external velocity squared, which is consistent with the observations made by Bjorkman *et al*. However, the current approach provides an explanation that is based on the physical quantities and phenomena associated with the mass transport model developed in the current study and has consistent physical units of time.

7. Conclusions

A mass transport model for smoke detector response has been developed that accounts for external flow conditions and detector geometry. The mass transport model is based upon a set of governing partial differential equations that were simplified into a one-dimensional format based on the application of relevant boundary conditions, findings from the fluid mechanics literature, experimental data collected as part of this study, and nondimensionalizing the equations. The simplified one-dimensional species equation was solved using the Lax-Wendroff explicit finite difference scheme. This explicit scheme was solved using a spreadsheet program and, therefore, could easily be adopted

for routine use by fire protection engineers and practitioners. In addition, a lumped form of the model was developed which resulted in a linear first-order differential equation that was solved for in terms of response time. The characteristic time for the lumped form of the mass transport model was been shown to have an uncertainty of 20 to 48%. The routine use of the mass transport model in either the 1D or lumped form developed in the current study is dependent upon further refinement of the elements that make up the engineering framework demonstrated in this paper.

An inlet velocity boundary condition for the photoelectric and ionization detector was developed from incompressible insect screen pressure drop correlations presented in the fluid mechanics literature which were refined with the velocity data collected in the experimental portion of this study. This boundary condition was used in applying the mass transport model to smoke detector response.

The mass transport model predictions for response time were adjusted to account for convective transport occurring outside the sensing chamber control volume using experimental data collected during the ramp exposure tests for the photoelectric detector evaluated in this study. The general trend for the four aerosol types and external flow conditions in this study was that the mass transport model typically underestimated the smoke detector response time.

In examining the model results relative to the experimental data collected in the current study, it was shown through the percent residual in the predicted response time that

ordinary diffusion does not have a significant role in smoke detector mass transport model. This is consistent with the dimensional scaling arguments used to develop the mass transport model and is also consistent with previous observations by Heskestad (1977) and Cleary *et al* (2000).

In examining the model results relative to the existing methods of predicting smoke detector response, several observations were made. The characteristic time from the current study and that used by Heskestad were equated to each other. This comparison revealed that Heskestad's characteristic length is a lumped parameter that is consistent with physical length scale of the detector and the resistance factor of the smoke detector. The experimental data collected in the current study was used to derive Heskestad's characteristic length. This value was used in conjunction with the resistance factor developed for the same detector and it was shown that the physical length scale of the detector, which is taken to be the diameter of the sensing chamber, was reproduced within the same order of magnitude as the measured value of the sensing chamber diameter. Furthermore, the observation made by Bjorkman *et al* that the characteristic length behaves as to the inverse square of velocity at low velocities was also investigated. This behavior was found to be consistent with the characteristic time formulated in the current approach which is a function of external velocity and Reynolds number. It was demonstrated mathematically that the characteristic time developed in the current study does contain the inverse of velocity squared through the external velocity and the Reynolds number which appears in the resistance factor. Therefore, the physically correct units of time are given by the current approach and is consistent with the

observation made by Bjorkman *et al* with regard to the behavior of the characteristic length at velocities below 0.2 m/s. This aspect further demonstrates that Heskestad's characteristic length is a lumped parameter that can be recast in terms of physical quantities relevant to the smoke detector mass transport problem, as was done in the current study.

The comparison of the mass transport model to the curve fitting methods of Cleary *et al* and Brozovksy *et al* provided additional confirmation that the model incorporates the relevant physics. The curve fitting methods are based on detector response test data and provide a result that couples the relevant fluid mechanics and mass transport processes. The experimental data collected in the current study was used to develop the curve fitting coefficients appropriate to the two methods. The mass transport model was then compared to the curve fitting methods as well as the respective experimental data set for detector response time and was shown to have very favorable agreement which was characterized as the mean values of each method and the experimental data being within the uncertainty band of characteristic time of the mass transport model. As the mass transport model developed in the current approach considers convective mass transport driven by the internal velocity of the smoke detector, this agreement with the existing curve fitting methods indicates and experimental data confirms that the model has captured the relevant physics. Therefore, the mass transport problem, even at "low" velocities (0.07 m/s), is consistent with a convective transport process and ordinary diffusion is not a significant factor.

The engineering framework used to develop this mass transport model provides some areas for future improvement. A more detailed experimental study of the inlet velocity boundary condition or *resistance factor* for smoke detectors is one such area for future improvement. The resistance factor was shown to have an estimated uncertainty on the order to 20 to 36% which in turn has implications on the calculated internal velocity value when using this inlet velocity boundary condition in a mass transport model. This detailed study of external and internal velocity in relation to smoke detector geometry could lead towards the development of a general correlation for smoke detectors and potentially reduce the associated uncertainty. Such general correlations were discovered in the fluid mechanics literature where incompressible flow past insect screens have been established and verified in numerous studies. However, such studies involve insect screens that occupy the entire cross section of a pipe or duct. Additional research is needed before such a general correlation relating external velocity and detector geometry to internal velocity can be established.

References

Baines, W.D., E.G. Peterson, "An Investigation of Flow Through Screens," *Transactions of the ASME*, vol. 73, pp.467-480, (1951).

Beyer, W.H., *CRC Standard Mathematical Tables and Formulae, 29th Edition*, p. 105, CRC Press, Boca Raton, FL, (1991).

Brundrett, E., "Prediction of pressure drop for incompressible flow through screens," *Journal of Fluids Engineering*, 155(2), pp. 239-242, (1993).

Bukowski, R.W., R.J. O'Laughlin, and C.E. Zimmerman, *Fire Alarm Signaling Systems Handbook*, National Fire Protection Association, Quincy, MA (1987).

Cleary, T. G., Chernovsky, A., Grosshandler, W. L., Anderson, M., "Particulate Entry Lag in Spot-Type Smoke Detectors," Fire Safety Science. Proceedings. Sixth (6th) International Symposium. International Association for Fire Safety Science (IAFSS). July 5-9, 1999, Poitiers, France, Intl. Assoc. for Fire Safety Science, Boston, MA, Curtat, M., Editor(s), pp. 779-790, (2000).

DiNenno, P.J., *SFPE Handbook of Fire Protection Engineering, 2nd Edition*, Appendix B, Table B-2, National Fire Protection Association, Quincy, MA, (1995).

Dobbins and Mulholland, *Journal of Atmospheric Environment,* 28(5), pp. 889-897 (1994).

Edwards, C.H. and D.E. Penney, *Calculus and Analytic Geometry, 3rd Edition*, Prentice Hall, Englewood Cliffs, NJ, (1990).

Evans, D.D., "Ceiling Jet Flows," *SFPE Handbook of Fire Protection Engineering, 2nd Edition*, Section 2, Chapter 4, pp 2/32-39, National Fire Protection Association, Quincy, MA, (1995).

Fahien, R.W., *Fundamentals of Transport Phenomena*, McGraw-Hill, New York, NY, (1983).

Hershey, D., *Transport Analysis*, Plenum Press, New York, NY, (1973).

Idelchick, I.E., G.R. Malyavskaya, O.G. Martynenko, and E. Fried, *Handbook of Hydraulic Resistance,* 2nd Ed., Hemisphere, Washington, DC, (1986).

Ierardi, J.A., *Characterizing the Entry Resistance of Smoke Detectors*, Ph.D. Dissertation, Worcester Polytechnic Institute, Worcester, MA, (2005).

Iserles, A., *A First Course in Numerical Analysis of Differential Equations*, Cambridge University Press, (1996).

Laws, E.M., A.K. Ouazzane, A. Erdal, "Short Installations for Accurate Orifice Plate Flow Metering," *Society of Mechanical Engineers, Fluids Engineering Division (Publication) FED*, v 193, Turbulence Control, pp. 27-36, (1994).

Mills, A.F., *Basic Heat and Mass Transfer*, Irwin, Boston, MA, (1995).

Motevalli, V., Marks, C.H., "Characterizing the Unconfined Ceiling Jet Under Steady-State Conditions: A Reassessment," International Association for Fire Safety Science. Fire Safety Science. Proceedings. 3rd International Symposium. July 8-12, 1991, Edinburgh, Scotland, Elsevier Applied Science, New York, Cox, G.; Langford, B., Editors, pp. 301-312, (1991).

Mountain, R.D., G.W. Mulholland, H. Baum, "Simulation of aerosol agglomeration in the free molecular and continuum regimes," *Journal of Colloid and Interface Science*, 114 (1), pp. 67-81 (1986).

Munson, B.R., D.F. Young, T.H. Okiishi, *Fundamentals of Fluid Mechanics, 2nd Edition*, John Wiley & Sons, New York, NY, (1994).

Newman, J.S., "Modified theory for the characterization of ionization smoke detectors," Proceedings of the Fourth International Symposium on Fire Safety Science, pp. 785-792, (1994).

Qualey, J., "Smoke Detector Response and the Use of Antistatic Materials: An Empirical Study," (Abstract submitted to NFPA Research Foundation Detection and Suppression Symposium, Orlando, FL, January 2004)

Sissom, L.E. and Pitts, D.R., *Elements of Transport Phenomena*, McGraw-Hill, New York, NY, (1972).

Snegirev, A.Y., G.M. Makhviladze, J.P. Roberts, "The effect of particle coagulation and fractal structure on the optical properties and detection of smoke," *Fire Safety Journal*, 36, pp. 73-95 (2001).

Teitel, M. and A. Shklyar, "Pressure drop across insect-proof screens," *Transactions of the American Society of Agricultural Engineers*, 41(6), pp. 1829-1834, (1998).

6 Conclusions

An engineering framework has been established for predicting smoke detector response that accounts for detector geometry and external flow conditions. A mass transport model for fully developed flow in the sensing chamber of spot-type smoke detectors was derived from conservation equations for mass, species, momentum, and energy. The modeling approach considers an incompressible isothermal Newtonian fluid with constant properties. The aerosol is treated as dilute binary mixture in air. The solid walls of the sensing chamber were treated as no slip velocity boundaries with no aerosol deposition or mass transport across them.

An inlet velocity boundary condition was developed from experimental measurements made for both external and internal velocity. The velocity measurements were made with a Laser Doppler Velocimeter which provided a means for measuring internal velocity in detectors modified to provide optical access to the sensing chamber. The inlet boundary condition relates the external flow velocity and detector geometry to the internal velocity and is expressed in terms of a resistance factor for smoke detectors. The resistance factor developed in this study was shown to have an uncertainty in the range of 20 to 36% over a range of external velocities of 0.07 to 0.50 m/s. The resulting interior velocity value calculated with the resistance factor was shown to have an estimated uncertainty of 20 to 48%.

The characteristic time for the species equation in the mass transport model is based on the physical length scale of the sensing chamber and the internal velocity, which are parameters relevant to the convective mass transport process occurring in the sensing chamber. This is in contrast to existing lag time methods with characteristic times that are based on external flow velocity and a characteristic length that is often 1 to 2 orders of magnitude larger than the physical length scale of the detector. It was demonstrated that Heskestad's characteristic length is a lumped parameter consistent with the physical length scale of the detector and the resistance factor. Observations made by Bjorkman *et al* regarding the inverse square relation on external velocity for flows below 0.2 m/s have been confirmed using the characteristic response time developed in the current approach. In relating the internal velocity to the exterior velocity via the resistance factor it was shown that an inverse square relationship to velocity is present in the characteristic response time via the external velocity and Reynolds number. However, since the Reynolds number is dimensionless this inverse square relationship to velocity has physically consistent units of time and is also in agreement with the observation made by Bjorkman *et al* of experimental measurements of characteristic length in accordance with Heskestad's model.

The mass transport model developed in the current study has also been used to demonstrate that ordinary diffusion does not have a significant impact on smoke detector response. This was demonstrated by dimensional scaling arguments used in developing the mass transport model as well as by comparing the simplified form of the mass transport model (both 1D and lumped) to other existing methods as well as experimental

data. In examining the model results relative to the experimental data collected in the current study, it was shown through the percent residual in the predicted response time that ordinary diffusion does not have a significant role in smoke detector mass transport model. This is consistent with the dimensional scaling arguments used to develop the mass transport model and is also consistent with previous observations by Heskestad (1977) and Cleary *et al* (2000).

In examining the model results relative to the existing methods of predicting smoke detector response, several observations were made. The characteristic time from the current study and that used by Heskestad were equated to each other. This comparison revealed that Heskestad's characteristic length is a lumped parameter that is consistent with physical length scale of the detector and the resistance factor of the smoke detector. The experimental data collected in the current study was used to derive Heskestad's characteristic length. This value was used in conjunction with the resistance factor developed for the same detector and it was shown that the physical length scale of the detector, which is taken to be the diameter of the sensing chamber, was reproduced within the same order of magnitude as the measured value of the sensing chamber diameter. Furthermore, the observation made by Bjorkman *et al* that the characteristic length behaves as to the inverse square of velocity at low velocities was also investigated. This behavior was found to be consistent with the characteristic time formulated in the current approach which is a function of external velocity and Reynolds number. It was demonstrated mathematically that the characteristic time developed in the current study does contain the inverse of velocity squared through the external velocity and the

Reynolds number which appears in the resistance factor. Therefore, the physically correct units of time are given by the current approach and is consistent with the observation made by Bjorkman *et al* with regard to the behavior of the characteristic length at velocities below 0.2 m/s. This aspect further demonstrates that Heskestad's characteristic length is a lumped parameter that can be recast in terms of physical quantities relevant to the smoke detector mass transport problem, as was done in the current study.

The comparison of the mass transport model to the curve fitting methods of Cleary *et al* and Brozovksy *et al* provided additional confirmation that the model incorporates the relevant physics. The curve fitting methods are based on detector response test data and provide a result that couples the relevant fluid mechanics and mass transport processes. The experimental data collected in the current study was used to develop the curve fitting coefficients appropriate to the two methods. The mass transport model was then compared to the curve fitting methods as well as the respective experimental data set for detector response time and was shown to have very favorable agreement which was characterized as the mean values of each method and the experimental data being within the uncertainty band of characteristic time of the mass transport model. As the mass transport model developed in the current approach considers convective mass transport driven by the internal velocity of the smoke detector, this agreement with the existing curve fitting methods indicates and experimental data confirms that the model has captured the relevant physics. Therefore, the mass transport problem, even at "low"

velocities (0.07 m/s), is consistent with a convective transport process and ordinary diffusion is not a significant factor.

The response times predicted by the mass transport model were adjusted to account for transport delays outside the sensing chamber control volume. The inlet species boundary condition used in the mass transport model assumed that the internal species concentration was equal to the exterior species concentration. The experimental portion of this study did not assess the appropriateness of this assumption. The mass transport model was found to underpredict the measured values for both the response time for 0.2%Ob/ft alarm and the time to steady state. However, from a practical standpoint of detecting a 50 kW wastebasket fire with an addressable smoke detection system, the range of residuals are within the typical polling time of the addressable smoke detectors which is on the order of 5 to 10 seconds. Therefore, this engineering framework for predicting smoke detector response with a mass transport model and a resistance factor correlation shows promise. With further improvement this engineering framework may result in a predictive tool for smoke detector response that incorporates characteristics of the smoke detector and the external conditions.

One particular area of improvement that is needed before this goal can be obtained is the development of a general form of the resistance factor similar to the existing correlations for incompressible fluid flow in the fluid mechanics literature. Having a general form of the smoke detector resistance factor would eliminate the need for an engineer or designer to collect internal and external velocity measurements in order to develop their own

specific resistance factor correlation for the detector of interest. Additional research focused on the influence of geometry on the resistance factor would help further this goal of developing a general correlation accounting for smoke detector geometry.

7 Future Work

The overall goal of this study was to develop an engineering framework that incorporated the external flow conditions and detector geometry into smoke detector response predictions. A limited number of experiments were conducted to address the aerodynamic and mass transport aspects of this framework. These limited experiments were used to demonstrate the overall framework. Specific areas for future work are suggested in an effort to advance and refine the engineering framework for predicting smoke detector response.

- A general correlation for the inlet velocity boundary condition is one area for improvement. The existing correlations for incompressible flow past insect screens in the fluid mechanics literature can be used as a template to further refine the initial development used in this study for smoke detectors. In general, the existing correlations are based on screen porosity and screen Reynolds number. In this study, the same insect screen was used throughout, and therefore, the screen porosity was constant. A more detailed experimental study that addresses variations in screen porosity as well as screen Reynolds number could be used to develop a generalized correlation for smoke detectors. A larger sampling of smoke detectors would need to be involved in such an investigation. The impact of the detector cover geometry needs to be addressed in the development of a general correlation. While the insect screen introduces

190

a significant amount of resistance, the external cover geometry does play a role in the entry resistance.

- Another area of this framework in need of improvement is the inlet species boundary condition. In the current study it was assumed that the internal species concentration was equal to the external species concentration. However, the response lag measurements made in the ramp-type aerosol exposure experiments seem to indicate otherwise. It is reasonable to expect that the sensor processing or alarm verification delay would be a constant value that is independent of velocity. However, the response lag from the ramp exposure experiments indicated that the response lag time had an exponential dependence upon velocity with the delay increasing as velocity decreased. This could suggest that additional phenomena are responsible for the response lag. Furthermore, it could be that external mixing is taking place at the entrance region and the inlet species concentration is not equal to the exterior species concentration. It is possible that the response lag measurements made in this study lumped together external mixing processes of the aerosol at the entrance region as well as any sensor processing or alarm verification delays. A more detailed experimental and theoretical study of the response lag could help to decouple any potential mixing of aerosol at the entrance region from the signal processing delay. This would require the development of an inlet species boundary condition that properly accounts for the difference between internal and external species concentrations as a function of detector geometry, Reynolds number, and additional controlling parameters that may be identified.

- Once the inlet velocity and inlet species boundary conditions have been better established, the relationship between these two quantities may be worth further investigating to determine if a single relationship can be established. It is possible that the inlet velocity and the inlet species boundary conditions are both functions of detector and geometry and Reynolds number. Therefore, it may be possible to establish a single relationship between the aerodynamic and mass transport aspects of smoke detector which would reduce the amount experimental measurements necessary to characterize smoke detectors for response modeling purposes.

- The inlet velocity boundary condition has been developed for duct flow conditions. The relationship between duct flow and typical ceiling jet conditions is another aspect of this engineering framework that is worth investigating in additional detail. Such an investigation could involve correlating measurements made in the smoke box and full scale room fires in the UL 217/268 test protocol.

Appendix A.1: LDV Setup

An Argon-Ion laser operating in multimode with an aperture setting of 3 was used to power the LDV apparatus. The laser was first tuned to maximum power output. Horizontal and vertical adjustments were made to the laser mirrors. The photodiode of a laser power meter was placed at the output window of the laser in order to measure laser power. A horizontal adjustment to the laser mirror was made until a maximum value was identified on the laser power meter display. Then a vertical adjustment to the laser mirror was made until a maximum value was identified on the laser power meter. This process was repeated several times until it was found that further adjustments provided no discernable improvement in the laser power meter display.

After the laser was tuned to maximum power it was aligned with the optical breadboard surface using two alignment blocks. Each alignment block contained a small hole for the laser beam to pass through at a height of 4.25" above the surface of the optical breadboard. This distance corresponds to the height that the laser beam exits the laser as well as the height of the inlet of the multicolor separator. The two alignment blocks were placed at distances of 2" and 36" from the output window of the laser. Adjustments were made to the feet of the laser until the laser beam passed through each alignment block with a thin even halo. This indicated acceptable alignment of the laser beam to the optical breadboard surface. The laser was locked into position. The alignment of the laser with the alignment blocks was verified a second time to ensure that the laser was not disturbed when it was being secured to the optical breadboard.

The multicolor beam separator was placed on the optical breadboard approximately 4" away from the output window of the laser. Alignment masks were installed on the output ports of the multicolor beam separator. The alignment of the laser beam with the inlet aperture of the multicolor beam separator was checked while the alignment of separated beams were roughly aligned with the alignment masks on the outlet ports. The multicolor beam separator was locked into position on the optical breadboard once this initial alignment was verified. The separated beams were then translated into the center of the outlet port alignment masks using horizontal and vertical mirror adjustments on the multicolor beam separator.

After aligning and adjusting the multicolor beam separator the Bragg cell was adjusted to provide a second laser beam in each of the two colors that was shifted in frequency. The RF power adjust on the ColorLink+ unit was adjusted to a location halfway between its two stops. This provided power to both the shifted and unshifted sides of the multicolor beam separator. The photodiode of the laser power meter was placed over the alignment mask on the blue shifted side of the multicolor beam separator outlet port. The Bragg cell angle was adjusted until the power for the shifted blue side was maximized. The power meter readings for both the shifted and unshifted blue sides were noted. The RF power was adjusted until the power meter readings for the shifted and unshifted blue sides were nominally equal.

The alignment masks were removed and fiberoptic couplers were installed on the four outlet ports on the multicolor beam separator. An alignment mask was placed on each

fiberoptic coupler and the beam was translated into the approximate center of the mask target. The fiberoptic cables for the shifted and shifted green and blue were attached to their respective fiberoptic coupler. The four transmitting fibers were attached to a junction box. The junction box sends the transmitting fibers into the fiberoptic probe.

The next task was to properly steer the laser beam from each fiberoptic coupler into the respective transmitting fiber. The goal of this task was to maximize the power output of each fiber. Achieving maximum power was an indication that the laser beam was properly steered into the transmitting fiber and would minimize power loss in the coupling process. The output power from each transmitting fiber was measured with a laser power meter. The laser power meter photodiode was placed at the approximate location of the beam crossing point of the fiberoptic probe. The shutters on each fiber optic coupler were in the closed position and only the shutter of the transmitting fiber of interest was opened. The steering knobs and focusing ring were adjusted until the maximum value on the laser power meter display was achieved. This process was repeated several times until further iteration yielded no significant can in the laser power meter display. This process was repeated until all four transmitting fibers were optimized.

With the four transmitting fibers optimized, the next step was to verify the quality of the beam crossing from the fiberoptic probe. This was done by using a microscope objective to project the beam crossing patterns from the fiberoptic probe onto a wall. The microscope objective contained both 10x and 40x lenses. The fiberoptic probe was

clamped down to the optical breadboard surface to ensure that it was level. The aperture of the microscope objective was adjusted to coincide with the height of the beam crossing point at 4.25in. The first step was to verify that the intensity of the four laser beams were approximately of the same intensity. This was done by moving the microscope objective with a 10x lens to a point just beyond the beam crossing point in order to project the four separate beams onto the wall. The intensity of the four beams was judged by eye. The second step was to verify that the two crossing points were at least 50% coincident. The microscope objective with a 40x lens was used to verify the coincidence of the two crossing points by focusing on the crossing point of the four beams. The crossing points showed coincidence that was approximately 100% judged by eye, although this was not quantified. Verifying the approximate equal intensity of all four beams as well as the degree of coincidence at the crossing point demonstrated that the optical system was properly aligned to make velocity measurements.

The fiberoptic probe was detached from the optical breadboard and mounted in a vertical position on the traversing system. The traversing system was placed underneath a Plexiglass sheet for optical access to the test section of the FE/DE. The centerline of a smoke detector was marked in order to provide a target to zero the location of the fiberoptic probe in the plan dimensions. The measurement volume was translated with the traverse in the vertical direction until the four beams were focused close to the crossing point. The four narrowly focused beams were used to target the market spot at the top of the duct. The vertical component was adjusted with the traverse until the four

beams appeared to form one spot at the top of the duct, indicating the crossing location of all four beams. The traverse locations were zeroed.

The frequency shift of 200kHz was used for both velocity components. It is recommended that the shift frequency be at least twice the frequency associated with the maximum expected negative velocity. The frequency associated with the negative velocity is the absolute value of velocity in m/s divided by the fringe spacing of the interference pattern in microns. The fringe spacing of the LDV is 3.54 microns. Using half the frequency shift value, or 100kHz, and the 3.54 micron fringe spacing, the negative velocity associated with the 200kHz frequency shift is -0.35 m/s. This value is expected to be adequate for the experiments of interest because the maximum streamwise freestream velocity to be tested will be on the order 0.5m/s. The next step was to determine the proper seeding of the flow and to select the appropriate range of signal filters.

Seeding the Flow

An attempt was made to seed the flow with 500nm PSL microspheres. However, it was found that it was not possible to create a strong backscatter signal with the microspheres. It is possible that the particle concentration of microspheres was insufficient. Therefore, the flow was seeded with atomized vegetable oil using a TSI Six-Jet Atomizer. The number of jets that could be used ranged from 1 to 6. The dilution air pressure could be varied from approximately 0 to 100psi. A dilution air pressure of 30psi was used to seed the flows for velocity measurements.

A series of velocity measurements were made in the freestream region of the FE/DE test section at several fan speed settings while operating 1 to 6 oil jets in increments of 1. The measurement location was 70mm below the top of the top of the FE/DE test section. The fan speed settings evaluated were 25, 20, 15, 10, 5 and 0 Hz. It should be noted that at the 0 Hz fan speed setting the velocity is not expected to be zero. The exhaust fan is operating and the resultant pressure drop is expected to produce a non-zero velocity value in the FE/DE. The fan speed was set to the setting of interest and allowed to equilibrate for approximately 3 minutes with a single oil jet operating. The velocity was measured by collecting 20 000 data points with the LDV. After the data set was collected, two oil jets were opened for approximately 1 minute to allow for the system to equilibrate. The velocity was then measured. This process was repeated in a similar fashion until all six oil jets were operating. After velocity data for all six oil jet settings was collected, the fan speed was changed to the next setting and the process was repeated for all fan speeds at the six oil jet settings. The mean and standard deviation was computed on the 20 000 data points collected at each fan speed and oil jet combination. The results of this analysis are shown in Figure 63.
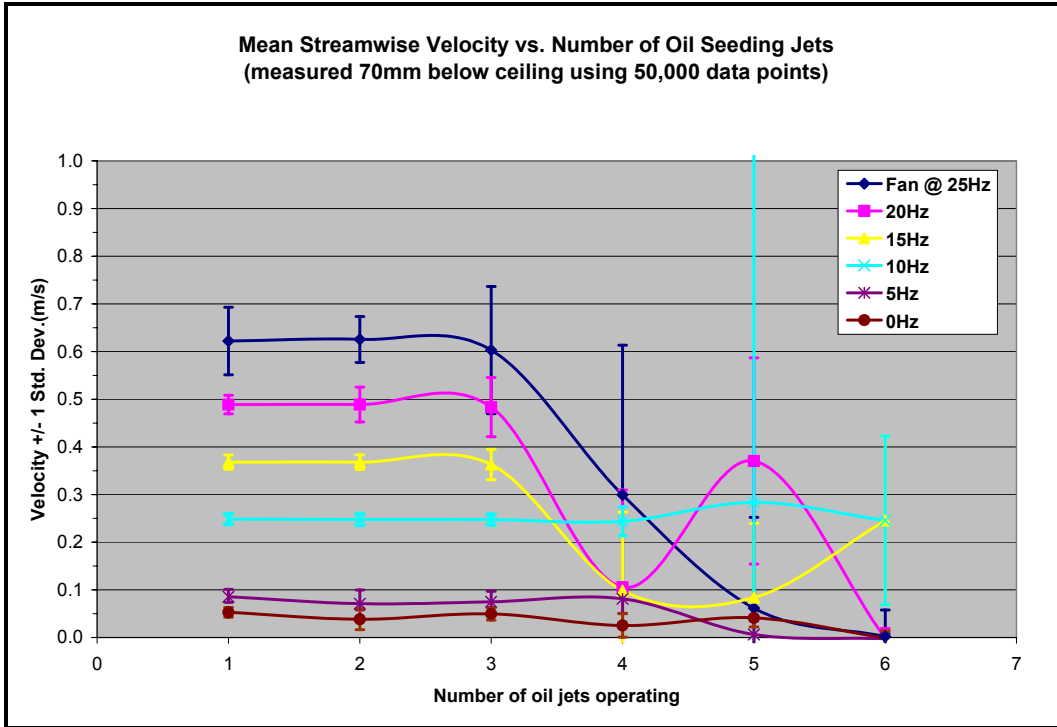
Figure 63 -- Mean streamwise velocity with 1 to 6 oil jets seeding for several fan speeds.

If the number of oil jets seeding the flow had no impact on the velocity measured by the LDV, the mean velocity values would be nominally constant with the same nominal standard deviation. However, Figure 63 shows that while the mean velocity values are nominally constant for 1 to 3 oil jets there is a significant variation for 4 or more oil jets operating. This variation might be explained by the medium being optically thick when operating 4 or more oil jets. This could lead to the backscatter signal from the measurement volume being absorbed and/or scattered by the optically thick medium. In addition, the standard deviation in the velocity measurements increases when 4 or more oil jets are operating relative to the case of 1 to 3 oil jets. For fan speeds of 20Hz or below, the standard deviation is minimized when 1 oil jet operates. Therefore, 1 oil jet will be used to seed the flow.

With seed particles injected into the flow, the FIND software was used to select the appropriate range of signal filters. This process was done automatically by the FIND software. The algorithm selects several different filtering combinations until the optimal data collection rate is found. For both Channels 1 and 2 the filter ranges were determined the FIND software to be 30 to 300kHz.

Laser Power Setting

The issue of laser power was examined by making 10 consecutive velocity measurements at the same location for different laser power settings. If laser power has no impact on the measured velocity, the plot of 10 consecutive points would show nominally constant velocity with the same nominal standard deviation. Laser power settings of 400, 500, 600, and 800mW were evaluated for a single oil jet seeding the flow and a 10Hz fan speed setting. The mean velocity value with error bars of one standard deviation are plotted for the ten consecutive measurements in Figure 64. A total of 50 000 data points were collected for each measurement and used in the subsequent statistical analyses.
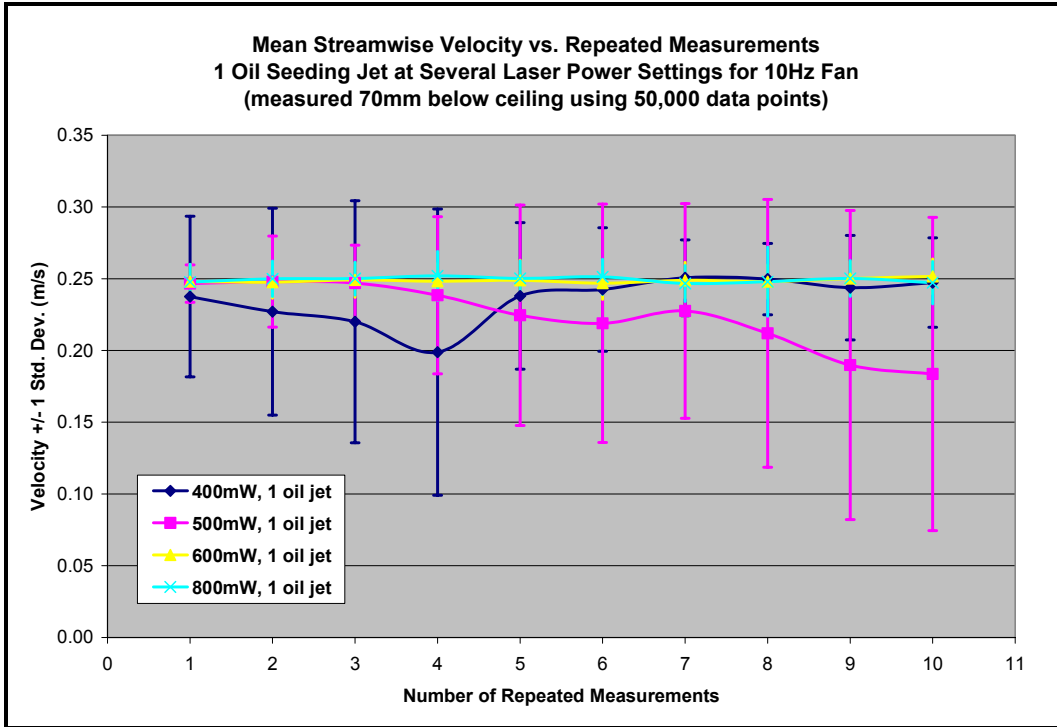
Figure 64 -- Consecutive velocity measurements made with different laser power settings for 1 oil jet and a 10Hz fan setting.

It can be seen in Figure 64 that there is more variation in the consecutive velocity measurements made at 400 and 500mW laser power setting relative to measurements made at 600 and 800mW. The fact that the measured velocity values for 400 and 500mW are at times below the mean velocity of approximately 0.25m/s indicates that these laser power settings may not be providing a sufficiently strong backscatter signal to the photodiode receiver in the fiberoptic probe. Therefore, the laser power setting used in subsequent testing will be 600mW. It should be noted that the laser power setting refers to the output power measured at the Argon-Ion laser and is not indicative of the actual power of the laser beams used to form the measurement volume. This can be attributed to the optical loses that occur when the laser beam passes through all the optical

components of the LDV system such as the beam separator, fiber optic couplers, optical fibers and the fiber optic probe.

Number of LDV Data Points

The number of data points collected by the LDV was examined by collecting 20 000 data points at a vertical location of 70mm below the ceiling at a fan speed of 20Hz. This location was in the approximate freestream velocity location and was along the centerline of a smoke detector in the duct. Statistical analysis was performed on the data set for this data point. The analysis was conducted to calculate the mean and standard deviation for both the x and y components of velocity. The number of data points used in the analysis was varied in order to locate the optimal number of data collection points. The number of data points evaluated were 20 000, 10 000, 7 500, 5 000, 2 500, and 1 000. These data points were from the original set of 20 000 collected data points.   The mean velocity was plotted against the number of data points with one standard deviation error bars for the velocity values in Figure 65.
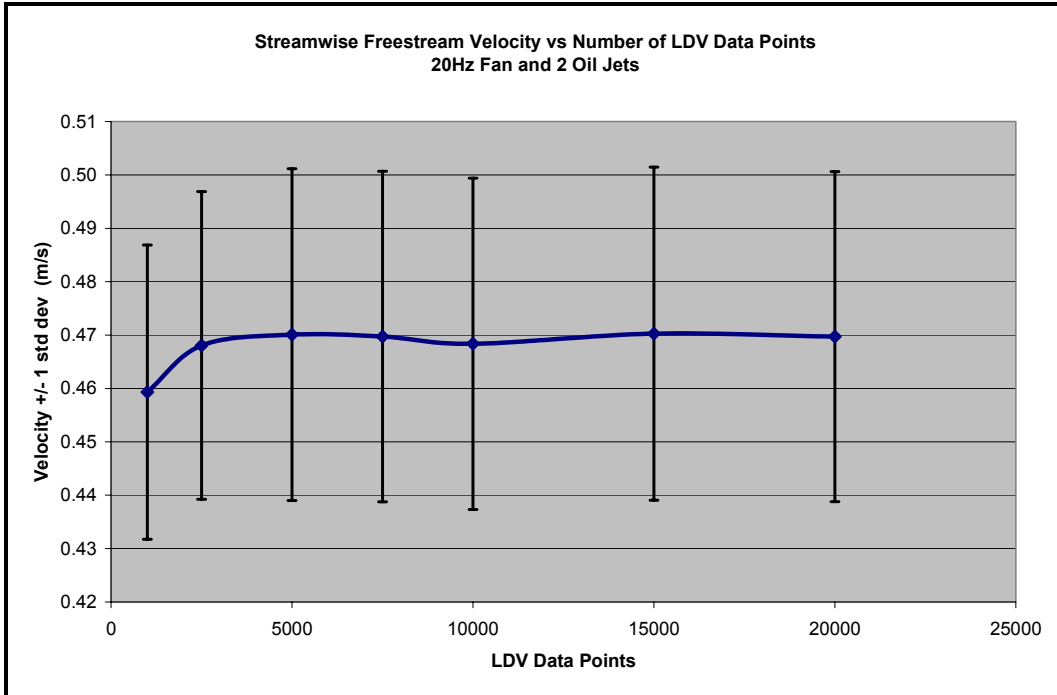
Figure 65 -- Mean velocity with standard deviation versus number of points in data set.

There wasn't any significant variation in the streamwise mean velocity values for 5 000 to 20 000 data points. However, there was a distinct downward trend in the mean velocity values observed for less than 5 000 collected data points. Therefore, 5 000 data points was selected as the optimal value to be used in subsequent testing.

Appendix A.2: Preliminary and Prototype Experiments

Comparison of Velocity Measurements with LDV and Thermal Anemometer

A comparison of time averaged velocity measurements was made between the LDV and a thermal anemometer in the FE/DE. The purpose of this comparison was to demonstrate that the LDV was capable of providing velocity measurements through the Plexiglass viewing window of the FE/DE test section. The thermal anemometer is the standard device for measuring freestream velocity in the FE/DE and was used as the reference measurement for this comparison. The time variation in velocity was represented as one statistical standard deviation in the velocity data set. The time variation as represented by the standard deviation was used as an estimate of the uncertainty in the velocity measurement. It should be noted that a detailed study of the turbulent behavior in the FE/DE flow field was not the primary focus of these velocity measurements. Rather, the time averaged velocity was used as a "forcing function" for the convective transport process in smoke detectors.

The thermal anemometer used was an Omega Model FMA-902-V with an accuracy of 2.5% for flows below 5 m/s. The measurement location was at a distance approximately 70mm below the top of the FE/DE test section and was along the centerline of the width. The LDV measurement location was approximately 2mm upstream of the thermal anemometer. This essentially provided a simultaneous measurement of velocity at this location. This particular distance of 70mm below the top of the test section was used

because it was the fixed location of the thermal anemometer installed in the FE/DE. This measurement location also corresponded to the freestream of the flow field based on observations made of the flow field when preliminary LDV measurements were taken.

Thermal anemometer data was collected over 60 seconds at a rate of 1 data point per second.   The LDV data was collected over 60 seconds which corresponded to approximately 80,000 collected data points.   Data was collected for external mean velocities in the range of 0.05 to 0.5 m/s. The velocity results for the LDV are plotted against those for the thermal anemometer reference measurement in Figure 66. The error bars represent one standard deviation for each data point which is being used as an estimate of the measurement uncertainty.   The solid line represents ideal agreement between the LDV and the reference measurement.
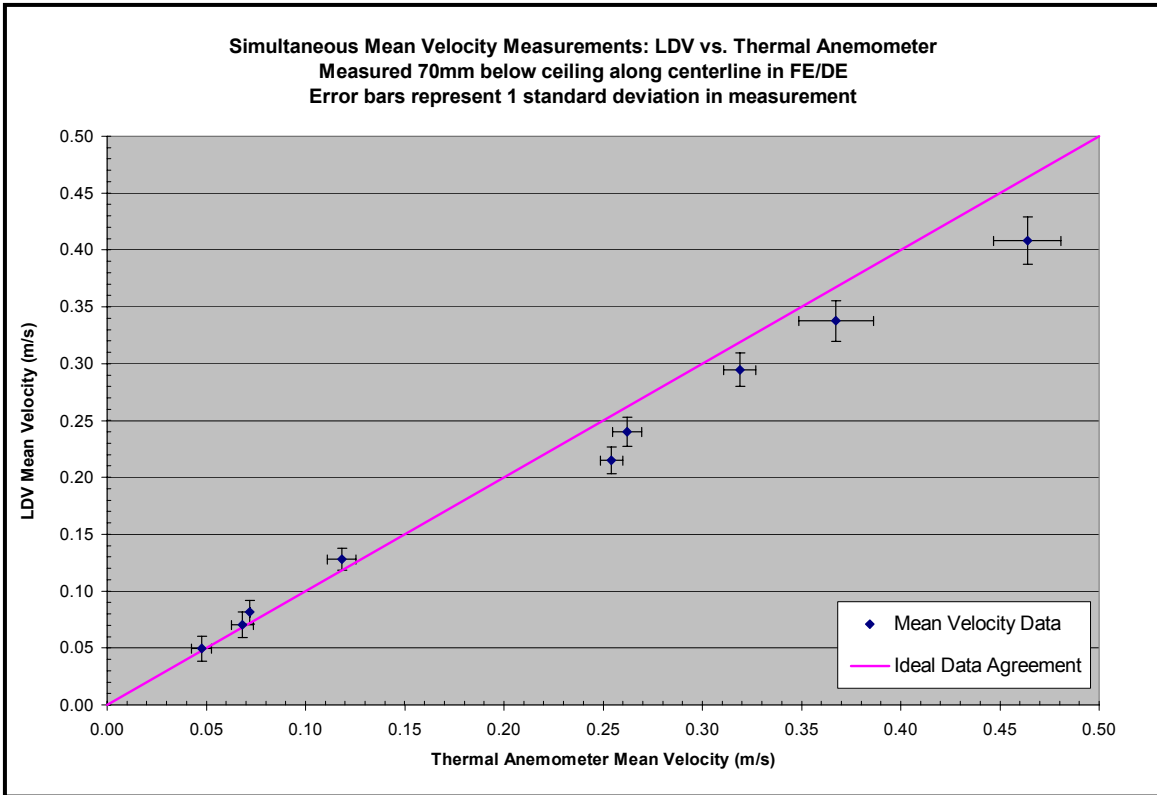
Figure 66 -- Freestream velocity measurements made with LDV and thermal anemometer.

The standard deviations in Figure 66 range from 2 to 10% of the mean values for the thermal anemometer and from 5 to 22% of the mean values for the LDV. There seems to be general agreement between the LDV and thermal anemometer velocity measurements within their respective uncertainties. There is a great deal of agreement at velocities below 0.15 m/s as measurement uncertainties are within the ideal data agreement line. It should be noted that for flows below 0.05 m/s the thermal anemometer experiences convective air flows due to self-heating.

Velocity Profiles in FE/DE Test Section

The LDV was used to measure vertical profiles of the streamwise velocity component along the centerline of the FE/DE for several fan speed settings as shown in Figure 67. The error bars represent 1 standard deviation in the measurement and is used as an estimate of the measurement uncertainty. This series of measurements was made to characterize the typical time averaged velocity profiles in the vicinity of the detectors for the range of FE/DE fan speeds. The velocity profiles were measured to provide an indication of the typical vertical velocity distribution and freestream velocity at the detector location. The time averaged velocity values are plotted over the range of FE/DE fan speeds in Figure 67. The error bars in the x-direction are one statistical standard deviation for the velocity data set at each measurement location and used as an estimate of the measurement uncertainty.
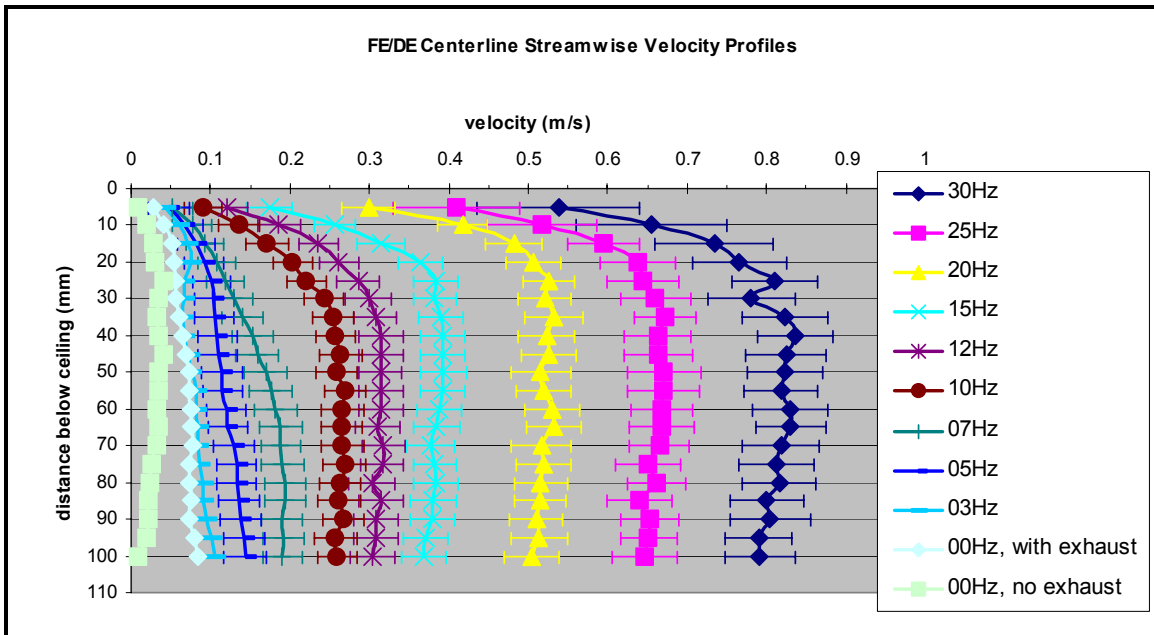
Figure 67 -- Streamwise vertical velocity profiles along centerline of FE/DE test section.

The standard deviation, used as an estimate of the measurement uncertainty, ranges from 6 to 10% for mean freestream velocity values for fan speeds of 10 to 30Hz and from 16 to 34% for 0 to 7Hz. The time averaged velocity values along with the standard deviation and percent turbulence intensity (standard deviation as a percent of means velocity) are shown in Table 30.

The turbulence intensity is the standard deviation of the velocity measurement divided by the mean velocity.

$$V\ TI\% = \frac{\sigma_m}{V_{mean}}(100\%)$$

(117)

Table 30 – Time Averaged Velocity Data from Freestream Region of FE/DE.

FE/DE Time Averaged Velocity			
Fan (Hz)	V,mean (m/s)	Std dev	V TI%
30	0.822	0.048	5.85
25	0.668	0.045	6.71
20	0.520	0.035	6.81
15	0.392	0.028	7.20
12	0.314	0.027	8.70
10	0.264	0.026	9.84
7	0.168	0.027	16.07
5	0.113	0.025	22.07
3	0.077	0.024	31.27
0	0.072	0.024	33.81

Prototype Experiments

A series of prototype experiments were conducted to assess the velocity measurements made with the LDV relative to a reference source. The first prototype experiment was a comparative measurement of vertical velocity with the LDV and a Pitot probe (reference measurement) through a glass plate parallel to the streamwise flow. The glass plate was the same material and thickness as the glass discs used as optical windows for the detectors. The comparison between velocity profiles was used to determine if the glass plate had adverse effects on the optical system of the LDV such as reflections.

The second prototype experiment was the simultaneous measurement of internal velocity with the LDV and a Pitot probe (reference measurement) for a simple detector mockup. The simple detector mockup had a piece of insect screen material mounted perpendicular to the streamwise flow direction at the leading edge of the glass plate and the top and sides were partially enclosed with an open back. The open back of the mockup allowed for the Pitot probe to be placed inside the simple mockup. The comparison between mean velocity values was used to determine if sufficient seed particles were penetrating the insect screen and providing a reliable scatter frequency to the LDV photodetector.

Vertical Velocity Profiles Through a Glass Plate with LDV and Pitot Probe

The first prototype experiment investigated the ability to measure velocity through a piece of glass parallel to the streamwise flow of the FE/DE. The main concern was that the optical glass may create reflections that could adversely affect the scatter signal

received by the photodiode in the fiberoptic probe. A section of glass 178mm long by 43mm wide by 4mm thick was suspended 53mm below the top of the FE/DE test section. This glass plate was the same material and thickness as the optical windows used in the detectors. The tests were conducted under steady state flow conditions.

Velocity above and below the glass surface was measured with the LDV and a comparative measurement was made with a Pitot probe used as a reference measurement. The thermal anemometer, which was used as the reference measurement device in the velocity profile measurements, was not used for this set of prototype experiments because it was installed in a fixed position oriented vertically in the FE/DE. These limitations did not provide a convenient method for making a series of velocity measurements above and below the glass plate. The Pitot probe used in this set of prototype experiments was mounted to a vertical translation stage and provided a convenient a reliable method for making this series of velocity measurements. The LDV measurements were made at distances of 1.5 and 3.0cm past the leading edge of the glass plate and at vertical locations from 20 to 85mm below the ceiling in 5mm increments. The Pitot probe measurements were made at vertical locations of 20, 30, 40, 50, 65, 75, and 85mm below the ceiling. Data was collected for 60 seconds at each measurement point and the error bars represent one standard deviation.

The results are shown for an external freestream veleocity of 0.52 m/s in Figure 68 and Figure 69 where the error bars represent 1 standard deviation in the measurement data set.

210
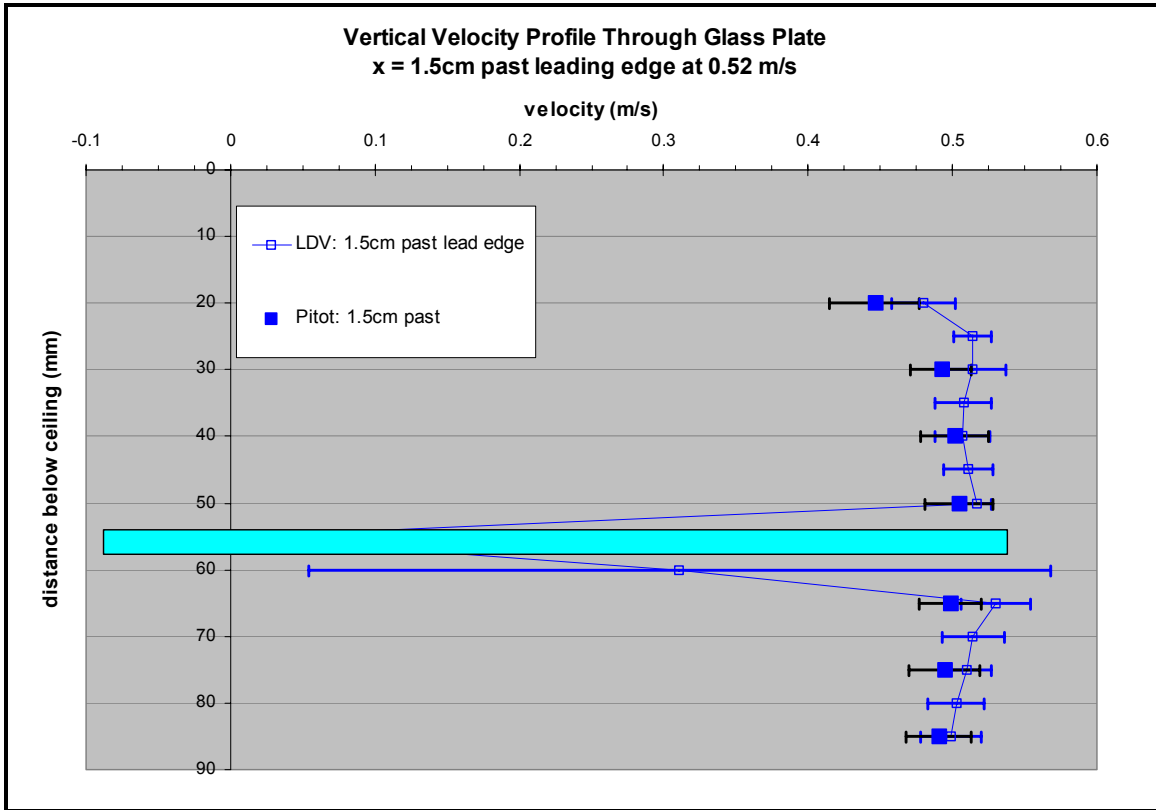
Figure 68 -- Streamwise vertical velocity profiles through glass plate at 1.5cm past lead edge.
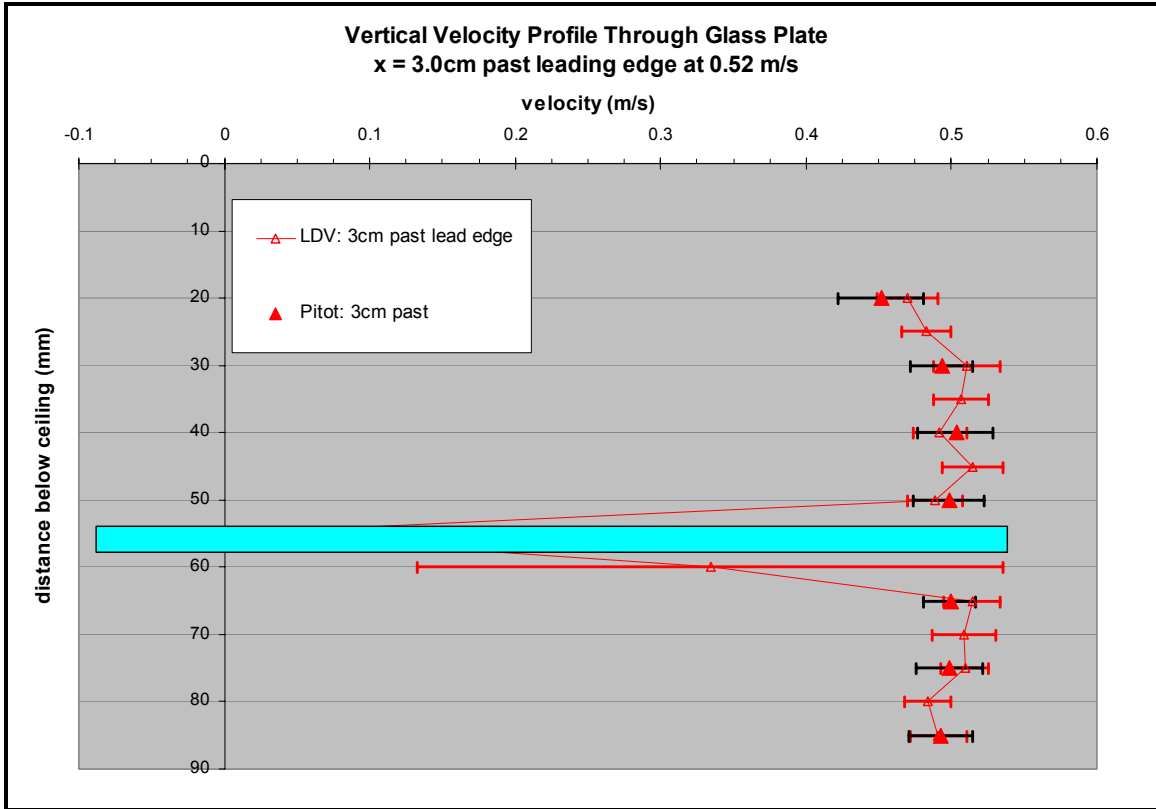
Figure 69 -- Streamwise vertical velocity profiles through glass plate at 3.0cm past lead edge.

The standard deviations in Figure 68 range from 2 to 5% of the LDV mean velocity values and from 4 to 7% of the Pitot mean values for 1.5cm past the leading edge. The standard deviations in Figure 69 range from 3 to 5% of the LDV mean velocity values and from 4 to 7% of the Pitot mean values for 3.0cm past the leading edge. The standard deviations at 55 and 60mm are ignored due to the length of the measurement volume intersecting the glass plate. The variation in mean values is in the range of 0.1 to 4.8% for 1.5cm past the leading edge and 0.7 to 5.8% for 3.0cm past the leading edge. The variation was computed in terms of the Pitot probe mean values relative to the LDV mean values.

The agreement between the LDV and Pitot probe reference measurements for this series of experiments (shown in Figure 68 and Figure 69) can be characterized as favorable. This characterization is based on the time averaged velocity values being within 6% of the Pitot probe reference measurement, the similarity in the magnitude of the standard deviations from both devices, and the high degree of overlap in the standard deviations.

Internal Velocity for a Simple Mockup with LDV and Pitot Probe

The second prototype experiment investigated the ability to measure velocity through a piece of glass for a simple resistive element at the leading edge. The main concern was that a resistive element, such as the insect screen, may reduce the number of seed particles entering the measurement area, resulting in an insufficient scatter signal. The section of glass from the first prototype experiment was used and had a portion of insect screen affixed to the leading edge. The top and sides of the glass were partially enclosed so that the insect screen was the only path for seed particles to enter the internal section of this simple mockup, however, this also allowed for a Pitot probe to be placed for a comparative measurement of internal velocity. An isometric view of the simple detector mockup is shown in Figure 70.
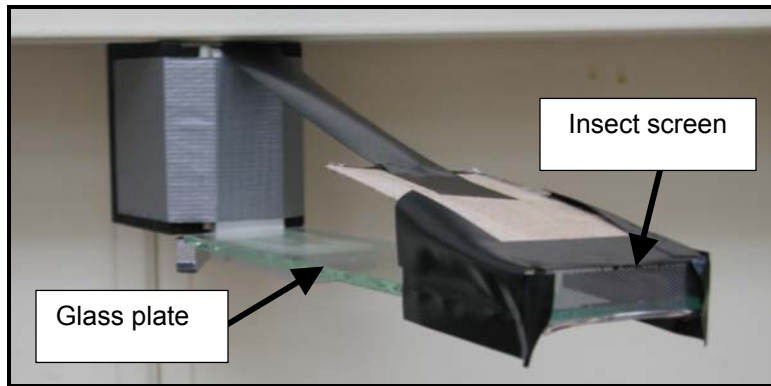
Figure 70 -- Simple detector mockup with insect screen at lead edge and partially enclosed.

The velocity measurements were made by both the LDV and the Pitot probe (reference measurement) at 1.5cm past the leading edge, along the centerline, and at the midpoint of the internal height. Data was collected for 60 seconds for steady state external velocities in the range of 0.40 to 1.30 m/s. The time averaged internal velocity values from these tests are shown in Figure 71 where the LDV measurements are plotted against the Pitot probe reference measurements. A solid line indicating ideal agreement on a 1 to 1 basis for the two measurement techniques is provided. The error bars represent one standard deviation in each respective measurement and was used as estimate of the measurement uncertainty.
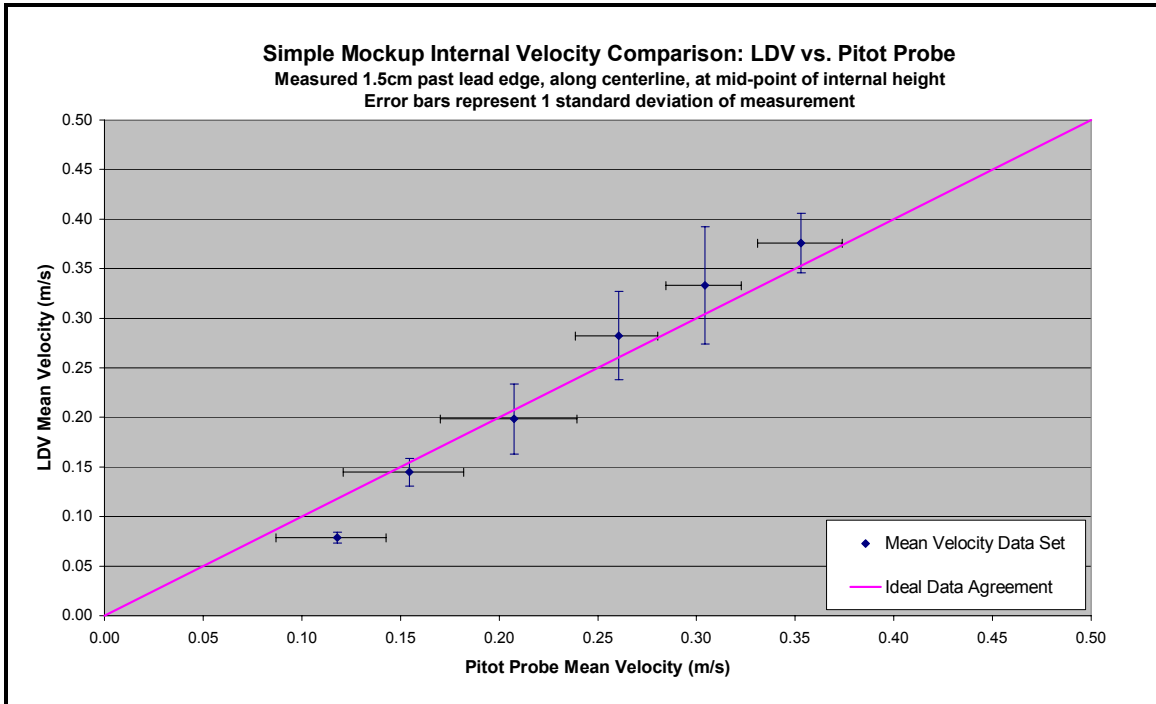
Figure 71 -- Streamwise internal velocity comparison for simple detector mockup.

The comparative measurements of internal velocity between the LDV and Pitot probe as shown in Figure 71 can be characterized as favorable. This characterization is based on the agreement between the time averaged values and the ideal fit line as well as the degree of overlap the standard deviations have with the ideal fit line. Therefore, the glass and restrictive element were found not have a negative impact on the ability of the LDV to measure internal velocity.

Appendix A.3: LDV Internal Velocity Screening Criteria

The LDV data was screened to remove anomalous data points. The process began with a qualitative examination of the data. The data for all 45 measurement locations was plotted to show both the number of valid data points (particle counts) as well as mean velocity on the same y-axis. This plotting procedure was used in order to determine if a sufficient number of valid points were collected at a particular measurement location and if the resulting mean velocity value was consistent with the general trend of the data set. Examples of this plotting procedure are shown in Figure 72 and Figure 73.
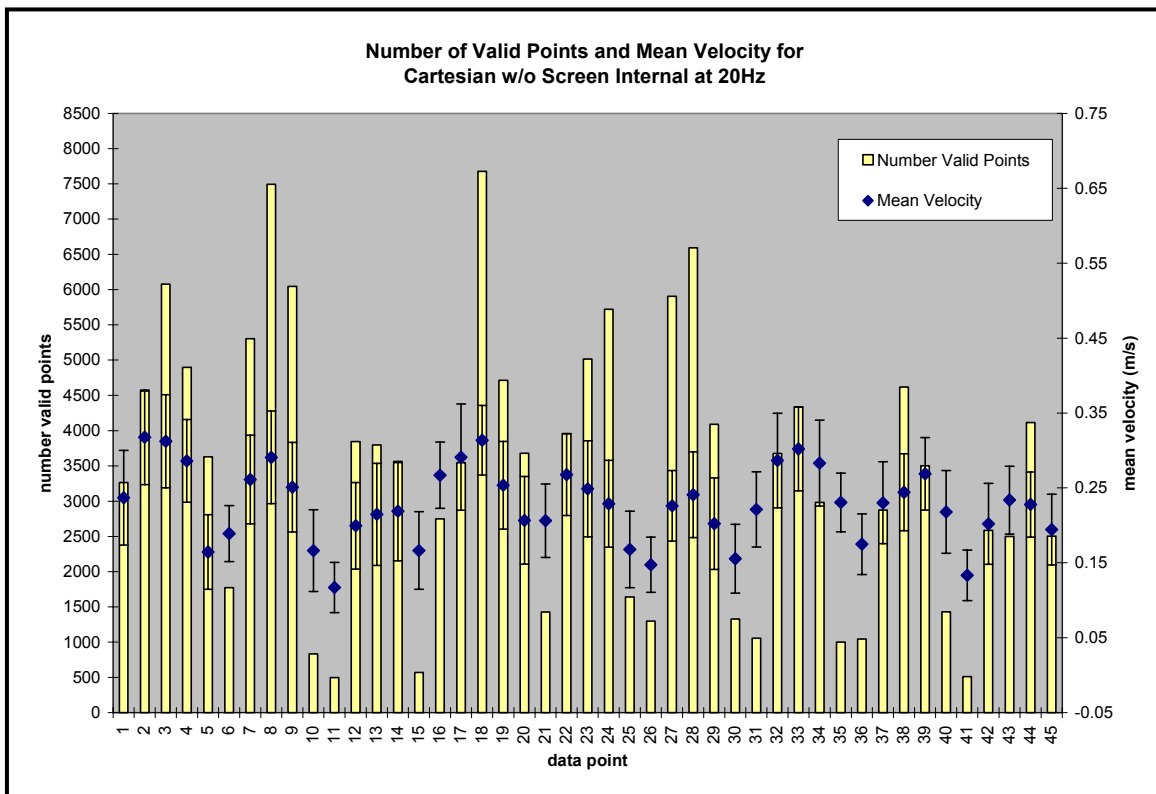
Figure 72 -- Valid points and mean velocity for rectangular model detector without insect screen for 0.52 m/s external flow field.

Figure 72 above is representative of a velocity scan where a sufficient number of data points have been collected (at least 500 valid points in this particular case) and the standard deviation (represented as the y-direction error bars) is consistent at each measurement location. This was typical of most data sets collected for the rectangular model detector with and without the insect screen. This data set would be considered to be internally consistent.
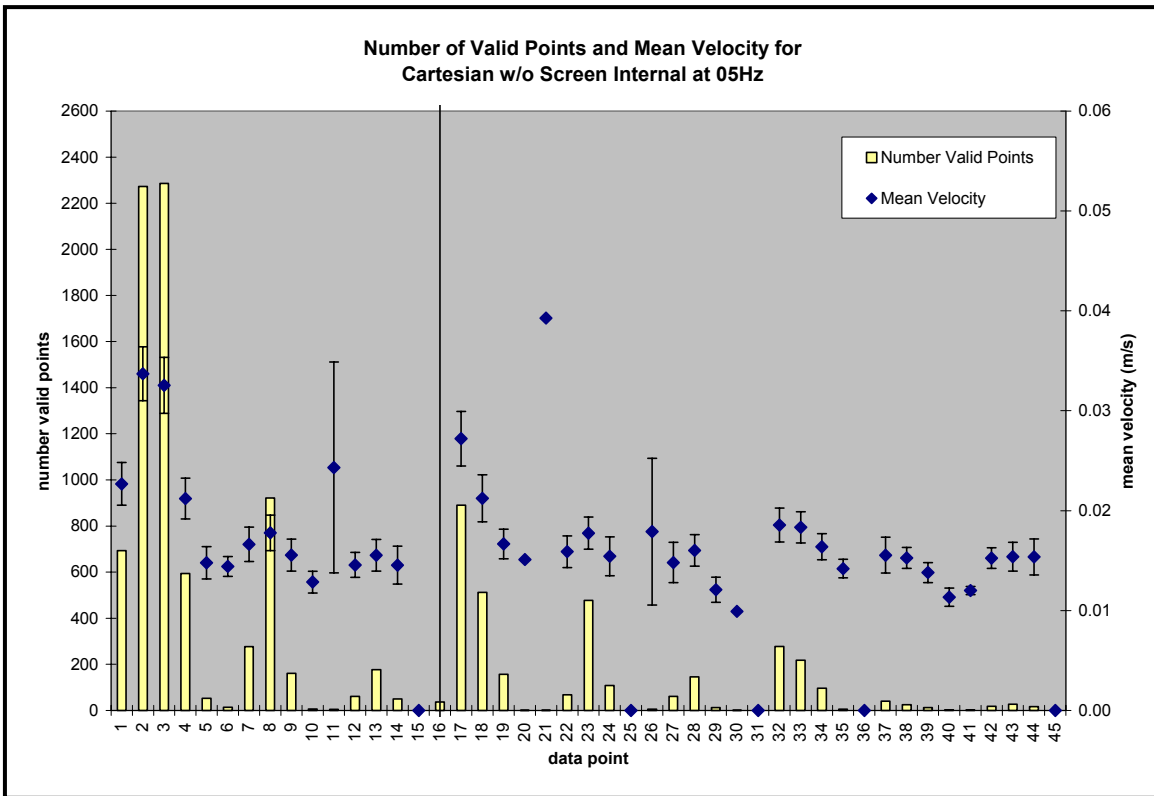
Figure 73 -- Valid data points and mean velocity for rectangular detector without insect screen at 0.11 m/s external flow field.

Figure 73 above is representative of a velocity scan where an insufficient number of data points have been collected at a few isolated locations and the standard deviation at some locations is inconsistent with general trend in the overall data set. This data set would be considered to be internally inconsistent. A qualitative examination of the data sets

217

indicated that some data points were anomalous relative to the majority based on a low number of valid particle counts or a large standard deviation value. Therefore, quantitative screen criteria were developed in order to remove the anomalous data points identified in the qualitative examination in a consistent manner.

The screen criteria developed for the data sets was based on a threshold number of valid data points collected a particular measurement location and maximum turbulence intensity for a particular measurement location. Both criteria were met in order for a data point to be allowed into the screened data set. The threshold number of valid data points was 10. This was based on the observation that in cases where a physically inconsistent velocity value appeared in the data set (indicated as a value of zero, or a value in excess of the external velocity) there were less than 10 data valid points collected at the particular measurement location. Additionally, anomalous data points were observed at locations where a sufficient number of valid data points were collected but the standard deviation was internally inconsistent with the rest of the data set. Turbulence intensity was used to measure because it is the standard deviation divided by the mean velocity. By using the turbulence intensity percentage, a consistent criterion could be applied over the range of velocity values. An observation of all the data sets collected revealed that the turbulence intensity ranged from approximately 50 to 5% over the entire range of external flow velocities. A turbulence intensity value above 100% was used as the screening criteria to exclude specific data points that were internally inconsistent.

To summarize, the LDV measurement at a given location was considered appropriate if it passed *both* of the following criteria:

- Number of valid collected data points > 10

- Turbulence intensity < 100%

Appendix A.4: Detector Internal Velocity Profiles

The screening method described in Appendix A.3 was applied to the internal velocity measurements for the rectangular model detector. Representative velocity profiles for the rectangular detector model with and without the insect screen in place are shown in Figure 72 and Figure 73. The peak velocity values were 0.241 m/s for the rectangular model without the insect screen in place and 0.045 m/s with the insect screen in place. This example shows that the insect screen is a significant resistive element in the rectangular model.
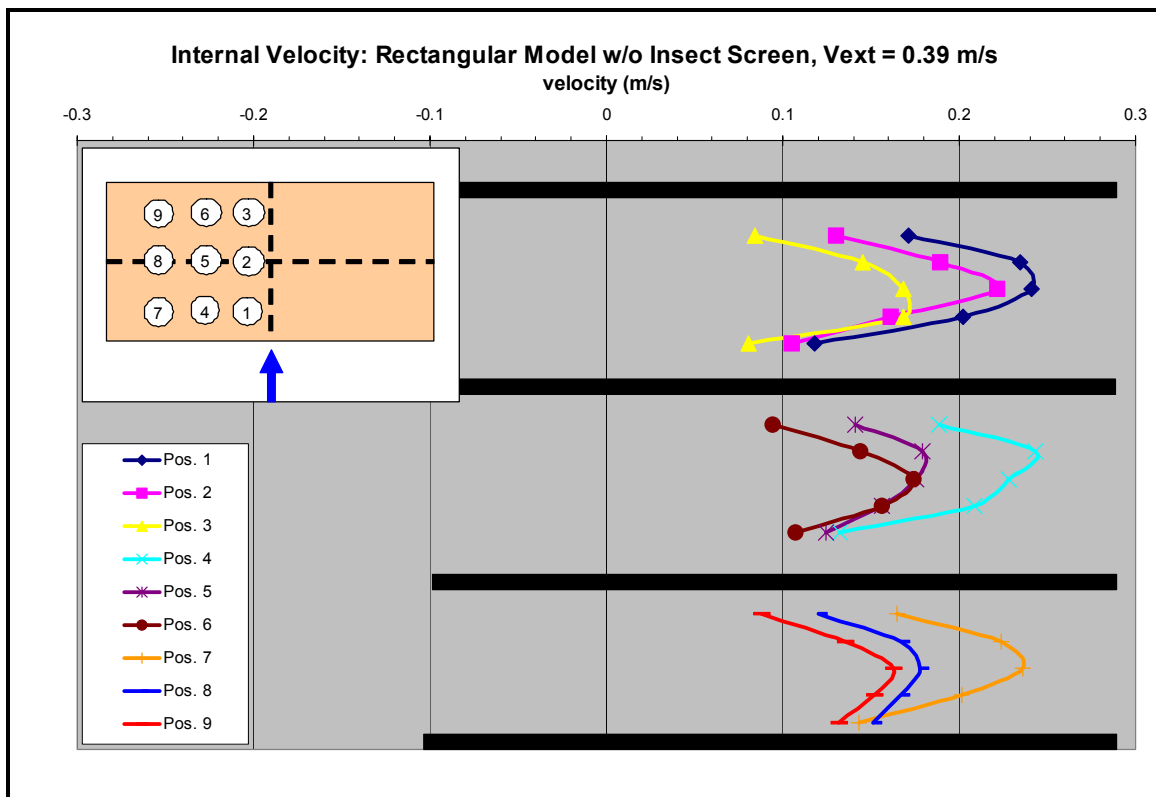
Figure 74 -- Internal vertical velocity profiles for rectangular model detector without insect screen.
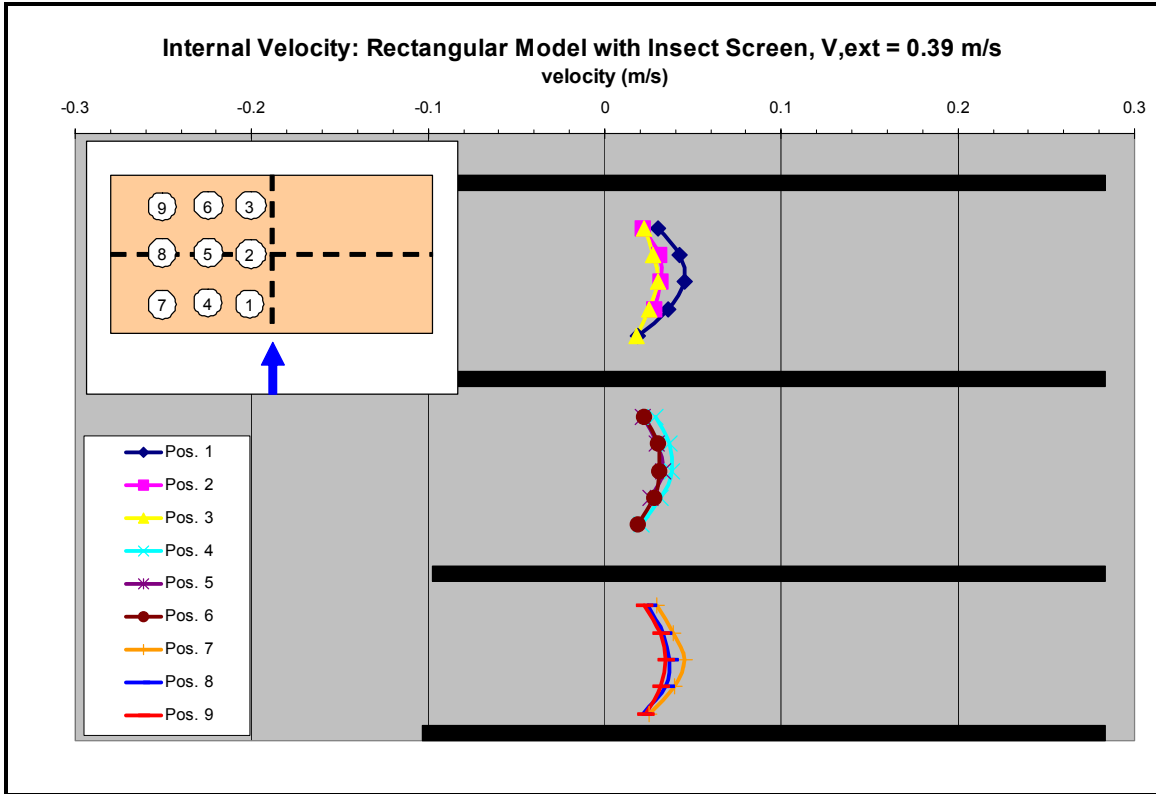
Figure 75 -- Internal vertical velocity profiles for rectangular model detector with insect screen.

The screened data sets for the rectangular detector are summarized in Table 31 below. The data is presented as time averaged velocity in units of meters per second, one statistical standard deviation, and the percent turbulence intensity.

Table 31 – External and internal velocity data including standard deviation and turbulence intensity for rectangular model detector.

Fan (Hz)	FE/DE Time Avg Velocity			Cartesian Detector W/O Screen			Cartesian Detector W/Screen		
	V,ext (m/s)	Std dev	V TI%	V,int (m/s)	Std dev	V TI%	V,int (m/s)	Std dev	V TI%
30	0.822	0.048	5.85	0.381	0.108	28.29	0.132	0.018	13.53
25	0.668	0.045	6.71	0.253	0.071	27.93	0.095	0.011	11.45
20	0.520	0.035	6.81	0.267	0.057	21.36	0.067	0.007	11.04
15	0.392	0.028	7.20	0.198	0.035	17.89	0.036	0.003	9.17
12	0.314	0.027	8.70	0.144	0.029	19.90	0.022	0.002	10.29
10	0.264	0.026	9.84	0.094	0.013	13.39	0.014	0.004	25.66
7	0.168	0.027	16.07	0.037	0.002	6.53	0.005	0.003	55.54
5	0.113	0.025	22.07	0.019	0.002	9.26	0.003	0.002	84.31

The time averaged internal velocity for the rectangular detector with and without the insect screen in place is shown in Figure 76 to demonstrate the relative impact of this resistive element.
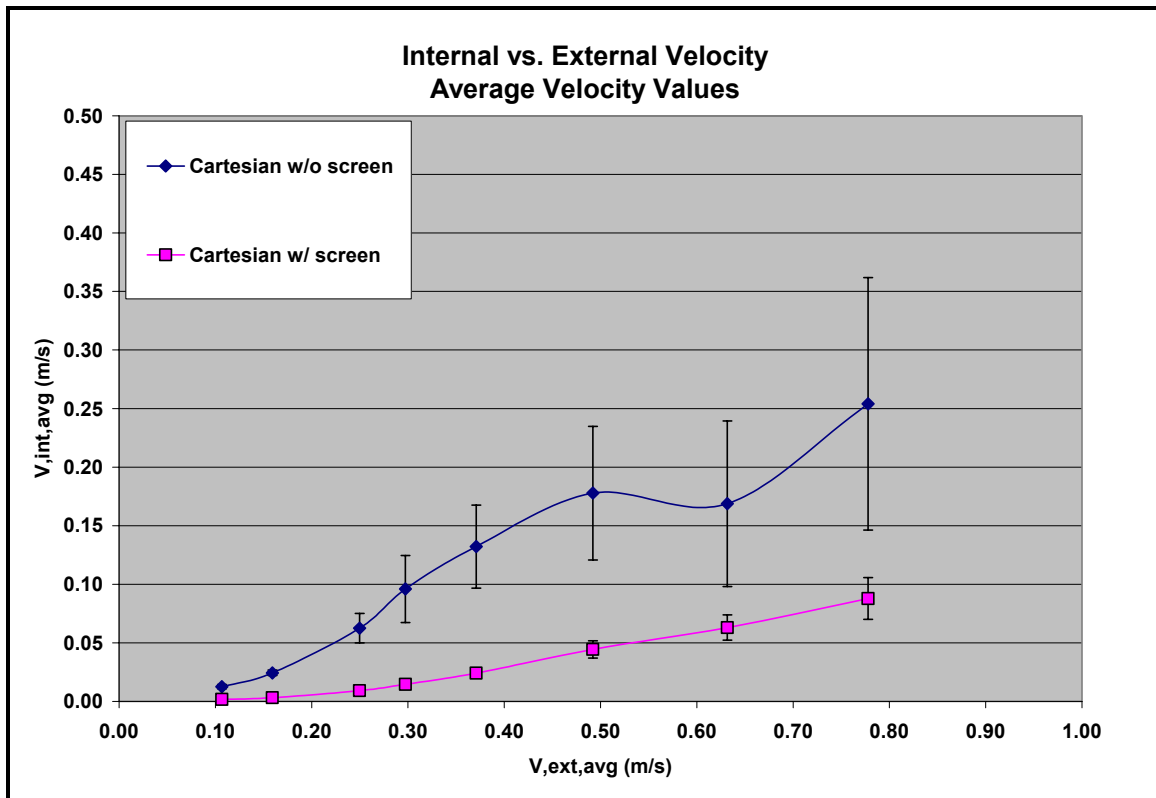
Figure 76 -- Internal vs. external velocity for rectangular model detector with and without insect screen.

Figure 76 shows a statistically significant trend of the internal velocity measurements being 3 to 8 times smaller for the insect screen being in place relative to having the screen removed. The magnitude of the standard deviations, which provides an indication of the fluctuations in the mean flow, is larger for the case with the insect screen removed. This comparison indicates that the insect screen provides a significant amount of

resistance to the flow entering the detector and that the screen also helps to dampen the

fluctuations in the mean flow, as indicated by the standard deviations in the velocity data.

Appendix A.5: Viscous Flow Analysis

The velocity data set for the rectangular model was analyzed using concepts from viscous fluid flow. The Reynolds numbers for the external bulk flow field in the FE/DE and the rectangular model were examined to determine if laminar or turbulent characteristics were present. The purpose of this analysis was to provide a general characterization of the flow field based on Reynolds number and was not a detailed fluid mechanics study. The internal flow field for the rectangular detector model was compared to the analytical solution for the velocity distribution of laminar viscous fluid flow between fixed parallel plates.

4.3.1 Reynolds Number

The Reynolds numbers for both the external flow in the FE/DE as well as the internal velocity for the rectangular model were computed.

$$\mathrm{Re} = \frac{uD}{\nu}$$

(118)

A kinematic viscosity value, ν, of 1.684 E-05 for air at 300K was used. The characteristic dimension, D, was computed using the hydraulic diameter for a rectangular cross section. The hydraulic diameter, D_h, is defined as (Munson, 1994):

$$D_h = \frac{4A_c}{P_w}$$

<div align="right">(119)</div>

Where A_c is the cross sectional area and P_w is the wetted perimeter of the non-circular duct.

The height and width of the FE/DE test section is 0.33m by 0.67m and results in a hydraulic diameter of 0.44m. The maximum external freestream velocity of 0.82 m/s results in a Reynolds number of 21,500. Therefore, the external flow is turbulent at the upper bound of freestream velocities. The critical velocity for the transition to turbulent flow was computed from Equation 118 by using a critical Reynolds number of 2,300.

$$u_{cr} = \frac{\mathrm{Re}_{cr}\, \nu}{D} = \frac{(2300)\left(1.684E - 05\, m^2/s\right)}{0.44m} = 0.09\, m/s$$

<div align="right">(120)</div>

Since all tests were conducted at external velocities above this value, the external bulk flow field can be considered to have turbulent characteristics.

The height and width for the interior space of the rectangular model, as shown in for the baffles, is 0.014m by 0.160m and corresponds to a hydraulic diameter of 0.0257m. The maximum internal velocity of 0.5 m/s was measured with the LDV for an external flow velocity of 0.82 m/s without the insect screen in place. This scenario represents the upper

bound for the Reynolds number and was found to be 760. Therefore, the internal flows

for the rectangular model can be considered to have laminar characteristics because the

maximum expected Reynolds number for these flow conditions is well below the critical

Reynolds number of 2,300 for the transition to turbulent flow.

4.3.2 Laminar Flow of Viscous Fluid Between Two Parallel Plates

The solution for steady laminar flow of a viscous fluid between fixed parallel plates from

the Navier-Stokes equations (Munson, 1994) was used to examine the general nature of

the time averaged internal velocity profiles in the rectangular detector model.   The

scenario considered in this case is shown below in Figure 77.
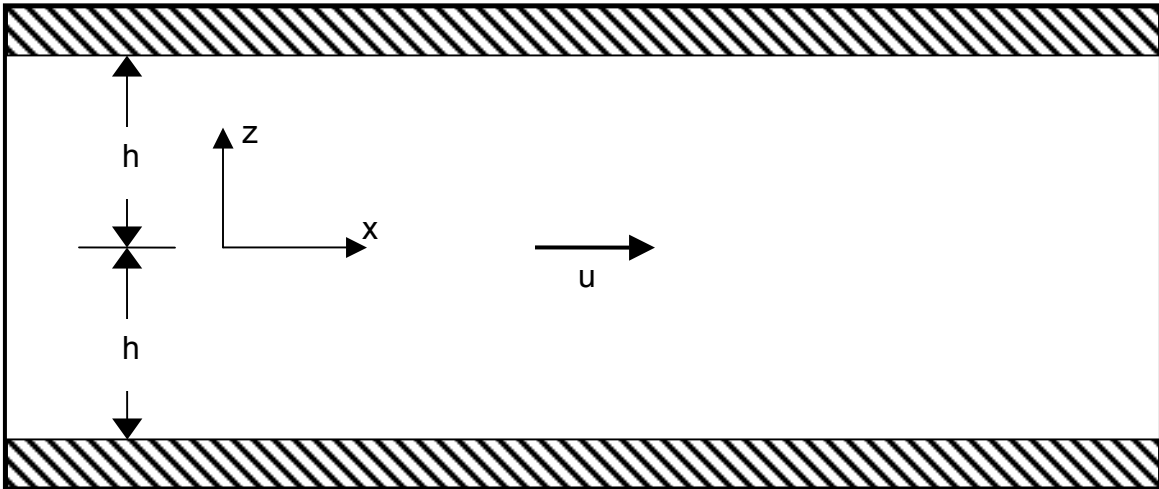
Figure 77 -- Viscous fluid flow between fixed parallel plates with coordinate system.

The velocity distribution for this specific case is (Munson, 1994)

$$u = \frac{1}{2\mu}\left(\frac{\partial p}{\partial x}\right)\left(z^2 - h^2\right)$$

(121)

Where u is fluid velocity, μ is the fluid dynamic viscosity, z is the vertical location of interest, h is the half-height of the plate spacing, and the partial differential term is the pressure gradient in the x-direction.

The maximum velocity is expected to occur at $z = 0$ and Equation 121 becomes

$$u_{max} = -\frac{h^2}{2\mu}\left(\frac{\partial p}{\partial x}\right)$$

(122)

The velocity profiles obtained with the LDV measurements were compared to the theoretical distribution in Equation 121. The maximum velocity measured with the LDV was substituted into Equation 122 along with the known values of h and μ to solve for the pressure gradient. The computed pressure gradient was used to calculate the velocity profile. A typical comparison between the calculated and measured velocity values is shown in Figure 78.
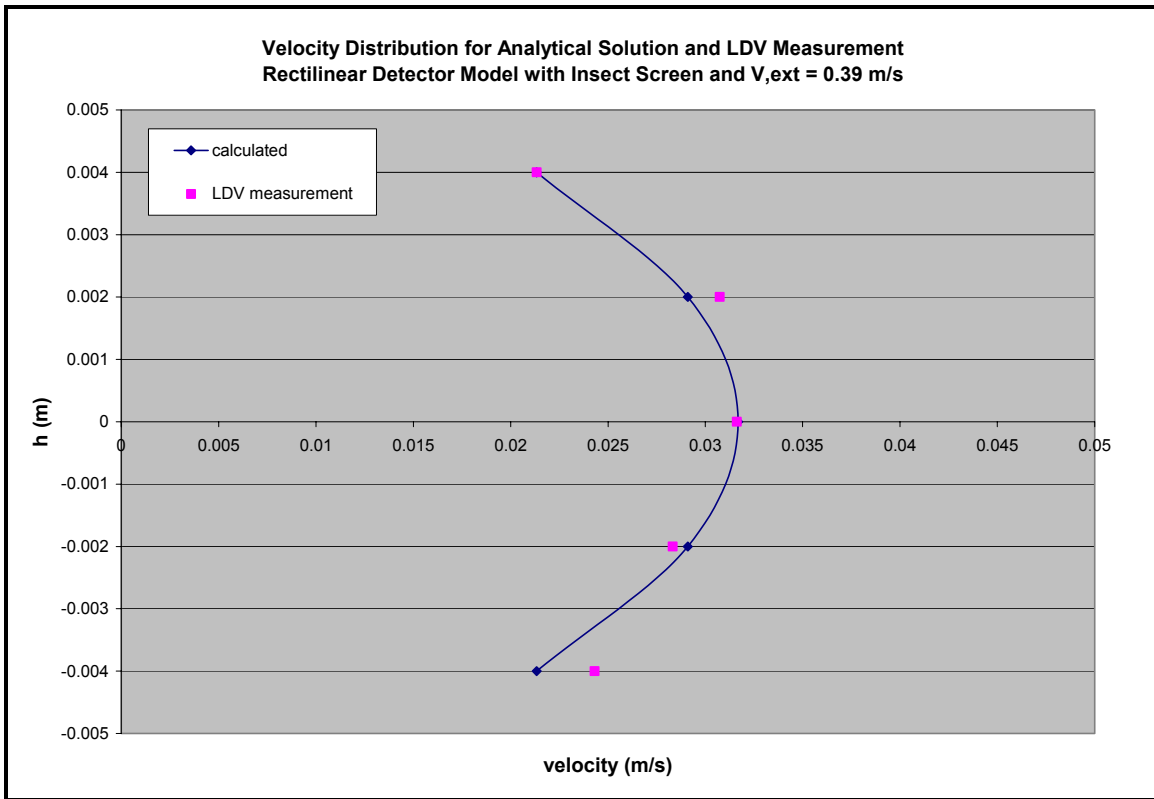
Figure 78 -- Comparison of LDV measured velocity profile to analytic solution.

The average variation in the LDV measurements relative to the calculated theoretical velocity profile for the range of external flow speeds is summarized in Table 32 below. The comparison was made between the 5 points measured with the LDV at Position 2.

Table 32 -- Average variation in LDV velocity profile with respect to analytic solution.

	Average Variation wrt Analytical	
V,ext (m/s)	Without Screen	With Screen
0.52	0.039	0.060
0.39	0.100	0.045
0.31	0.081	0.031
0.26	0.115	0.116
0.17	0.081	0.232
0.11	0.081	0.254

The average variation for both cases is in the range of 4 to 12% with the exception of the model with the insect screen below 0.20 m/s. The standard deviations in the internal velocity measurements were 50% and 100% of the mean values for 0.11 and 0.17 m/s, respectively, and may account for the relatively poor comparison to the analytic solution.

The flow fields inside the rectangular model are consistent with laminar flow based on both Reynolds number calculations as well as a favorable comparison of the LDV velocity profiles to the analytic solution for laminar flow between fixed parallel plates. These findings are also consistent with observations made of Figure 76 for the rectangular detector with and without the insect screen in place. The comparison of internal velocities as a function of external velocity indicated that the insect screen helps to reduce the magnitude of internal velocity and the magnitude of the velocity fluctuations relative to the scenario where an insect screen is not used.

Appendix B: Experimental Data Compilation

The experimental data collected for this study are presented. The data sets fall into three main categories; screen resistance, velocity scans, and response tests. The experimental conditions for each type of test conducted within each main category are summarized and the data sets are reported in tabular format.

Screen Resistance

The screen resistance was assessed with velocity measurements at up and downstream locations for a typical insect screen. These tests were performed as a prototype experiment to gauge if the LDV was capable of making velocity measurements downstream of an insect screen by comparing to reference measurements made with a Pitot probe.

- **FE/DE fan speeds:** 15, 20, 25, 30, 35, 40 Hz at steady state

- **X measurement location:** 15mm downstream of screen interior

- **Y measurement location:** center of screen width

- **Z measurement location:** 50mm below duct ceiling, center of screen height

- **Data collection period:** 10 seconds for LDV, 30 seconds for Pitot

- **Data points collected:** nominally 5,000 for LDV, 30 for Pitot

Table 33 -- Insect screen external (freestream) and internal (downstream) velocity measurements.

	EXTERNAL			INTERNAL						
	LDV			LDV			Pitot			
Fan (Hz)	V_{mean}(m/s)	Std dev	V TI%	V_{mean}(m/s)	Std dev	V TI%	V_{mean}(m/s)	Std dev +	Std dev -	V TI% (avg)
40	1.6 (est.)	N/A	N/A	0.375895	0.029920	7.959611	0.352959	0.020785	0.022088	6.073273
35	1.3 (est.)	N/A	N/A	0.333256	0.059042	17.716770	0.304215	0.018488	0.019687	6.274451
30	0.822367	0.048144	5.854278	0.282505	0.044360	15.702217	0.260456	0.020053	0.021732	8.021432
25	0.668003	0.044853	6.714438	0.198460	0.035286	17.779824	0.207643	0.031776	0.037614	16.708783
20	0.520169	0.035418	6.808926	0.144924	0.013919	9.604350	0.154476	0.027439	0.033510	19.727596
15	0.392089	0.028238	7.201976	0.078674	0.005576	7.087865	0.118001	0.024559	0.031254	23.649568

Velocity Scans

Velocity scans were conducted with the LDV under steady state flow conditions to characterize the streamwise flow field in the FE/DE as well as the internal velocity fields for the rectangular detector model, ionization detector, and photoelectric detector.

FE/DE Streamwise Velocity Characterization

The purpose of this set of experiments was to characterize the streamwise velocity field along the centerline of the FE/DE. The data was collected under the following conditions:

- **FE/DE fan speeds:** 0, 3, 5, 7, 10, 12, 15, 20, 25, 30 Hz at steady state

- **X measurement location:** 10mm upstream of typical detector leading edge

- **Y measurement location:** duct centerline

- **Z measurement locations below ceiling:** 5 – 100 mm in 5mm increments

- **Data collection period:** 5 seconds at each location

- **Data points collected:** nominally 3,300 at each location

The data presented in Table 34 includes the mean velocity, standard deviation, and percent turbulence intensity based on nominally 3,300 data points at each measurement location for each fan speed setting.

Table 34 -- FE/DE Steady State Streamwise Velocity Characterization Data Sets 0 to 30Hz.

	00Hz			03Hz			05Hz			07Hz			10Hz		
z (mm)	Vmean(m/s)	V std	V TI%	Vmean(m/s)	V std	V TI%	Vmean(m/s)	V std	V TI%	Vmean(m/s)	V std	V TI%	Vmean(m/s)	V std	V TI%
5	0.027966	0.025562	91.4032	0.043607	0.026607	61.0144	0.047431	0.026809	56.5222	0.052576	0.025735	48.9487	0.090629	0.024647	27.1952
10	0.040838	0.025181	61.659	0.061259	0.024697	40.3161	0.066688	0.024854	37.2683	0.077038	0.0245	31.803	0.136368	0.026164	19.1865
15	0.051848	0.025077	48.3661	0.070893	0.024696	34.8358	0.081513	0.023692	29.0656	0.092717	0.024239	26.1425	0.170923	0.026719	15.6323
20	0.053053	0.024223	45.6582	0.074511	0.025253	33.892	0.091855	0.024955	27.1679	0.108555	0.023977	22.0872	0.203252	0.024717	12.1608
25	0.055903	0.024453	43.742	0.066548	0.024057	36.15	0.101692	0.024025	23.6255	0.118313	0.024408	20.6303	0.220063	0.024684	11.2169
30	0.055203	0.025386	45.9874	0.065973	0.024002	36.3812	0.104317	0.025158	24.1165	0.128794	0.024258	18.8348	0.242807	0.024624	10.1414
35	0.061385	0.024354	39.6743	0.064951	0.024886	38.3146	0.105241	0.025111	23.8606	0.140358	0.025694	18.3057	0.254734	0.026163	10.2707
40	0.064015	0.025057	39.1426	0.066569	0.02438	36.623	0.108298	0.024618	22.7319	0.153217	0.026092	17.0293	0.257021	0.024645	9.5885
45	0.06817	0.024931	36.5723	0.073013	0.023856	32.6728	0.109394	0.025067	22.9148	0.158558	0.02725	17.1863	0.263829	0.026199	9.93027
50	0.073234	0.02387	32.5936	0.075592	0.024124	31.9138	0.114223	0.024808	21.7193	0.169711	0.026885	15.8417	0.258708	0.026162	10.1124
55	0.073519	0.023858	32.4518	0.080982	0.02382	29.4143	0.114945	0.024838	21.6085	0.176542	0.026987	15.2864	0.270152	0.025666	9.50071
60	0.074478	0.023701	31.8234	0.082094	0.024602	29.9675	0.12043	0.024619	20.4423	0.181944	0.027004	14.8419	0.265521	0.026778	10.0851
65	0.07529	0.023395	31.0735	0.083896	0.023499	28.0094	0.121331	0.024912	20.5322	0.18826	0.026209	13.9215	0.264081	0.02588	9.80017
70	0.076577	0.024977	32.6162	0.084284	0.024298	28.8289	0.129532	0.02559	19.7557	0.188243	0.025423	13.5054	0.265718	0.026622	10.0189
75	0.07361	0.024977	33.9315	0.085974	0.024221	28.1721	0.132724	0.025547	19.2481	0.190704	0.026536	13.9147	0.268377	0.026544	9.8904
80	0.073174	0.024618	33.6437	0.090332	0.024954	27.6252	0.132714	0.02555	19.2517	0.193244	0.025874	13.3894	0.263435	0.025409	9.64531
85	0.076268	0.024334	31.9055	0.090691	0.024291	26.7848	0.135637	0.025721	18.9629	0.193624	0.025883	13.3676	0.261238	0.02717	10.4006
90	0.074088	0.024001	32.3949	0.095337	0.024601	25.804	0.138435	0.025822	18.6526	0.190499	0.025923	13.6077	0.267769	0.0263	9.82191
95	0.080619	0.024517	30.4109	0.100881	0.024788	24.5719	0.14208	0.025973	18.2806	0.190827	0.025799	13.5196	0.257167	0.026418	10.2726
100	0.084917	0.02429	28.6047	0.105405	0.025189	23.8974	0.143527	0.026138	18.2115	0.190224	0.025266	13.2822	0.259401	0.02543	9.80341

	12Hz			15Hz			20Hz			25Hz			30Hz		
z (mm)	Vmean(m/s)	V std	V TI%	Vmean(m/s)	V std	V TI%	Vmean(m/s)	V std	V TI%	Vmean(m/s)	V std	V TI%	Vmean(m/s)	V std	V TI%
5	0.119754	0.026652	22.2559	0.173604	0.028807	16.5934	0.298832	0.032672	10.9331	0.409023	0.079704	19.4864	0.538331	0.102569	19.0532
10	0.185889	0.02679	14.4116	0.256037	0.026116	10.2001	0.417545	0.031681	7.58745	0.516648	0.068593	13.2764	0.655414	0.094561	14.4277
15	0.235951	0.024843	10.5288	0.314619	0.029749	9.45545	0.481835	0.035529	7.37367	0.594934	0.044452	7.47168	0.734038	0.074693	10.1757
20	0.261341	0.024685	9.44553	0.364169	0.027202	7.46957	0.506245	0.034098	6.73546	0.63758	0.04776	7.49079	0.765526	0.058996	7.70656
25	0.286339	0.027084	9.45858	0.384032	0.02819	7.34052	0.526023	0.032423	6.16387	0.645692	0.045224	7.01052	0.81075	0.053955	6.65489
30	0.29896	0.028724	9.60786	0.382497	0.027067	7.07644	0.520886	0.033415	6.41506	0.660214	0.043523	6.59227	0.780665	0.055306	7.08448
35	0.307302	0.026824	8.72879	0.390336	0.028145	7.2104	0.53256	0.037196	6.98444	0.672849	0.038788	5.76473	0.822651	0.053736	6.53203
40	0.314569	0.028103	8.93387	0.392007	0.02795	7.13004	0.52301	0.035292	6.74786	0.66337	0.041635	6.27625	0.835928	0.047386	5.66864
45	0.315098	0.027691	8.78796	0.391492	0.028051	7.16525	0.525807	0.034102	6.48571	0.663021	0.043084	6.49815	0.824786	0.050131	6.0781
50	0.313864	0.026967	8.59189	0.392677	0.028778	7.32873	0.515814	0.037805	7.32923	0.670653	0.046623	6.95183	0.823779	0.047562	5.77364
55	0.314452	0.027463	8.73344	0.392097	0.027885	7.1117	0.518885	0.034346	6.61924	0.670336	0.044851	6.69088	0.818537	0.046738	5.70989
60	0.314942	0.028259	8.97262	0.387859	0.02819	7.2682	0.530465	0.034822	6.56444	0.668198	0.039627	5.93046	0.829653	0.04658	5.61434
65	0.310511	0.028233	9.09226	0.384672	0.029192	7.58884	0.53166	0.034613	6.5104	0.668176	0.03998	5.98345	0.830755	0.044487	5.355
70	0.317667	0.02761	8.6914	0.376989	0.02963	7.85966	0.516299	0.038288	7.41594	0.665136	0.038244	5.74974	0.818749	0.048476	5.92069
75	0.316297	0.027432	8.67278	0.382115	0.027573	7.2158	0.52018	0.034657	6.66243	0.650086	0.040727	6.26481	0.812472	0.048235	5.93686
80	0.303012	0.028867	9.5268	0.383729	0.028732	7.4875	0.51576	0.033225	6.4419	0.661681	0.036198	5.47066	0.81622	0.046048	5.64165
85	0.313703	0.02813	8.96701	0.379924	0.028942	7.61774	0.515432	0.03249	6.30341	0.640114	0.040423	6.31491	0.800177	0.046518	5.81341
90	0.308109	0.027317	8.86588	0.378724	0.028413	7.50238	0.51031	0.033316	6.52853	0.653157	0.036261	5.55167	0.804521	0.050081	6.22492
95	0.30805	0.028602	9.28494	0.37028	0.027507	7.42867	0.513358	0.035614	6.93751	0.651838	0.035106	5.38567	0.789922	0.042392	5.36664
100	0.304478	0.027781	9.12398	0.3695	0.027975	7.57117	0.504426	0.034861	6.91099	0.646629	0.041176	6.36774	0.791381	0.044375	5.60722

The freestream velocity value for each fan speed setting was determined by averaging the mean velocity values from Table 34 at 45, 50, and 55mm below the ceiling. These specific locations were selected because they corresponded to the typical location for aerosol entry in the detectors of interest to this study. The data presented in Table 35 shows fan speed setting and the averaged values for both mean velocity and standard deviation. These averaged values were used to represent the freestream, or external, velocity values throughout the rest of this study.

Table 35 -- FE/DE freestream flow values averaged for points 45, 50, and 55mm below ceiling.

Fan (Hz)	Averaged values		
	V,mean (m/s)	Std dev	V TI%
30	0.8224	0.0481	5.85
25	0.6680	0.0449	6.71
20	0.5202	0.0354	6.81
15	0.3921	0.0282	7.20
12	0.3145	0.0274	8.70
10	0.2642	0.0260	9.84
7	0.1683	0.0270	16.07
5	0.1129	0.0249	22.07
3	0.0765	0.0239	31.27
0	0.0716	0.0242	33.81

Rectangular Model Detector Velocity Scans

Internal velocity was measured with the LDV under steady state conditions for the rectangular model detector. The velocity scans were conducted with the insect screen in place and with the insect screen removed from the rectangular model detector. The data was collected under the following conditions:

- **FE/DE fan speeds:** 5, 7, 10, 12, 15, 20, 25, 30 Hz at steady state

- **Insect screen:** two scenarios: screen in place and screen removed

- **Measurement locations:** 45 total locations, 5 horizontal points internally at 9 different locations (indicated in tables)

- **Data collection period:** 5 seconds at each location

- **Data points collected:** varied throughout testing (see Screening Criteria)
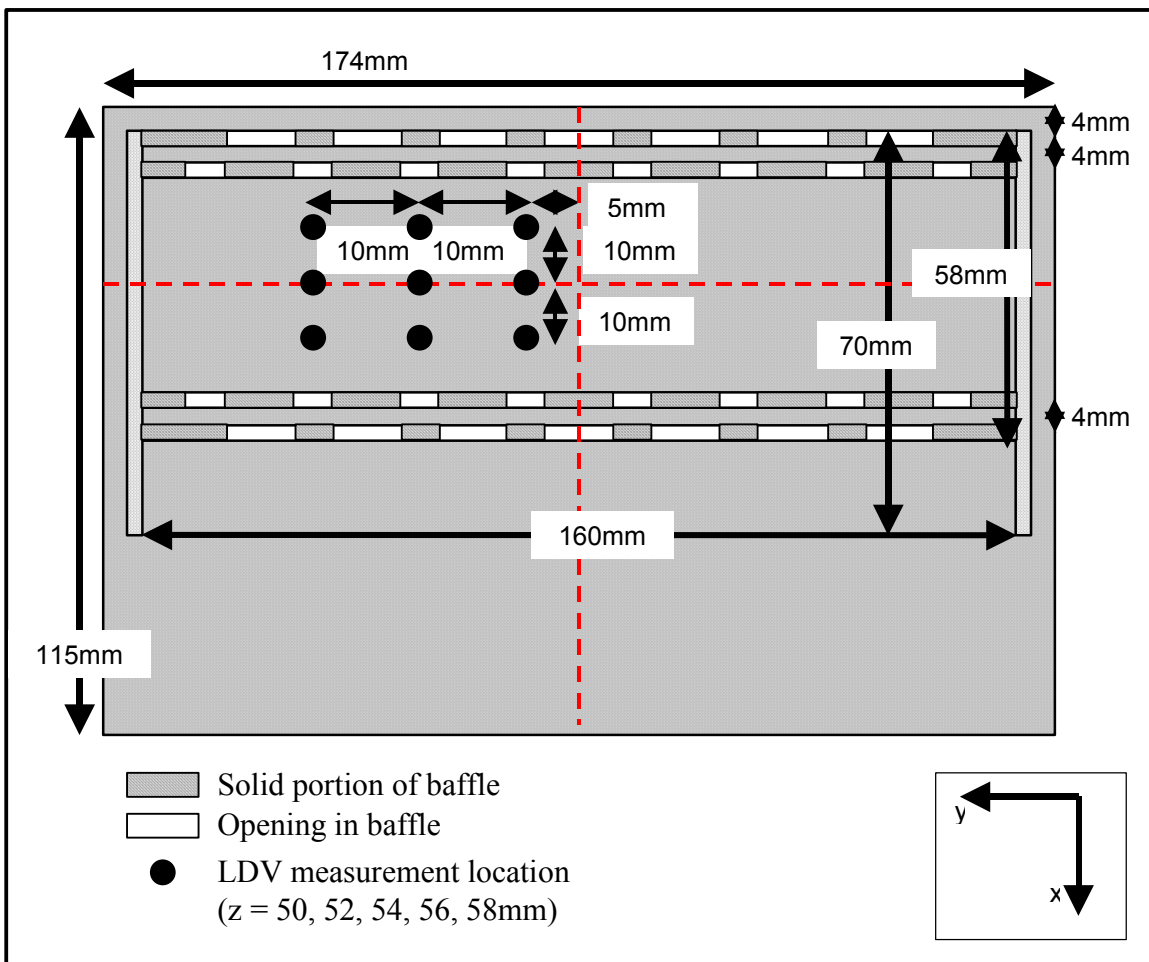
The measurement locations for the height of 54mm below the ceiling represented the approximate mid-point of the height inside the rectangular model detector. This location was used to represent the maximum internal velocity at each of the 9 measurement locations. The data presented in Table 34 includes the mean velocity, standard deviation, and percent turbulence intensity for scenarios with and without the insect screen in place.

<u>Screening Criteria for LDV Data Points</u>

The LDV data was screened to remove anomalous data points. The process began with a qualitative examination of the data. The data for all 45 measurement locations was plotted to show both the number of valid data points (particle counts) as well as mean velocity on the same y-axis. This plotting procedure was used in order to determine if a sufficient number of valid points were collected at a particular measurement location and if the resulting mean velocity value was consistent with the general trend of the data set. Examples of this plotting procedure are shown in Figure 79 and Figure 80.
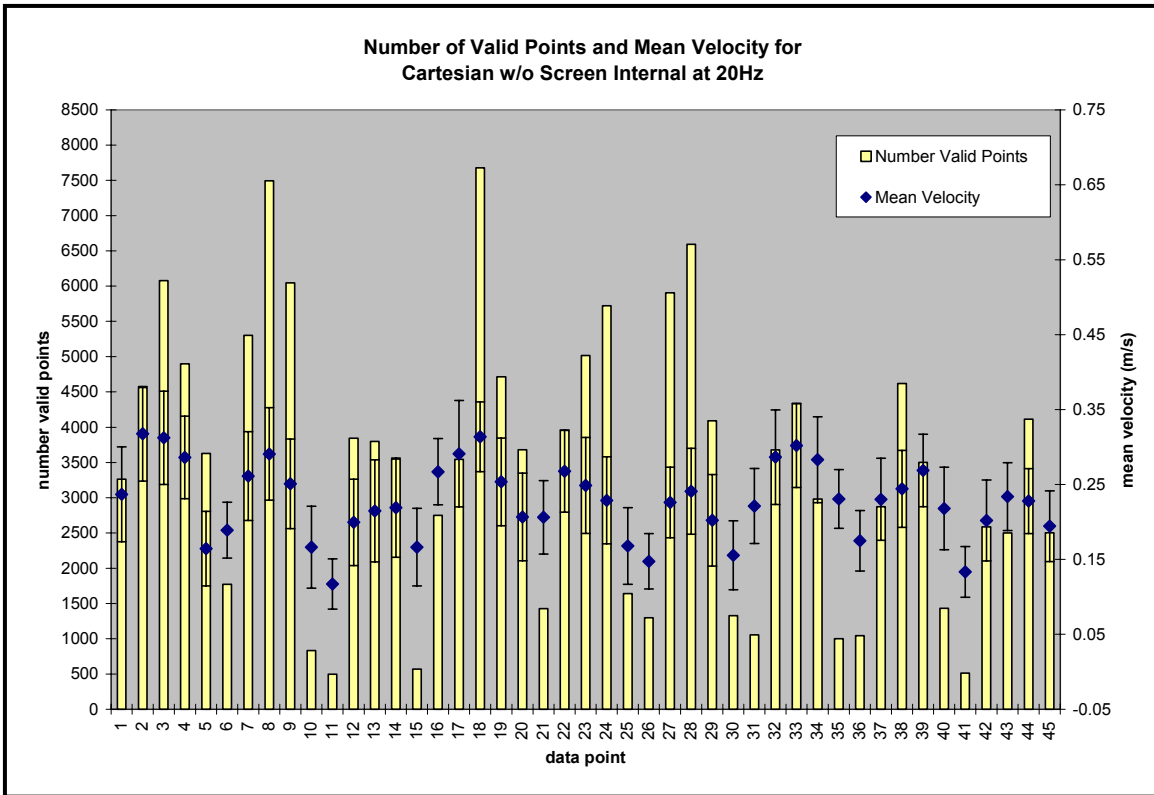
Figure 79 -- Valid points and mean velocity for rectangular model detector without insect screen for 0.52 m/s external flow field.

Figure 1 above is representative of a velocity scan where a sufficient number of data points have been collected (at least 500 valid points in this particular case) and the standard deviation (represented as the y-direction error bars) is consistent at each measurement location. This was typical of most data sets collected for the rectangular model detector with and without the insect screen. This data set would be considered to be internally consistent.
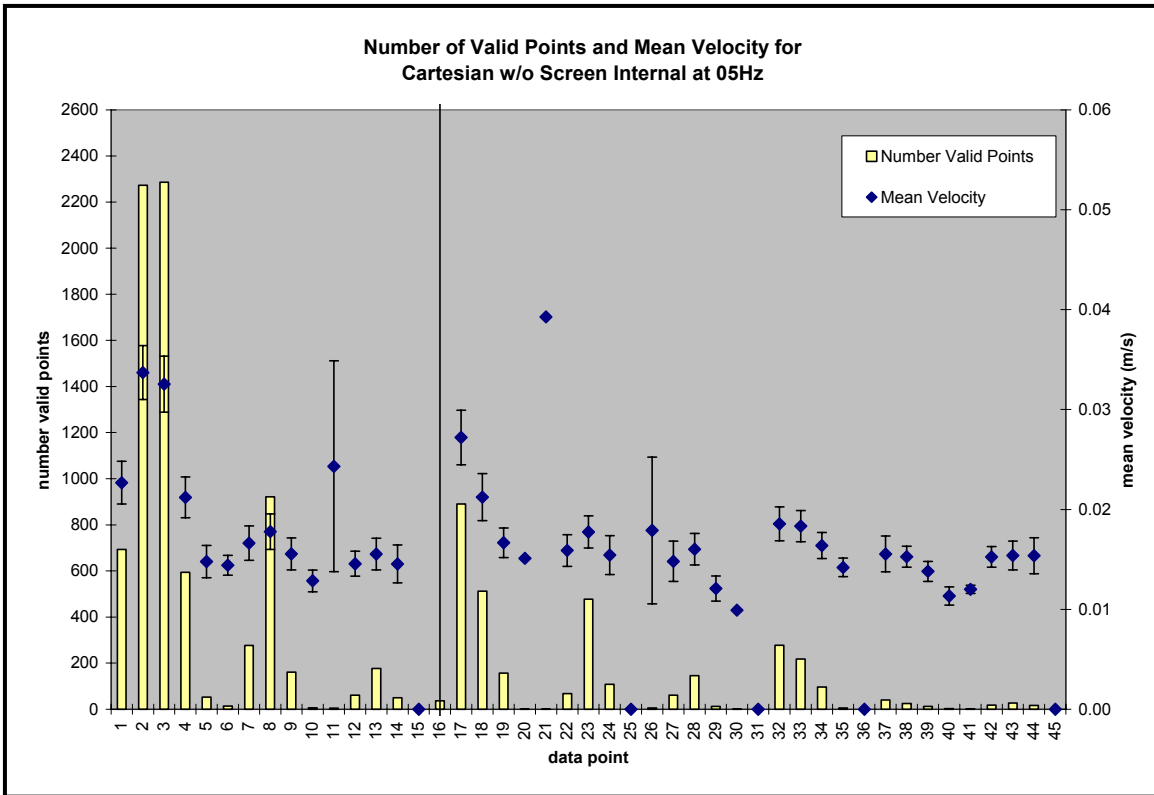
Figure 80 -- Valid data points and mean velocity for rectangular detector without insect screen at 0.11 m/s external flow field.

Figure 2 above is representative of a velocity scan where an insufficient number of data points have been collected at a few isolated locations and the standard deviation at some locations is inconsistent with general trend in the overall data set. This data set would be considered to be internally inconsistent. A qualitative examination of the data sets indicated that some data points were anomalous relative to the majority based on a low number of valid particle counts or a large standard deviation value. Therefore, quantitative screen criteria were developed in order to remove the anomalous data points identified in the qualitative examination in a consistent manner.

The screen criteria developed for the data sets was based on a threshold number of valid data points collected a particular measurement location and maximum turbulence

intensity for a particular measurement location. Both criteria were met in order for a data point to be allowed into the screened data set. The threshold number of valid data points was 10. This was based on the observation that in cases where a physically inconsistent velocity value appeared in the data set (indicated as a value of zero, or a value in excess of the external velocity) there were less than 10 data valid points collected at the particular measurement location. Additionally, anomalous data points were observed at locations where a sufficient number of valid data points were collected but the standard deviation was internally inconsistent with the rest of the data set. Turbulence intensity was used to measure because it is the standard deviation divided by the mean velocity. By using the turbulence intensity percentage, a consistent criterion could be applied over the range of velocity values. An observation of all the data sets collected revealed that the turbulence intensity ranged from approximately 50 to 5% over the entire range of external flow velocities. A turbulence intensity value above 100% was used as the screening criteria to exclude specific data points that were internally inconsistent.

To summarize, the LDV measurement at a given location was considered appropriate if it passed *both* of the following criteria:

- Number of valid collected data points > 10
- Turbulence intensity < 100%

The screened data sets for the rectangular detector are summarized below. The data is presented as time averaged velocity in units of meters per second, one statistical standard deviation, and the percent turbulence intensity.

Table 36 – Screened velocity data for rectangular detector.

Fan (Hz)	FE/DE Time Avg Velocity			Cartesian Detector W/O Screen			Cartesian Detector W/Screen		
	V,ext (m/s)	Std dev	V TI%	V,int	Std dev	V TI%	V,int	Std dev	V TI%
30	0.822	0.048	5.85	0.381	0.108	28.29	0.132	0.018	13.53
25	0.668	0.045	6.71	0.253	0.071	27.93	0.095	0.011	11.45
20	0.520	0.035	6.81	0.267	0.057	21.36	0.067	0.007	11.04
15	0.392	0.028	7.20	0.198	0.035	17.89	0.036	0.003	9.17
12	0.314	0.027	8.70	0.144	0.029	19.90	0.022	0.002	10.29
10	0.264	0.026	9.84	0.094	0.013	13.39	0.014	0.004	25.66
7	0.168	0.027	16.07	0.037	0.002	6.53	0.005	0.003	55.54
5	0.113	0.025	22.07	0.019	0.002	9.26	0.003	0.002	84.31

Photoelectric Detector Velocity Scans

The internal velocity data for the photoelectric detector was screened in the same manner as used for the rectangular model detector. The maximum velocity value from the data set was reported from the midpoint of the at a height of approximately The screened data sets for the photoelectric detector are summarized below. The data is presented as time averaged velocity in units of meters per second, one statistical standard deviation, and the percent turbulence intensity.

Table 37 – Screened velocity data for photo detector.

Fan (Hz)	FE/DE Time Avg Velocity			Photoelectric Detector		
	V,ext (m/s)	Std dev	V TI%	V,int (m/s)	Std dev	V TI%
30	0.822	0.048	5.85	0.149	0.045	30.26
25	0.668	0.045	6.71	0.089	0.019	20.91
20	0.520	0.035	6.81	0.060	0.008	13.04
15	0.392	0.028	7.20	0.030	0.004	11.74
12	0.314	0.027	8.70	0.014	0.002	17.00

Ionization Detector Velocity Scans

Table 38 – Screened velocity data for ionization detector.

Fan (Hz)	FE/DE Time Avg Velocity			Ionization Detector		
	V,ext (m/s)	Std dev	V TI%	V,int (m/s)	Std dev	V TI%
30	0.822	0.048	5.85	0.115	0.027	23.52
25	0.668	0.045	6.71	0.068	0.011	16.14
20	0.520	0.035	6.81	0.020	0.002	8.13
15	0.392	0.028	7.20	0.037	0.006	16.20
12	0.314	0.027	8.70	0.048	0.012	24.05
10	0.264	0.026	9.84	0.056	0.005	9.17
7	0.168	0.027	16.07	0.057	0.006	11.13
5	0.113	0.025	22.07	0.056	0.006	9.94
3	0.077	0.024	31.27	0.061	0.005	7.88

Response Tests

Addressable photoelectric and ionization type detectors were subjected to four different aerosols in NIST's FE/DE. The four aerosol types were vegetable oil droplets produced by both a nebulizer and an atomizer (NIST's Smoke Detector Tester) smoldering cotton wicks and flaming propene soot. Two types of exposures were used. The first was a ramp-type exposure where steady state flow conditions were developed in the FE/DE and then the aerosol was introduced at a constant rate. The ramp-type exposure of aerosol was the result of transition of clean air to a steady state aerosol concentration in the duct. The second exposure was a step type input of aerosol to the detector. For this type of exposure, the detector was isolated from the conditions in the duct by using a cylinder with a small amount of purge air to prevent contamination. Steady state flow and aerosol conditions were established in the duct. After reaching this steady state condition, the isolation cylinder was dropped and the purge air was shut off. This resulted in a nominal step input of aerosol to the detector.

241

Table 39 -- Average time to alarm for ionization detector step exposure tests.

Ionization Detector		Time to alarm (s)	
Aerosol Source	V,ext(m/s)	0.5%/ft	1.0%/ft
Cotton Wick	0.08	29.9	
	0.11		
	0.17	15.2	
	0.26	11.2	
	0.31	8.4	
	0.39	10.8	
	0.52	14.8	
Atomized Oil	0.08	48.3	
	0.11	39.0	
	0.17	26.4	
	0.26	19.9	
	0.31	20.9	
	0.39	9.4	
	0.52		
Propylene	0.08	34.8	
	0.11	25.3	
	0.17	16.3	
	0.26	10.1	
	0.31	7.7	20.7
	0.39	4.3	6.5
	0.52	2.9	5.1
Nebulized Oil	0.08		
	0.11		
	0.17		
	0.26		
	0.31		

Table 40 -- Time to alarm summary for photoelectric detector at worst orientation step exposure tests.

Photoelectric Detector @worst	Time to alarm (s)					
Aerosol Source	V,ext(m/s)	0.2%/ft	0.5%/ft	1.0%/ft	1.5%/ft	2%/ft	2.5%/ft
Cotton Wick	0.08	34.8					
	0.11	25.9					
	0.17	9.1					
	0.26	5.2					
	0.31	3.6					
	0.39	2.7					
	0.52	1.5					
Atomized Oil	0.08	14.2	17.8	21.4	27.2	33.1	39.9
	0.11	9.1	10.8	13.2	17.5	23.8	39.9
	0.17	4.3	5.2	6.7	8.6	10.1	13.2
	0.26	1.4	3.3			4.6	7.7
	0.31	1.4	2.1		2.4	3.1	5.0
	0.39	1.1		2.1	2.2		2.9
	0.52		1.5		1.8	2.9	
Propylene	0.08	15.9	23.1				
	0.11	12.5	17.8				
	0.17	6.0	8.2	17.8			
	0.26	4.6	6.3	15.1			
	0.31	3.6	4.1	6.3	14.7		
	0.39	2.2	2.9	10.8			
	0.52	2.9	10.8				
Nebulized Oil	0.08	24.2	34.1				
	0.11	19.2	27.4				
	0.17	12.2					
	0.26	5.0					
	0.31	4.1					

Table 41 -- Average time to alarm for photoelectric detector rotated 90 degrees step exposure tests.

Photoelectric Detector @90deg	Time to alarm (s)					
	V,ext(m/s)	0.2%/ft	0.5%/ft	1.0%/ft	1.5%/ft	2%/ft	2.5%/ft
Cotton Wick	0.08	20.2					
	0.11	13.9					
	0.17	6.0					
	0.26	3.1					
	0.31	2.6					
	0.39	1.7					
	0.52	1.2					
Atomized Oil	0.08	8.9	10.8	14.7	17.5	20.7	25.2
	0.11	8.6	10.5	12.2	13.7	15.1	16.2
	0.17	5.1	5.8	7.0	8.0	8.9	10.1
	0.26	1.8	2.1				3.6
	0.31				2.1		2.9
	0.39	1.4					2.6
	0.52				1.4	1.7	
Propylene	0.08	16.3	20.9				
	0.11	9.9	12.3				
	0.17	6.0	7.7	13.7			
	0.26	2.9	3.6	15.9			
	0.31	2.4	3.1	6.7			
Nebulized Oil	0.08	20.7	26.2				
	0.11	10.1	21.7				
	0.17	7.5					
	0.26	4.1					
	0.31	3.4					

Appendix C.1: Derivation of Governing Equations

The governing equations for the aerosol entry problem in smoke detectors are derived using the principles of conservation of mass, species, momentum, and energy in three dimensions for Cartesian coordinates.

The following assumptions are made:

- The fluid is non-reacting

- The fluid is isothermal

- The fluid is incompressible

- The fluid is Newtonian

- Aerosol deposition on surfaces is negligible

- The fluid consists of two components; air and aerosol

Nomenclature

A_n area normal to flux

c_v specific heat at constant volume

C_i concentration of species i

dW differential work

dx differential distance

D_A binary diffusion coefficient of species A

E energy

F force

g gravitational acceleration

$\bar{g}$ gravity vector

j diffusive mass flux

k thermal conductivity

$\hat{K}$ kinetic energy

m mass

$\dot{m}_{ti}$ total rate of mass flow in the i direction

n_{ti} total flux in the i direction

p pressure

q heat flux

$\bar{q}$ heat flux vector

Q heat energy

s displacement distance

t time

T temperature

$\hat{U}$ internal energy

v_i velocity component in i direction

$\bar{v}$ velocity vector

$\overline{v}$ mass average (bulk) velocity

v^* molar average (species) velocity

$\dot{V}$ volumetric flow rate

W work

$\dot{W}$ rate of work

Greek letters

Δ differential

μ fluid dynamic viscosity

ρ fluid density

τ_{ij} stress on the *i* face acting in the *j* direction

$\underline{\tau}$ stress tensor

Conservation of Mass

The conservation of mass considers an arbitrary differential volume as shown in Figure 1 below. The rate of accumulation of mass in the differential volume is the result of the net mass flow rate of mass entering and leaving the volume.

$$\sum\nolimits_{in}(\text{rate of mass}) - \sum\nolimits_{out}(\text{rate of mass}) = \text{rate of accumulation}$$

(123)
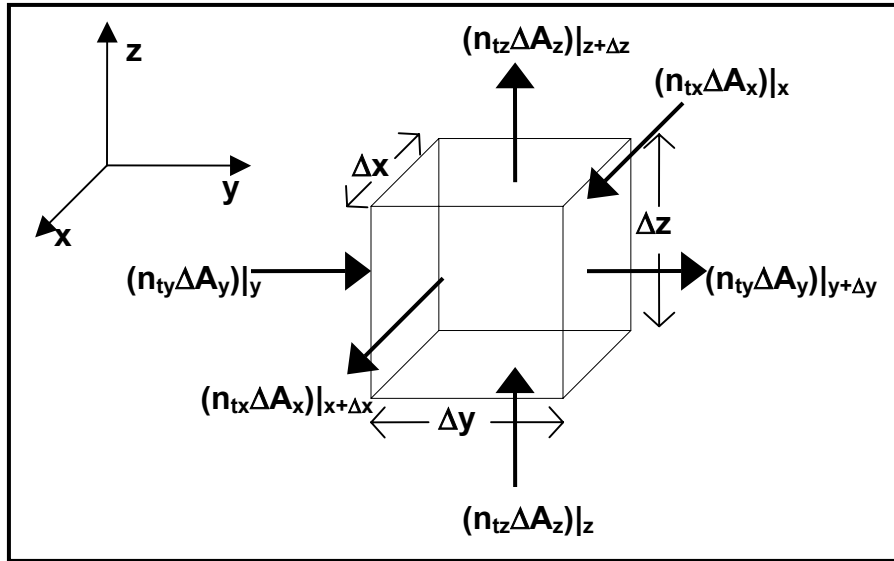
Figure 81 -- Arbitrary volume with fluxes acting on differential areas.

The total rate of mass flowing into or out of the arbitrary volume is defined as the product

of the total mass flux, n_{ti}, and the area normal to the flux, A_n (Fahien, 1983).

$$\dot{m}_{ti} = n_{ti} A_n$$

(124)

The total mass flux in the *i*-direction is defined as the product of the fluid density, ρ, and

the corresponding velocity component, v_i (Fahrien, 1983).

$$n_{ti} \equiv \rho v_i$$

(125)

248

The areas normal to the flux are $\Delta y \Delta z$ for the x-direction, $\Delta x \Delta z$ for the y-direction, and $\Delta x \Delta y$ for the z-direction.

The generation or depletion term ordinarily refers to a chemical reaction that either produces or consumes mass within the differential volume. The fluid has been assumed to be non-reacting, so the generation term is neglected.

The rate of accumulation of mass within the differential volume is defined as

$$\dot{m}_{acc} = \frac{\partial \rho}{\partial t}\left(\Delta x \Delta y \Delta z\right)$$

(126)

Using the definitions provided in Equations 124, 125, and 126 with the stated assumptions of a non-reacting flow with no deposition to surfaces, the general expression in Equation 123 becomes the following.

$$\left[\left(\rho v_x\right)\left(\Delta y \Delta z\right)\right]\Big|_x - \left[\left(\rho v_x\right)\left(\Delta y \Delta z\right)\right]\Big|_{x+\Delta x} + \left[\left(\rho v_y\right)\left(\Delta x \Delta z\right)\right]\Big|_y - \left[\left(\rho v_y\right)\left(\Delta x \Delta z\right)\right]\Big|_{y+\Delta y}$$
$$+ \left[\left(\rho v_z\right)\left(\Delta x \Delta y\right)\right]\Big|_z - \left[\left(\rho v_z\right)\left(\Delta x \Delta y\right)\right]\Big|_{z+\Delta z} = \frac{\partial}{\partial t}\left(\rho \Delta x \Delta y \Delta z\right)$$

(127)

Dividing both sides by the differential volume, $\Delta x \Delta y \Delta z$, yields,

$$\frac{\left[(\rho v_x)\right]\big|_x - \left[(\rho v_x)\right]\big|_{x+\Delta x}}{\Delta x} + \frac{\left[(\rho v_y)\right]\big|_y - \left[(\rho v_y)\right]\big|_{y+\Delta y}}{\Delta y} + \frac{\left[(\rho v_z)\right]\big|_z - \left[(\rho v_z)\right]\big|_{z+\Delta z}}{\Delta z} = \frac{\partial \rho}{\partial t}$$

(128)

The first three terms on the left hand side can be evaluated as the incremental distance, Δx, Δy, and Δz, approach zero using the definition of total derivative from calculus.

$$\lim_{\Delta x \to 0} \frac{f(x)\big|_{x+\Delta x} - f(x)\big|_x}{\Delta x} = \lim_{\Delta x \to 0} \frac{\Delta f}{\Delta x} = \frac{df}{dx}$$

(129)

Using the first term on the left hand side as an example, yields

$$\lim_{x \to 0} \frac{\left[(\rho v_x)\right]\big|_x - \left[(\rho v_x)\right]\big|_{x+\Delta x}}{\Delta x} = -\frac{\partial}{\partial x}(\rho v_x)$$

(130)

The partial derivative is used because the density and velocity component could be functions of all three coordinate directions and time.

Therefore, the conservation of mass equation reduces to

250

$$-\frac{\partial}{\partial x}\left(\rho v_x\right)-\frac{\partial}{\partial y}\left(\rho v_y\right)-\frac{\partial}{\partial z}\left(\rho v_z\right)=\frac{\partial\rho}{\partial t}$$

(131)

The fluid is assumed to be incompressible, or having a constant density. The density will not vary with time and, therefore, the right hand side of Equation 131 becomes zero. Since density is constant and the right hand side is zero, both sides can be divided by zero to yield the final form of conservation of mass for an incompressible fluid.

$$\frac{\partial v_x}{\partial x}+\frac{\partial v_y}{\partial y}+\frac{\partial v_z}{\partial z}=0$$

(132)

Conservation of Species

The fluid is assumed to consist of air and aerosol. The species in a multi-component system may move at different velocities. It is important to define mass-average and molar-average velocities for a multi-component fluid system.

The mass-average velocity of a multi-component fluid is

$$\overline{v}=\frac{\displaystyle\sum_{i=1}^{n}\rho_i\overline{v}_i}{\displaystyle\sum_{i=1}^{n}\rho_i}$$

(133)

251

The molar-average velocity of a multi-component fluid is

$$v^* = \frac{\sum_{i=1}^{n} C_i v_i}{\sum_{i=1}^{n} C_i}$$

(134)

The total mass flux for species A consists of diffusive mass flux and a convective mass flux. For consistency with the conservation of mass equation, the mass average velocity is considered.

$$n_{Ax} = j_{Ax} + \rho_A v_x$$

(135)

The diffusive mass flux can consist of ordinary, thermal, pressure, and forced diffusion fluxes (Fahien, 1983)

$$j_i = j_i^{(x)} + j_i^{(T)} + j_i^{(p)} + j_i^{(F)}$$

(136)

252

In this case only the ordinary diffusion flux will be considered. The reasons for ignoring the other diffusion fluxes are as follows. Thermal diffusion occurs when a temperature gradient is driving mass diffusion. The flow of aerosol is assumed to be isothermal, therefore, diffusion due to temperature gradients can be ignored. The diffusion flux due to pressure is ignored because large pressure gradients are not expected. Pressure diffusion is typically of interest in the study of centrifuges (Mills, 1995). The forced diffusion term pertains to applied electric fields on electrolytes and ionized gases (Mills, 1995) where each ionic species could be subjected to a different force (Fahien, 1983) and is ignored. Gravitational forces are not considered in forced diffusion because the force per unit mass of molecule is constant (Mills, 1995).

Ordinary diffusion is governed by Fick's first law of ordinary diffusion, which is expressed on a mass basis as (Fahien, 1983).

$$j_A = j_A^{(x)} = -D_A \left(\frac{\partial \rho_A}{\partial x} + \frac{\partial \rho_A}{\partial y} + \frac{\partial \rho_A}{\partial z} \right)$$

(137)

The total mass flux for species A for the x-direction is

$$n_{tx,A} = -D_A \left(\frac{\partial \rho_A}{\partial x} \right) + \rho_A v_x$$

(138)

253

The total mass flow of species A is expressed in a general form as

$$\dot{m}_{ti,A} = n_{ti,A} A_n$$

(139)

Using the x-direction as an example, results of Equation 138 can be substituted into the total mass flow for species A shown as in Equation 139 to produce

$$\dot{m}_{tx,A} = \left(-D_A \left(\frac{\partial \rho_A}{\partial x} \right) + \rho_A v_x \right) (\Delta y \Delta z)$$

(140)

The accumulation of species A within the differential volume is

$$\dot{m}_{acc,A} = \frac{\partial \rho_A}{\partial t} (\Delta x \Delta y \Delta z)$$

(141)

Substituting the known terms for species yields

$$
\left[\left(-D_A \left(\frac{\partial \rho_A}{\partial x} \right) + \rho_A v_x \right) (\Delta y \Delta z) \right]_x - \left[\left(-D_A \left(\frac{\partial \rho_A}{\partial x} \right) + \rho_A v_x \right) (\Delta y \Delta z) \right]_{x+\Delta x}
$$
$$
+ \left[\left(-D_A \left(\frac{\partial \rho_A}{\partial y} \right) + \rho_A v_y \right) (\Delta x \Delta z) \right]_y - \left[\left(-D_A \left(\frac{\partial \rho_A}{\partial y} \right) + \rho_A v_y \right) (\Delta x \Delta z) \right]_{y+\Delta y}
$$
$$
+ \left[\left(-D_A \left(\frac{\partial \rho_A}{\partial z} \right) + \rho_A v_z \right) (\Delta x \Delta y) \right]_z - \left[\left(-D_A \left(\frac{\partial \rho_A}{\partial z} \right) + \rho_A v_z \right) (\Delta x \Delta y) \right]_{z+\Delta z} = \frac{\partial \rho_A}{\partial t} (\Delta x \Delta y \Delta z)
$$

(142)

Dividing both sides by the differential volume, $\Delta x \Delta y \Delta z$, and taking the limit as the incremental distances, Δx, Δy, and Δz approach zero becomes

$$D_A\left(\frac{\partial^2 \rho_A}{\partial x^2}\right) - \frac{\partial \rho_A v_x}{\partial x} + D_A\left(\frac{\partial^2 \rho_A}{\partial y^2}\right) - \frac{\partial \rho_A v_y}{\partial y} + D_A\left(\frac{\partial^2 \rho_A}{\partial z^2}\right) - \frac{\partial \rho_A v_z}{\partial z} = \frac{\partial \rho_A}{\partial t}$$

(143)

Grouping like terms simplifies into the following form

$$D_A\left(\frac{\partial^2 \rho_A}{\partial x^2} + \frac{\partial^2 \rho_A}{\partial y^2} + \frac{\partial^2 \rho_A}{\partial z^2}\right) - \left(\frac{\partial \rho_A v_x}{\partial x} + \frac{\partial \rho_A v_y}{\partial y} + \frac{\partial \rho_A v_z}{\partial z}\right) = \frac{\partial \rho_A}{\partial t}$$

(144)

The chain rule of calculus is applied to the second group of terms on the left hand side and leads to the following.

$$D_A\left(\frac{\partial^2 \rho_A}{\partial x^2} + \frac{\partial^2 \rho_A}{\partial y^2} + \frac{\partial^2 \rho_A}{\partial z^2}\right) - \left(\rho_A\left(\frac{\partial v_x}{\partial x} + \frac{\partial v_y}{\partial y} + \frac{\partial v_z}{\partial z}\right) + v_x\frac{\partial \rho_A}{\partial x} + v_y\frac{\partial \rho_A}{\partial y} + v_z\frac{\partial \rho_A}{\partial z}\right) = \frac{\partial \rho_A}{\partial t}$$

(145)

Using the conservation of mass result for an incompressible fluid, as shown in Equation 132, reduces Equation 145 to the final form.

255

$$D_A \left(\frac{\partial^2 \rho_A}{\partial x^2} + \frac{\partial^2 \rho_A}{\partial y^2} + \frac{\partial^2 \rho_A}{\partial z^2} \right) - \left(v_x \frac{\partial \rho_A}{\partial x} + v_y \frac{\partial \rho_A}{\partial y} + v_z \frac{\partial \rho_A}{\partial z} \right) = \frac{\partial \rho_A}{\partial t}$$

(146)

Where the velocity is the mass average, or bulk, velocity.

Conservation of Momentum

Momentum is defined as the product of mass and the bulk velocity in the following manner

$$\text{momentum} \equiv mv$$

(147)

The net rate of momentum in and out of the differential element plus body forces acting on the element is equal to the rate of accumulation of momentum.

$$\sum_{in} \left(\begin{array}{c} \text{rate of} \\ \text{momentum} \end{array} \right) - \sum_{out} \left(\begin{array}{c} \text{rate of} \\ \text{momentum} \end{array} \right) + \left\{ \text{body forces} \right\} = \left\{ \begin{array}{c} \text{rate of momentum} \\ \text{accumulation} \end{array} \right\}$$

(148)

The time rate of change of momentum can be expressed as

$$\frac{d}{dt}(mv)$$

<div align="right">(149)</div>

Which has units of force, as shown below

$$\frac{d}{dt}(mv) = \left[\frac{1}{s}\right][kg]\left[\frac{m}{s}\right] = \left[\frac{kg \cdot m}{s^2}\right] = [N]$$

<div align="right">(150)</div>

The time rate of change of momentum due to convective motion of the fluid can be expressed as the product of the volumetric flow rate (volume/time) and the momentum per volume (momentum/volume) which has units of (momentum/time). The two terms are described below.

The volumetric flow through each face of the element can be expressed as the product of velocity and the area normal to the flow

$$\dot{V}_i = v_i A_n = \left[\frac{m}{s}\right][m^2] = \left[\frac{m^3}{s}\right]$$

<div align="right">(151)</div>

<div align="center">257</div>

The momentum per volume, with units of *(kg-m)/(m³-s)*, is the product of the fluid density and velocity

$$\rho v_i = \left[\frac{kg}{m^3}\right]\left[\frac{m}{s}\right]$$

(152)

The net rate of convective momentum in the x-direction can be expressed as

$$\sum_{in,x}\left(\begin{array}{c}\text{rate of}\\\text{momentum}\end{array}\right) - \sum_{out,x}\left(\begin{array}{c}\text{rate of}\\\text{momentum}\end{array}\right) = \left[\left(v_x \Delta y \Delta z\right)\left(\rho v_x\right)\right]\Big|_x - \left[\left(v_x \Delta y \Delta z\right)\left(\rho v_x\right)\right]\Big|_{x+\Delta x}$$

(153)

The above expression applies to the y and z-directions in a similar manner.

The body forces influencing momentum are pressure and gravitational forces. The pressure force acts on an area normal to the coordinate direction of interest. Therefore, in the net rate of momentum by pressure in the x-direction is

$$\sum_{net,x} F_p = \left[p \Delta y \Delta z\right]\Big|_x - \left[p \Delta y \Delta z\right]\Big|_{x+\Delta x}$$

(154)

258

The gravitational force acts on the entire differential volume and is expressed in the x-direction as

$$F_g = \rho g_x \Delta x \Delta y \Delta z$$

(155)

The surface forces arising from viscous shear stresses are considered. The net effect of shear stresses on the differential volume in the x-direction is

$$\sum_{net,x} F_{shear} = \left[\tau_{yx} \Delta x \Delta z \right]\Big|_y - \left[\tau_{yx} \Delta x \Delta z \right]\Big|_{y+\Delta y} + \left[\tau_{zx} \Delta x \Delta y \right]\Big|_z - \left[\tau_{zx} \Delta x \Delta y \right]\Big|_{z+\Delta z}$$
$$+ \left[\tau_{xx} \Delta x \Delta y \right]\Big|_x - \left[\tau_{xx} \Delta x \Delta y \right]\Big|_{x+\Delta x}$$

(156)

The rate of accumulation of momentum in the x-direction within the elemental volume is defined as

$$\frac{\partial}{\partial t}(mv)_{acc,x} = \frac{\partial}{\partial t}\left[\left(\Delta x \Delta y \Delta z \right)\left(\rho v_x \right) \right]$$

(157)

Combining the individual terms for the x-direction yields

259

$$\left[(v_x\Delta y\Delta z)(\rho v_x)\right]\Big|_x - \left[(v_x\Delta y\Delta z)(\rho v_x)\right]\Big|_{x+\Delta x} + \left[p\Delta y\Delta z\right]\Big|_x - \left[p\Delta y\Delta z\right]\Big|_{x+\Delta x}$$

$$+\rho g_x\Delta x\Delta y\Delta z + \left[\tau_{yx}\Delta x\Delta z\right]\Big|_y - \left[\tau_{yx}\Delta x\Delta z\right]\Big|_{y+\Delta y} + \left[\tau_{zx}\Delta x\Delta y\right]\Big|_z - \left[\tau_{zx}\Delta x\Delta y\right]\Big|_{z+\Delta z}$$

$$+\left[\tau_{xx}\Delta x\Delta y\right]\Big|_x - \left[\tau_{xx}\Delta x\Delta y\right]\Big|_{x+\Delta x} = \frac{\partial}{\partial t}\left[(\Delta x\Delta y\Delta z)(\rho v_x)\right]$$

(158)

Dividing both sides by the differential volume, $\Delta x\Delta y\Delta z$, and taking the limit as the incremental distances, Δx, Δy, and Δz approach zero becomes, in the x-direction

$$-\left(\frac{\partial}{\partial x}(\rho v_x v_x) + \frac{\partial}{\partial y}(\rho v_y v_x) + \frac{\partial}{\partial z}(\rho v_z v_x)\right) - \frac{\partial p}{\partial x} + \rho g_x - \left(\frac{\partial}{\partial x}\tau_{xx} + \frac{\partial}{\partial y}\tau_{yx} + \frac{\partial}{\partial z}\tau_{zx}\right) = \frac{\partial}{\partial t}(\rho v_x)$$

(159)

The result above is similar for the y and z directions. Assuming a Newtonian fluid, the shear stress - shear rate components are defined as (Hershey, 1973)

$$\tau_{xx} = -\mu\left[2\frac{\partial v_x}{\partial x} - \frac{2}{3}\left(\frac{\partial v_x}{\partial x} + \frac{\partial v_y}{\partial y} + \frac{\partial v_z}{\partial z}\right)\right]$$

(160a)

$$\tau_{yy} = -\mu\left[2\frac{\partial v_y}{\partial y} - \frac{2}{3}\left(\frac{\partial v_x}{\partial x} + \frac{\partial v_y}{\partial y} + \frac{\partial v_z}{\partial z}\right)\right]$$

(160b)

$$\tau_{zz} = -\mu \left[2\frac{\partial v_z}{\partial z} - \frac{2}{3}\left(\frac{\partial v_x}{\partial x} + \frac{\partial v_y}{\partial y} + \frac{\partial v_z}{\partial z} \right) \right]$$

<div align="right">(160c)</div>

$$\tau_{yz} = \tau_{zy} = -\mu \left[\frac{\partial v_y}{\partial z} + \frac{\partial v_z}{\partial y} \right]$$

<div align="right">(160d)</div>

$$\tau_{xy} = \tau_{yx} = -\mu \left[\frac{\partial v_x}{\partial y} + \frac{\partial v_y}{\partial x} \right]$$

<div align="right">(160e)</div>

$$\tau_{zx} = \tau_{xz} = -\mu \left[\frac{\partial v_z}{\partial x} + \frac{\partial v_x}{\partial z} \right]$$

<div align="right">(160f)</div>

The normal stress components are simplified in the following manner by recalling the definition of conservation of mass for an incompressible fluid as shown in Equation 132

$$\tau_{xx} = -\mu \left[2\frac{\partial v_x}{\partial x} \right]$$

<div align="right">(161a)</div>

$$\tau_{yy} = -\mu \left[2 \frac{\partial v_y}{\partial y} \right]$$

<div align="right">(161b)</div>

$$\tau_{zz} = -\mu \left[2 \frac{\partial v_z}{\partial z} \right]$$

<div align="right">(161c)</div>

Again, using the x-direction as an example, the appropriate shear stress- shear rate components (Equations 160d-f and 161a-c) are substituted into Equation 159. The shear stress term is worked out for clarity in the steps that follow.

$$\frac{\partial}{\partial x}\tau_{xx} + \frac{\partial}{\partial y}\tau_{yx} + \frac{\partial}{\partial z}\tau_{zx} = \frac{\partial}{\partial x}\left(-\mu\left[2\frac{\partial v_x}{\partial x}\right]\right) + \frac{\partial}{\partial y}\left(-\mu\left[\frac{\partial v_x}{\partial y} + \frac{\partial v_y}{\partial x}\right]\right) + \frac{\partial}{\partial z}\left(-\mu\left[\frac{\partial v_z}{\partial x} + \frac{\partial v_x}{\partial z}\right]\right)$$

<div align="right">(162)</div>

Performing the partial differentiation of each term yields

$$= \left(-\mu\left[2\frac{\partial^2 v_x}{\partial x^2}\right]\right) + \left(-\mu\left[\frac{\partial^2 v_x}{\partial y^2} + \frac{\partial^2 v_y}{\partial x\partial y}\right]\right) + \left(-\mu\left[\frac{\partial^2 v_z}{\partial x\partial z} + \frac{\partial^2 v_x}{\partial z^2}\right]\right)$$

<div align="right">(163)</div>

Combining like terms produces the following expression

<div align="center">262</div>

$$= \left(-\mu \left[2\frac{\partial^2 v_x}{\partial x^2} + \frac{\partial^2 v_y}{\partial x \partial y} + \frac{\partial^2 v_z}{\partial x \partial z} + \frac{\partial^2 v_x}{\partial y^2} + \frac{\partial^2 v_x}{\partial z^2} \right] \right)$$

(164)

The above expression can be expanded in the following manner by breaking down the first second order term.

$$= \left(-\mu \left[\left(\frac{\partial}{\partial x}\left(\frac{\partial v_x}{\partial x} + \frac{\partial v_y}{\partial y} + \frac{\partial v_z}{\partial z} \right) \right) + \frac{\partial^2 v_x}{\partial x^2} + \frac{\partial^2 v_x}{\partial y^2} + \frac{\partial^2 v_x}{\partial z^2} \right] \right)$$

(165)

Recalling the conservation of mass for an incompressible fluid from Equation 132 results in

$$= \left(-\mu \left[\left(\frac{\partial}{\partial x}(0) \right) + \frac{\partial^2 v_x}{\partial x^2} + \frac{\partial^2 v_x}{\partial y^2} + \frac{\partial^2 v_x}{\partial z^2} \right] \right) = -\mu \left[\frac{\partial^2 v_x}{\partial x^2} + \frac{\partial^2 v_x}{\partial y^2} + \frac{\partial^2 v_x}{\partial z^2} \right]$$

(166)

The simplified shear stress term shown above can be substituted into Equation 159 to yield the following for conservation of momentum in the x-direction

$$-\rho \left(\frac{\partial}{\partial x}(v_x v_x) + \frac{\partial}{\partial y}(v_y v_x) + \frac{\partial}{\partial z}(v_z v_x) \right) - \frac{\partial p}{\partial x} + \rho g_x + \mu \left[\frac{\partial^2 v_x}{\partial x^2} + \frac{\partial^2 v_x}{\partial y^2} + \frac{\partial^2 v_x}{\partial z^2} \right] = \frac{\partial}{\partial t}(\rho v_x)$$

(167a)

The conservation of momentum equations in the y and z directions are

$$-\rho\left(\frac{\partial}{\partial x}\left(v_x v_y\right)+\frac{\partial}{\partial y}\left(v_y v_y\right)+\frac{\partial}{\partial z}\left(v_z v_y\right)\right)-\frac{\partial p}{\partial y}+\rho g_y+\mu\left[\frac{\partial^2 v_y}{\partial x^2}+\frac{\partial^2 v_y}{\partial y^2}+\frac{\partial^2 v_y}{\partial z^2}\right]=\frac{\partial}{\partial t}\left(\rho v_y\right)$$

$$(167b)$$

$$-\rho\left(\frac{\partial}{\partial x}\left(v_x v_z\right)+\frac{\partial}{\partial y}\left(v_y v_z\right)+\frac{\partial}{\partial z}\left(v_z v_z\right)\right)-\frac{\partial p}{\partial z}+\rho g_z+\mu\left[\frac{\partial^2 v_z}{\partial x^2}+\frac{\partial^2 v_z}{\partial y^2}+\frac{\partial^2 v_z}{\partial z^2}\right]=\frac{\partial}{\partial t}\left(\rho v_z\right)$$

$$(167c)$$

The left hand side terms for Equations 167a-c can be simplified by first using the chain rule of calculus to expand the velocity terms and then apply the conservation of mass equation when appropriate. The density is neglected for clarity as the velocity terms are simplified. It will be included when the final simplified result is obtained.

The expansion of the velocity terms for the x, y, and z directions using the chain rule is carried out in the following manner.

$$\left(\frac{\partial}{\partial x}\left(v_x v_x\right)+\frac{\partial}{\partial y}\left(v_y v_x\right)+\frac{\partial}{\partial z}\left(v_z v_x\right)\right)=v_x\frac{\partial v_x}{\partial x}+v_x\frac{\partial v_x}{\partial x}+v_y\frac{\partial v_x}{\partial y}+v_x\frac{\partial v_y}{\partial y}+v_z\frac{\partial v_x}{\partial z}+v_x\frac{\partial v_z}{\partial z}$$

$$(168)$$

Combining like terms connected with the x-component of velocity reveals that the conservation of mass for an incompressible fluid can be applied to eliminate that term, as shown below.

$$v_x \left(\frac{\partial v_x}{\partial x} + \frac{\partial v_y}{\partial y} + \frac{\partial v_z}{\partial z} \right) + v_x \frac{\partial v_x}{\partial x} + v_y \frac{\partial v_x}{\partial y} + v_z \frac{\partial v_x}{\partial z} = v_x (0) + v_x \frac{\partial v_x}{\partial x} + v_y \frac{\partial v_x}{\partial y} + v_z \frac{\partial v_x}{\partial z}$$

(169)

The expansion of the velocity terms for the y direction is

$$\left(\frac{\partial}{\partial x}(v_x v_y) + \frac{\partial}{\partial y}(v_y v_y) + \frac{\partial}{\partial z}(v_z v_y) \right) = v_x \frac{\partial v_y}{\partial x} + v_y \frac{\partial v_x}{\partial x} + v_y \frac{\partial v_y}{\partial y} + v_y \frac{\partial v_y}{\partial y} + v_z \frac{\partial v_y}{\partial z} + v_y \frac{\partial v_z}{\partial z}$$

(170)

Combining like terms associated with the y-component of velocity and applying the conservation of mass for an incompressible fluid yields

$$v_y \left(\frac{\partial v_x}{\partial x} + \frac{\partial v_y}{\partial y} + \frac{\partial v_z}{\partial z} \right) + v_x \frac{\partial v_y}{\partial x} + v_y \frac{\partial v_y}{\partial y} + v_z \frac{\partial v_y}{\partial z} = v_y (0) + v_x \frac{\partial v_y}{\partial x} + v_y \frac{\partial v_y}{\partial y} + v_z \frac{\partial v_y}{\partial z}$$

(171)

Expanding the velocity terms associated with the z-direction yields

$$\left(\frac{\partial}{\partial x}\left(v_x v_z\right) + \frac{\partial}{\partial y}\left(v_y v_z\right) + \frac{\partial}{\partial z}\left(v_z v_z\right) \right) = v_x \frac{\partial v_z}{\partial x} + v_z \frac{\partial v_x}{\partial x} + v_y \frac{\partial v_z}{\partial y} + v_z \frac{\partial v_y}{\partial y} + v_z \frac{\partial v_z}{\partial z} + v_y \frac{\partial v_z}{\partial z}$$

(172)

Combining like terms associated with the z-component of velocity and applying the conservation of mass for an incompressible fluid yields

$$v_z \left(\frac{\partial v_x}{\partial x} + \frac{\partial v_y}{\partial y} + \frac{\partial v_z}{\partial z} \right) + v_x \frac{\partial v_z}{\partial x} + v_y \frac{\partial v_z}{\partial y} + v_z \frac{\partial v_z}{\partial z} = v_z \left(0\right) + v_x \frac{\partial v_z}{\partial x} + v_y \frac{\partial v_z}{\partial y} + v_z \frac{\partial v_z}{\partial z}$$

(173)

The above results can be combined with the density and summarized using vector notation

$$\rho \left[v_x \left(\frac{\partial v_x}{\partial x} + \frac{\partial v_y}{\partial x} + \frac{\partial v_z}{\partial x} \right) + v_y \left(\frac{\partial v_x}{\partial y} + \frac{\partial v_y}{\partial y} + \frac{\partial v_z}{\partial y} \right) + v_z \left(\frac{\partial v_x}{\partial z} + \frac{\partial v_y}{\partial z} + \frac{\partial v_z}{\partial z} \right) \right] = \rho \left(\vec{v} \cdot \nabla \vec{v} \right)$$

(174)

The pressure terms for all three coordinate directions can be expressed in vector notation as

$$\frac{\partial p}{\partial x} + \frac{\partial p}{\partial y} + \frac{\partial p}{\partial z} = \nabla p$$

(175)

The gravitational terms become

$$\rho\left(g_x + g_y + g_z\right) = \rho\bar{g}$$

(176)

The shear stress terms can be grouped in the following manner

$$\frac{\partial^2 v_x}{\partial x^2} + \frac{\partial^2 v_x}{\partial y^2} + \frac{\partial^2 v_x}{\partial z^2} + \frac{\partial^2 v_y}{\partial x^2} + \frac{\partial^2 v_y}{\partial y^2} + \frac{\partial^2 v_y}{\partial z^2} + \frac{\partial^2 v_z}{\partial x^2} + \frac{\partial^2 v_z}{\partial y^2} + \frac{\partial^2 v_z}{\partial z^2}$$

(177)

Which can be expressed in vector notation as (Fahien, 1983)

$$\nabla \cdot \underline{\tau}$$

(178)

The accumulation terms are combined and are written in vector notation as

$$\rho\left(\frac{\partial v_x}{\partial t} + \frac{\partial v_y}{\partial t} + \frac{\partial v_y}{\partial t}\right) = \rho\frac{\partial \bar{v}}{\partial t}$$

(179)

267

The simplified terms of the conservation of momentum for an incompressible Newtonian fluid as shown in Equations 174, 175, 176, 177, and 179 can be expressed in Cartesian coordinates as

$$-\rho\left[v_x\left(\frac{\partial v_x}{\partial x}+\frac{\partial v_y}{\partial x}+\frac{\partial v_z}{\partial x}\right)+v_y\left(\frac{\partial v_x}{\partial y}+\frac{\partial v_y}{\partial y}+\frac{\partial v_z}{\partial y}\right)+v_z\left(\frac{\partial v_x}{\partial z}+\frac{\partial v_y}{\partial z}+\frac{\partial v_z}{\partial z}\right)\right]-\left(\frac{\partial p}{\partial x}+\frac{\partial p}{\partial y}+\frac{\partial p}{\partial z}\right)+\rho\left(g_x+g_y+g_z\right)$$
$$+\mu\left(\frac{\partial^2 v_x}{\partial x^2}+\frac{\partial^2 v_x}{\partial y^2}+\frac{\partial^2 v_x}{\partial z^2}+\frac{\partial^2 v_y}{\partial x^2}+\frac{\partial^2 v_y}{\partial y^2}+\frac{\partial^2 v_y}{\partial z^2}+\frac{\partial^2 v_z}{\partial x^2}+\frac{\partial^2 v_z}{\partial y^2}+\frac{\partial^2 v_z}{\partial z^2}\right)=\rho\left(\frac{\partial v_x}{\partial t}+\frac{\partial v_y}{\partial t}+\frac{\partial v_z}{\partial t}\right)$$

(180)

Or in vector notation as

$$-\rho\left(\bar{v}\cdot\nabla\bar{v}\right)-\nabla p+\rho\bar{g}+\nabla\cdot\underline{\tau}=\rho\frac{\partial\bar{v}}{\partial t}$$

(181)

The velocity terms can be combined and expressed in terms of the substantial derivative, which is defined for an arbitrary quantity, ϕ, as (Whitaker, 1977).

$$\frac{D\phi}{Dt}=\frac{\partial\phi}{\partial t}+v_x\frac{\partial\phi}{\partial x}+v_y\frac{\partial\phi}{\partial y}+v_z\frac{\partial\phi}{\partial z}$$

(182)

Or in vector notation as

268

$$\frac{D\phi}{Dt} = \frac{\partial\phi}{\partial t} + \left(\vec{v}\cdot\nabla\phi\right)$$

<div align="right">(183)</div>

In this case the quantity is the velocity vector

$$\rho\frac{\partial\vec{v}}{\partial t} + \rho\left(\vec{v}\cdot\nabla\vec{v}\right) = -\nabla p + \rho\vec{g} + \nabla\cdot\underline{\tau}$$

<div align="right">(184)</div>

Therefore, the final result in vector notation is

$$\boxed{\rho\frac{D\vec{v}}{Dt} = -\nabla p + \rho\vec{g} + \nabla\cdot\underline{\tau}}$$

<div align="right">(185)</div>

The velocity in Equations 180 and 185 is the mass average, or bulk, velocity.

Conservation of Energy

The conservation of energy equation is based on the first law of thermodynamics which can be stated in words as (Fahien, 1983)

$$
\begin{pmatrix}
\text{rate of change} \\
\text{of internal and} \\
\text{kinetic energy} \\
\text{of system}
\end{pmatrix}
=
\begin{pmatrix}
\text{net rate of entry of} \\
\text{internal and kinetic} \\
\text{energy into system by} \\
\text{bulk flow and diffusion}
\end{pmatrix}
+
\begin{pmatrix}
\text{rate of work} \\
\text{being done by} \\
\text{surroundings} \\
\text{on system}
\end{pmatrix}
+
\begin{pmatrix}
\text{rate of production of} \\
\text{thermal energy within} \\
\text{system due to transformation} \\
\text{from other forms of energy}
\end{pmatrix}
$$

(186)

The accumulation rate of internal and kinetic energy in the differential volume is

$$
\frac{\Delta\left[\rho\left(\hat{U} + \hat{K}\right)\Delta x \Delta y \Delta z \right]}{\Delta t}
$$

(187)

Where $\hat{U}$ is the internal energy per unit mass and $\hat{K}$ is the kinetic energy per unit mass which can be defined as (Fahien, 1983)

$$
\hat{K} \equiv \frac{1}{2}v^2
$$

(188)

It is instructive to define the rate of work by recalling the definition of work by a constant force F moving an object a distance s as being

$$
W = Fs
$$

(189)

270

The differential work done by a force in the x-direction to move an object a distance dx is

$$dW = F_x dx$$

(190)

The rate of work being done is therefore defined in the following manner

$$\dot{W} = \frac{dW}{dt} = F_x \frac{dx}{dt}$$

(191)

The term dx/dt is the bulk velocity component in the x-direction. For a force acting on the differential volume the rate of work done is

$$\Delta \dot{W} = \Delta F_x v_x$$

(192)

The gravitational body force can be expressed as

$$\Delta F_{gx} = \rho g_x \left(\Delta x \Delta y \Delta z \right)$$

(193)

The corresponding rate of work done by gravitational forces in the three coordinate directions is

$$\Delta \dot{W}_g = \Delta F_{gx} v_x + \Delta F_{gy} v_y + \Delta F_{gy} v_y = \rho \left(g_x v_x + g_y v_y + g_z v_z \right) \left(\Delta x \Delta y \Delta z \right)$$

(194)

The surface force of pressure in the x-direction evaluated at x can be expressed as

$$\Delta F_{px} \big|_x = \left[P \Delta A_x \right]_x = \left[P \Delta y \Delta z \right]_x$$

(195)

The corresponding rate of work due to pressure surface forces in the x-direction evaluated at x is

$$\Delta \dot{W}_{px} \big|_x = \left[P \left(\Delta y \Delta z \right) v_x \right]_x$$

(196)

The force from viscous forces in the x-direction evaluated at x is

$$\Delta F_{vx} = \left[\left(\tau_{xx} + \tau_{xy} + \tau_{xz} \right) \left(\Delta y \Delta z \right) \right]_x$$

(197)

The corresponding rate of work due to viscous forces in the x-direction evaluated at x is

$$\Delta \dot{W}_{vx} = \left[\left(\tau_{xx} v_x + \tau_{xy} v_y + \tau_{xz} v_z \right) \left(\Delta y \Delta z \right) \right]\Big|_x$$

(198)

The diffusion of heat in the x-direction evaluated at x is

$$Q_{dx} = \left[q_x \left(\Delta y \Delta z \right) \right]\Big|_x$$

(199)

The bulk flow of internal and kinetic energy evaluated at x is

$$E_{bx} = \left[\rho \left(\hat{U} + \hat{K} \right) \left(\Delta y \Delta z \right) v_x \right]\Big|_x$$

(200)

Internal heat generation is ignored because the flow is assumed to be non-reacting. Therefore, combining the various rate of work and energy terms from above in accordance with general expression of the conservation of energy, dividing both sides by the differential volume $\Delta x \Delta y \Delta z$ and taking the limit as the incremental distances approach zero yields the following result

273

$$\frac{\partial\left[\rho\left(\hat{U}+\hat{K}\right)\right]}{\partial t} = \rho\left(g_x v_x + g_y v_y + g_z v_z\right) - \frac{\partial\left(Pv_x\right)}{\partial x} - \frac{\partial\left(Pv_y\right)}{\partial y} - \frac{\partial\left(Pv_z\right)}{\partial z}$$

$$-\frac{\partial}{\partial x}\left(\tau_{xx}v_x + \tau_{xy}v_y + \tau_{xz}v_z\right) - \frac{\partial}{\partial y}\left(\tau_{yx}v_x + \tau_{yy}v_y + \tau_{yz}v_z\right) - \frac{\partial}{\partial z}\left(\tau_{zx}v_x + \tau_{zy}v_y + \tau_{zz}v_z\right)$$

$$-\frac{\partial\left[\rho\left(\hat{U}+\hat{K}\right)v_x\right]}{\partial x} - \frac{\partial\left[\rho\left(\hat{U}+\hat{K}\right)v_y\right]}{\partial y} - \frac{\partial\left[\rho\left(\hat{U}+\hat{K}\right)v_z\right]}{\partial z} - \frac{\partial q_x}{\partial x} - \frac{\partial q_y}{\partial y} - \frac{\partial q_z}{\partial z}$$

$$(201)$$

Which can be expressed in vector notation as

$$\frac{\partial\left[\rho\left(\hat{U}+\hat{K}\right)\right]}{\partial t} = \rho\bar{g}\cdot\bar{v} - \nabla\cdot p\bar{v} - \nabla\cdot\underline{\tau}\cdot\bar{v} - \nabla\cdot\left[\rho\left(\hat{U}+\hat{K}\right)\bar{v}\right] - \nabla\cdot\bar{q}$$

$$(202)$$

By arranging the two internal and kinetic energy terms and recalling the definition of the substantial derivative from Equation 182 yields

$$\rho\frac{D\left(\hat{U}+\hat{K}\right)}{Dt} = \rho\bar{g}\cdot\bar{v} - \nabla\cdot p\bar{v} - \nabla\cdot\underline{\tau}\cdot\bar{v} - \nabla\cdot\bar{q}$$

$$(203)$$

The total energy equation consists of internal and kinetic energy terms. It is helpful to eliminate the kinetic energy term in order to focus on the internal energy portion from the total energy equation. In this development the substantial derivate is used.

The kinetic energy portion of the total energy equation can be evaluated in terms of the substantial derivative and recalling the dot product of two velocity vectors as $\bar{v} \cdot \bar{v} = v^2$. Where the velocity squared term is a scalar quantity.

$$\rho \frac{D(v^2/2)}{Dt} = \rho \frac{D(\bar{v} \cdot \bar{v})}{2Dt}$$

(204)

Using the chain rule of calculus in evaluating the above expression yields

$$\rho \frac{D(\bar{v} \cdot \bar{v})}{2Dt} = \frac{\rho}{2} \left(\bar{v} \cdot \frac{D\bar{v}}{Dt} + \bar{v} \cdot \frac{D\bar{v}}{Dt} \right) = \rho \bar{v} \cdot \frac{D\bar{v}}{Dt}$$

(205)

We can form the mechanical energy equation by using the result above and recalling the conservation of momentum equation, as shown in Equation 185. The conservation of momentum equation is

$$\rho \frac{D\bar{v}}{Dt} = -\nabla p + \rho \bar{g} + \nabla \cdot \underline{\tau}$$

(206)

The kinetic energy term from Equation 205 can be formed by the dot product of the mass average, or bulk, velocity vector $\bar{v}$ and the conservation of momentum equation.

$$\vec{v} \cdot \rho \frac{D\vec{v}}{Dt} = \rho \frac{D(v/2)}{Dt} = -\vec{v} \cdot \nabla \cdot \underline{\tau} - \vec{v} \cdot \nabla p + \rho \vec{g} \cdot \vec{v}$$

(207)

The mechanical energy from Equation 207 can be substituted into the total energy equation from Equation 203 to yield the internal energy equation. The following vector identities (Fahien, 1983) are necessary to develop the internal energy equation.

$$\nabla \cdot \underline{\tau} \cdot \vec{v} \equiv \underline{\tau} : \nabla \vec{v} + \vec{v} \cdot \nabla \cdot \underline{\tau}$$

(208)

$$\nabla \cdot p\vec{v} \equiv p\nabla \cdot \vec{v} + \vec{v} \cdot \nabla p$$

(209)

Substituting the mechanical energy equation into the total energy equation yields

$$\rho \frac{D\hat{U}}{Dt} = \left(\vec{v} \cdot \nabla \cdot \underline{\tau} + \vec{v} \cdot \nabla p - \rho \vec{g} \cdot \vec{v} \right) + \rho \vec{g} \cdot \vec{v} - \nabla \cdot p\vec{v} - \nabla \cdot \underline{\tau} \cdot \vec{v} - \nabla \cdot \vec{q}$$

(210)

Which simplifies to

$$\rho \frac{D\hat{U}}{Dt} = \left(\vec{v} \cdot \nabla \cdot \underline{\tau} - \nabla \cdot \underline{\tau} \cdot \vec{v} \right) + \left(\vec{v} \cdot \nabla p - \nabla \cdot p\vec{v} \right) - \nabla \cdot \vec{q}$$

(211)

Using the vector identities shown in Equations 208 and 209 yields the internal energy equation.

$$\rho \frac{D\hat{U}}{Dt} = -\underline{\tau} : \nabla \vec{v} - p\nabla \cdot \vec{v} - \nabla \cdot \vec{q}$$

(212)

The internal energy equation can be expressed in terms of temperature by using the following expression from thermodynamics for a pure substance that is a function of temperature and pressure (Fahien, 1983).

$$d\hat{U} = c_v dT + \left[-T \left(\frac{\partial p}{\partial T} \right)_{\rho} \right] d\frac{1}{\rho}$$

(213)

Substituting Equation 213 into Equation 212 results in

$$\rho c_v \frac{DT}{Dt} = -\underline{\tau} : \nabla \vec{v} - T \left(\frac{\partial p}{\partial T} \right)_{\rho} \nabla \cdot \vec{v} - \nabla \cdot \vec{q}$$

(214)

277

For an incompressible fluid Equation 214 becomes

$$\rho c_v \frac{DT}{Dt} = -\underline{\tau} : \nabla \vec{v} - \nabla \cdot \vec{q}$$

(215)

Fourier's Law can be applied to the heat diffusion term in the following manner

$$\nabla \cdot \vec{q} = \nabla \cdot \left(k \nabla T \right) = k \nabla^2 T$$

(216)

Substituting the result above into Equation 215 yields

$$\rho c_v \frac{DT}{Dt} = -\underline{\tau} : \nabla \vec{v} - k \nabla^2 T$$

(217)

The viscous dissipation term can be neglected because it applies to high-speed flows (Fahien, 1983). The fluid is also been assumed to be isothermal. The temperature will not vary in time or space and, therefore, the substantial derivative on the left hand side and the heat diffusion term on the right hand side are zero. Therefore, the energy equation is not applicable to the problem of interest.

References

Fahien, R.W., *Fundamentals of Transport Phenomena*, McGraw-Hill, New York, NY, (1983).

Hershey, D., *Transport Analysis*, Plenum Press, New York, NY, (1973).

Mills, A.F., *Basic Heat and Mass Transfer*, Irwin, Boston, MA, (1995).

Whitaker, S. *Fundamental Principles of Heat Transfer*, Pergamon Press, New York, NY, (1977).

Appendix C.2: Simplifying the Governing Equations

The three dimensional governing equations for conservation of momentum and species were simplified with the procedures shown in the sections below. The components of the momentum equation are considered for fully developed flow conditions within an infinitely long channel. The developing flow conditions at the entrance region have been ignored. As discussed in Section 3.2, it is appropriate to consider fully developed flow conditions for situations where an insect screen is in place. The species equation considers mass transport in a channel with insulated boundaries at y and z surfaces. The partial differential equations are integrated and known boundary conditions are applied to further simplify the governing equations.

Y-Momentum

The three dimensional momentum equation can be simplified by first considering the y component. The y-momentum equation considers fully developed flow conditions within an infinitely long channel and neglects entrance effects. The y-momentum equation is shown in a rearranged format below.

$$\frac{\partial\left(\rho v_y\right)}{\partial t} + \frac{\partial\left(\rho v_x v_y\right)}{\partial x} + \frac{\partial\left(\rho v_y v_y\right)}{\partial y} + \frac{\partial\left(\rho v_z v_y\right)}{\partial z} = -\frac{\partial p}{\partial y} + \rho g_y + \mu\left(\frac{\partial^2 v_y}{\partial x^2} + \frac{\partial^2 v_y}{\partial y^2} + \frac{\partial^2 v_y}{\partial z^2}\right)$$

$$(218)$$

The left hand side terms can be shown to be the material derivative of y-momentum. This is demonstrated in the steps below in order to bring physical meaning to the left hand side of the y-momentum equation.

The left hand side terms can be expanded by using the chain rule after factoring out the constant density for an incompressible fluid in the following manner

$$\rho\left(\frac{\partial(v_y)}{\partial t}+\frac{\partial(v_x v_y)}{\partial x}+\frac{\partial(v_y v_y)}{\partial y}+\frac{\partial(v_z v_y)}{\partial z}\right)=$$
$$\rho\left(\frac{\partial(v_y)}{\partial t}+v_x\frac{\partial(v_y)}{\partial x}+v_y\frac{\partial(v_x)}{\partial x}+v_y\frac{\partial(v_y)}{\partial y}+v_y\frac{\partial(v_y)}{\partial y}+v_z\frac{\partial(v_y)}{\partial z}+v_y\frac{\partial(v_z)}{\partial z}\right)$$

(219)

Grouping like terms and applying the continuity equation yields

$$\rho\left(\frac{\partial(v_y)}{\partial t}+v_x\frac{\partial(v_y)}{\partial x}+v_y\frac{\partial(v_y)}{\partial y}+v_z\frac{\partial(v_y)}{\partial z}+v_y\left[\frac{\partial(v_x)}{\partial x}+\frac{\partial(v_y)}{\partial y}+\frac{\partial(v_z)}{\partial z}\right]\right)$$
$$=\rho\left(\frac{\partial(v_y)}{\partial t}+v_x\frac{\partial(v_y)}{\partial x}+v_y\frac{\partial(v_y)}{\partial y}+v_z\frac{\partial(v_y)}{\partial z}+v_y[0]\right)$$

(220)

The resulting expression represents the material derivative of y-momentum as shown below.

$$\rho\left(\frac{\partial(v_y)}{\partial t}+v_x\frac{\partial(v_y)}{\partial x}+v_y\frac{\partial(v_y)}{\partial y}+v_z\frac{\partial(v_y)}{\partial z}\right)=\rho\frac{D(v_y)}{Dt}$$

(221)

The above material derivative is the time rate of change of y-momentum. The y-momentum equation can be rewritten as

$$\rho \frac{D(v_y)}{Dt} = -\frac{\partial p}{\partial y} + \rho g_y + \mu \left(\frac{\partial^2 v_y}{\partial x^2} + \frac{\partial^2 v_y}{\partial y^2} + \frac{\partial^2 v_y}{\partial z^2} \right)$$

(222)

Therefore, the left hand side term represents the time rate of change of the y-component of momentum. The time rate of change of y-momentum is balanced by the net forces acting in the y-direction that appear on the right hand side. The right hand side terms represent the net forces in the y-direction which are pressure, body, and viscous forces, respectively.

The stationary walls of the detector do not allow for the application of force in the y-direction. Therefore, there is no change in pressure in the y-direction. The body force term in the y-direction is zero because the gravitational force has no y-component. The stationary walls of the detector will result in viscous forces that act in the x-direction only. Therefore, the viscous force terms in the y-direction are zero. The y-component of the momentum equation can now be expressed as

$$\rho \frac{D(v_y)}{Dt} = 0$$

(223)

The time rate of change of the y-component of momentum is equal to zero. This result can now be evaluated by applying the no slip boundary condition for the y-component of

velocity at the y and z boundary surfaces of the gas phase control volume. The evaluation of the integral terms will be easier to conduct by using the original form of the left hand side terms in the momentum equation. The original form was shown to be equal to the material derivative.

$$\rho\frac{D\left(v_y\right)}{Dt}=\rho\left(\frac{\partial\left(v_y\right)}{\partial t}+\frac{\partial\left(v_x v_y\right)}{\partial x}+\frac{\partial\left(v_y v_y\right)}{\partial y}+\frac{\partial\left(v_z v_y\right)}{\partial z}\right)=0$$

(224)

Both sides can be divided by the constant density to yield

$$\left(\frac{\partial\left(v_y\right)}{\partial t}+\frac{\partial\left(v_x v_y\right)}{\partial x}+\frac{\partial\left(v_y v_y\right)}{\partial y}+\frac{\partial\left(v_z v_y\right)}{\partial z}\right)=0$$

(225)

The no slip boundary conditions are

$$v_y\big|_{y=-\frac{w}{2},\frac{w}{2}}=0$$

(226)

$$v_y\big|_{z=-\frac{h}{2},\frac{h}{2}}=0$$

(227)

$$v_z\big|_{y=-\frac{w}{2},\frac{w}{2}}=0$$

(228)

283

$$v_z\big|_{z=-\frac{h}{2},\frac{h}{2}} = 0$$

(229)

This requires recalling that the integral of a derivative is the function evaluated at the limits of integration and assuming that the derivative of the function is continuous (Edwards and Penney, 1990)

$$\int_a^b F'(x)\,dx = \left[F(x)\right]_a^b = F(b) - F(a)$$

(230)

Setting up the y-momentum equation for integration with respect to the y direction

$$\int_{-\frac{w}{2}}^{\frac{w}{2}} \left(\frac{\partial(v_y)}{\partial t} + \frac{\partial(v_x v_y)}{\partial x} + \frac{\partial(v_y v_y)}{\partial y} + \frac{\partial(v_z v_y)}{\partial z} = 0 \right) dy$$

(231)

Integrating the applicable partial derivatives yields

$$\left(\int_{-\frac{w}{2}}^{\frac{w}{2}} \left(\frac{\partial(v_y)}{\partial t} + \frac{\partial(v_x v_y)}{\partial x} + \frac{\partial(v_z v_y)}{\partial z} \right) dy + \left[v_y v_y \right]\Big|_{-\frac{w}{2}}^{\frac{w}{2}} = 0 \right)$$

(232)

Evaluating the y component of velocity using the no slip boundary condition results in

$$\left(\int_{-\frac{w}{2}}^{\frac{w}{2}} \left(\frac{\partial \left(v_y \right)}{\partial t} + \frac{\partial \left(v_x v_y \right)}{\partial x} + \frac{\partial \left(v_z v_y \right)}{\partial z} \right) dy + \left[(0)(0) - (0)(0) \right] = 0 \right)$$

(233)

The evaluated terms on the left hand side of the expression above show that the y-momentum in the y-direction is zero. Additionally, there are no sources or sinks of y-momentum in the y-direction. The evaluation of the integrated form of the y-momentum governing equation shows that the y-momentum in the y-direction is zero. Therefore, this term can be eliminated from the pre-integrated form of the y-momentum equation because the change in y-momentum with respect to the y-direction would be zero. The modified pre-integrated form of the y-momentum equation becomes

$$\left(\frac{\partial \left(v_y \right)}{\partial t} + \frac{\partial \left(v_x v_y \right)}{\partial x} + \frac{\partial \left(v_z v_y \right)}{\partial z} \right) = 0$$

(234)

Setting up the modified y-momentum equation for integration with respect to the z direction

$$\int_{-\frac{h}{2}}^{\frac{h}{2}} \left(\frac{\partial \left(v_y \right)}{\partial t} + \frac{\partial \left(v_x v_y \right)}{\partial x} + \frac{\partial \left(v_z v_y \right)}{\partial z} = 0 \right) dz$$

(235)

Integrating the applicable partial derivatives yields

$$\left(\int_{-\frac{h}{2}}^{\frac{h}{2}} \left(\frac{\partial \left(v_y \right)}{\partial t} + \frac{\partial \left(v_x v_y \right)}{\partial x} \right) dz + \left[v_z v_y \right] \Big|_{-\frac{h}{2}}^{\frac{h}{2}} = 0 \right)$$

(236)

Evaluating the y and z components of velocity using the no slip boundary condition results in

$$\left(\int_{-\frac{h}{2}}^{\frac{h}{2}} \left(\frac{\partial \left(v_y \right)}{\partial t} + \frac{\partial \left(v_x v_y \right)}{\partial x} \right) dz + \left[(0)(0) - (0)(0) \right] = 0 \right)$$

(237)

The evaluated terms on the left hand side of the expression above show that the y-momentum in the z-direction is zero. Additionally, there are no sources or sinks of y-momentum in the z-direction. The evaluation of the integrated form of the y-momentum governing equation shows that the y-momentum in the z-direction is zero. Therefore, this term can be eliminated from the pre-integrated form of the y-momentum equation because the change in y-momentum with respect to the z-direction would be zero. The pre-integrated form of the y-momentum equation becomes

$$\frac{\partial \left(v_y \right)}{\partial t} + \frac{\partial \left(v_x v_y \right)}{\partial x} = 0$$

(238)

The elimination of the y-momentum terms with respect to the y and z directions on the left hand side of the expression above shows that the y-momentum in the yz plane is zero. Additionally, there are no sources or sinks of y-momentum in the yz plane.

286

There are no sources or sinks of y-momentum in the x direction and, therefore, the change in y-momentum with respect to the x direction is zero as well.

The time rate of change of y-momentum is zero and is consistent with the y-momentum being a constant value of zero. Since the y-momentum is zero the y component of velocity must be constant. From the no slip boundary conditions that were applied the constant value of y-velocity is zero. The y-component of velocity being equal to zero is consistent with zero y-momentum for a non-zero fluid density.

Z-Momentum

The z-component of the momentum equation is examined next and rearranged below.

$$\frac{\partial(\rho v_z)}{\partial t} + \frac{\partial(\rho v_x v_z)}{\partial x} + \frac{\partial(\rho v_y v_z)}{\partial y} + \frac{\partial(\rho v_z v_z)}{\partial z} = -\frac{\partial p}{\partial z} + \rho g_z + \mu\left(\frac{\partial^2 v_z}{\partial x^2} + \frac{\partial^2 v_z}{\partial y^2} + \frac{\partial^2 v_z}{\partial z^2}\right)$$

(239)

The left hand side terms can be expressed in terms of the material derivative as was shown for the y-momentum equation. For this case the material derivative is

$$\rho\left(\frac{\partial(v_z)}{\partial t} + \frac{\partial(v_x v_z)}{\partial x} + \frac{\partial(v_y v_z)}{\partial y} + \frac{\partial(v_z v_z)}{\partial z}\right) = \rho\frac{D(v_z)}{Dt}$$

(240)

287

This material derivative is the time rate of change of momentum in the z-direction as represented by the terms on the left hand side of the z-momentum equation. The right hand side terms of the z-momentum equation represent the net force acting in the z-direction and include pressure, body, and viscous forces, respectively.

Again, the stationary walls of the detector will result in viscous forces that act in the x-direction only. Therefore, the viscous force terms in the z-direction are zero. The gravitational body force acts in the z-direction. Therefore, the net force in the z-direction is that the pressure change in z is balanced by the buoyancy force acting in the z-direction. The stationary walls of the detector to not allow for the application of any additional pressure force to act in the z-direction. The z-component of the momentum equation becomes

$$\rho\left(\frac{\partial(v_z)}{\partial t}+\frac{\partial(v_x v_z)}{\partial x}+\frac{\partial(v_y v_z)}{\partial y}+\frac{\partial(v_z v_z)}{\partial z}\right)=-\frac{\partial p}{\partial z}+\rho g_z$$

(241)

This result can now be evaluated by applying the previously stated no slip boundary conditions for the y and z-components of velocity at the y and z boundary surfaces of the gas phase control volume.

Setting up the z-momentum equation for integration with respect to the y direction

288

$$\int_{-\frac{w}{2}}^{\frac{w}{2}} \left(\rho \left(\frac{\partial (v_z)}{\partial t} + \frac{\partial (v_x v_z)}{\partial x} + \frac{\partial (v_y v_z)}{\partial y} + \frac{\partial (v_z v_z)}{\partial z} \right) = -\frac{\partial p}{\partial z} + \rho g_z \right) dy$$

(242)

Integrating the applicable terms yields

$$\left(\rho \int_{-\frac{w}{2}}^{\frac{w}{2}} \left(\frac{\partial (v_z)}{\partial t} + \frac{\partial (v_x v_z)}{\partial x} + \frac{\partial (v_z v_z)}{\partial z} \right) dy + \rho \left[v_y v_z \right] \Big|_{-\frac{w}{2}}^{\frac{w}{2}} = \int_{-\frac{w}{2}}^{\frac{w}{2}} \left(-\frac{\partial p}{\partial z} + \rho g_z \right) dy \right)$$

(243)

Evaluating the terms at the limits of integration results in

$$\left(\rho \int_{-\frac{w}{2}}^{\frac{w}{2}} \left(\frac{\partial (v_z)}{\partial t} + \frac{\partial (v_x v_z)}{\partial x} + \frac{\partial (v_z v_z)}{\partial z} \right) dy + \rho \left[(0)(0) - (0)(0) \right] = \int_{-\frac{w}{2}}^{\frac{w}{2}} \left(-\frac{\partial p}{\partial z} + \rho g_z \right) dy \right)$$

(244)

The evaluated terms on the left hand side of the expression above show that the z-momentum in the y-direction is zero. Additionally, there are no sources or sinks of z-momentum in the y-direction. The evaluation of the integrated form of the z-momentum governing equation shows that the z-momentum in the y-direction is zero. Therefore, this term can be eliminated from the pre-integrated form of the z-momentum equation because the change in z-momentum with respect to the y-direction would be zero. The modified pre-integrated form of the z-momentum equation becomes

$$\rho\left(\frac{\partial(v_z)}{\partial t}+\frac{\partial(v_xv_z)}{\partial x}+\frac{\partial(v_zv_z)}{\partial z}\right)=-\frac{\partial p}{\partial z}+\rho g_z$$

<div align="right">(245)</div>

Setting up the modified z-momentum equation for integration with respect to the z direction

$$\int_{-\frac{h}{2}}^{\frac{h}{2}}\left(\rho\left(\frac{\partial(v_z)}{\partial t}+\frac{\partial(v_xv_z)}{\partial x}+\frac{\partial(v_zv_z)}{\partial z}\right)=-\frac{\partial p}{\partial z}+\rho g_z\right)dz$$

<div align="right">(246)</div>

Integrating the applicable terms yields

$$\left(\rho\int_{-\frac{h}{2}}^{\frac{h}{2}}\left(\frac{\partial(v_z)}{\partial t}+\frac{\partial(v_xv_z)}{\partial x}\right)dz+\rho\left[v_zv_z\right]\Big|_{-\frac{h}{2}}^{\frac{h}{2}}=-\left[p\right]\Big|_{-\frac{h}{2}}^{\frac{h}{2}}+\rho\left[g_zz\right]\Big|_{-\frac{h}{2}}^{\frac{h}{2}}\right)$$

<div align="right">(247)</div>

Evaluating the terms at the limits of integration

$$\left(\rho\int_{-\frac{h}{2}}^{\frac{h}{2}}\left(\frac{\partial(v_z)}{\partial t}+\frac{\partial(v_xv_z)}{\partial x}\right)dz+\rho\left[(0)(0)-(0)(0)\right]=-\left[p\right]\Big|_{-\frac{h}{2}}^{\frac{h}{2}}+\rho\left[g_z\left(\frac{h}{2}\right)-g_z\left(-\frac{h}{2}\right)\right]\right)$$

<div align="right">(248)</div>

Which simplifies to

$$\left(\rho \int_{-\frac{h}{2}}^{\frac{h}{2}} \left(\frac{\partial (v_z)}{\partial t} + \frac{\partial (v_x v_z)}{\partial x} \right) dz + \rho[(0)] = -[p]\Big|_{-\frac{h}{2}}^{\frac{h}{2}} + \rho g_z h \right)$$

(249)

The third term on the left hand side of the expression above shows that the z-momentum in the z direction is zero. Additionally, there are no sources or sinks of z-momentum in the z-direction.

The net force above is the pressure change in the z-direction is balanced by a hydrostatic pressure distribution. However, the typical height of the sensing chamber, *h*, is on the order of 1.27cm (0.5 in). Therefore, the resulting hydrostatic pressure difference is

$$\rho g_z h = (1.23)(9.81)(0.0127) = 0.15 Pa$$

(250)

This pressure difference relative to atmospheric pressure at 101,300*Pa* represents a difference of 0.00015%. Therefore, the hydrostatic pressure can be neglected because it is such a relatively small quantity. Additionally, the pressure term in the z-direction is neglected as well because no other force is applied in the z-direction due to the stationary walls of the detector. As a result there is no net force acting in the z-direction.

The integrated form of the z-momentum equation becomes

$$\rho \int_{-\frac{h}{2}}^{\frac{h}{2}} \left(\frac{\partial (v_z)}{\partial t} + \frac{\partial (v_x v_z)}{\partial x} \right) dz = 0$$

<div align="right">(251)</div>

The evaluation of the integrated form of the z-momentum governing equation shows that the z-momentum in the z-direction is zero. Therefore, this term can be eliminated from the pre-integrated form of the z-momentum equation because the change in z-momentum with respect to the z-direction would be zero. The pre-integrated form of the z-momentum equation becomes the following after dividing both sides by the constant density

$$\frac{\partial (v_z)}{\partial t} + \frac{\partial (v_x v_z)}{\partial x} = 0$$

<div align="right">(252)</div>

There are no sources or sinks of z-momentum in the x direction and, therefore, the change in z-momentum with respect to the x direction is zero as well.

The time rate of change of z-momentum is zero and is consistent with the z-momentum being a constant value of zero. Since the z-momentum is zero the z component of velocity must be constant. From the no slip boundary conditions that were applied the constant value of z-velocity is zero. The z-component of velocity being equal to zero is consistent with zero z-momentum for a non-zero fluid density.

Continuity

The y and z components of velocity have been shown to be zero in simplifying the y and z components of the momentum equation. Therefore, the continuity equation becomes

$$\frac{\partial v_x}{\partial x} = 0$$

(253)

This implies that the x-component of velocity is constant in the x-direction for a given elevation.

X-Momentum

The x-component of the momentum equation is rearranged in the form shown below.

$$\frac{\partial \left(\rho v_x \right)}{\partial t} + \frac{\partial \left(\rho v_x v_x \right)}{\partial x} + \frac{\partial \left(\rho v_y v_x \right)}{\partial y} + \frac{\partial \left(\rho v_z v_x \right)}{\partial z} = -\frac{\partial p}{\partial x} + \rho g_x + \mu \left(\frac{\partial^2 v_x}{\partial x^2} + \frac{\partial^2 v_x}{\partial y^2} + \frac{\partial^2 v_x}{\partial z^2} \right)$$

(254)

The above form of the momentum equation shows that the time rate of change of momentum in the x-direction is equal to the net force applied in the x-direction.

It has been shown in simplifying the y and z components of the momentum equation that velocity in y and z are zero. Additionally, there is no x-component of the gravitational body force. Therefore, the x-component of the momentum equation becomes

$$\frac{\partial\left(\rho v_{x}\right)}{\partial t}+\frac{\partial\left(\rho v_{x}v_{x}\right)}{\partial x}=-\frac{\partial p}{\partial x}+\mu\left(\frac{\partial^{2}v_{x}}{\partial x^{2}}+\frac{\partial^{2}v_{x}}{\partial y^{2}}+\frac{\partial^{2}v_{x}}{\partial z^{2}}\right)$$

(255)

The width of the detector sensing chamber control volume is considered to be much larger than the height. Therefore, the viscous force term with respect to the y direction is neglected as being small in comparison to the x and z directions.

The x-momentum equation takes the following form

$$\frac{\partial\left(\rho v_{x}\right)}{\partial t}+\frac{\partial\left(\rho v_{x}v_{x}\right)}{\partial x}=-\frac{\partial p}{\partial x}+\mu\left(\frac{\partial^{2}v_{x}}{\partial x^{2}}+\frac{\partial^{2}v_{x}}{\partial z^{2}}\right)$$

(256)

The density of the bulk fluid is constant for an incompressible fluid and can be factored out of the storage and convective terms resulting in

$$\rho\left(\frac{\partial v_{x}}{\partial t}+\frac{\partial\left(v_{x}v_{x}\right)}{\partial x}\right)=-\frac{\partial p}{\partial x}+\mu\left(\frac{\partial^{2}v_{x}}{\partial x^{2}}+\frac{\partial^{2}v_{x}}{\partial z^{2}}\right)$$

(257)

The convective term can be expanded by using the chain rule

$$\rho\left(\frac{\partial v_{x}}{\partial t}+v_{x}\frac{\partial v_{x}}{\partial x}+v_{x}\frac{\partial v_{x}}{\partial x}\right)=-\frac{\partial p}{\partial x}+\mu\left(\frac{\partial^{2}v_{x}}{\partial x^{2}}+\frac{\partial^{2}v_{x}}{\partial z^{2}}\right)$$

(258)

The simplified continuity equation is the partial of x-velocity with respect to x is zero. The second derivative of x-velocity with respect to x will also be zero and the viscous term with respect to x will become zero.

$$\frac{\partial v_x}{\partial x} = 0 \quad \therefore \quad \frac{\partial^2 v_x}{\partial x^2} = 0$$

(259)

The final simplified form of the momentum equation is

$$\left(\rho \frac{\partial v_x}{\partial t} \right) = -\frac{\partial p}{\partial x} + \mu \left(\frac{\partial^2 v_x}{\partial z^2} \right)$$

(260)

Dividing both sides by the density and setting the equation equal to zero yields

$$\frac{\partial v_x}{\partial t} + \frac{1}{\rho} \frac{\partial p}{\partial x} - \nu \left(\frac{\partial^2 v_x}{\partial z^2} \right) = 0$$

(261)

Species

The three dimensional species equation is rearranged below with the storage and convective terms on the left hand side and the ordinary diffusion terms on the right hand side.

$$\frac{\partial \rho_A}{\partial t} + \left(\frac{\partial (\rho_A v_x)}{\partial x} + \frac{\partial (\rho_A v_y)}{\partial y} + \frac{\partial (\rho_A v_z)}{\partial z} \right) = D_A \left(\frac{\partial^2 \rho_A}{\partial x^2} + \frac{\partial^2 \rho_A}{\partial y^2} + \frac{\partial^2 \rho_A}{\partial z^2} \right)$$

(262)

295

The y and z boundary surfaces of the gas phase control volume are shared with the solid phase boundaries of the detector. No mass transport via diffusion will take place through the y and z boundaries of the gas phase control volume.

$$\left.\frac{\partial \rho_A}{\partial y}\right|_{y=-\frac{w}{2},+\frac{w}{2}} = 0$$

(263)

$$\left.\frac{\partial \rho_A}{\partial z}\right|_{z=-\frac{h}{2},+\frac{h}{2}} = 0$$

(264)

A no slip boundary condition applies for the y and z components of velocity at the y and z boundary surfaces of the gas phase control volume. The no slip boundary conditions were presented in simplifying the momentum equations. Additionally, there is no deposition at the control volume boundaries for y and z.

The species equation is setup for integration with respect to the y direction

$$\int_{-\frac{w}{2}}^{\frac{w}{2}} \left(\frac{\partial \rho_A}{\partial t} + \left(\frac{\partial(\rho_A v_x)}{\partial x} + \frac{\partial(\rho_A v_y)}{\partial y} + \frac{\partial(\rho_A v_z)}{\partial z} \right) = D_A \left(\frac{\partial^2 \rho_A}{\partial x^2} + \frac{\partial^2 \rho_A}{\partial y^2} + \frac{\partial^2 \rho_A}{\partial z^2} \right) \right) dy$$

(265)

The appropriate terms of the species equation are integrated below.

296

$$\int_{-\frac{w}{2}}^{\frac{w}{2}} \left(\frac{\partial \rho_A}{\partial t} + \frac{\partial (\rho_A v_x)}{\partial x} + \frac{\partial (\rho_A v_z)}{\partial z} \right) dy + \left[\rho_A v_y \right]\Big|_{-\frac{w}{2}}^{\frac{w}{2}} = D_A \left(\int_{-\frac{w}{2}}^{\frac{w}{2}} \left(\frac{\partial^2 \rho_A}{\partial x^2} + \frac{\partial^2 \rho_A}{\partial z^2} \right) dy + \left[\frac{\partial \rho_A}{\partial y} \right]\Big|_{-\frac{w}{2}}^{\frac{w}{2}} \right)$$

(266)

The no-slip and insulated boundary conditions are applied at the limits of integration

$$\int_{-\frac{w}{2}}^{\frac{w}{2}} \left(\frac{\partial \rho_A}{\partial t} + \frac{\partial (\rho_A v_x)}{\partial x} + \frac{\partial (\rho_A v_z)}{\partial z} \right) dy + \left[\rho_A(0) - \rho_A(0) \right] = D_A \left(\int_{-\frac{w}{2}}^{\frac{w}{2}} \left(\frac{\partial^2 \rho_A}{\partial x^2} + \frac{\partial^2 \rho_A}{\partial z^2} \right) dy + \left[(0) - (0) \right] \right)$$

(267)

The fourth term on the left hand side indicates that there is no convective mass flux in the y direction. Additionally, there are no sources or sinks of convective mass flux in the y direction. The third term on the right hand side indicates that there is no diffusive mass flux in the y direction. Likewise, there are no sources or sinks of diffusive mass flux in the y direction. Therefore, the concentration gradient in the y direction will be constant and have a flat profile. The convective and diffusive mass flux terms in the y direction have been shown to be equal to zero after being evaluated in the integrated form. Therefore, these terms will also be zero in the pre-integrated form of the species equation. The modified pre-integrated form of the species equation becomes

$$\frac{\partial \rho_A}{\partial t} + \left(\frac{\partial (\rho_A v_x)}{\partial x} + \frac{\partial (\rho_A v_z)}{\partial z} \right) = D_A \left(\frac{\partial^2 \rho_A}{\partial x^2} + \frac{\partial^2 \rho_A}{\partial z^2} \right)$$

(268)

The modified species equation is set up for integration with respect to the z direction

297

$$\int_{-\frac{h}{2}}^{\frac{h}{2}} \left(\frac{\partial \rho_A}{\partial t} + \left(\frac{\partial (\rho_A v_x)}{\partial x} + \frac{\partial (\rho_A v_z)}{\partial z} \right) \right) = D_A \left(\frac{\partial^2 \rho_A}{\partial x^2} + \frac{\partial^2 \rho_A}{\partial z^2} \right) dz$$

(269)

The appropriate terms of the species equation are integrated below.

$$\int_{-\frac{h}{2}}^{\frac{h}{2}} \left(\frac{\partial \rho_A}{\partial t} + \frac{\partial (\rho_A v_x)}{\partial x} \right) dz + \left[\rho_A v_z \right]_{-\frac{h}{2}}^{\frac{h}{2}} = D_A \left(\int_{-\frac{h}{2}}^{\frac{h}{2}} \frac{\partial^2 \rho_A}{\partial x^2} dz + \left[\frac{\partial \rho_A}{\partial z} \right]_{-\frac{h}{2}}^{\frac{h}{2}} \right)$$

(270)

The no-slip and insulated boundary conditions are applied at the limits of integration

$$\int_{-\frac{h}{2}}^{\frac{h}{2}} \left(\frac{\partial \rho_A}{\partial t} + \frac{\partial (\rho_A v_x)}{\partial x} \right) dz + \left[\rho_A(0) - \rho_A(0) \right] = D_A \left(\int_{-\frac{h}{2}}^{\frac{h}{2}} \frac{\partial^2 \rho_A}{\partial x^2} dz + \left[(0) - (0) \right] \right)$$

(271)

The third term on the left hand side indicates that there is no convective mass flux in the z direction. Additionally, there are no sources or sinks of convective mass flux in the z direction. The second term on the right hand side indicates that there is no diffusive mass flux in the z direction. Likewise, there are no sources or sinks of diffusive mass flux in the z direction. Therefore, the concentration gradient in the z direction will be constant and have a flat profile. The convective and diffusive mass flux terms in the z direction have been shown to be equal to zero after being evaluated in the integrated form. Therefore, these terms will also be zero in the pre-integrated form of the species equation. The pre-integrated form of the species equation now becomes

$$\frac{\partial \rho_A}{\partial t} + \frac{\partial(\rho_A v_x)}{\partial x} = D_A\left(\frac{\partial^2 \rho_A}{\partial x^2}\right)$$

<div align="right">(272)</div>

The convective term can be expanded using the chain rule

$$\frac{\partial \rho_A}{\partial t} + \left(\rho_A \frac{\partial v_x}{\partial x} + v_x \frac{\partial \rho_A}{\partial x}\right) = D_A\left(\frac{\partial^2 \rho_A}{\partial x^2}\right)$$

<div align="right">(273)</div>

Applying the simplified continuity equation yields the final form of the species equation

$$\frac{\partial \rho_A}{\partial t} + v_x \frac{\partial \rho_A}{\partial x} = D_A\left(\frac{\partial^2 \rho_A}{\partial x^2}\right)$$

<div align="right">(274)</div>

Setting the above equation equal to zero yields

$$\frac{\partial \rho_A}{\partial t} + v_x \frac{\partial \rho_A}{\partial x} - D_A\left(\frac{\partial^2 \rho_A}{\partial x^2}\right) = 0$$

<div align="right">(275)</div>

The species equation has become one-dimensional due to no slip and no mass transport conditions at the y and z boundaries and takes the following simplified form.

Appendix C.3 Screen Resistance Factor

Incompressible pressure drop correlations for flow through an insect screen were identified from various sources in the fluid mechanics literature (Brundrett, 1993, Baines and Peterson, 1951, Munson, 1988). These correlations share the same general form in relating the upstream velocity and geometric characteristics of the insect screen to the pressure drop. These correlations were examined but were found to be inappropriate for the smoke detector mass transport problem.   The incompressible pressure drop correlations for insect screens were developed for pipe flow situations where the insect screen occupied the entire cross section of the flow region. Therefore, the entire mass flow rate of fluid upstream of the screen would pass through the screen. For the smoke detector mass transport problem, the insect screen and detector profile occupy a fraction of the flow field. This situation applies to detectors in the FE/DE as well as ceiling mounted smoke detectors exposed to a ceiling jet from a fire.   In these situations a portion of the upstream flow is diverted underneath the detector and a portion passes through the insect screen.   In this situation mass is conserved over the entire cross sectional area of the duct or ceiling jet region.

Therefore, a method was devised to account for this flow situation for an insect screen occupying only a portion of the entire flow field. This approach is semi-empirical as it uses elements from fluid mechanics theory and empirical data from research literature as well as data from this study. Therefore, this approach cannot be considered a rigorous treatment of the physics involved in fluid flow through the insect screen for the smoke

detector mass transport problem. Developing a general form of the resistance coefficient that is dependent upon both geometry and Reynolds number is beyond this scope of this work. Rather, an engineering relationship has been developed that expresses the ratio of internal to external velocity as a function of the Reynolds number. The particular expressions that have been developed are valid for the specific detector geometries and flow conditions used in this study. These expressions should not be used beyond the experimental conditions presented in this work nor should they be applied to different detector geometries. The development of a general smoke detector resistant correlation that is a function of both geometry and flow conditions would require detailed measurements of velocity for a wide range of Reynolds numbers and detector geometries.

The principle of conservation of mass forms the basis for this analysis. Observations from the fluids mechanics literature, and where appropriate, confirmation from the experiments conducted in this study are applied to characterize the flow field. Portions of the flow field approaching the detector profile are assumed to be deflected underneath the detector. For the purposes of this analysis, the mass flow associated any part of the flow field perpendicular to a solid area of the detector is assumed to be deflected underneath the detector. The mass flow associated with any part perpendicular to the insect screen is assumed to have a portion deflected underneath the detector and the remaining portion is transported across the insect screen.

Concepts from previous studies of incompressible fluid flow for insect screens occupying the entire cross section of a pipe or duct are used as the foundation for developing a

resistance factor for smoke detectors. This resistance factor is a function of screen porosity and wire Reynolds number of the screen. A screen porosity function commonly used in insect screen resistance correlations for incompressible flow and screens occupying the entire cross section has been applied in developing the resistance factor for smoke detectors. Velocity measurements up and downstream of an insect screen from this study are used to determine the functional dependence of the resistance factor on the wire Reynolds number.

Control Volume

The control volume is chosen to be slightly upstream and downstream of the detector's leading edge as shown in Figure 82. It has been assumed that the boundaries of the control volume are in regions of fully developed flow conditions and do not account for the mixing processes expected to occur at the leading edge of the detector as well as in the developing flow region downstream of the insect screen within the detector.
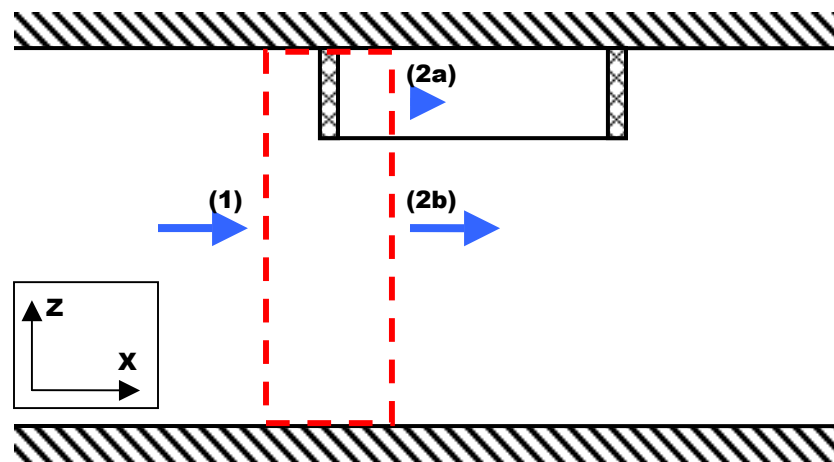
Figure 82 -- Mass conservation across FE/DE duct cross section.

The flow conditions have been assumed to be two-dimensional with the flow variation occurring in the x and z directions only. The width of the detector is assumed to be large with respect to the duct width and located far from the boundary layer on the sides of the duct.

The velocity profiles in each region are assumed to have the following characteristics as shown in Figure 83.
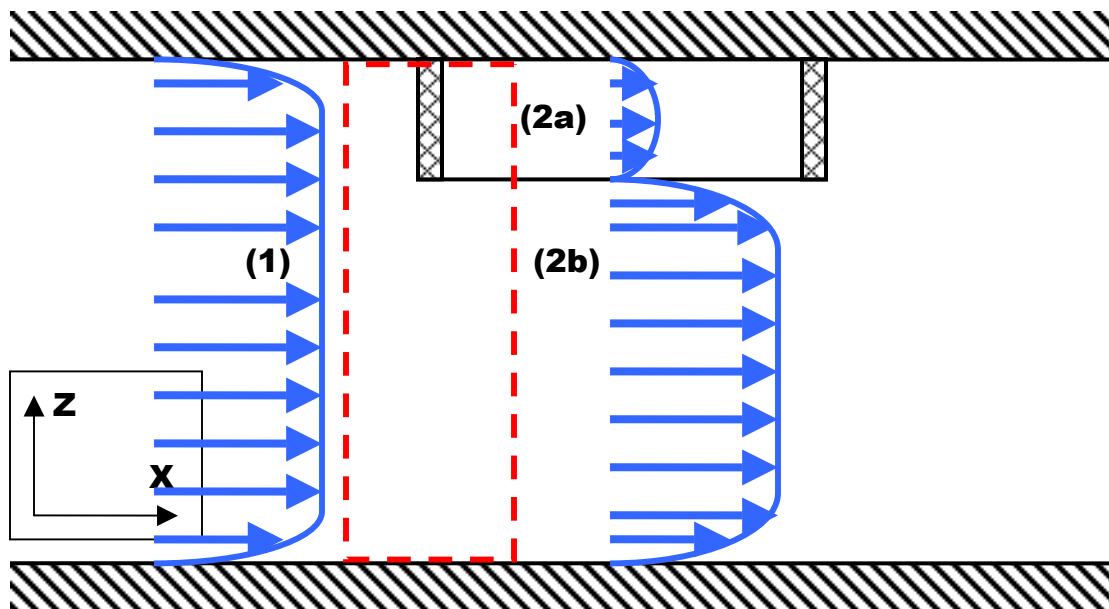
Figure 83 -- Assumed velocity profiles upstream and downstream of control volume.

In regions (1) and (2b) the velocity profile is assumed to be turbulent. This is based partially on a Reynolds number calculation for a rectangular duct and range of velocities examined in this study. This calculation was confirmed with LDV measurements of the velocity profile in this region (see Internal Velocity Paper). The velocity profile in region

(2a) is assumed to be laminar based on previous work on flows through insect screens (Baines and Peterson, 1951) and was confirmed in this study with LDV measurements of internal velocity profiles for the rectangular detector (see Internal Velocity Paper).

Conservation of Mass

Mass is conserved on each boundary of the gas phase control volume for each region.

$$\dot{m}_{(1)} = \dot{m}_{(2a)} + \dot{m}_{(2b)}$$

(276)

The mass flux of fluid can be expressed as the product of fluid density, area perpendicular to the flow direction, and the average velocity.

$$\rho A_{(1)} \bar{V}_{(1)} = \rho A_{(2a)} \bar{V}_{(2a)} + \rho A_{(2b)} \bar{V}_{(2b)}$$

(277)

The perpendicular area for each region can be specified in the following manner, assuming that the width of the region is much larger relative to the height.

$$\rho y z_{(1)} \bar{V}_{(1)} = \rho y z_{(2a)} \bar{V}_{(2a)} + \rho y z_{(2b)} \bar{V}_{(2b)}$$

(278)

The values of fluid density and width are the same in all three terms and can be eliminated.

304

$$z_{(1)}\bar{V}_{(1)} = z_{(2a)}\bar{V}_{(2a)} + z_{(2b)}\bar{V}_{(2b)}$$

$$(279)$$

Average Velocity

The mass flow rates at each of the three regions identified in Figure X are determined from the average velocity. The average velocity in each region is determined by integrating over the velocity profile. As mentioned previously, the velocity profiles are assumed to be turbulent in regions (1) as well as (2b) and assumed to be laminar within the detector in region (2a).

Average Velocity for Laminar Velocity Profile

The average velocity within the detector is developed by integrating over the laminar velocity profile and dividing by the height. The laminar velocity profile for incompressible flow between parallel plates is given as (Munson, 1994)

$$u = \frac{1}{2\mu}\left(\frac{\partial p}{\partial x}\right)\left(z^2 - h^2\right)$$

$$(280)$$

The maximum velocity is located at the apex of the profile, where the vertical location, z, is equal to zero at the origin. Therefore, the maximum velocity is

$$u_{max} = \frac{1}{2\mu}\left(\frac{\partial p}{\partial x}\right)\left(-h^2\right)$$

$$(281)$$

The pressure drop can be solved for in terms of the maximum velocity in the following manner

$$\left(\frac{\partial p}{\partial x}\right) = \frac{u_{max}(2\mu)}{-h^2}$$

(282)

The expression for pressure drop can be substituted into the equation for the laminar velocity profile

$$u = \frac{1}{2\mu}\left(\frac{u_{max}(2\mu)}{-h^2}\right)\left(z^2 - h^2\right)$$

(283)

Which simplifies to

$$u = u_{max}\left(\frac{z^2 - h^2}{-h^2}\right)$$

(284)

$$u = u_{max}\left(1 - \frac{z^2}{h^2}\right)$$

(285)

This expression for the laminar velocity profile relates the maximum velocity to the half height of the space between two parallel plates. This expression can be integrated over the half height, h, and divided by the distance in order to determine the average velocity.

$$\bar{u} = \frac{u_{max} \int_0^h \left(1 - \frac{z^2}{h^2}\right) dz}{h}$$

(286)

Setting up and performing the integration leads to the following

$$\bar{u} = \frac{u_{max} \left[z - \frac{z^3}{3h^2} \right]_0^h}{h} = \frac{u_{max} \left[h - \frac{h^3}{3h^2} \right]}{h} = \frac{u_{max} \left[h - \frac{h}{3} \right]}{h} = \frac{u_{max} \left[\frac{2h}{3} \right]}{h}$$

(287)

The above can be simplified into the following expression for average velocity as a function of the maximum velocity in a laminar velocity profile.

$$\bar{u} = \frac{2}{3} u_{max}$$

(288)

Average Velocity for Turbulent Velocity Profile

The time-averaged velocity profile for turbulent pipe flow can be characterized by three regions; (1) a *viscous sublayer*, the narrow region near the pipe wall where laminar shear stress is dominant in the boundary layer, (2) an *outer layer*, the region away from the wall where the turbulent portion of the shear stress is dominant in the freestream, and (3) an *overlap layer*, the transitional region between the *viscous sublayer* and the *outer layer* (Munson, 1994).

307

For circular pipes, the three turbulent regions are defined in terms of the ratio of position y to the pipe radius h at a Reynolds number of 5 x10^5 (Schetz and Fuhs, 1999). The viscous sublayer has been defined as occurring within the distance $y/h = 0.0005$ away from the wall surface (Schetz and Fuhs, 1999). The overlap layer has been defined as occurring from $y/h = 0.0005$ to 0.0035 away from the wall surface (Schetz and Fuhs, 1999). Logarithmic behavior of the turbulent velocity profile has been defined as occurring from $y/h = 0.0035$ to 0.19 away from the wall surface (Schetz and Fuhs, 1999). A nearly constant velocity profile has been defined for the region $y/h > 0.19$ away from the wall surface (Schetz and Fuhs, 1999).

One approximation describing the turbulent velocity profile in a pipe at locations that are away from walls and away from the centerline is the *power-law velocity profile* (Munson, 1994):

$$\frac{u}{U} = \left(1 - \frac{r}{R}\right)^{1/7}$$

(289)

The above expression for the turbulent profile can be assumed to apply for the entire two-dimensional profile and can be rewritten in terms of the height of the FE/DE test section.

$$\frac{u}{U} = \left(1 - \frac{z}{h}\right)^{1/7}$$

(290)

Arranging for local velocity results in the following

$$u = U\left(1 - \frac{z}{h}\right)^{1/7}$$

(291)

The average velocity between two arbitrary vertical locations is determined by integrating the turbulent velocity profile over the height of interest and dividing by the associated distance.

$$\bar{u} = \frac{\int_{z_1}^{z_2} U\left(1 - \frac{z}{h}\right)^{1/7} dz}{\left(z_2 - z_1\right)}$$

(292)

The general form of the integration is of the form (Penney and Edwards, 1995)

$$\int x^n dx = \left(\frac{1}{n+1}\right) x^{n+1}$$

(293)

In this particular case

$$x = \left(1 - \frac{z}{h}\right)$$

$$dx = -\frac{dz}{h}; \; dz = -hdx$$

(294)

Applying these to the integral yields the following

309

$$\bar{u} = \frac{-Uh \int_{z_1}^{z_2} (x)^{1/7} \, dx}{(z_2 - z_1)}$$

(295)

Performing the integration results in

$$\bar{u} = \frac{-Uh \left[\frac{(x)^{8/7}}{(8/7)} \right] \Big|_{z_1}^{z_2}}{(z_2 - z_1)}$$

(296)

Substituting the expression for the variable x leads to the following result

$$\bar{u} = \frac{-\frac{7Uh}{8} \left[\left(1 - \frac{z}{h} \right)^{8/7} \right] \Big|_{z_1}^{z_2}}{(z_2 - z_1)}$$

(297)

Which can be further simplified to the final result

$$\bar{u} = \frac{-\frac{7Uh}{8} \left[\left(1 - \frac{z_2}{h} \right)^{8/7} - \left(1 - \frac{z_1}{h} \right)^{8/7} \right]}{(z_2 - z_1)}$$

(298)

310

Screen Resistance

The screen resistance for a smoke detector can be developed by considering the impact of the solid and open portions of the detector on the flow field. The flow is assumed to be two-dimensional as shown in Figure 84.
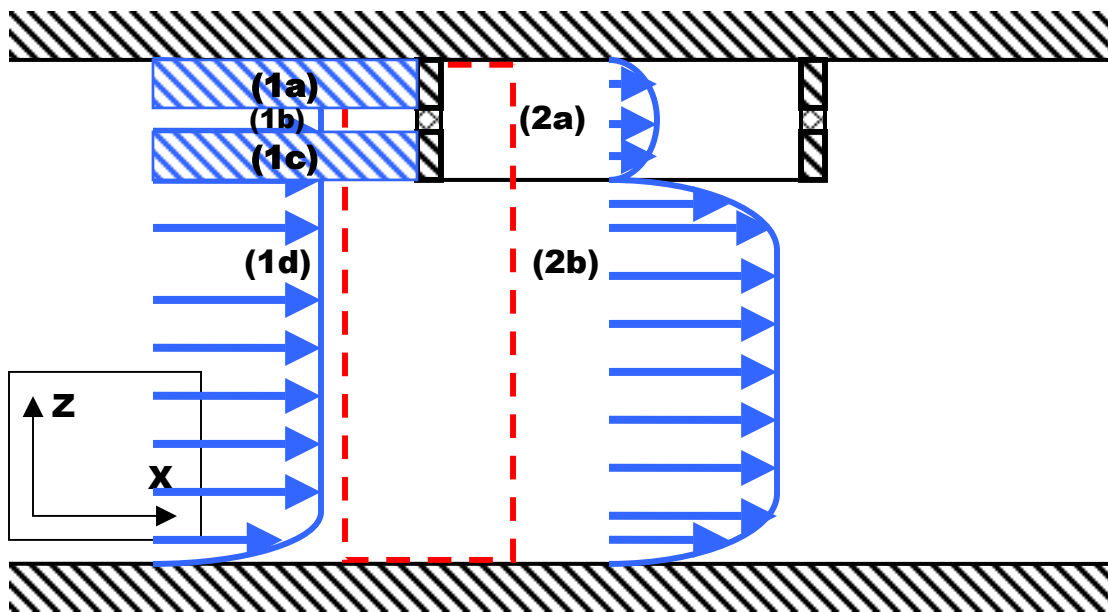
Figure 84 -- Assumed two-dimensional velocity profiles where shaded portions are assumed to be deflected.

The mass flow associated with the solid portions of the detector, indicated as areas (1a) and (1c), are assumed to be deflected below the detector. In the case of a detector with no openings, the entire mass flow perpendicular to the solid profile would be deflected underneath the detector, conserving the total mass flow. The mass flow associated with the detector opening is assumed to have a portion deflected underneath the detector and the remaining portion transported across the insect screen.

A resistance factor, R, is introduced to relate the resistance to the screen geometry and wire Reynolds number. The resistance coefficient, K, developed for insect screens occupying the entire cross section for incompressible pipe flow conditions was used as an example in the development of the resistance factor. The term *resistance factor* and the associated variable R will be used to distinguish it from the resistance coefficient developed for incompressible pipe flow through insect screens. For incompressible pipe flow, the resistance coefficient of the screen is typically expressed as a function of the screen porosity and Reynolds number (based on wire diameter) (Munson, 1988).

$$K = K(\alpha, \text{Re}_d)$$

(299)

One particular function for screen porosity, α, that has shown widespread agreement in the development of incompressible screen resistance correlations is (Brundrett, 1993)

$$f(\alpha) = \frac{(1 - \alpha^2)}{\alpha^2}$$

(300)

The wire Reynolds number, Re_d, is based on the external flow velocity and hydraulic diameter of the insect screen openings. In this formulation the average external velocity was used and was determined by integrating the velocity profile over the aerosol entry height of a given detector.

$$\text{Re}_d = \frac{\overline{V}_{ext} d_{screen}}{\nu}$$

(301)

The porosity function and wire Reynolds number will be applied in the development of the resistance factor for smoke detectors. Therefore, the resistance factor for smoke detector insect screens can be expressed in general as

$$R = \left(\frac{1-\alpha^2}{\alpha^2} \right) f\left(\text{Re}_d\right)$$

(302)

The functional dependence upon the wire Reynolds number was determined by applying the internal velocity data sets collected in the experimental portion of this study (see Internal Velocity Paper).

In this case the screen was perpendicular to the flow and occupied the vertical space from 42 to 55mm below the top of the duct. The insect screen was the only obstruction in the flow filed for these prototype experiments. The screen was enclosed by solid surfaces on all faces parallel to the flow direction and the back face of the enclosure was open. As a consequence, deflection of the flow field by solid obstructions was not a factor and will not be considered in determining the insect screen resistance factor for this particular configuration. The prototype experiment arrangement for the insect screen is shown in Figure 85.
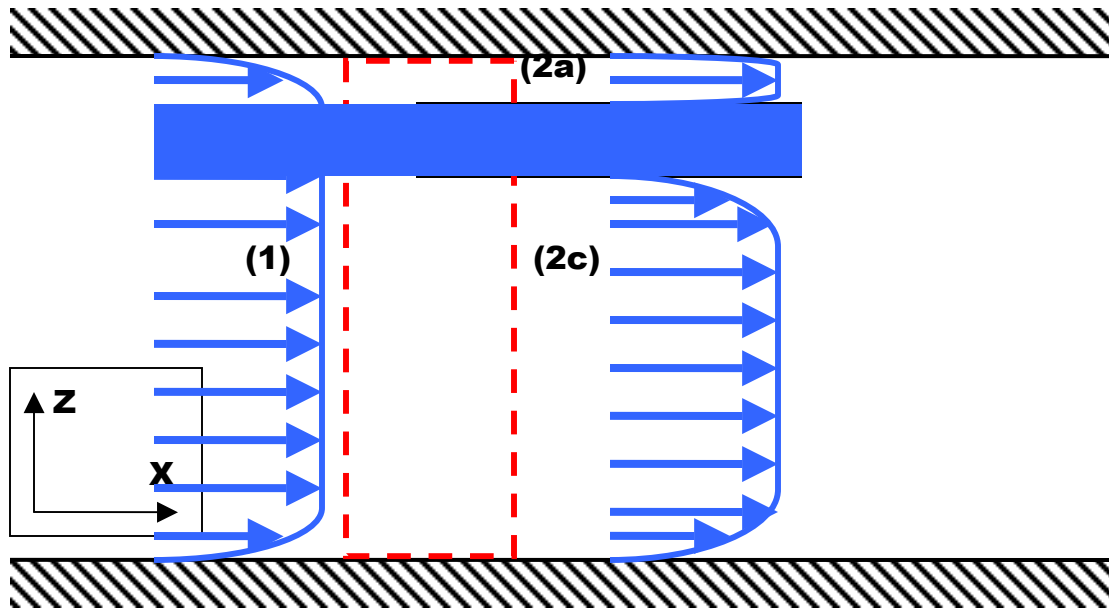
Figure 85 -- Assumed velocity profiles for screen in isolation where shaded portion is area of interest.

Mass is conserved across the entire cross section. It is assumed that mass is conserved across the insect screen (indicated as the shaded portion in Figure 85 above) in the following manner; a portion of the upstream mass is deflected underneath the detector and the remaining portion of the upstream mass passes through the screen. The control volume for mass conservation at the detector entrance area is shown in Figure 86.
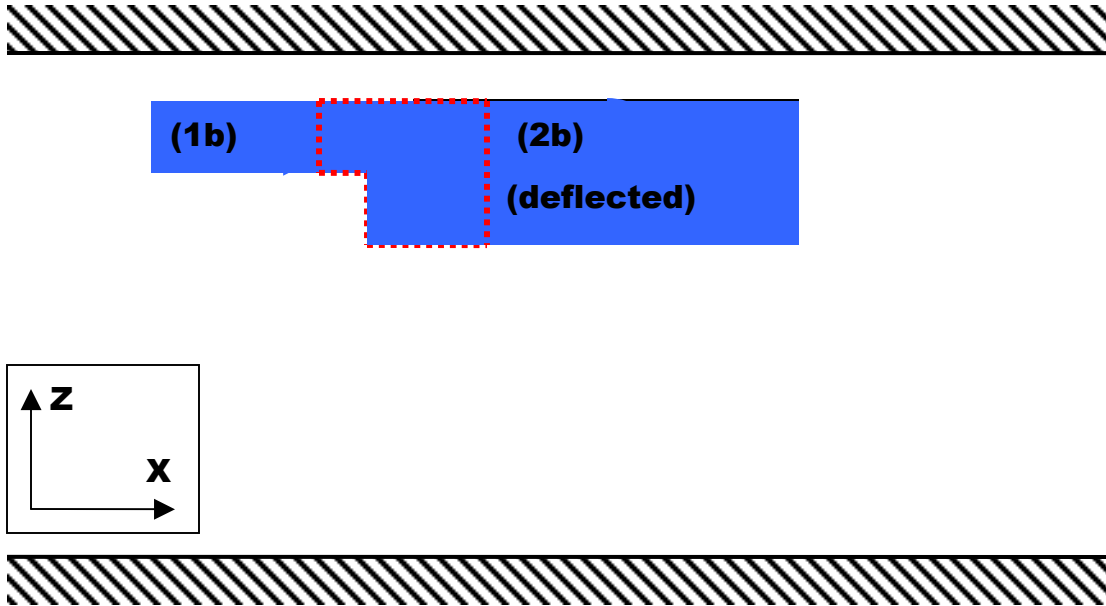
Figure 86 – Control volume at detector entrance region indicating portions of upstream flow that are deflected and transported across screen.

The mass conservation for this situation is expressed as

$$\dot{m}_{(1b)} = \dot{m}_{(2b)} + \dot{m}_{(deflected)}$$

(303)

Expanding the mass flow rate terms on each side yields

$$\rho A_{(1b)} \bar{V}_{(1b)} = \rho A_{(2b)} \bar{V}_{(2b)} + \rho A_{(deflected)} \bar{V}_{(deflected)}$$

(304)

The density for each area is constant and leads to the following simplification.

$$A_{(1b)} \bar{V}_{(1b)} = A_{(2b)} \bar{V}_{(2b)} + A_{(deflected)} \bar{V}_{(deflected)}$$

(305)

However, the area and velocity of the deflected portion of the flow were not measured as part of this study. Instead, the mass conservation equation was reformulated to express the deflected mass flow as a fraction, X, of the upstream mass flow in the following manner.

$$\dot{m}_{(1b)} = \dot{m}_{(2b)} + X\dot{m}_{(1b)}$$

(306)

Equating the upstream mass flows from the mass conservation equation at the insect screen leads to

$$\left(1 - X\right)\dot{m}_{(1b)} = \dot{m}_{(2b)}$$

(307)

Dividing the internal mass flow by the external mass flow

$$\frac{\dot{m}_{(2b)}}{\dot{m}_{(1b)}} = \left(1 - X\right)$$

(308)

The mass flow terms can be expanded to yield

$$\frac{\rho A_{(2b)}\overline{V}_{(2b)}}{\rho A_{(1b)}\overline{V}_{(1b)}} = \left(1 - X\right)$$

(309)

The density and areas for regions 1b and 2b are the same and the quantity *(1-X)* can be expressed as the resistance factor, *R*. These simplifications lead to the following result.

$$\frac{\overline{V}_{(2b)}}{\overline{V}_{(1b)}} = R$$

<div align="right">(310)</div>

This expression for the resistance factor is consistent with experimental measurements conducted as part of this study as the two velocities are not expected to be the same due to the resistance of the insect screen. The resistance factor is used to relate the external to the internal average velocity. This specific formulation relates the nondimensional velocity (average internal velocity scaled to average external velocity) to the resistance factor. At this point the subscripts for the internal and external velocity values are changed from *(1b)* and *(2b)* to the more descriptive *int* and *ext* for the remainder of this development.

$$V* = \frac{\overline{V}_{(1b)}}{\overline{V}_{(2b)}} = \frac{\overline{V}_{int}}{\overline{V}_{ext}} = R$$

<div align="right">(311)</div>

The general form of the resistance factor can be substituted to expand this expression to

$$\frac{\overline{V}_{int}}{\overline{V}_{ext}} = f\left(\frac{1-\alpha^2}{\alpha^2}\right)(\mathrm{Re}_d)$$

<div align="right">(312)</div>

The average external velocity was determined by integrating the turbulent approach velocity profile between the aerosol entry locations and dividing by the height of the opening for the range of velocities. The average velocity for the external turbulent profile was determined to be within the region where the power law velocity profile is valid. The literature indicates that this region exists at a y/h distance greater than 0.19 from the wall surface. For the FE/DE, h would be equal to 0.167m (half height of duct test section) and results in a distance of y greater than 32mm from the wall being within the region governed by the power law velocity profile. This distance is less than the highest aerosol entry location of 38mm on the photoelectric detector. Therefore, integrating the approach velocities with the turbulent velocity profile is appropriate for the range of detectors examined in this study.

The average internal velocity was determined from the previous development for laminar velocity profiles. The maximum internal velocity value was multiplied by 2/3 in order to obtain the average velocity. The sections that follow summarize the external average velocity and the corresponding average internal velocity values for the insect screen in isolation as well as the detectors examined in this study.

Insect Screen in Isolation

The integration points for determining the average external velocity were from 42 to 55 mm in the z direction.

Table 42 – Time averaged and integrated velocity values for screen in isolation.

	FE/DE Time Avg Velocity Profiles			Screen in Isolation				
Fan (Hz)	V,mean (m/s)	Std dev	V TI%	V,ext,avg	V,int,max	V,int,avg	Std dev	V TI%
30	0.822	0.048	5.85	0.783	0.283	0.188	0.044	15.70
25	0.668	0.045	6.71	0.636	0.198	0.132	0.035	17.78
20	0.520	0.035	6.81	0.495	0.145	0.097	0.014	9.60
15	0.392	0.028	7.20	0.373	0.079	0.052	0.006	7.09

Rectangular Model Detector with Insect Screen

The integration points for determining the average external velocity were from 50 to 58 mm in the z direction.

Table 43 – Time averaged and integrated velocity values for rectangular detector model.

	FE/DE Time Avg Velocity Profiles			Cartesian Detector W/Screen				
Fan (Hz)	V,mean (m/s)	Std dev	V TI%	V,ext,avg	V,int,max	V,int,avg	Std dev	V TI%
30	0.822	0.048	5.85	0.778	0.132	0.088	0.018	13.53
25	0.668	0.045	6.71	0.632	0.095	0.063	0.011	11.45
20	0.520	0.035	6.81	0.492	0.067	0.044	0.007	11.04
15	0.392	0.028	7.20	0.371	0.036	0.024	0.003	9.17
12	0.314	0.027	8.70	0.297	0.022	0.015	0.002	10.29
10	0.264	0.026	9.84	0.250	0.014	0.009	0.004	25.66
7	0.168	0.027	16.07	0.159	0.005	0.003	0.003	55.54
5	0.113	0.025	22.07	0.107	0.003	0.002	0.002	84.31

Photoelectric Detector

The integration points for determining the average external velocity were from 38 to 44 mm in the z direction.

Table 44 – Time averaged and integrated velocity values for photo detector.

Fan (Hz)	FE/DE Time Avg Velocity Profiles			Photoelectric Detector				
	V,mean (m/s)	Std dev	V TI%	V,ext,avg	V,int,max	V,int,avg	Std dev	V TI%
30	0.822	0.048	5.85	0.790	0.149	0.100	0.045	30.26
25	0.668	0.045	6.71	0.642	0.089	0.059	0.019	20.91
20	0.520	0.035	6.81	0.500	0.060	0.040	0.008	13.04
15	0.392	0.028	7.20	0.377	0.030	0.020	0.004	11.74
12	0.314	0.027	8.70	0.302	0.014	0.010	0.002	17.00

Ionization Detector

The integration points for determining the average external velocity were from 56 to 59 mm in the z direction. It should be noted that only a limited number of velocity sets at relatively high external velocities were found to be suitable. The ionization detector features two sets of offset baffles and an insect screen. It is likely that these geometric features limited the amount of seed particles entering the detection chamber for the purposes of taking LDV measurements.

Table 45 – Time averaged and integrated velocity values for ion detector.

Fan (Hz)	FE/DE Time Avg Velocity Profiles			Ionization Detector				
	V,mean (m/s)	Std dev	V TI%	V,ext,avg	V,int,max	V,int,avg	Std dev	V TI%
30	0.822	0.048	5.85	0.774	0.115	0.077	0.027	23.52
25	0.668	0.045	6.71	0.629	0.068	0.045	0.011	16.14
20	0.520	0.035	6.81	0.490	0.020	0.013	0.002	8.13

The average internal velocity was plotted against the average external velocity for the screen in isolation, the rectangular detector, ionization detector, and photoelectric detector.

Figure 87 -- Average internal velocity plotted against average external velocity.

It is interesting to note that the general trend indicates that the ratio of internal to external velocity decreases as the object's resistance to flow increases. The screen in isolation has a higher degree of resistance to the flow relative to the rectangular detector without the insect screen. This is demonstrated by the relatively lower ratio of internal to external velocity. The group consisting of the rectangular detector with the insect screen and the photoelectric and ionization detectors has the highest degree of resistance relative to the screen in isolation. This is demonstrated by the relatively low ratios of internal to external velocity.

The functional relationship between the nondimensional velocity to resistance factor terms for geometry and Reynolds number is developed in the discussion that follows.

The screen porosity, α, is the ratio of open area to the total area and is expressed as (Teitel and Shklyar, 1998)

$$\alpha = \frac{(m-d)(n-d)}{mn}$$

(313)

Where m, n, and d are the relevant dimensions of the screen as shown in Figure 88 below.
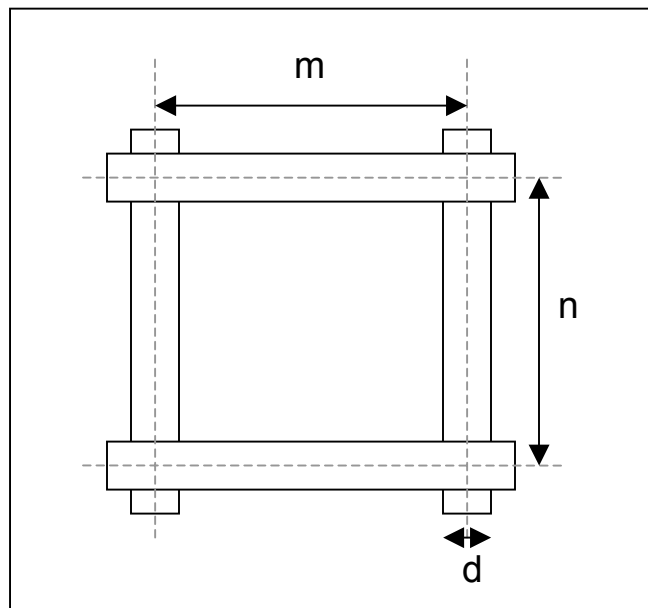
Figure 88 -- Relevant dimensions of screen section.

A digital image of the insect screen used in the experiments was enlarged and the relevant dimensions of the screen were obtained by scaling. The openings in the insect screen were a series of regular hexagons in a staggered pattern as depicted in Figure 89.
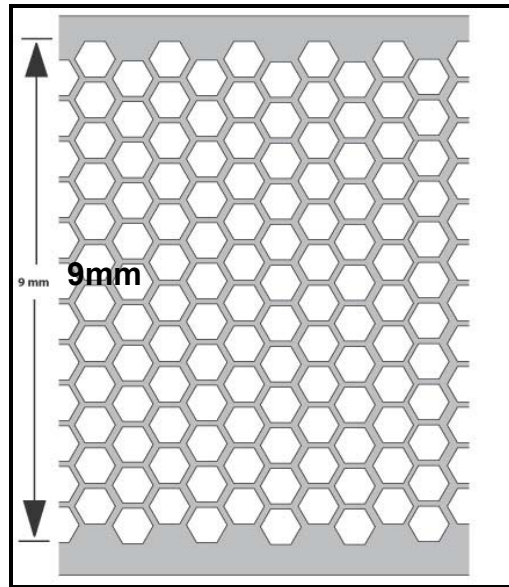
Figure 89 -- Insect screen section of regular hexagons in staggered pattern used in detectors.

The hexagons were approximated as area equivalent squares for the purposes of conforming to the screen model shown in Figure 88. The process of converting the regular hexagon into an area equivalent square is illustrated in Figure 90.
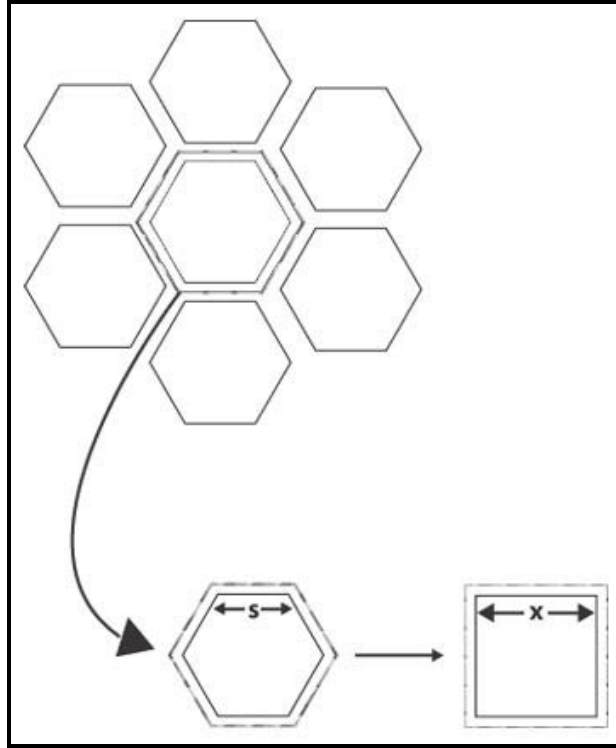
Figure 90 -- Converting regular hexagon into area equivalent square.

The area of a regular hexagon is (Beyer, 1991)

$$A_{hexagon} = 2.59808s^2$$

(314)

Where s is the length of each side of the regular hexagon.

The area of a square is

$$A_{square} = x^2$$

(315)

324

The areas are set equal to each other and the square root of each side is taken. Therefore, the length of each side of the square corresponding to the area equivalent of a regular hexagon is

$$x = 1.61186s$$

(316)

The outer portions of the regular hexagons in the insect screen have sides that were scaled as 0.442mm. The inner portions of the regular hexagons in the insect screen have sides that were scaled as 0.360mm. These sides of the regular hexagon are converted into an area equivalent square with sides that are 0.7124mm and 0.5803mm, respectively.

The screen dimensions m and n are equal to each other and have a value of 0.7124mm. The screen dimension d is computed from the difference between the outer and inner squares and has a value of 0.1321mm.

Therefore, the screen porosity is computed to be

$$\alpha = \frac{(m-d)(n-d)}{mn} = \frac{(0.7124-0.1321)(0.7124-0.1321)}{(0.7124)(0.7124)} = 0.664$$

(317)

Substituting this value for screen porosity in the general expression for the resistance factor

325

$$R = \left(\frac{1-\alpha^2}{\alpha^2}\right) f\left(\mathrm{Re}_d\right) = \left(\frac{1-\left(0.664\right)^2}{0.664^2}\right) f\left(\mathrm{Re}_d\right)$$

$$(318)$$

$$R = 1.268 f\left(\mathrm{Re}_d\right)$$

$$(319)$$

Substituting this expression into the relationship between the nondimensional velocity and resistance factor leads to the following

$$\frac{\overline{V}_{int}}{\overline{V}_{ext}} = 1.268 f\left(\mathrm{Re}_d\right)$$

$$(320)$$

The functional dependence upon the Reynolds number was determined by plotting the nondimensional velocity against the resistance factor terms. This plot, shown in Figure 91, indicated a linear relationship. A linear curve fit was applied with the constraint that the y intercept being equal to zero. This constraint satisfies the condition that as the Reynolds number approaches zero, the nondimensional velocity ratio goes to zero.
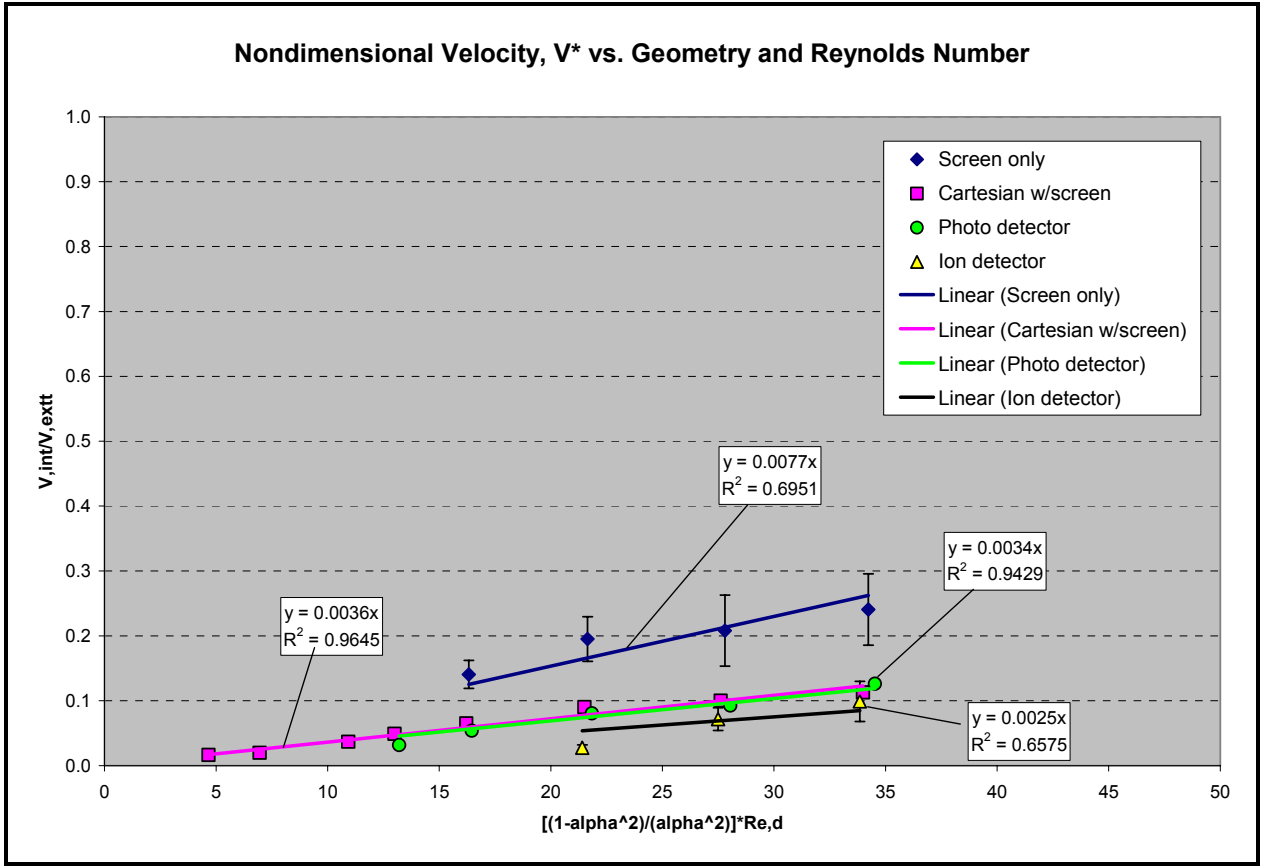
Figure 91 -- Nondimensional velocity plotted against the product of the porosity function and wire Reynolds number.

The error bars shown for the insect screen in isolation represents one statistical standard deviation in the associated velocity measurement and is used as estimate of the measurement uncertainty. The error bars indicate that the linear curve fit is within the measurement uncertainty despite the relatively poor correlation coefficient. However, this poor degree of correlation can be partially attributed to the limited number of data points collected. Likewise, the limited number of data points collected for the ionization detector can be partially attributed to the poor degree of correlation as indicated by the R^2 value for the linear curve fit.

The following functional relationships resulted from the linear curve fitting procedure as shown above. The corresponding screen porosity and range of screen Reynolds numbers are indicated for each relationship.

Insect Screen in Isolation

$$\frac{\bar{V}_{int}}{\bar{V}_{ext}} = 0.0077\left[\left(\frac{1-\alpha^2}{\alpha^2}\right)\mathrm{Re}_d\right] \ for \ \alpha = 0.664 \ and \ 16 < \mathrm{Re}_d < 27$$

(321)

Rectangular Model Detector with Insect Screen

$$\frac{\bar{V}_{int}}{\bar{V}_{ext}} = 0.0036\left[\left(\frac{1-\alpha^2}{\alpha^2}\right)\mathrm{Re}_d\right] \ for \ \alpha = 0.664 \ and \ 5 < \mathrm{Re}_d < 34$$

(322)

Photoelectric Detector

$$\frac{\bar{V}_{int}}{\bar{V}_{ext}} = 0.0034\left[\left(\frac{1-\alpha^2}{\alpha^2}\right)\mathrm{Re}_d\right] \ for \ \alpha = 0.664 \ and \ 10 < \mathrm{Re}_d < 27$$

(323)

Ionization Detector

$$\frac{\bar{V}_{int}}{\bar{V}_{ext}} = 0.0025\left[\left(\frac{1-\alpha^2}{\alpha^2}\right)\mathrm{Re}_d\right] \ for \ \alpha = 0.664 \ and \ 17 < \mathrm{Re}_d < 27$$

(324)

References

Baines, W.D., E.G. Peterson, "An Investigation of Flow Through Screens," *Transactions of the ASME*, vol. 73, pp.467-480, (1951).

Brundrett, E., "Prediction of pressure drop for incompressible flow through screens," *Journal of Fluids Engineering*, 155(2), pp. 239-242, (1993).

Munson, B.R., D.F. Young, T.H. Okiishi, *Fundamentals of Fluid Mechanics, 2nd Edition*, John Wiley & Sons, New York, NY, (1994).

Munson, B.R., "Very Low Reynolds Number Flow Through Screens," *Journal of Fluids Engineering*, Vol. 110, pp. 462-463, (1988).

Schetz, J.A., A.E. Fuhs, *Fundamentals of Fluid Mechanics*, John Wiley & Sons, New York, NY, (1999).

Appendix C.4: Nondimensionalization

The following characteristic quantities were used to define the nondimensional variables for the governing equations as well as boundary and initial conditions for the problem. The characteristic quantities that are listed are found in the governing equations and boundary and initial conditions.

U fully developed internal velocity

L length of sensing chamber

h height of sensing chamber

$\rho_{A,\max}$ maximum concentration of aerosol

p_{stag} stagnation point pressure

t_c characteristic time (to be determined in analysis)

The nondimensional variables are

$$v_x^* = \frac{v_x}{U}$$

$$x^* = \frac{x}{L}$$

$$z^* = \frac{z}{h}$$

$$p^* = \frac{p}{p_{stag}}$$

$$\rho_A^* = \frac{\rho_A}{\rho_{A,\max}}$$

$$t^* = \frac{t}{t_c}$$

The variables can be expressed by rearranging the nondimensional variables into the following format to be substituted into the simplified governing equations.

$$v_x = v_x^* U$$

$$x = x^* L$$

$$z = z^* h$$

$$p = p^* p_{stag}$$

$$\rho_A = \rho_A^* \rho_{A,\max}$$

$$t = t^* t_c$$

The simplified governing equations are nondimensionalized in the following manner.

Continuity

$$\frac{\partial v_x}{\partial x} = 0$$

(325)

Substituting the rearranged nondimensional terms

$$\frac{\partial \left(v_x^* U \right)}{\partial \left(x^* L \right)} = 0$$

(326)

The characteristic quantities for freestream velocity and length in the x direction are constants and, therefore, can be factored out of the partial derivative.

$$\left[\frac{U}{L} \right] \frac{\partial v_x^*}{\partial x^*} = 0$$

(327)

Both sides of the equation can be divided by the constants and leads to the following result for the nondimensional continuity equation.

$$\boxed{\frac{\partial v_x^*}{\partial x^*} = 0}$$

(328)

Species

The simplified species governing equation is

$$\frac{\partial \rho_A}{\partial t} + v_x \frac{\partial \rho_A}{\partial x} - D_A \left(\frac{\partial^2 \rho_A}{\partial x^2} \right) = 0$$

(329)

Substituting the rearranged nondimensional values into the species equation yields

$$\frac{\partial\left(\rho_A^* \rho_{A,\max}\right)}{\partial\left(t^* t_c\right)}+\left(v_x^* U\right)\frac{\partial\left(\rho_A^* \rho_{A,\max}\right)}{\partial\left(x^* L\right)}-D_A\left(\frac{\partial^2\left(\rho_A^* \rho_{A,\max}\right)}{\partial\left(x^* L\right)^2}\right)=0$$

(330)

The characteristic quantities are constants that can be factored out in the following manner

$$\left[\frac{\rho_{A,\max}}{t_c}\right]\frac{\partial\rho_A^*}{\partial t^*}+\left[\frac{U\rho_{A,\max}}{L}\right]v_x^*\frac{\partial\rho_A^*}{\partial x^*}-\left[\frac{D_A\rho_{A,\max}}{L^2}\right]\left(\frac{\partial^2\rho_A^*}{\partial x^{*2}}\right)=0$$

(331)

Both sides can be divided by the maximum species concentration

$$\left[\frac{1}{t_c}\right]\frac{\partial\rho_A^*}{\partial t^*}+\left[\frac{U}{L}\right]v_x^*\frac{\partial\rho_A^*}{\partial x^*}-\left[\frac{D_A}{L^2}\right]\left(\frac{\partial^2\rho_A^*}{\partial x^{*2}}\right)=0$$

(332)

Both sides can be divided by the fully developed internal velocity

$$\left[\frac{1}{t_c U}\right]\frac{\partial\rho_A^*}{\partial t^*}+\left[\frac{1}{L}\right]v_x^*\frac{\partial\rho_A^*}{\partial x^*}-\left[\frac{D_A}{L^2 U}\right]\left(\frac{\partial^2\rho_A^*}{\partial x^{*2}}\right)=0$$

(333)

The group of characteristic quantities for the diffusive term contains the Peclet number, where $\mathrm{Pe}=\dfrac{UL}{D_A}$

333

$$\left[\frac{1}{t_c U}\right]\frac{\partial \rho_A^*}{\partial t^*} + \left[\frac{1}{L}\right]v_x^* \frac{\partial \rho_A^*}{\partial x^*} - \left[\frac{1}{PeL}\right]\left(\frac{\partial^2 \rho_A^*}{\partial x^{*2}}\right) = 0$$

(334)

Both sides of the nondimensional equation can be multiplied by the fully developed internal velocity in order to isolate the characteristic time associated with the storage term.

$$\boxed{\left[\frac{1}{t_c}\right]\frac{\partial \rho_A^*}{\partial t^*} + \left[\frac{U}{L}\right]v_x^* \frac{\partial \rho_A^*}{\partial x^*} - \left[\frac{U}{PeL}\right]\left(\frac{\partial^2 \rho_A^*}{\partial x^{*2}}\right) = 0}$$

(335)

Momentum

The simplified governing equation for the conservation of momentum is

$$\frac{\partial v_x}{\partial t} + \frac{1}{\rho}\frac{\partial p}{\partial x} - \nu\left(\frac{\partial^2 v_x}{\partial z^2}\right) = 0$$

(336)

The rearranged nondimensional terms can be substituted in the following manner

$$\frac{\partial \left(v_x^* U\right)}{\partial \left(t^* t_c\right)} + \frac{1}{\rho}\frac{\partial \left(p^* p_{stag}\right)}{\partial \left(x^* L\right)} - \nu\left(\frac{\partial^2 \left(v_x^* U\right)}{\partial \left(z^* h\right)^2}\right) = 0$$

(337)

The associated constants can be factored out to yield

$$\left[\frac{U}{t_c}\right]\frac{\partial v_x^*}{\partial t^*}+\left[\frac{p_{stag}}{\rho L}\right]\frac{\partial p^*}{\partial x^*}-\left[\frac{\nu U}{h^2}\right]\left(\frac{\partial^2 v_x^*}{\partial z^{*2}}\right)=0$$

(338)

Both sides can be divided by the fully developed internal velocity squared

$$\left[\frac{1}{t_c U}\right]\frac{\partial v_x^*}{\partial t^*}+\left[\frac{p_{stag}}{\rho U^2 L}\right]\frac{\partial p^*}{\partial x^*}-\left[\frac{\nu}{U h^2}\right]\left(\frac{\partial^2 v_x^*}{\partial z^{*2}}\right)=0$$

(339)

The pressure term contains the Euler number, where $Eu=\dfrac{p_{stag}}{\rho U^2}$, and the viscous term

contains the Reynolds number with respect to the height dimension, where $Re_h=\dfrac{Uh}{\nu}$

$$\left[\frac{1}{t_c U}\right]\frac{\partial v_x^*}{\partial t^*}+\left[\frac{Eu}{L}\right]\frac{\partial p^*}{\partial x^*}-\left[\frac{1}{Re_h h}\right]\left(\frac{\partial^2 v_x^*}{\partial z^{*2}}\right)=0$$

(340)

Both sides can be multiplied by the fully developed internal velocity in order to isolate

the characteristic time for the nondimensional momentum equation

$$\boxed{\left[\frac{1}{t_c}\right]\frac{\partial v_x^*}{\partial t^*}+\left[\frac{Eu\,U}{L}\right]\frac{\partial p^*}{\partial x^*}-\left[\frac{U}{Re_h h}\right]\left(\frac{\partial^2 v_x^*}{\partial z^{*2}}\right)=0}$$

(341)

The boundary and initial conditions can be nondimensionalized in the following manner.

The following boundary conditions apply to both scenarios

1. No slip boundary at walls

$$v_x\big|_{z=-\frac{h}{2},\frac{h}{2}} = 0$$

(342)

Substituting the rearranged nondimensional variables leads to

$$\left(v_x^* U\right)\big|_{z^* h=-\frac{h}{2},\frac{h}{2}} = 0$$

(343)

The freestream velocity is a constant. Dividing both sides of the boundary condition equation by the freestream velocity and dividing the evaluation point by the vertical height yields

$$\boxed{\left(v_x^*\right)\big|_{z^*=-\frac{1}{2},\frac{1}{2}} = 0}$$

(344)

2. Pressure at control volume boundary

$$p\big|_{x=0} = p_{ext} - \frac{1}{2} K_{lumped}\, \rho U_\infty^2$$

(345)

Substituting the rearranged nondimensional terms

336

$$\left. \left(p^* p_{stag} \right) \right|_{x^* L = 0} = p_{ext} - \frac{1}{2} K_{lumped} \rho U_\infty^2$$

(346)

Dividing both sides by the stagnation point pressure and the evaluation point by length

$$\boxed{\left. p^* \right|_{x^* = 0} = \frac{p_{ext} - \frac{1}{2} K_{lumped} \rho U_\infty^2}{p_{stag}}}$$

(347)

3. Steady external velocity

$$\left. v_x \right|_{x=0} = U$$

(348)

Substituting the rearranged nondimensional terms

$$\left. \left(v_x^* U \right) \right|_{x^* L = 0} = U$$

(349)

Dividing both sides by the fully developed internal velocity and the evaluation point by length yields

$$\boxed{\left. \left(v_x^* \right) \right|_{x^* = 0} = 1}$$

(350)

Initial Conditions

1. No aerosol inside sensing chamber control volume

$$\rho_A\big|_{x>0} = 0 \text{ at } t = 0$$

(351)

Substituting the rearranged nondimensional terms

$$\left(\rho_A^* \rho_{A,\max}\right)\big|_{x^* L > 0} = 0 \text{ at } \left(t^* t_c\right) = 0$$

(352)

Dividing both sides by the maximum species concentration, the evaluation point by length, and the time specification by characteristic time results in

$$\boxed{\left(\rho_A^*\right)\big|_{x^*>0} = 0 \text{ at } t^* = 0}$$

(353)

For step exposure scenarios

Boundary Conditions

4a. Constant inlet species concentration (species A)

$$\rho_A\big|_{x=0} = \rho_{A,\max}$$

(354)

Substituting the rearranged nondimensional terms

$$\left(\rho_A^* \rho_{A,\max}\right)\Big|_{x^*L=0} = \rho_{A,\max}$$

(355)

Dividing both sides by the maximum species concentration and the evaluation point by length leads to

$$\boxed{\left(\rho_A^*\right)\Big|_{x^*=0} = 1}$$

(356)

Initial Conditions

2a. No initial flow field inside sensing chamber control volume

$$v_x\Big|_{x>0} = 0 \text{ at } t = 0$$

(357)

Substituting the rearranged nondimensional terms

$$\left(v_x^* U\right)\Big|_{x^*L>0} = 0 \text{ at } \left(t^* t_c\right) = 0$$

(358)

Dividing both sides by the fully developed internal velocity, the evaluation point by length, and the time specification by the characteristic time leads to

$$\boxed{\left(v_x^*\right)\Big|_{x^*>0} = 0 \text{ at } t^* = 0}$$

(359)

For ramp exposure scenarios

Boundary Conditions

4b. Time-dependent inlet mass fraction of aerosol (species A) which is linear from time zero until the steady state concentration is reached.

The ramp portion is

$$\rho_A\big|_{x=0} = \frac{\rho_{A,\max}}{t_{ss}} t \quad \text{for} \ \ 0 \le t \le t_{ss}$$

(360)

Substituting the rearranged nondimensional terms

$$\left(\rho_A^* \rho_{A,\max}\right)\big|_{x^* L=0} = \frac{\rho_{A,\max}}{t_{ss}}\left(t^* t_c\right) \quad \text{for} \ \ 0 \le \left(t^* t_c\right) \le t_{ss}$$

(361)

Dividing both sides by the maximum species concentration, the evaluation point by length, and the time specification by the characteristic time results in

$$\boxed{\left(\rho_A^*\right)\big|_{x^*=0} = \frac{t^* t_c}{t_{ss}} \quad \text{for} \ \ 0 \le \left(t^*\right) \le \left(\frac{t_{ss}}{t_c}\right)}$$

(362)

The steady state portion is

$$\rho_A\big|_{x=0} = \rho_{A,\max} \quad \text{for} \ \ t > t_{ss}$$

(363)

340

Substituting the rearranged nondimensional terms

$$\left(\rho_A^* \rho_{A,\max} \right)\Big|_{x^* L = 0} = \rho_{A,\max} \quad \text{for} \quad \left(t^* t_c \right) > t_{ss}$$

(364)

Dividing both sides by maximum concentration, the evaluation point by length, and the time specification by the characteristic time yields

$$\boxed{\left(\rho_A^* \right)\Big|_{x^* = 0} = 1 \quad \text{for} \quad \left(t^* \right) > \left(\frac{t_{ss}}{t_c} \right)}$$

(365)

Initial Conditions

2b. Steady state velocity field inside sensing chamber control volume

$$v_x \Big|_{x>0,z} = v_{ss}(x,z) \quad \text{at} \quad t = 0$$

(366)

Substituting the rearranged nondimensional terms

$$\left(v_x^* U \right)\Big|_{x^* L > 0, z^* h} = v_{ss}(x,z) \quad \text{at} \quad \left(t^* t_c \right) = 0$$

(367)

Dividing both sides by fully developed internal velocity, the evaluation point by length, and the time specification by the characteristic time results in

341

$$\left. \left(v_x^* \right) \right|_{x^* > 0, z^* h} = \frac{v_{ss}(x, z)}{U} \text{ at } \left(t^* \right) = 0$$

(368)

Appendix C.5: Numerical Method Preliminaries

Finite Difference Method

The linear advection equation can be solved using the Lax-Wendroff finite differencing scheme which is an explicit method that is second order accurate (Iserles, 1996)

$$u_j^{n+1} = u_j^n - \alpha\Delta t \frac{u_{j+1}^n - u_{j-1}^n}{2\Delta x} + \frac{1}{2}(\alpha\Delta t)^2 \frac{u_{j-1}^n - 2u_j^n + u_{j+1}^n}{(\Delta x)^2}$$

(369)

The superscripts refer to the current time step, $n+1$, and the previous time step, n, while the subscripts refer to computational nodes before, $j-1$, and after, $j+1$, the current node, j. A schematic representation of the Lax-Wendroff finite differencing method is illustrated in Figure 92.
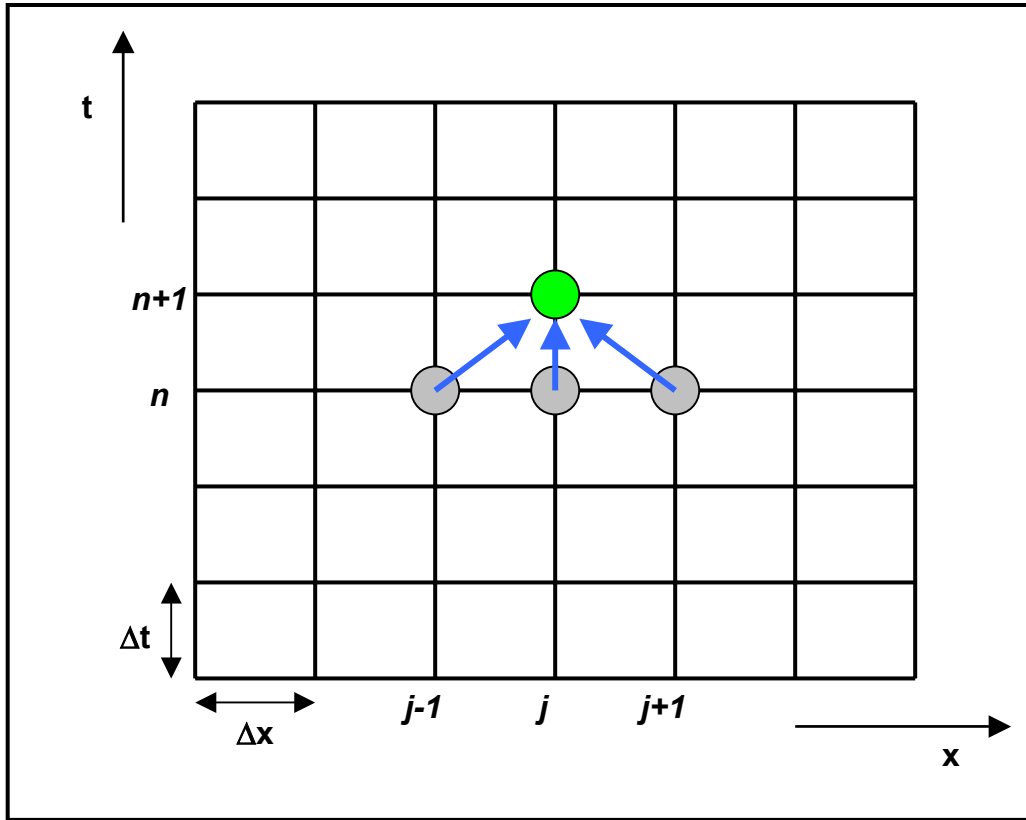
Figure 92 -- Schematic representation of Lax-Wendroff finite difference method.

The stability of finite difference solutions is dependent upon the relationship between the physical phenomenon, such as velocity or diffusion, and the discretization scheme in terms of time step, Δt, and computational node spacing, Δx. This relationship is known as the Courant-Friedrich-Levy (CFL) condition, or the Courant number. The CFL condition necessary for a stable solution of the Lax-Wendroff finite difference scheme is (Iserles, 1996)

$$|\alpha|\frac{\Delta t}{\Delta x} \leq 1$$

(370)

Therefore, in the context of this analysis the CFL condition will be used to select an appropriate time step for the known velocity and spatial discretization.

The Lax-Wendroff scheme and associated CFL condition are now expressed in terms of the species equation in order to clarify the nomenclature for the problem at hand. The Lax-Wendroff scheme for the simplified nondimensional form of the species equation is

$$\rho *_j^{n+1} = \rho *_j^n - v * \Delta t \frac{\rho *_{j+1}^n - \rho *_{j-1}^n}{2\Delta x} + \frac{1}{2}(v * \Delta t)^2 \frac{\rho *_{j-1}^n - 2\rho *_j^n + \rho *_{j+1}^n}{(\Delta x)^2}$$

(371)

The corresponding CFL condition becomes

$$|v *|\frac{\Delta t}{\Delta x} \le 1$$

(372)

It is assumed that the location of interest for the mass transport in smoke detectors is the center of the control volume. It is at this location that the sensing element is assumed to be monitoring the aerosol concentration.

Spatial Discretization

The appropriate number of computational nodes for solving the species equation was determined by examining the nature of the developing solution at nondimensional times, $t*$, of 0.33, 0.66, and 0.99. The linear space was discretized to provide 5 consistent interior monitor points as shown in Figure 93.

345
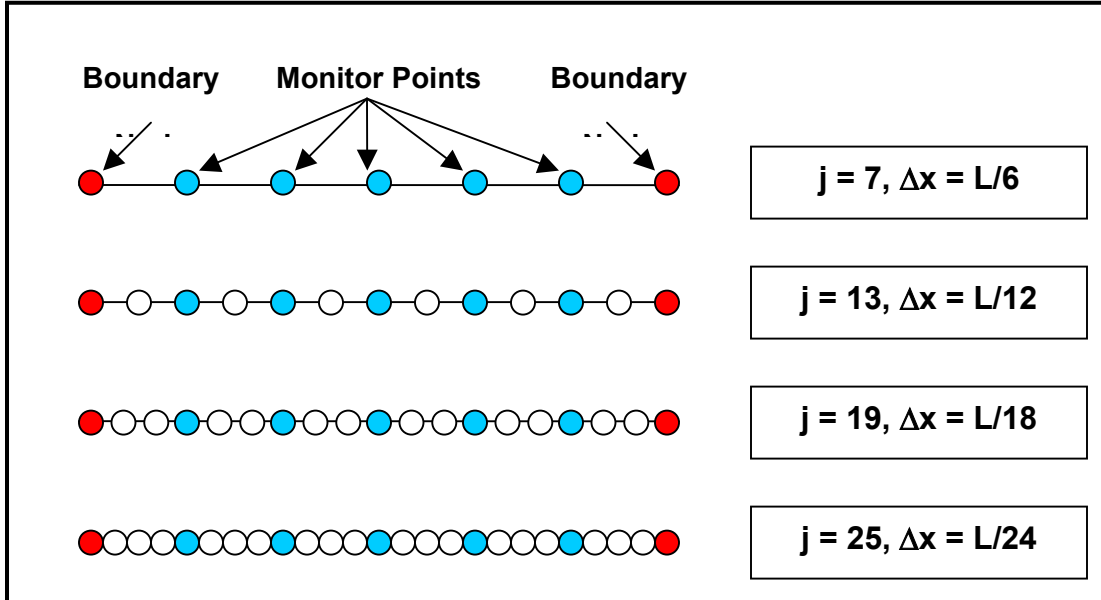
Figure 93 -- Spatial discretization approach to provide 5 consistent interior monitor points.

The initial number of computational nodes was 7 and provided 5 interior monitor points. The two boundary nodes were ignored because they are independent of spatial discretization, *i.e.*, the boundary condition value does not change by adding additional computational nodes. The spatial discretization was further refined by adding computational nodes in increments of 6 to preserve the location of the 5 interior monitor points. The impact of spatial discretization was examined with by using 7, 13, 19, 25, 31, and 37 computational nodes. Each level of refinement was assessed by computing the percent change in solution value relative to the previous node spacing. The percent change in solution, or *percent relative error*, was calculated in the following manner:

$$\% \text{ Relative Error} = 100\left(\frac{\left|X_{current} - X_{previous}\right|}{X_{previous}}\right)$$

(373)

The percent relative error for each level of refinement in spatial discretization was plotted at nondimensional times of 0.33, 0.66 and 0.99 and are shown in the Figures that follow.
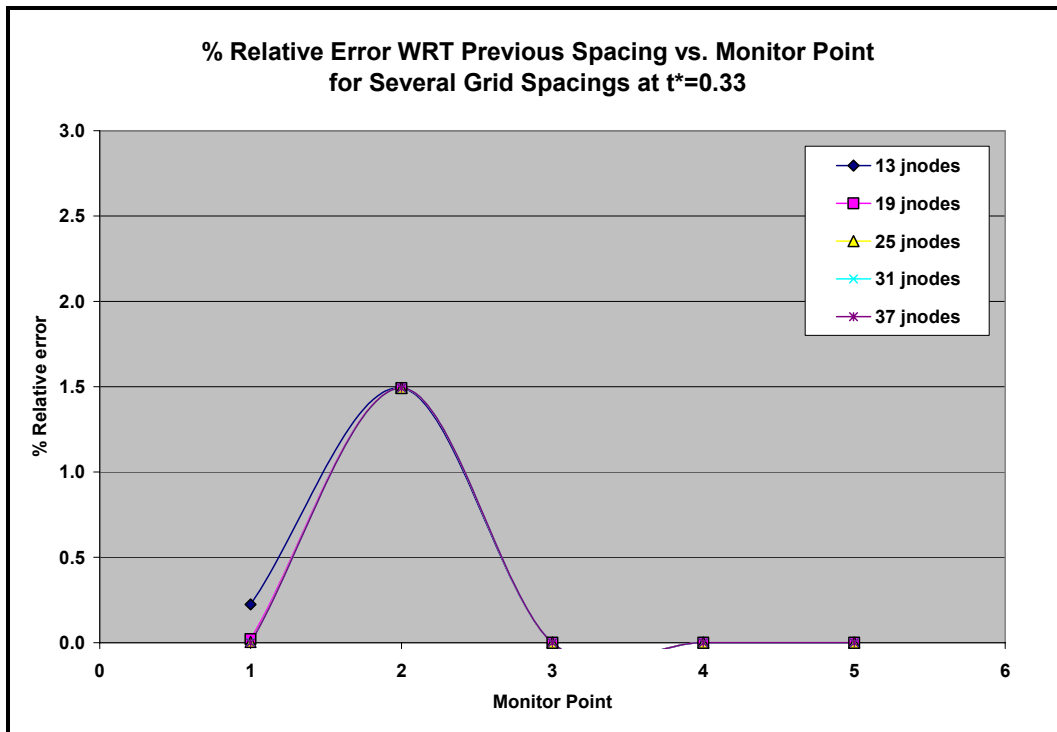
Figure 94 -- Relative error at each monitor point for several node spacings at t*=0.33.

Figure 94 shows that the general trend of the relative error is the same for all node spacings at the nondimensional time of 0.33. However, at monitor point 1, the relative error is minimized for spatial discretization of 19 nodes or more.

**% Relative Error WRT Previous Spacing vs. Monitor Point
for Several Grid Spacings at t*=0.66**
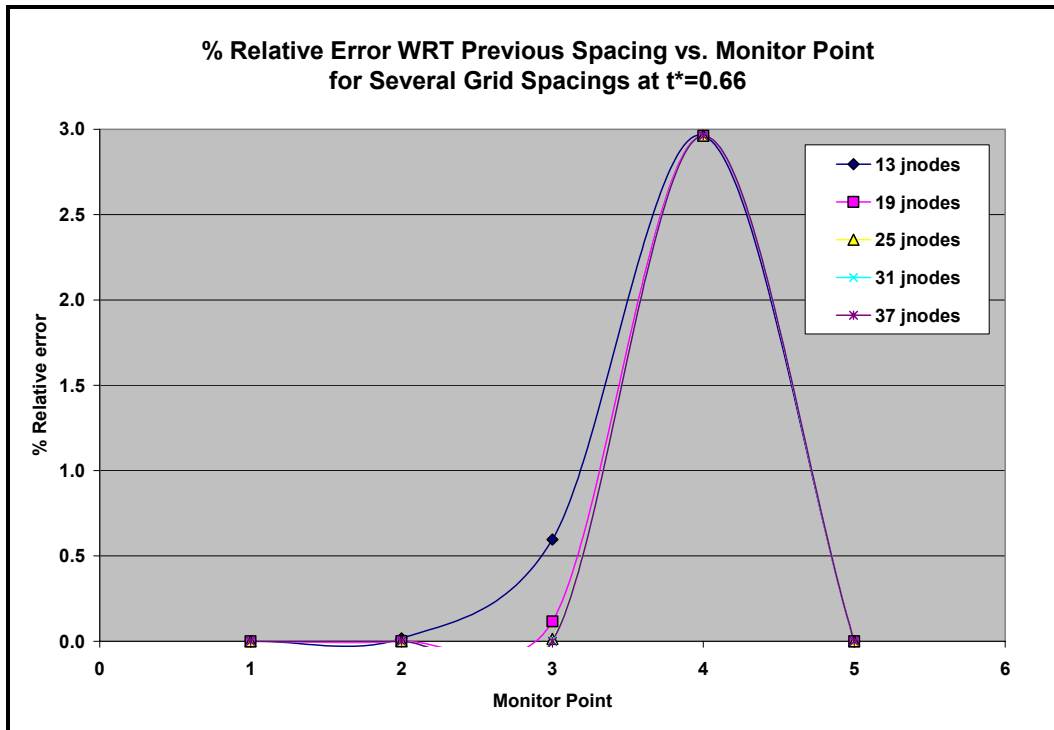
Figure 95 -- Relative error at each monitor point for several node spacings at t*=0.66.

Again, the general trend of the relative error in Figure 95 is the same for all node spacings at the nondimensional time of 0.66. However, at monitor point 3, the relative error is minimized for spatial discretization of 25 nodes or more.
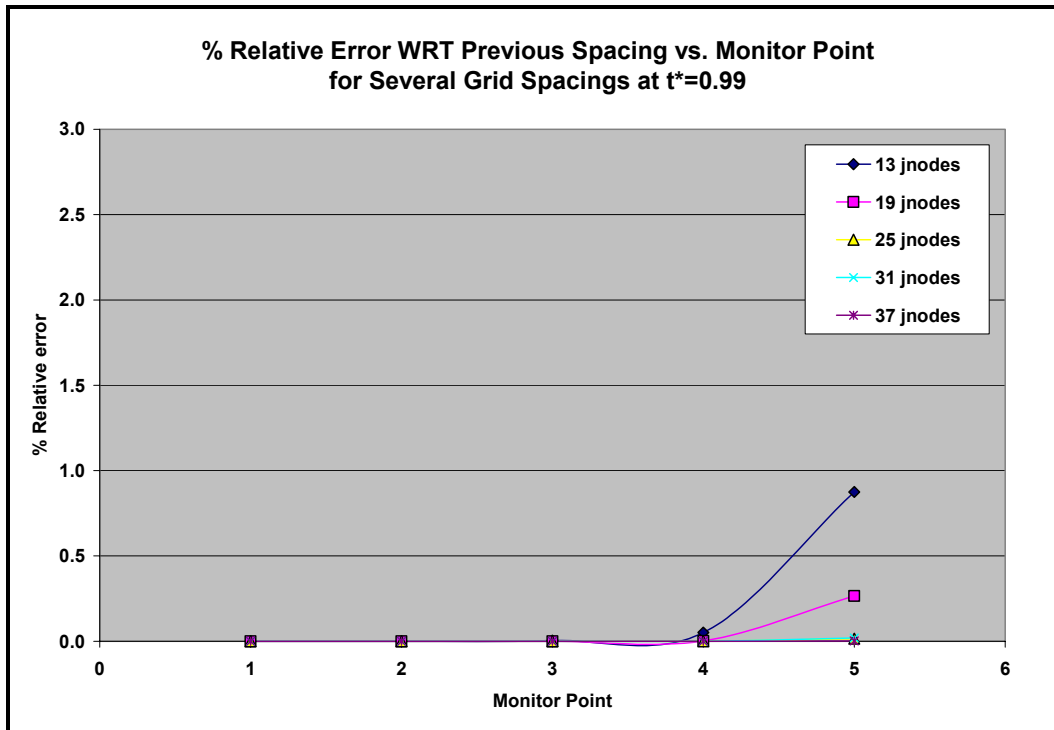
Figure 96 -- Relative error at each monitor point for several node spacings at t*=0.99.

The general trend of the relative error is the same at monitor points 1, 2, and 3 for all node spacings at the nondimensional time of 0.99, as shown in Figure 96. However, at monitor point 5, the relative error is minimized for spatial discretization of 25 nodes or more.

Based on the examination of relative error as a function of spatial discretization, a grid independent solution is expected for 25 nodes. This level of grid refinement minimizes the relative error in the finite difference solution. Additional grid refinement provides minimal improvement in relative error. Therefore, a spatial discretization of 25 computational nodes will be used in the Lax-Wendroff finite difference method for the mass transport model.

349

Inlet Boundary Condition

The nondimensional concentration at L/2, or x* = 0.5, was plotted against the nondimensional time to examine the impact of the concentration boundary condition at x=0, denoted as $\rho^*(0)$. The example shown in Figure 97 is for a nondimensional velocity of 0.2.
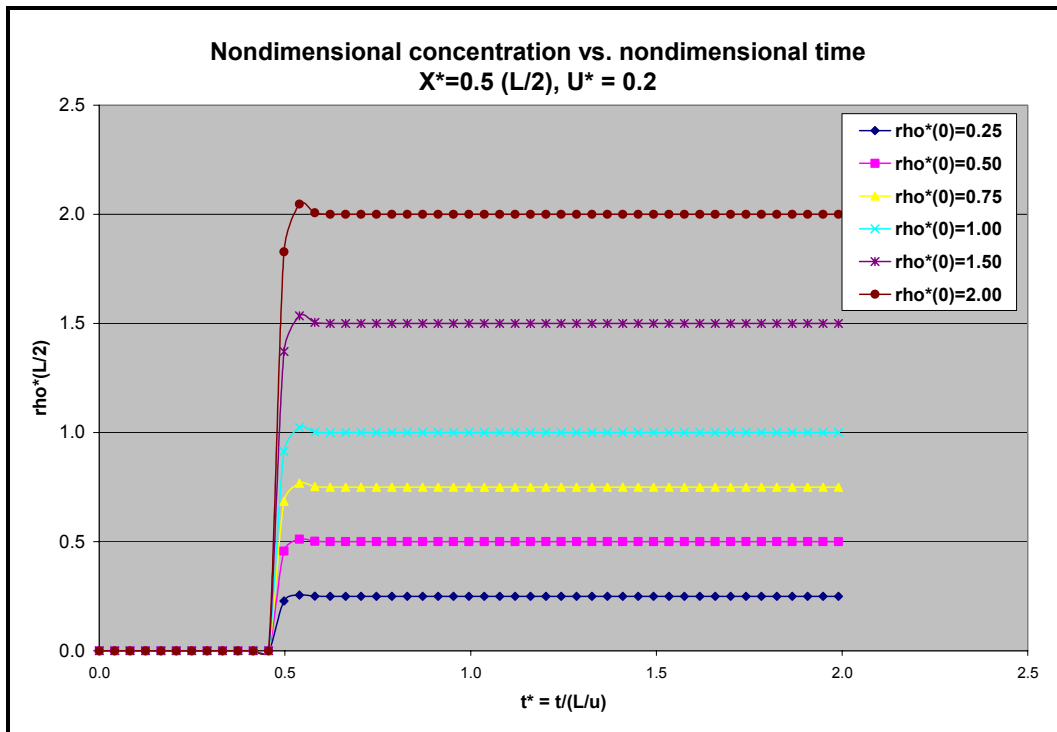
Figure 97 -- Nondimensional concentration at center of detector vs. nondimensional time.

Solution Sensitivity to Exit Boundary Condition

The analysis up to this point has assumed that the boundary condition for concentration at x=L is 0. The sensitivity of the finite difference solution to the boundary condition at X=L was examined to determine it importance. The inlet boundary condition was held

constant and the exit boundary condition was varied. The exit boundary condition would

be expected to have a minimum value of 0 and maximum value equal to the inlet

boundary condition. This upper bound would represent a smoke detector immersed in a

ceiling jet flow with a nominally uniform aerosol concentration.

The sensitivity analysis of the exit boundary condition assumes that the concentration is a

constant value expressed as a fraction of the inlet boundary condition. The sensitivity

analysis of the solution to the exit boundary condition considered the following values:

$$\rho*(L,t) = 0$$
$$\rho*(L,t) = 0.25\rho*(0,t)$$
$$\rho*(L,t) = 0.50\rho*(0,t)$$
$$\rho*(L,t) = 0.75\rho*(0,t)$$
$$\rho*(L,t) = 1.00\rho*(0,t)$$

The results of this sensitivity analysis are shown in Table 46.

Table 46 -- Sensitivity Analysis of Solution to Exit BC expressed as fraction of Inlet BC.

Exit BC: ρ^* (L) =	Inlet BC: ρ^* (0)=1				
	0*(ρ^* (0))	0.25*(ρ^* (0))	0.50*(ρ^* (0))	0.75*(ρ^* (0))	1.00*(ρ^* (0))
t*	ρ^* (L/2)	ρ^* (L/2)	ρ^* (L/2)	ρ^* (L/2)	ρ^* (L/2)
0.00	0	0	0	0	0
0.04	0	0	0	0	0
0.08	0	0	0	0	0
0.12	0	0	0	0	0
0.17	0	0	0	0	0
0.21	0	0	0	0	0
0.25	0	0	0	0	0
0.29	0	0	0	0	0
0.33	0	0	0	0	0
0.37	0	0	0	0	0
0.41	0	0	0	0	0
0.46	0	0	0	0	0
0.50	0.913759323	0.913759323	0.913759323	0.913759323	0.913759323
0.54	1.023136314	1.023136314	1.023136314	1.023136314	1.023136314
0.58	1.003156556	1.003156556	1.003156556	1.003156556	1.003156556
0.62	0.999706143	0.999706143	0.999706143	0.999706143	0.999706143
0.66	0.999936931	0.999936931	0.999936931	0.999936931	0.999936931
0.70	1.000002282	1.000002282	1.000002282	1.000002282	1.000002282
0.75	1.000000958	1.000000958	1.000000958	1.000000958	1.000000958
0.79	0.999999998	0.999999998	0.999999998	0.999999998	0.999999998
0.83	0.999999988	0.999999988	0.999999988	0.999999988	0.999999988
0.87	1	1	1	1	1
0.91	1	1	1	1	1
0.95	1	1	1	1	1
1.00	1	1	1	1	1
1.04	1	1	1	1	1

The results in Table 46 show that the numerical values of the solution (out to 9 decimal places) do not change for the exit boundary conditions evaluated in the sensitivity analysis. Therefore, the sensitivity analysis has demonstrated that the solution is not influenced by the specific value of the exit boundary condition. The exit boundary condition used in the mass transport model will be set equal to the value of the inlet boundary condition.

Solution Sensitivity to Inlet Velocity Boundary Condition

The internal velocity for the sensing chamber control volume has been assumed to be one-dimensional. The average value of the internal velocity has been used to represent the one-dimensional velocity. The actual velocity profile has been assumed to be a parabolic distribution consistent with laminar flow between two parallel plates. The assumption of a parabolic velocity distribution is based on findings from the fluid mechanics literature for flows through insect screens (Baines and Patterson, 1951) which were confirmed with LDV measurements of internal velocity (see Internal Velocity paper). The average velocity value was determined by integrating the parabolic velocity distribution and resulted in the average velocity being equal to 2/3 the maximum internal velocity.

The impact of the one-dimensional internal velocity assumption on the mass transport model solution was investigated by a sensitivity analysis. The mass transport model solution was evaluated for three different internal velocity values while holding all other variables constant. The baseline internal velocity was the average internal velocity, or 2/3 the maximum internal velocity. The baseline value was varied +50% and -50% to encompass an upper bound of the maximum internal velocity and a lower bound of 1/3 the maximum internal velocity.

The average value of the nondimensional concentration in the control volume was plotted as a function of time to examine the impact of the sensitivity analysis, as shown in Figure 98.
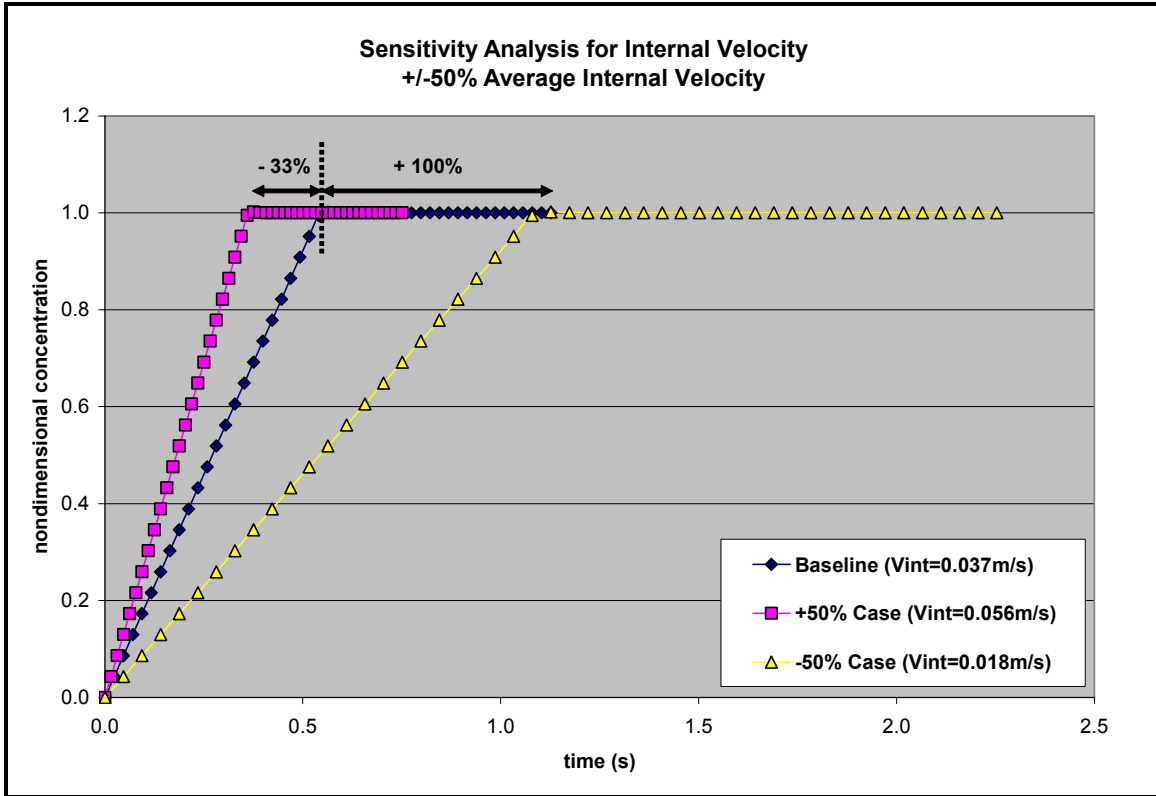
Figure 98 -- Sensitivity of nondimensional concentration to internal velocity.

The time for each scenario to reach a nondimensional concentration of unity was used to assess the relative impact of varying the inlet velocity. The inlet velocity values, nondimensional velocities, and response times for the sensitivity analysis are summarized in Table 47.

Table 47 -- Results of sensitivity analysis of time to steady state on internal velocity.

Scenario	V_{int} [m/s]	V*	$t(\rho^*_{avg}=1)$ [s]	%Variation in $t(\rho^*avg=1)$ WRT Baseline
Baseline	0.037	0.074	0.54	N/A
+50%	0.056	0.111	0.36	-33%
-50%	0.019	0.037	1.08	100%

Increasing the baseline velocity by 50% results in a 33% decrease in predicted response time relative to the baseline scenario. Decreasing the baseline velocity by 50% results in a 100% increase in predicted response time relative to the baseline scenario. This sensitivity analysis indicates that using the maximum internal velocity value in the mass transport model would result in underpredicting the response time of a smoke detector. Therefore, the use of maximum internal velocity could result in under-predicted smoke detector response times. In the context of using this mass transport model as an engineering tool for performance based engineering predictions, the maximum velocity value should not be used.

The sensitivity to internal velocity was also examined by investigating the time to steady state over a range of external velocities from 0.07 to 0.50 m/s which were consistent with the experimental conditions. The average value of nondimensional concentration for the control volume was plotted as a function of time for the photoelectric detector at each external velocity. The results of this investigation are shown in Figure 99.
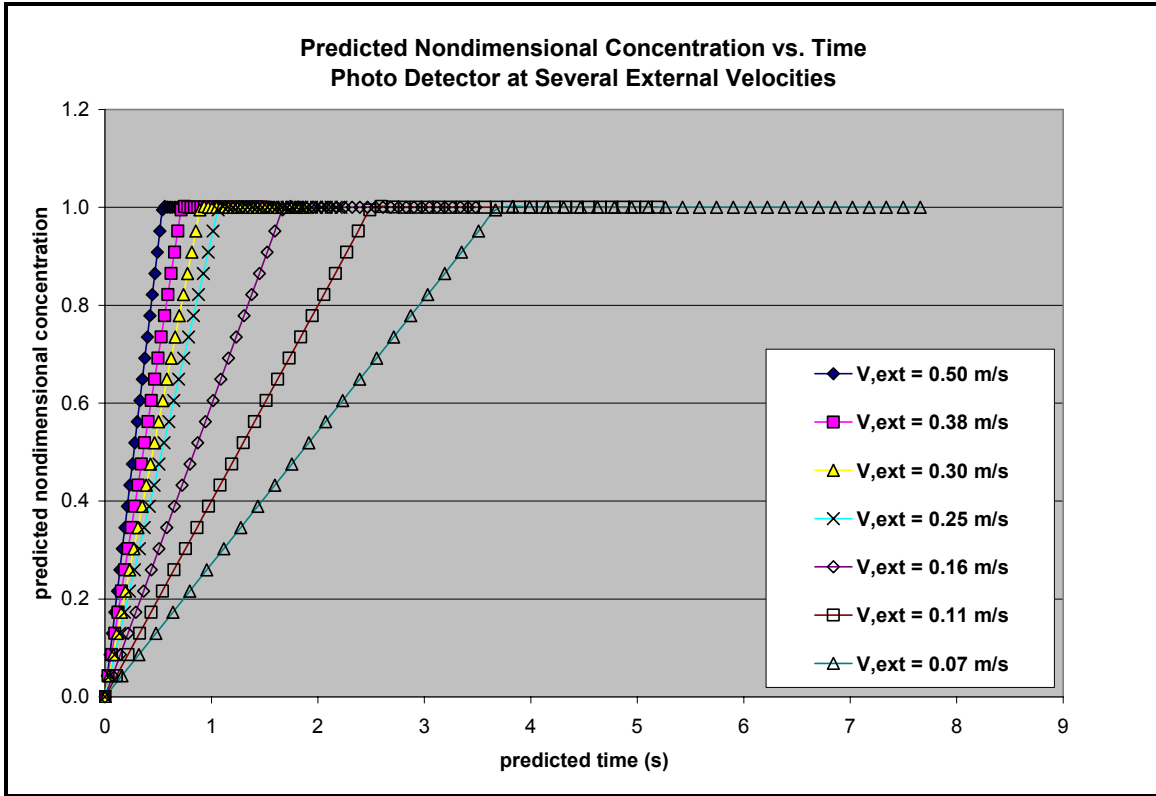
Figure 99 -- Nondimensional concentration vs time for photo detector at several external velocities.
The general trend indicated in Figure 99 is that, for a constant inlet concentration boundary condition, the average nondimensional concentration for the control volume increases linearly. The time for the average nondimensional concentration to reach steady state increases as external velocity decreases.

The time to steady state nondimensional concentration was plotted as a function of external velocity for the baseline and +50% and -50% internal velocity cases. The results are shown in Figure 100.
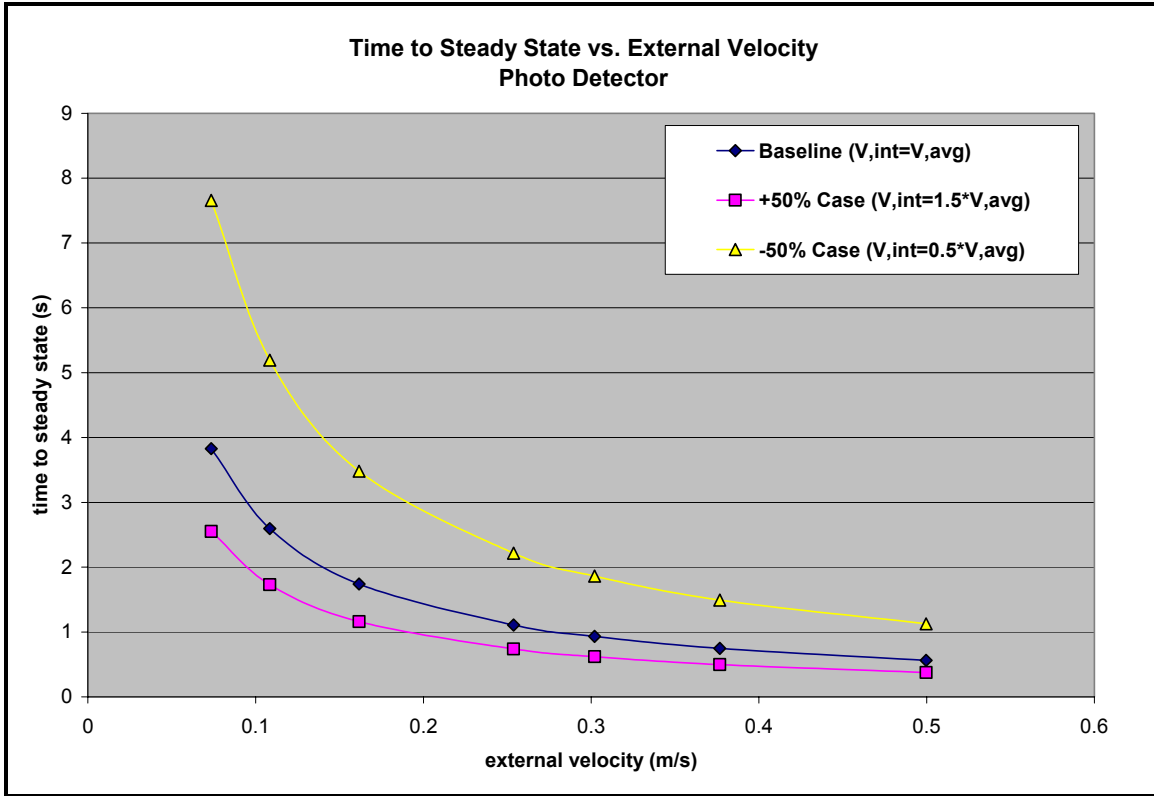
Figure 100 -- Time to steady state nondimensional concentration vs time for photo detector with sensitivity to internal velocity.

The general trend for the time to steady state versus time is exponential in nature. It should be noted that this behavior is similar to that observed by previous researchers such as Brozovsky and Bjorkman et al for detector response time as function of velocity.

The time to steady state nondimensional concentration for each inlet velocity variation were plotted against those for the baseline scenario as shown in Figure 101. A line representing an ideal 1:1 correspondence is shown with dashed lines representing the boundaries for +50% and -50% variation. Data points falling along this ideal fit line would indicate that the solution is insensitive to the inlet velocity variation. Data points within the 50% boundaries would indicate that the impact on the solution is of equal or

smaller magnitude than the input variation. Data points outside either 50% boundary would indicate that the solution the impact on the solution is of greater magnitude than the input variation.
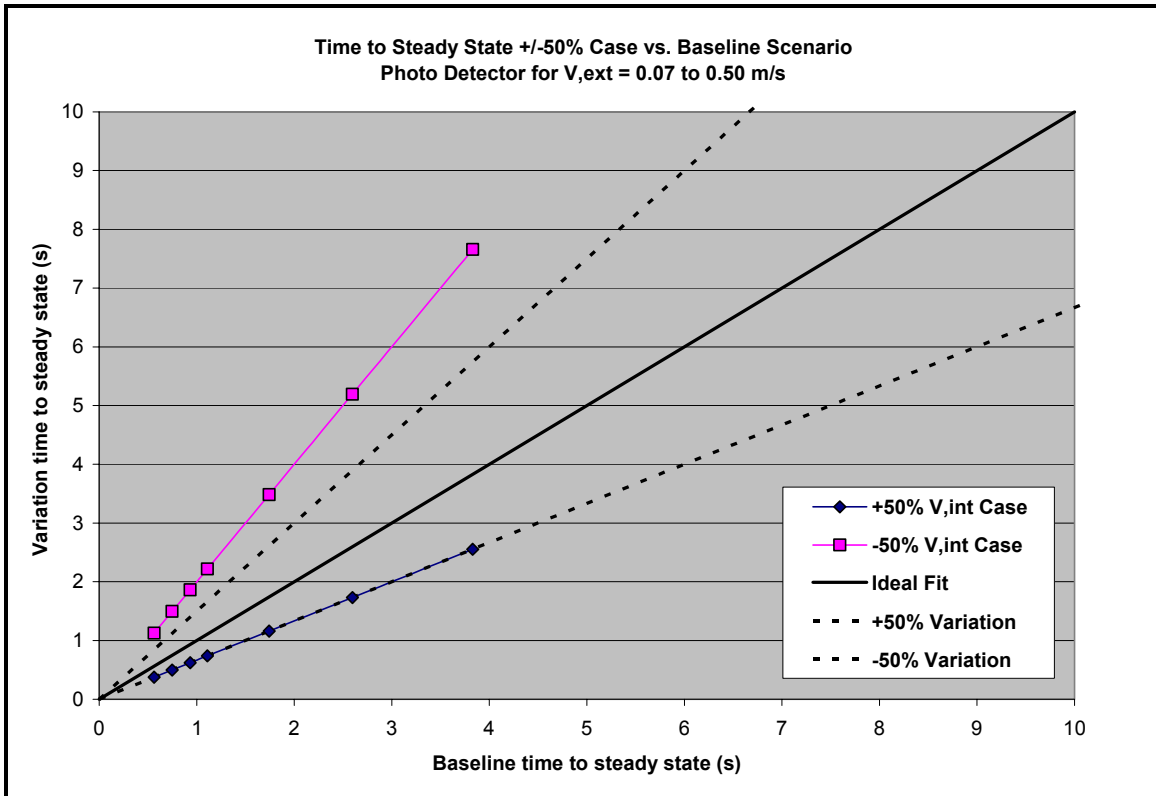
Figure 101 -- Time to steady state for variation and baseline cases.

It can be seen that for a +50% variation in average internal velocity the time to steady state is decreased by 50% relative to the baseline scenario. The impact of the +50% internal velocity variation on the solution is of the same magnitude. However, a -50% variation in average internal velocity the time to steady state is increased 100% relative to the baseline scenario. The impact of the -50% internal velocity variation on the solution is twice the magnitude. The input variation in this case is amplified in the solution by a factor of 2.

Appendix C.6: Transport Delay Outside Control Volume

The mass transport model considers a gas phase control volume inside the sensing chamber where fully developed flow conditions exist. The model predicts the time for the sensing chamber to exceed the alarm threshold for a given external velocity and external aerosol concentration. The experimentally determined detector response times from the step exposure tests involves additional transport delays that are not accounted for in the model. Therefore, it was necessary to account for these additional transport delays and adjust the response time predicted with the mass transport model accordingly. The additional delays include the time for the aerosol to be transported from the laser transmittance measurement location to the leading edge of the detector and the time for the aerosol to be transported from the leading edge of the detector to the leading boundary of the gas phase control volume. The nominal distance between the laser transmittance location and the leading edge of the detector was 3 cm. The aerosol was assumed to travel at the average velocity for the external and internal flow conditions. The distance from the leading edge of the detector to the leading edge of the control volume was based on the findings of Baines and Peterson (1951). Flow conditions can be considered fully developed at a distance 5-10 screen diameters downstream of the insect screen [Baines and Peterson, 1951]. The insect screens in this study had openings approximately 0.58mm in diameter which would correspond to fully developed flow conditions existing at a distance between 2.9 and 5.8mm downstream from the screen. The upper limit of 5.8mm was used in calculating the associated transport delay.
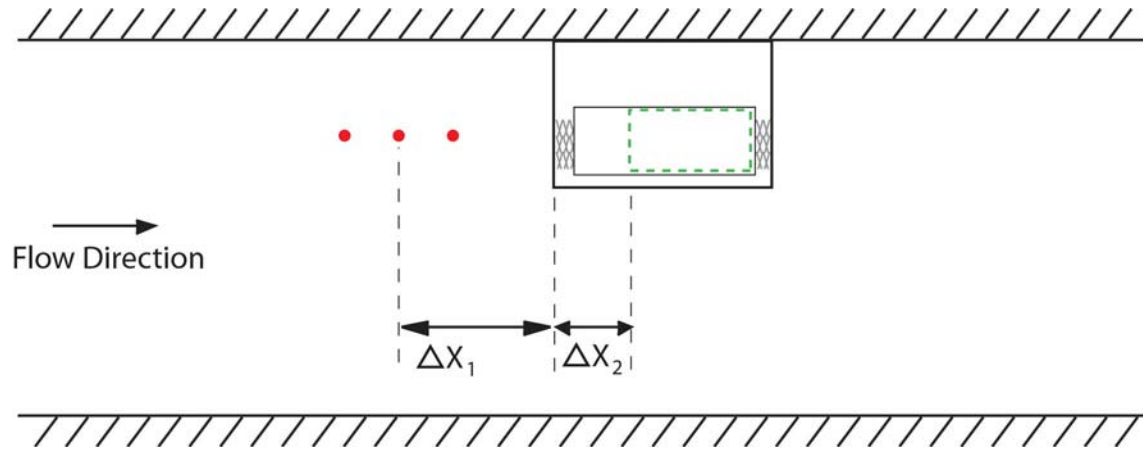
Figure 102 -- Transport delays outside of sensing chamber control volume.

$$t_{response} = t_{transport,ext} + t_{transport,int} + t_{model} \qquad (374)$$

The transport time for each segment was calculated in the following manner.

$$t_{transport,ext} = \frac{\Delta x_1}{\bar{V}_{ext}} \; ; \; t_{transport,int} = \frac{\Delta x_2}{\bar{V}_{int}} \qquad (375)$$

The resulting transport delay times for the photoelectric and ionization detectors are summarized in the tables that follow.

Table 48 –Transport delay times outside control volume for photo detector.

Photoelectric Detector		
$V_{avg,ext}$ (m/s)	$V_{avg,int}$ (m/s)	$t_{transport}$ (s)
0.500	0.037	0.217
0.377	0.021	0.355
0.302	0.014	0.527
0.254	0.010	0.725
0.162	0.004	1.681
0.108	0.002	3.601
0.074	0.001	7.637

Table 49 – Transport delay times outside control volume for ion detector.

Ionization Detector		
$V_{avg,ext}$ (m/s)	$V_{avg,int}$ (m/s)	$t_{transport}$ (s)
0.490	0.026	0.283
0.369	0.015	0.471
0.296	0.010	0.707
0.249	0.007	0.979
0.158	0.003	2.306
0.106	0.001	4.988
0.072	0.001	10.649

Figure 103 -- Transport delay time to reach sensing chamber control volume as a function of external velocity for photo and ion detectors.

These values were used to adjust the response time predicted with the mass transport model in accordance with Equation 374.

Appendix C.7: Smoke Concentration Calculation

A comparison was made between the interior and exterior smoke concentrations that were measured during the detector exposure tests. The exterior smoke concentration was derived from the laser transmittance value measured by a Helium-Neon laser. The interior smoke concentration was derived from the smoke detector output which is expressed in terms of %Ob/ft per UL 217/268. The purpose of this comparison was to determine if the assumption that the interior and exterior smoke concentrations are equal under steady state conditions is appropriate. The derivation of smoke concentration from the laser transmittance and the detector output are presented. The derivations express the product of the extinction coefficient and concentration as a function of the measured quantities of laser transmittance and percent obscuration per foot, respectively. The product of extinction coefficient and concentration was used because the extinction coefficient, which depends upon aerosol type and wavelength of light used to make the measurement, was not explicitly measured in this study. A comparison between the derived smoke concentration values was made for both the photoelectric and ionization smoke detectors evaluated in this study.

The exterior smoke concentration was derived from the laser transmittance measurement made across the duct near the entrance region. The transmittance, τ, through a medium over a pathlength, L, is

$$\tau = \left(\frac{I}{I_o}\right) = e^{-kCL}$$

(376)

Where, I is the intensity of light, I_o is the intensity of the light source, k is the coefficient of absorption of the particular aerosol, and C is the smoke concentration. Transmittance was measured in the experiments over a known pathlength of 5 ft. The product of the absorption coefficient and concentration was determined by arranging the transmittance equation into the following format by taking the natural log of both sides.

$$\ln(\tau) = -kCL$$

(377)

The product of the absorption coefficient and concentration is

$$\boxed{kC = -\frac{\ln(\tau)}{L}}$$

(378)

The interior smoke concentration was derived from the smoke detector sensor output expressed in units of percent obscuration per foot, $\%O_u$. Percent obscuration per unit length is expressed as a function of the transmittance through the medium and the pathlength.

$$\%O_u = 100 \left[1 - \left(\frac{I}{I_o} \right)^{1/L} \right]$$

(379)

363

The ratio of light intensity relative to the source intensity is the transmittance, as shown in Equation 376. Substituting this expression yields:

$$\frac{\%O_u}{100} = \left[1 - \left(e^{-kCL} \right)^{1/L} \right]$$

(380)

The pathlengths cancel each other out.

$$\frac{\%O_u}{100} = \left[1 - \left(e^{-kC} \right) \right]$$

(381)

Rearranging the previous expression results in the following:

$$e^{-kC} = 1 - \frac{\%O_u}{100}$$

(382)

Taking the natural log of both sides:

$$-kC = \ln\left(1 - \frac{\%O_u}{100} \right)$$

(383)

The product of the absorption coefficient and concentration as a function of the percent

obscuration per foot is expressed in final form as:

$$kC = -\ln\left(1 - \frac{\%O_u}{100}\right)$$

<div align="right">(384)</div>

Likewise, concentration can be expressed as

$$C = \frac{-\ln\left(1 - \frac{\%O_u}{100}\right)}{k}$$

<div align="right">(385)</div>

Appendix C.8: Ceiling Jet Velocity Calculations

The ceiling jet velocity for a wastebasket-sized fire under a typical ceiling height was considered in order to put the mass transport model results into a practical context. The fire scenario is described, the ceiling jet correlations used in this evaluation are explained, and the results are presented.

Fire Scenario

The wastebasket fire scenario used in this evaluation is based on 50 kW heat release rate for a typical polyethylene wastebasket filled with empty milk cartons (Babrauskas, 1982). A typical ceiling height of 2.44m (8 ft) is used. The 6.46m (21.21 ft) radial distance from the detector to the fire is based on the maximum distance possible for an array of four smoke detectors located 9.14m (30 ft) on center. A plan view of the fire relative to the smoke detectors is shown in Figure 104.
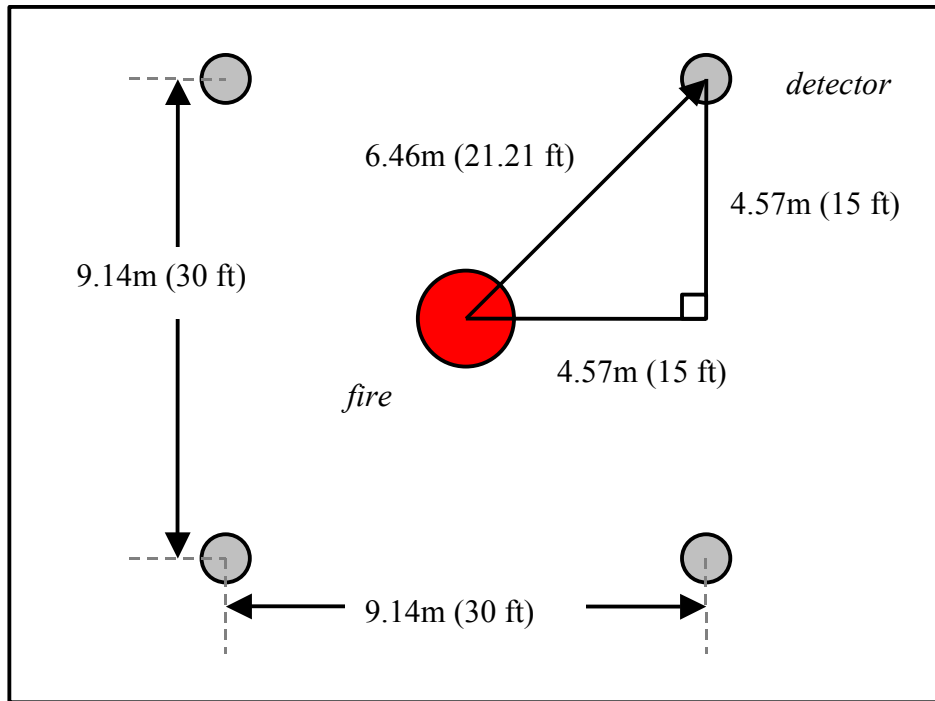
Figure 104 -- Plan view of wastebasket fire scenario.

Ceiling Jet Correlations

Two ceiling jet correlations were used to evaluate the given fire scenario. One of the ceiling jet correlations used was developed by Alpert and is based on experimental data for fire sizes in the range of 668kW to 98MW under ceiling heights in the range of 4.6 to 15.5m (Evans, 1995) which are much larger than the 50kW fire size and 2.44m ceiling height in this scenario. Therefore, an examination of the nondimensional heat release rate, Q^*, for Alpert's experimental conditions and the wastebasket scenario were compared. Additionally, a second ceiling jet correlation developed by Motevalli and Marks for reduced scale conditions was used as a means of bounding the problem at lower limit in terms of scale as opposed to the upper bound of Alpert's correlation.

The nondimensional heat release rate is (Evans, 1995):

$$Q* = \frac{\dot{Q}}{\rho_o c_p T_o g^{1/2} H^{5/2}}$$

(386)

The following table summarizes the nondimensional heat release rate values for Alpert's experiments and the wastebasket fire scenario for an ambient air temperature of 298K.

Table 50 –Nondimensional HRR comparison between Alpert experiments and wastebasket scenario.

Condition	Q' (kW)	H (m)	Q*
Alpert Experiments	668	4.6	0.0131
	668	15.5	0.0006
	98,000	4.6	1.928
	98,000	15.5	0.0925
Wastebasket Scenario	50	2.44	0.0048

The results above indicate that the Alpert correlation was developed for nondimensional heat release rates in the range of 0.0006 to 1.928. The wastebasket fire scenario, although smaller in magnitude, has a nondimensional heat release rate of 0.004 which is within the range of Q* values for Alpert's experimental conditions. Therefore, the use of Alpert's correlation for predicting the ceiling jet velocity for the wastebasket scenario is a reasonable approach.

Alpert's ceiling jet velocity correlation for r/H > 0.15 (r/H = 2.65 for the wastebasket scenario) is (Evans, 1995):

$$U = \frac{0.195\dot{Q}^{1/3}H^{1/2}}{r^{5/6}}$$

<div align="right">(387)</div>

Where U is the ceiling jet velocity, Q' is the fire heat release rate, H is the ceiling height, and r is the radial distance from the fire. For a 50 kW heat release rate under a 2.44m ceiling at a 6.46 radial distance, the ceiling jet velocity using Alpert's correlation is 0.24 m/s.

A ceiling jet correlation based on reduced scale fire experiments developed by Motivalli and Marks (1991) was also used to evaluate the wastebasket fire scenario.   The experimental conditions consisted of fire sizes in the range of 0.75 to 2.0 kW under ceiling heights of 0.5 to 1.0m, which is much smaller than the 50kW fire size and 2.44m ceiling height in the wastebasket scenario. A comparison of nondimensional heat release rates between the experimental conditions used to develop the Motevalli and Marks correlation and the wastebasket fire scenario was conducted.   The results of this comparison are summarized in the table below.

Table 51 – Nondimensional HRR comparison between Motevalli and Marks experiments and wastebasket scenario.

Condition	Q' (kW)	H (m)	Q*
Motevalli and	0.5	0.5	0.0025
Marks Experiments	0.5	1	0.0004
	2	0.5	0.0101
	2	1	0.0018
Wastebasket Scenario	50	2.44	0.0048

The results above indicate that the Motevalli and Marks correlation was developed for nondimensional heat release rates in the range of 0.0004 to 0.0101. The wastebasket fire scenario, although larger in magnitude, has a nondimensional heat release rate of 0.004 which is within the range of Q* values for Motevalli and Mark's experimental conditions. Therefore, the use of this correlation for predicting the ceiling jet velocity for the wastebasket scenario is a reasonable approach.

Motevalli and Marks's ceiling jet velocity correlation is expressed in terms of nondimensional velocity (Motevalli and Marks, 1991):

$$v* = 0.0415 (r/H)^{-2} + 0.427 (r/H)^{-1} + 0.281$$

(388)

The nondimensional velocity is scaled to the actual velocity in the following manner:

$$v* = \frac{v}{Q_c^{*1/3} \sqrt{gH}}$$

(389)

The nondimensional heat release rate for the Motevalli and Marks correlation is similar to the form used in Equation 386 with the exception that it is based on convective heat release rate rather than the total heat release rate. Therefore, in order to distinguish these two expressions of nondimensional heat release rate, the subscript c is added for this

particular instance where convective heat release rate is used. The nondimensional heat

release for the Motevalli and Marks is expressed as:

$$Q_c^* = \frac{\dot{Q}_c}{\rho_o c_p T_o g^{1/2} H^{5/2}}$$

(390)

The nondimensional heat release rate based on convection heat release rate for the

wastebasket scenario using a convective fraction of 0.70 and an ambient air temperature

of 298K is 0.0034. The nondimensional velocity for the wastebasket scenario with an r/H

of 2.65 is calculated with Equation 388 as 0.448. The resulting dimensional velocity for

the wastebasket scenario computed with Equation 389 is 0.33 m/s.

Therefore, the ceiling jet velocity for the wastebasket fire scenario is expected to be in the

range of 0.24 to 0.33 m/s according to the two ceiling jet correlations evaluated in this

analysis.

References

Babrauskas, V., "Will the Second Item Ignite?" *Fire Safety Journal*, (4) pp 287-292 (1982).

Evans, D.D., "Ceiling Jet Flows," *SFPE Handbook of Fire Protection Engineering, 2nd Edition*, Section 2, Chapter 4, pp 2/32-39, National Fire Protection Association, Quincy, MA, (1995).

Motevalli, V., Marks, C.H., "Characterizing the Unconfined Ceiling Jet Under Steady-State Conditions: A Reassessment," International Association for Fire Safety Science. Fire Safety Science. Proceedings. 3rd International Symposium. July 8-12, 1991, Edinburgh, Scotland, Elsevier Applied Science, New York, Cox, G.; Langford, B., Editors, pp. 301-312, (1991).

Appendix C.9: Lumped Mass Transport Model

The one-dimensional species equation from the mass transport model was lumped in the x-direction in order to recast the model as a function of time only. The lumped form of the model allowed for an examination of the characteristic quantities for this simplified approach. One advantage of this simplified form of the model is that it could be used as an engineering tool without the need for solving a finite difference equation. This approach assumes steady state flow conditions with a constant inlet species boundary condition.

General Approach

The general concept for the lumped model is that the species concentration gradient inside the control volume is constant in the x-direction, or averaged over the x-direction. The following figure illustrates this concept relative to the one-dimensional form of the model. Figure 105 shows the species concentration as a function of distance in a diagrammatical fashion for the one-dimensional and lumped forms of the mass transport model.
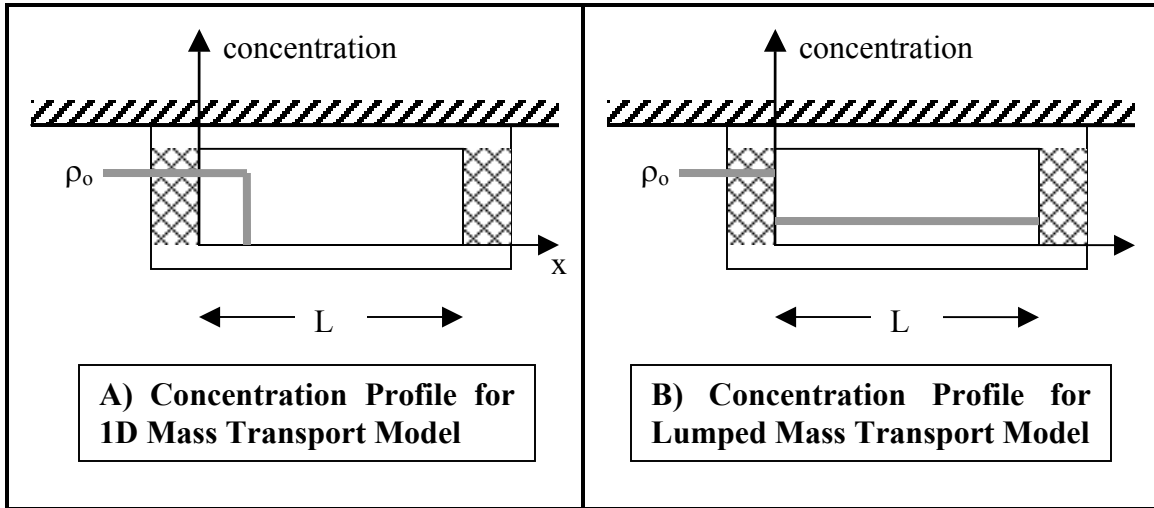
Figure 105 – Arbitrary concentration profiles for 1D and lumped versions of the mass transport model.

The process used to recast the one-dimensional species equation into a lumped form is detailed in the discussion that follows.

The one-dimensional species equation from the mass transport model is:

$$\frac{\partial \rho_A}{\partial t} + v_x \frac{\partial \rho_A}{\partial x} = 0$$

(391)

Boundary and Initial Conditions

The boundary and initial conditions for the lumped analysis are as follows. The gas phase control volume of the sensing chamber spans from $x = 0$ to $x = L$. A constant inlet species concentration boundary condition is used

$$\rho_A\left(x=0,t\right)=\rho_{A,o}$$

(392)

The initial condition of the interior of the detector is that the interior species concentration is zero at time zero.

$$\rho_A\left(x=L,t=0\right)=0$$

(393)

Additionally, it is assumed that at steady state conditions, the interior species concentration is equal to the exterior species concentration.

$$\rho_A\left(x=L,t=t_{ss}\right)=\rho_{A,o}$$

(394)

Nondimensionalization

The following nondimensional variables relate dimensional variables to their respective characteristic quantities and were used to express the species equation in nondimensional form. The characteristic quantities for developing the nondimensional terms were identified from examining the boundary and initial conditions.

$$\rho^* = \frac{\rho_A}{\rho_{A,o}}$$

(395)

$$v^* = \frac{v_{int}}{v_{ext}}$$

(396)

$$x^* = \frac{x}{L}$$

(397)

The characteristic quantity for time is unknown at this time, but will be determined as part of this lumped analysis. Therefore, a generic characteristic time, t_c, is used.

$$t^* = \frac{t}{t_c}$$

(398)

The nondimensional expressions are rearranged in the following manner

$$\rho_A = \rho_{A,o}\rho^*$$

(399)

$$v_{int} = v_{ext}v^*$$

(400)

$$x = Lx^*$$

(401)

376

$$t = t_c t*$$

$$(402)$$

Substituting the rearranged form of the nondimensional expressions into the one-dimensional species equation results in the following

$$\frac{\partial\left(\rho_{A,o}\rho*\right)}{\partial\left(t_c t*\right)} + \left(v_{ext}v*\right)\frac{\partial\left(\rho_{A,o}\rho*\right)}{\partial\left(Lx*\right)} = 0$$

$$(403)$$

The constants are separated from each term to yield

$$\left[\frac{\rho_{A,o}}{t_c}\right]\frac{\partial\left(\rho*\right)}{\partial\left(t*\right)} + \left[\frac{v_{ext}\rho_{A,o}}{L}\right]\left(v*\right)\frac{\partial\left(\rho*\right)}{\partial\left(x*\right)} = 0$$

$$(404)$$

The exterior species concentration is common to both terms and can be eliminated by dividing both sides by this term

$$\left[\frac{1}{t_c}\right]\frac{\partial\left(\rho*\right)}{\partial\left(t*\right)} + \left[\frac{v_{ext}}{L}\right]\left(v*\right)\frac{\partial\left(\rho*\right)}{\partial\left(x*\right)} = 0$$

$$(405)$$

Therefore, the characteristic time can be assumed to be

$$t_c = \frac{L}{v_{ext}}$$

(406)

It should be noted that the nondimensional velocity is also a constant due to the continuity equation. Therefore, the characteristic time from Equation 405 can also be assumed to be

$$t_c = \frac{L}{v_{ext} v*} = \frac{L}{v_{ext}\left(\dfrac{v_{int}}{v_{ext}}\right)} = \frac{L}{v_{int}}$$

(407)

This alternative form of the characteristic time based on interior velocity is noted at this time. However, the lumped form of the mass transport model will continue to be developed with the initial characteristic time based on exterior velocity. These two variations will be addressed at the conclusion of the lumped analysis.

The non-dimensional form of the species equation becomes

$$\frac{\partial \rho*}{\partial t*} + v* \frac{\partial \rho*}{\partial x*} = 0$$

(408)

378

The constant inlet species boundary condition for this situation is

$$\rho^*\left(x^* = 0, t^*\right) = 1$$

(409)

The initial condition for the exterior of the detector is that the exterior species concentration is at a maximum value at time zero. This initial condition is consistent with the constant inlet species boundary condition.

$$\rho^*\left(x^* = 0, t^* = 0\right) = 1$$

(410)

The initial condition for the interior of the detector is that the interior species concentration is zero at time zero.

$$\rho^*\left(x^* = 1, t^* = 0\right) = 0$$

(411)

It is assumed that at steady state conditions, the interior species concentration is equal to the exterior species concentration. The steady state condition for this situation is

$$\rho^*\left(x^* = 1, t^* = 1\right) = 1$$

(412)

379

Assumptions

The following assumptions are made in developing the lumped form of the nondimensional mass transport model.

- The nondimensional velocity is a constant $(v^* = const)$ which is consistent with the continuity equation; and
- The exterior species concentration is a constant $(\rho_o^* = const)$.

Solution

Equation 408 is rearranged as

$$\frac{\partial \rho^*}{\partial t^*} = -v^* \frac{\partial \rho^*}{\partial x^*}$$

(413)

Both sides are integrated with respect to x. The limits of integration in the x direction span from the inlet boundary (x* = 0) to inside portion of the gas phase control volume (x* = $1^{(-)}$) where the interior species concentration is assumed to have a single averaged, or lumped, value. The lumped species concentration is denoted as $\bar{\rho}^*$. It should be noted that the upper limit of integration at x* = $1^{(-)}$ captures the interior concentration within the control volume as opposed to the outlet boundary value at x* = 1.

$$\int_{x^*=0}^{x^*=1^{(-)}} \frac{\partial \rho^*}{\partial t^*} dx = -v^* \int_{x^*=0}^{x^*=1^{(-)}} \frac{\partial \rho^*}{\partial x^*} dx$$

(414)

380

Evaluating both sides and recalling for the right hand side that the integral of a derivative is the variable. It is assumed that there are no sources or sinks of species in the control volume.

$$\left[\frac{\partial \rho *}{\partial t *} x *\right]\Bigg|_{x*=0}^{x*=1^{(-)}} = -v *\left[\rho *\right]\Big|_{x*=0}^{x*=1^{(-)}}$$

(415)

This result is evaluated at the limits of integration as

$$\frac{d\rho *}{dt *}\left[1-0\right] = -v *\left[\overline{\rho} *-1\right]$$

(416)

The resulting expression simplifies to the following

$$\frac{d\rho *}{dt *} = v *\left(1-\overline{\rho} *\right)$$

(417)

An alterative approach based on physical reasoning can also be used to determine the average species concentration in an informal manner. The species concentration gradient can be expanded by considering that the limits of the control volume are from $x*=0$ to

381

$x^*=1$ (i.e., $x=0$ to $x=L$ in dimensional form). The species concentration at $x^*=0$ is unity due to the constant inlet species concentration boundary condition. The species concentration inside the control volume at $x^*=1$ changes with time, therefore, the variable ρ^* is used. Applying the inlet species boundary condition and stated assumptions, the species concentration gradient term is expanded in the following manner

$$\frac{d\rho^*}{dx^*} = \frac{\left[\rho^*(x^*=0)\right]-\left[\rho^*(x^*=1)\right]}{\left[x^*=0\right]-\left[x^*=1\right]} = \frac{1-\rho^*}{-1}$$

(418)

Substituting this result for the integration term shown on the right hand side of Equation 414 would produce the same result as Equation 417. As demonstrated in the preceding description, the average species concentration determined informally by physical reasoning is consistent with the result obtained by formally integrating out the x direction.

The right hand side of Equation 417 can be expanded into the following

$$\frac{d\rho^*}{dt^*} = v^* - v^*\overline{\rho}^*$$

(419)

The expression is a linear first-order differential equation that can be separated by combining like terms in the following manner

382

$$\int \frac{d\rho *}{\left(v*-v*\overline{\rho}*\right)} = \int dt*$$

The left hand side is examined by considering the following.

$$u = \left(v*-v*\overline{\rho}*\right)$$

This term is differentiated and becomes

$$du = \left(-v*d\rho *\right)$$

Therefore, prior to integration, it is noted that the left hand side takes the following general form.

$$\frac{\left(-v*d\rho *\right)}{\left(v*-v*\overline{\rho}*\right)} = \frac{du}{u}$$

However, the left hand side of Equation 420 does not fit the general form shown in Equation 423 due to the absence of the term, $-v*$. Therefore, both sides are multiplied by this term to fit the general form.

$$\int \frac{(-v*)}{(v*-v*\bar{\rho}*)} d\rho* = \int (-v*) dt*$$

(424)

The integral of the left hand side of this general form is the natural logarithm (Edwards and Penny, 1990).

$$\int \frac{du}{u} = \ln(|u|) + C$$

(425)

Performing the appropriate integration to both sides of the equation yields

$$\ln(v*-v*\bar{\rho}*) = -v*t* + C$$

(426)

Both sides are raised to the exponential

$$(v*-v*\bar{\rho}*) = e^{-v*t*} + e^{C}$$

(427)

The right hand side simplifies to the following

$$\left(v^* - v^* \overline{\rho}^*\right) = K e^{-v^* t^*}$$

(428)

Where

$$K = e^C$$

(429)

The constant K is determined by evaluating the expression with the initial condition.

$$\left(v^* - v^*(0)\right) = K e^{-v^*(0)}$$

(430)

Which simplifies to

$$K = v^*$$

(431)

The value for the integration constant is substituted.

$$\left(v^* - v^* \overline{\rho}^*\right) = v^* e^{-v^* t^*}$$

(432)

The preceding expression can be simplified and solved for nondimensional species concentration by dividing both sides by the nondimensional velocity.

$$\boxed{\bar{\rho}^* = 1 - e^{-v^* t^*}}$$

(433)

The nondimensional terms are replaced with the dimensional quantities.

$$\frac{\bar{\rho}_A}{\rho_{A,o}} = 1 - e^{-\left(\frac{v_{int}}{v_{ext}}\right)\left(\frac{t}{\left(\frac{L}{v_{ext}}\right)}\right)}$$

(434)

Which simplifies to

$$\boxed{\frac{\bar{\rho}_A}{\rho_{A,o}} = 1 - e^{-\left(\frac{v_{int} t}{L}\right)}}$$

(435)

Therefore, the characteristic time for the lumped form of the model is expressed as the ratio of detector physical length, L, to internal velocity, v_{int}, which has units of time.

$$t_c = \frac{L}{v_{int}}$$

(436)

Discussion of Results

It is interesting to note that the characteristic time for the lumped form of the model is similar to that used by Heskestad. The characteristic time used by Heskestad is the detector characteristic length divided by external velocity.

$$t_c = \frac{L}{v_{ext}}$$

(437)

The experimentally determined values of characteristic length for smoke detectors reported in the literature range from 1.8 to 18 m, which is approximately 2 orders of magnitude larger than the physical dimension of the detector. The external velocity is larger than the internal velocity of the detector due to the degree of entry resistance from the detector geometry such as openings and the insect screen.

An alternative form of the characteristic time for the lumped model can be derived by examining Equation 434 and recalling that the resistance factor, R, is the ratio of internal velocity to external velocity.

387

$$t_c = \frac{L}{Rv_{ext}}$$

(438)

Considering the characteristic time expression used by Heskestad, it is possible that the characteristic length could actually be a lumped parameter that is the physical length scale of the detector divided by the resistance factor. This could possibly explain why experimentally determined values of Heskestad's characteristic length reported in the literature are typically 1 to 2 orders of magnitude larger than the physical length scale of the detector. In order to assess this possibility, the nomenclature used in the expressions for characteristic time is made more specific to differentiate the current approach from that used in Heskestad's model. Therefore, the variable L_c is used for Heskestad's characteristic length and the variable L_p is used for the physical length of the detector used in the current approach.

It is assumed that the characteristic time for both Heskestad's model and the current approach are equal. The general form of Heskestad's model is based on the optical density outside at response D_{ur}, the optical density inside the sensing chamber D_{uo}, characteristic length L_c, external velocity v_{ext}, and the time rate of change of optical density outside the detector, $\frac{dD_u}{dt}$.

$$D_{ur} = D_{uo} + \frac{L_c}{v_{ext}}\left(\frac{dD_u}{dt}\right)$$

(439)

The preceding expression can be arranged as

$$\frac{dD_u}{dt} = \frac{D_{ur} - D_{uo}}{\left(\dfrac{L_c}{v_{ext}}\right)}$$

(440)

The characteristic time for this method will be denoted as $\tau = \dfrac{L_c}{v_{ext}}$

$$\frac{dD_u}{dt} = \frac{D_{ur} - D_{uo}}{(\tau)}$$

(441)

Like terms are grouped as follows

$$\frac{dD_u}{(D_{ur} - D_{uo})} = \frac{dt}{(\tau)}$$

(442)

Each side is integrated

$$\int_0^{D_{uo}} \frac{dD_u}{(D_{ur} - D_{uo})} = \int_0^t \frac{dt}{(\tau)}$$

(443)

With the following result

$$-\ln(D_{ur} - D_{uo}) = \frac{t}{(\tau)}$$

(444)

Which simplifies to

$$\left(D_{ur} - D_{uo}\right) = e^{\frac{-t}{(\tau)}}$$

(445)

Therefore, it is reasonable to assume that the characteristic time for Heskestad's model and the current approach are equal to each other.

The characteristic times for the two methods are examined in the following manner. The characteristic time for Heskestad's model, $t_{c,H}$, is set equal to the characteristic time for the current approach, $t_{c,I}$

$$t_{c,H} = t_{c,I}$$

(446)

Substituting the characteristic quantities that correspond to each method yields

$$\frac{L_c}{v_{ext}} = \frac{L_p}{R v_{ext}}$$

(447)

The external velocity is common to both terms and cancels out. Heskestad's characteristic length can be solved for in terms of the current approach as

$$L_c = \frac{L_p}{R}$$

(448)

Therefore, this analysis indicates that Heskestad's characteristic length could be a lumped parameter that consists of the physical length of the detector divided by the detector's resistance factor. The characteristic length for the photoelectric detector used in this study was determined in accordance with Heskestad's model and was found to have an average value of 3.2m (10.5 ft). The details of determining the characteristic length of this detector are provided in Appendix C.10. The characteristic length of the photoelectric detector used in the current study and the resistance factors developed from the subsequent experimental program were used to evaluate if Heskestad's characteristic length is a lumped parameter as indicated by the previous analysis. Equation 448 was rearranged in terms of the detector physical length as follows:

$$L_p = L_c R$$

(449)

$$L_p = (L_c)\left(f * \left(\frac{1-\alpha^2}{\alpha^2} \right) * (\mathrm{Re}_d) \right)$$

(450)

The known values for characteristic length and resistance factor were substituted into Equation 450 in order to calculate the physical length of the detector. The resistance factor is a function of velocity via the screen Reynolds number and therefore, was evaluated at the lower and upper bounds of velocity. The screen Reynolds numbers

ranged from approximately 5 to 20 in this study.   The resistance factor is also a function of screen porosity and a curve fit coefficient, however, these are fixed quantities.

The physical length at the lower bound of velocity was determined in the following manner:

$$L_{p,1} = (3.25m)(1.268*0.0034*5) = 0.07m$$

(451)

The physical length at the upper bound of velocity was determined in the following manner:

$$L_{p,2} = (3.25m)(1.268*0.0034*20) = 0.28m$$

(452)

The calculated physical length for the photoelectric detector ranges from 7cm (3 in) to 28cm (11 in), which is consistent with the measured diameter dimensions of 4.8 cm (2 in) at the sensing chamber, 10.2 cm (4 in) at the aerosol entry location of the external housing, and 12.4 cm (5 in) at the detector base. Therefore, this comparison indicates that Heskestad's characteristic length could be a lumped parameter of physical length divided by the resistance factor.

The alternative form of the characteristic time for the lumped model shown in Equation 438 can be expanded upon by recalling that the general expression for the resistance factor is a function of the screen porosity and screen Reynolds number. Therefore, the alternative form of the characteristic time for the lumped model becomes

$$t_c = \frac{L}{\left(\dfrac{1-\alpha^2}{\alpha^2}\right) f\left(\mathrm{Re}_d\right) v_{ext}} = \frac{L}{\left(\dfrac{1-\alpha^2}{\alpha^2}\right) f\left(\dfrac{v_{ext}d}{\upsilon}\right) v_{ext}}$$

(453)

This can be further simplified to

$$t_c = \frac{L}{\left(\dfrac{1-\alpha^2}{\alpha^2}\right) f\left(\dfrac{[v_{ext}]^2 d}{\upsilon}\right)}$$

(454)

It is interesting to note that examining this expanded form of the characteristic time for the lumped model indicates an inverse relationship to external velocity squared. This form of the characteristic time where external velocity appears as a square is similar to the observation made by researchers at VTT that for velocities below 0.20 m/s the characteristic time appeared to behave as velocity squared.

393

In order to assess this observation with regards to the inverse square dependency on external velocity in the characteristic time, several external velocities were examined to observe the relative impact. The results are summarized in the table that follows where the left hand side is the external velocity and the right hand side is the external velocity squared.

Table 52 – Comparison of external velocity and external velocity squared.

V,ext	$(V,ext)^2$
1.50	2.25
1.25	1.56
1.00	1.00
0.75	0.56
0.50	0.25
0.30	0.09
0.20	0.04
0.15	0.02
0.10	0.01

The preceding table shows that the external velocity and the external velocity squared are of the same order of magnitude for velocities of approximately 0.30 m/s and larger. This would explain the relative agreement in characteristic time that would be observed between Heskestad's model and a similar approach where characteristic time is a function of external velocity squared for relative large velocities (*i.e.*, greater than 0.20 m/s). However, as originally pointed out by Bjorkman *et al* and confirmed with the results in the previous table, that for velocities of approximately 0.20 m/s and below the external velocity is one order of magnitude larger than the external velocity squared. This would explain the observations made by Bjorkman *et al* where an increased degree of resistance was seen relative to Heskestad's form of the characteristic time. This increased resistance at low velocities can be explained by the order of magnitude difference between the describing characteristic time as the inverse of velocity and describing the

characteristic time as the inverse of velocity squared. The hypothesis of characteristic time being inversely proportional to external velocity squared proposed by Bjorkman *et al* was based on experimental measurements, however, could not be physically justified within the confines of Heskestad's model because the resulting characteristic time would have inconsistent units of s^2/m. However, the characteristic time developed by the current approach is based on the physical length scale of the detector divided by the product of the nondimensional resistance factor and the external velocity, which has units of time. The expanded form of the characteristic time used in the lumped form of the current approach indicates an inverse dependency on external velocity squared, which is consistent with the observations made by Bjorkman *et al*. However, the current approach provides an explanation that is based on the physical quantities and phenomena associated with the mass transport model developed in the current study and has consistent physical units of time.

Appendix C.10: Characteristic Length Determination

The detector response data collected in this study was used to determine the characteristic length in accordance with Heskestad's lag time model. Characteristic length is determined by plotting external optical density per unit length at response versus the time rate of change of external optical density per unit length divided by velocity (Heskestad, 1977).

$$D_{u,r} \text{ vs. } \frac{\left(\dfrac{dD_u}{dt}\right)}{v_{ext}}$$

(455)

Whereas Heskestad's model depends upon the time rate of change of optical density, the experimental data collected for the "ramp" exposure tests in the current study where used. The "ramp" exposure tests used an atomized vegetable oil source that was delivered in a manner that approximated a linear increase in optical density as a function of time until steady state conditions were achieved. It should be noted that since the "step" exposure tests were designed to approximate a step input of aerosol to the detector, these tests were not used as the time rate of change for this condition is infinite, *i.e.*, a finite increase in optical density over an instantaneous, or mathematically zero, time.

A linear curve fit is applied to the plotted data in the form shown in Equation 455 and the slope of the resulting line is the characteristic length.

Formatting Data

The procedures used to determine the variables associated with Equation 455 are described in the sections that follow. This is followed by plots of the data and the determination of the characteristic length.

Velocity

The velocity term was based on the time-averaged exterior velocity measured with the LDV for the particular steady state test condition. The values were determined as part of the velocity characterization presented previously.

Time Rate of Change of External Optical Density Per Unit Length

The time rate of change of optical density was based on laser transmittance measurements made in the upper portion of the FE/DE test chamber during a particular "ramp" exposure test. The laser transmittance measurement was converted into optical density per unit length in the following manner.

$$D_u = \frac{-10 \cdot \log_{10}(\tau)}{L}$$

(456)

Where L is the pathlength of the transmittance measurement. The optical density per unit length was plotted as a function of time in order to identify the linear increase in optical density during the exposure test. The beginning and end points of this nominally linear

portion were identified by visual inspection of the optical density plot. A linear curve fit was applied to the optical density data included in the ramp portion of the plot. The slope of this linear curve fit was used to represent the time rate of change of optical density per unit length. The R^2 value was determined in order to assess the goodness of fit. In general, the linear curve fits resulted in an R^2 value on the order of 0.98 or higher. Therefore, it is reasonable to assume that the "ramp" exposures were nominally linear.

Optical Density Per Unit Length at Detector Response

The optical density per unit length at detector response was determined by identifying the value corresponding to specific alarm points. In general, the detector reached alarm thresholds of 0.2%/ft and 0.5%/ft during the exposure tests.

Data Plots

The data plots for the detector at the 0.2%/ft and 0.5%/ft alarm points at two different orientations are shown in the following figures. The error bars in the x direction represent the uncertainty estimate in the time rate of change of optical density divided by exterior velocity. The statistical standard deviation in the laser transmittance measurement under steady state conditions was used to calculate the resulting uncertainty in the optical density per unit length. The statistical standard deviation of the external velocity measurement was used to represent the uncertainty in velocity. A linear curve fit was applied to the data in accordance with Heskestad's method where the resulting slope represent the characteristic length of the detector.
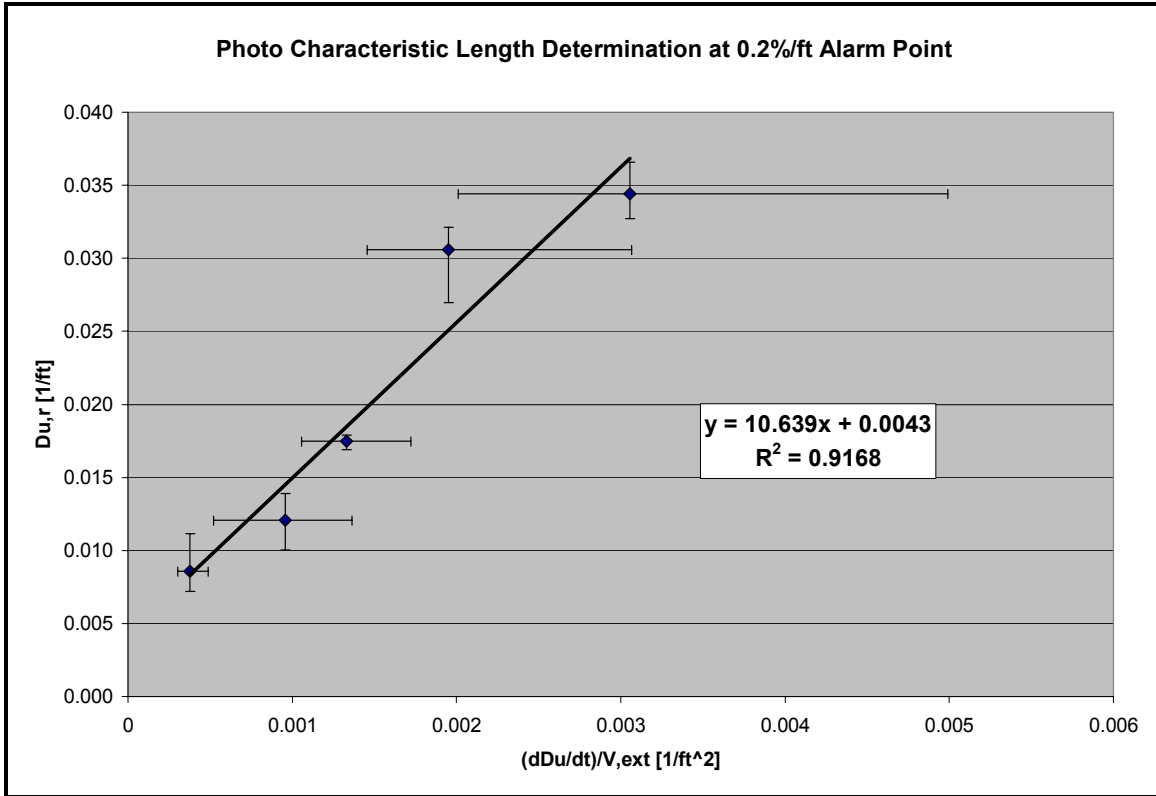
Figure 106 -- Characteristic length determination for photo detector at 0.2%Ob/ft alarm point.

Based on the linear curve fit to the data shown in Figure 106, the characteristic length at the 0.2%/ft alarm point is 10.64 ft, or 3.24 m. The characteristic length of the photoelectric detector was also determined for the 0.5%Ob/ft alarm threshold. The results for this situation are shown in the figure that follows.
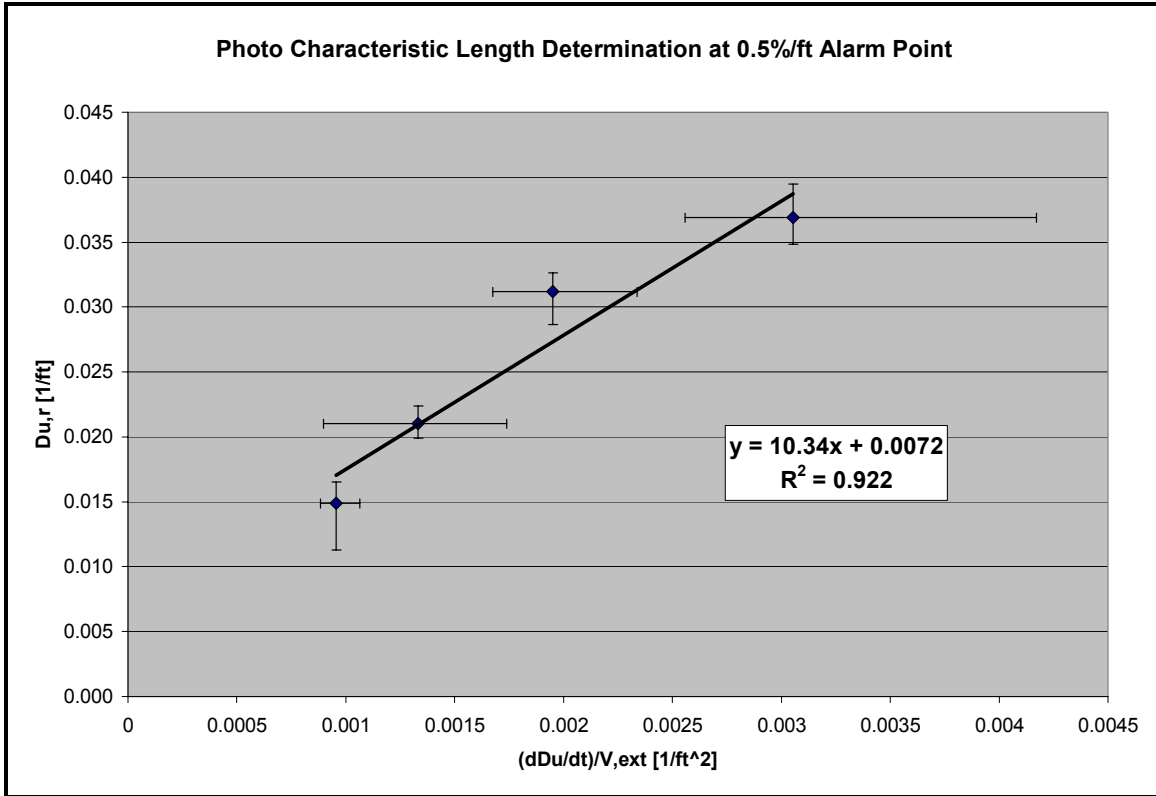
Figure 107 -- Characteristic length determination for photo detector at 0.5%Ob/ft alarm point.

Based on the linear curve fit to the data shown in Figure 107, the characteristic length at the 0.5%/ft alarm point is 10.34 ft, or 3.15 m. This result is consistent with the characteristic length determination at the 0.2%Ob/ft alarm point of 10.64 ft, or 3.24 m. These characteristic length values are within 3% of each other. The characteristic length for this photoelectric detector will be reported in terms of the average value of 3.2 m (10.5 ft).

The characteristic lengths of photoelectric detectors reported in the literature, as summarized in the Background chapter, range from 5.3 to 18.4 m. It should be noted that, in general, the historic record has indicates a decrease in the characteristic length of photoelectric detectors which can probably be attributed to newer designs. For example,

Heskestad reports a characteristic length value of 15 m for a photoelectric detector in 1977 while Bjorkman *et al* report values for a collection of photoelectric detectors in the range of 5.3 +/- 2.7 m in 1992. Therefore, the characteristic length value determined in this study for a photoelectric detector manufactured in early 2000 is consistent with the overall trend in the historic record and is within the range of the most recent available values reported by Bjorkman, *et al*. In addition, the head of research and development for the detector manufacturer has indicated through a personal communication that the particular photoelectric detector used in this study was specifically designed to be more aerodynamic (i.e., more conducive to smoke entry) than the preceding model.

Appendix C.11: Cleary Model Parameters Determination

The detector response data collected in this study was used to determine the dwell time and mixing time parameters in accordance with Cleary's detector model (1998). The dwell time, δt, is based on an assumed plug flow region of length, L_e, that is a function of mass flow rate of smoke into the detector, $\dot{m}$, that scales with the Reynolds number (based on external velocity) raised to a power, c.

$$\delta t \equiv \frac{L_e \rho A}{\dot{m}} \approx a u_e^{-c}$$

$$(457)$$

The mixing time, τ, is based on the assumption of a perfectly stirred region within the sensing chamber volume, V, that is a function of mass flow rate of smoke into the detector that scales with the Reynolds number raised to a power, c'.

$$\tau \equiv \frac{\rho V}{\dot{m}} \approx b u_e^{-c'}$$

$$(458)$$

The "step" exposure tests conducted as part of the current study were used to determine the model parameters in accordance with Cleary's model. The dwell time is defined as the delay between when aerosol first reaches the detector and when the aerosol initially reaches the sensing chamber as indicated by the initial response from the detector output

signal. The procedure used to determine this is demonstrated in the sections that follow. The mixing time is defined as the first order response of the sensor.

Formatting Data

The procedures used to determine the variables associated with each term are described in the sections that follow. This is followed by plots of the data and the determination of the model parameters via a power law curve fitting procedure.

Velocity

The velocity term was based on the time-averaged exterior velocity measured with the LDV for the particular steady state test condition. The values were determined as part of the velocity characterization presented previously.

Dwell Time

In the "step" exposure tests the time of initial exposure was known and the transport delay from the outer edge of the isolation can to the leading edge of the detector was determined as shown in Appendix X. The dwell time was quantified as the time of initial sensor response after the start of the test (corrected for transport delay from the leading edge of the isolation can to the leading edge of the detector). An example of this determination for three repeated tests is shown in Figure 108.
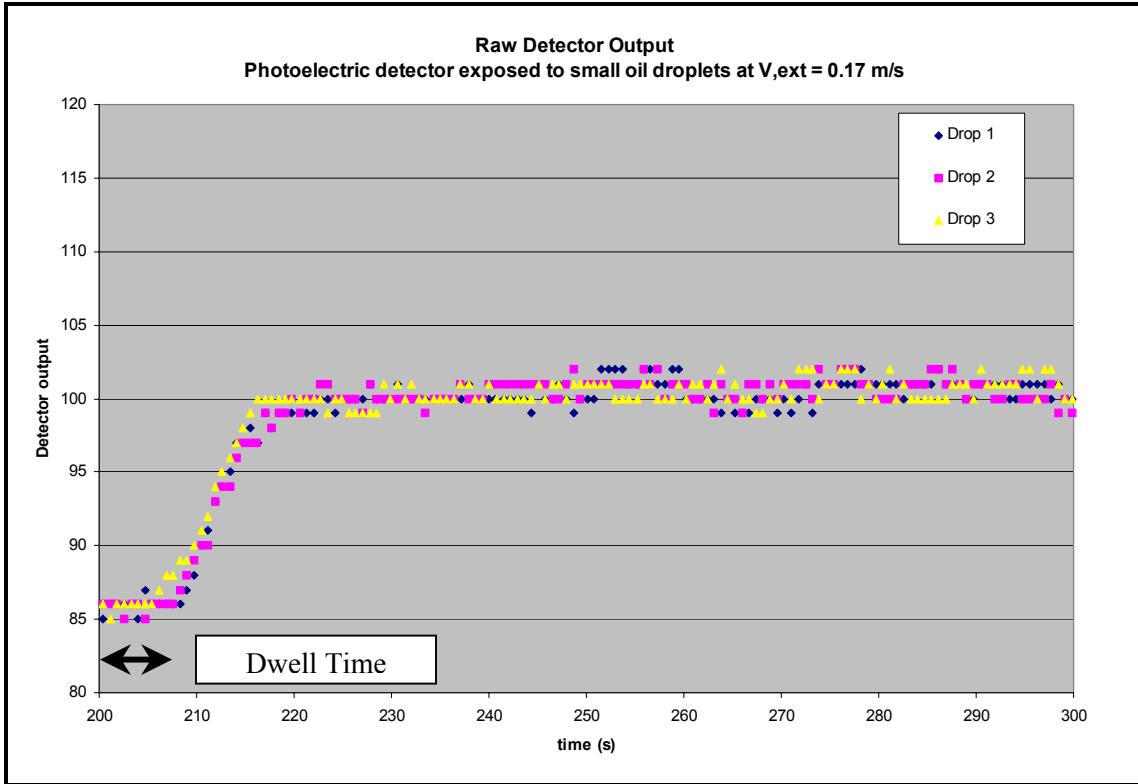
Figure 108 -- Detector output signals from three tests of a photoelectric detector exposed to nebulized vegetable oil at 0.17 m/s.

Mixing Time

The mixing time was determined by calculating the characteristic time for the assumed first order response of the sensor. The first order response is based on the following

$$\frac{Y(t)}{Y_o} = 1 - e^{-\left(\frac{t}{\tau}\right)}$$

(459)

The detector output signal was normalized to itself so that the clean air baseline signal was 0 and the steady state sensor output value was 1. The data set was shifted in time to remove the dwell time so that the sensor response portion began at an adjusted time zero. The response portion of the data set from normalized 0 to 1 was fit in accordance with Equation 459. An example of the time shifted data for three repeated tests is shown in Figure 109.
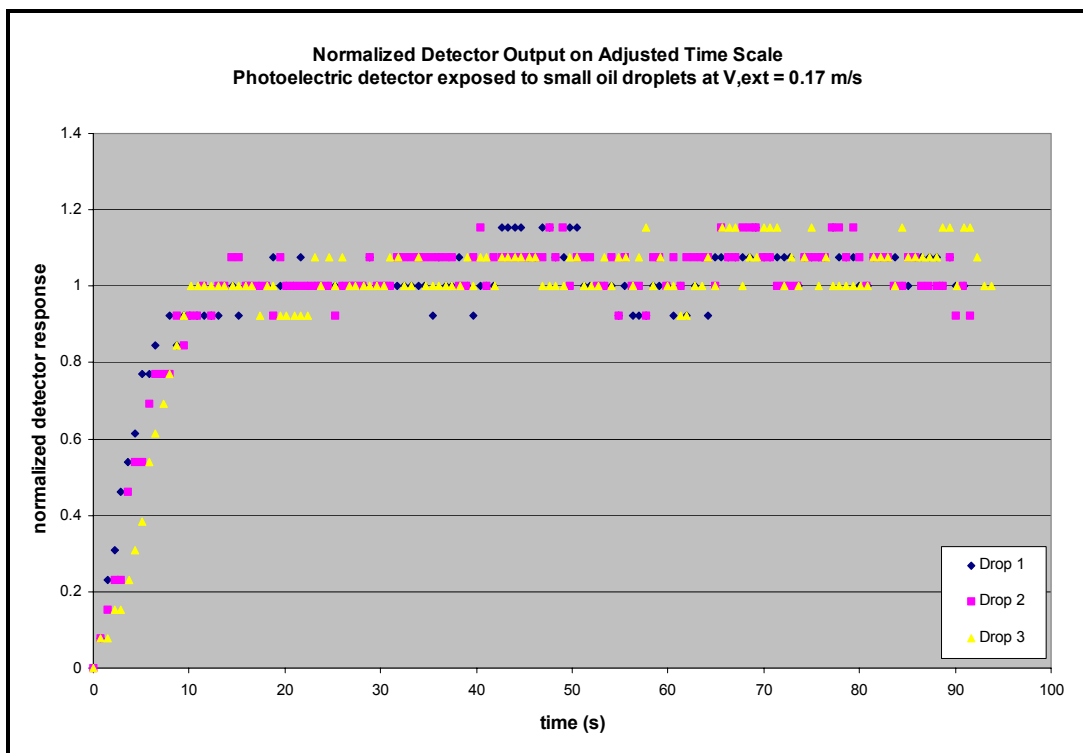
Figure 109 -- Time shifted data set for normalized detector output.

Data Plots

The dwell time and mixing time values for each aerosol type were plotted as a function of external velocity. The x error bars represent the statistical standard deviation in the velocity measurements which was used as an estimate of the measurement uncertainty.

The y error bars represent the maximum and minimum variation in the dwell or mixing time with respect to the mean value of three repeated tests. The plots that follow illustrate the power law curve fitting procedure that was applied to each data set in order to determine the coefficients for the pre-exponential and exponential terms. The following figures demonstrate the power law curve fit and associated correlation coefficient, R^2, of the dwell time and the mixing time data for all four aerosol types.
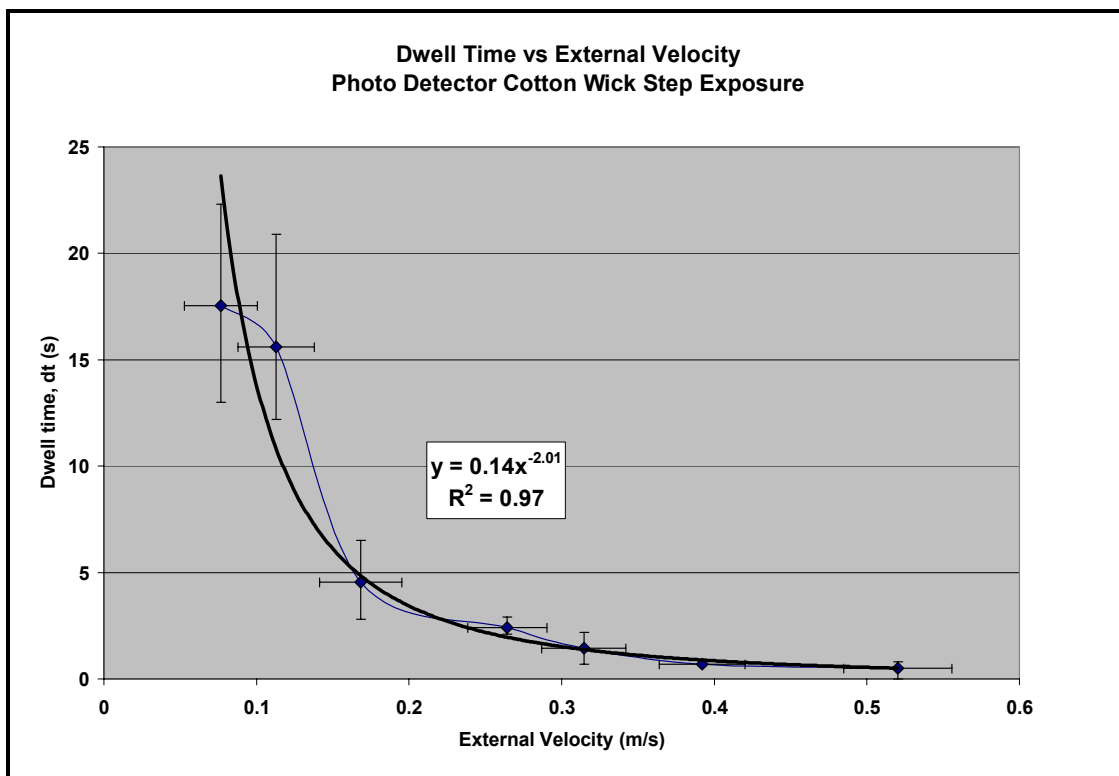
Figure 110 -- Dwell time versus external velocity for photo detector and cotton wick exposure.
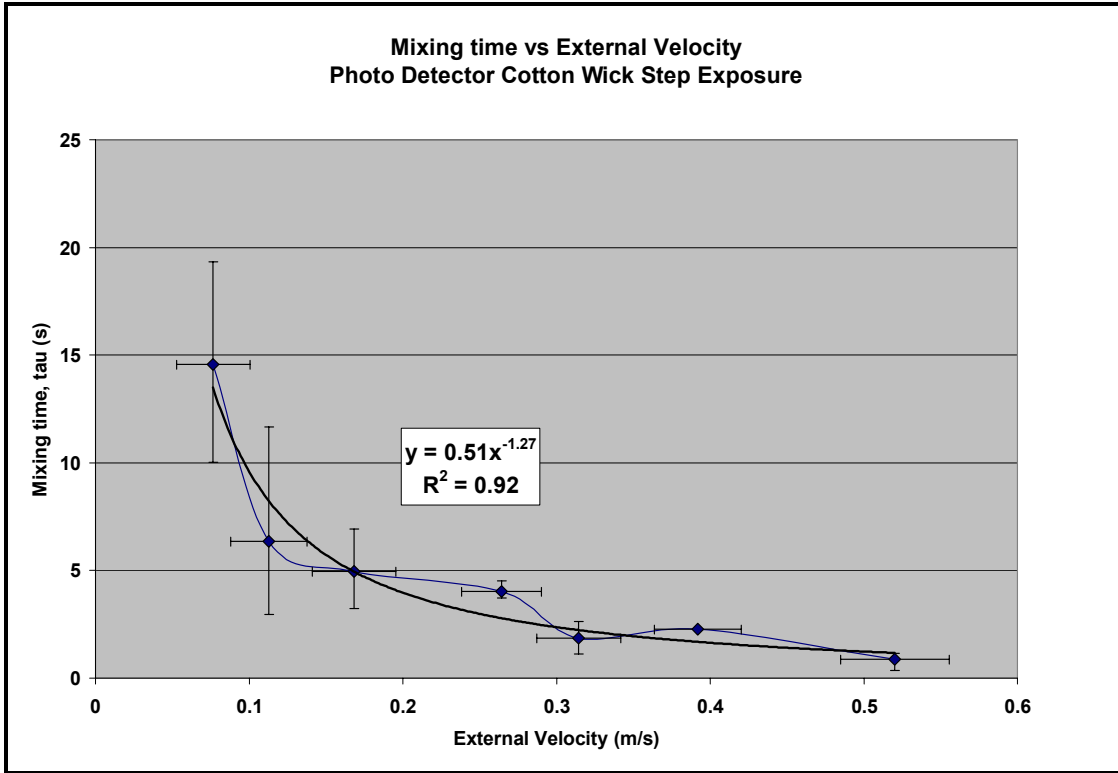
Figure 111 -- Mixing time versus external velocity for photo detector and cotton wick exposure.
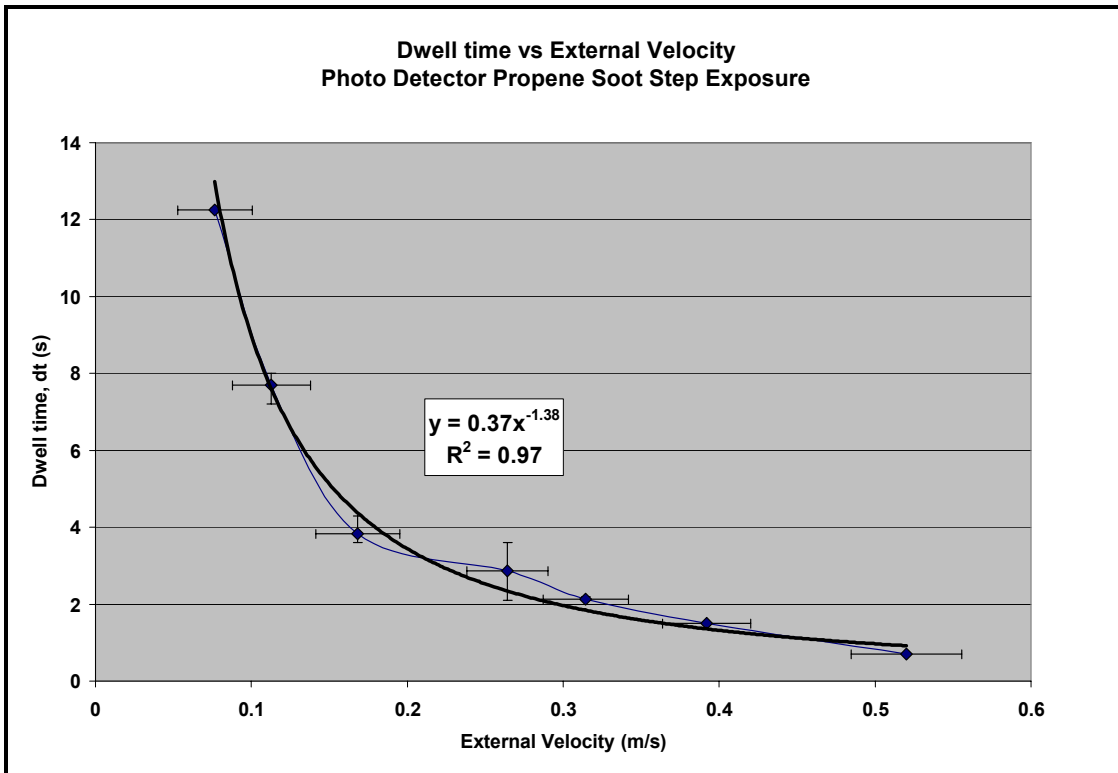
Figure 112 -- Dwell time versus external velocity for photo detector and propene soot exposure.
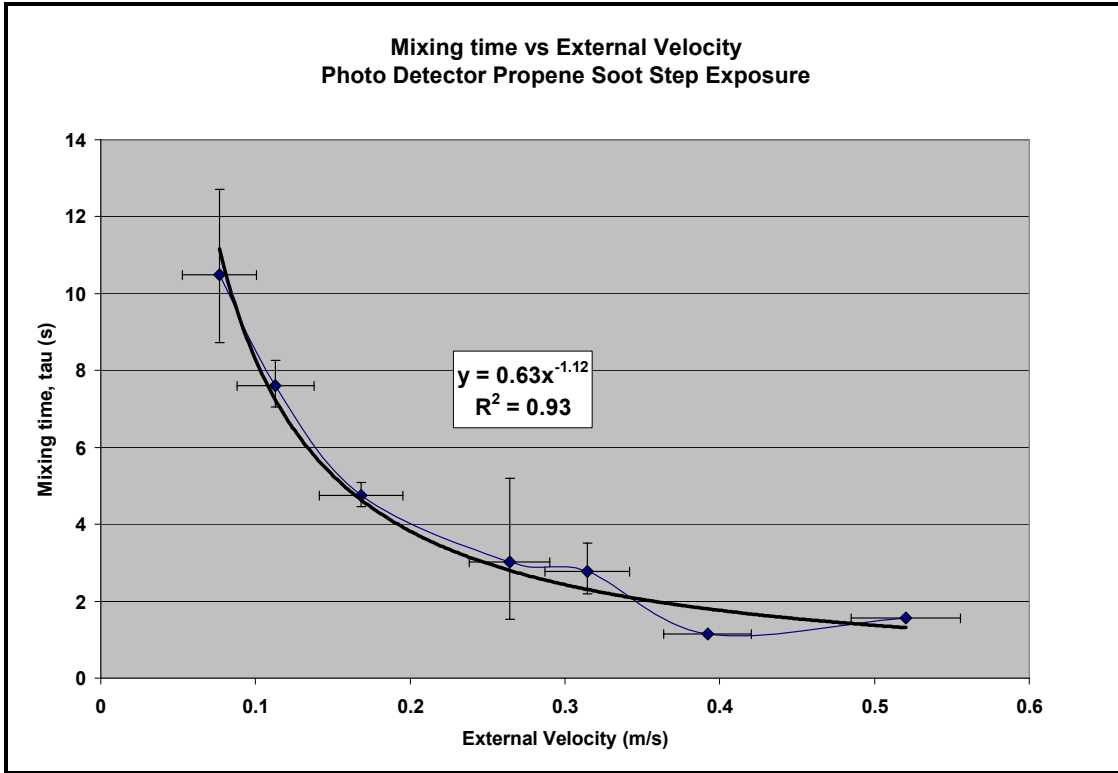
Figure 113 -- Mixing time versus external velocity for photo detector and propene soot exposure.
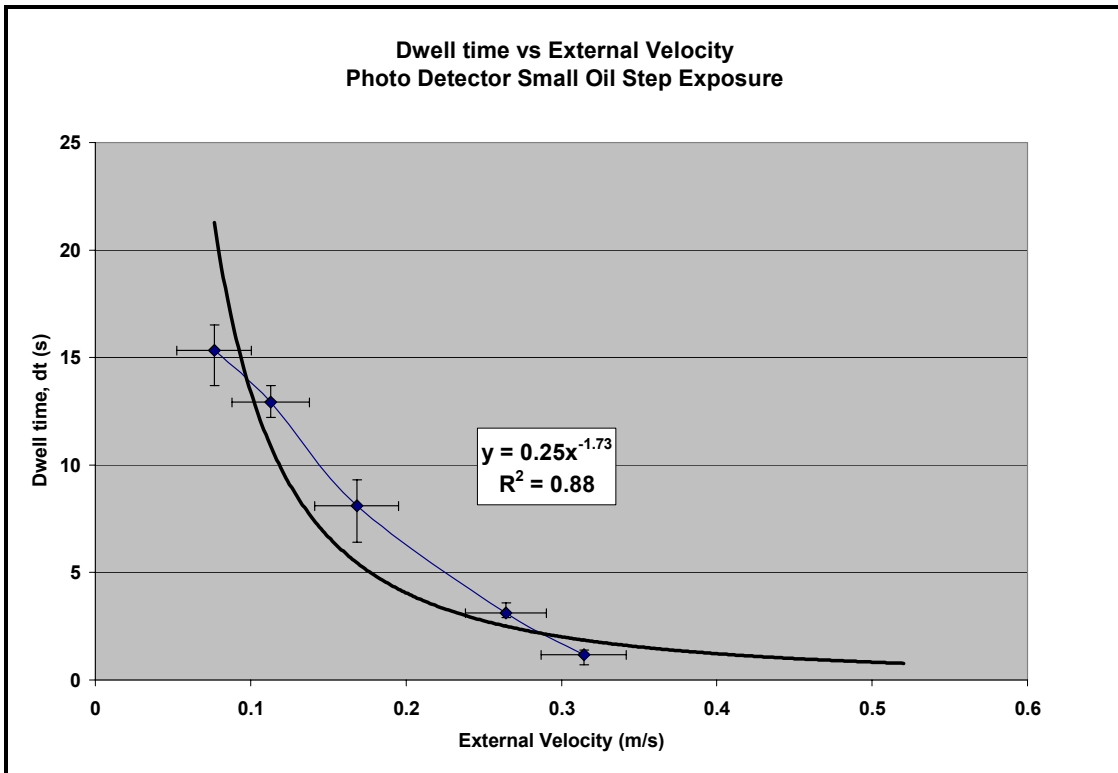
Figure 114 -- Dwell time versus external velocity for photo detector and small oil exposure.
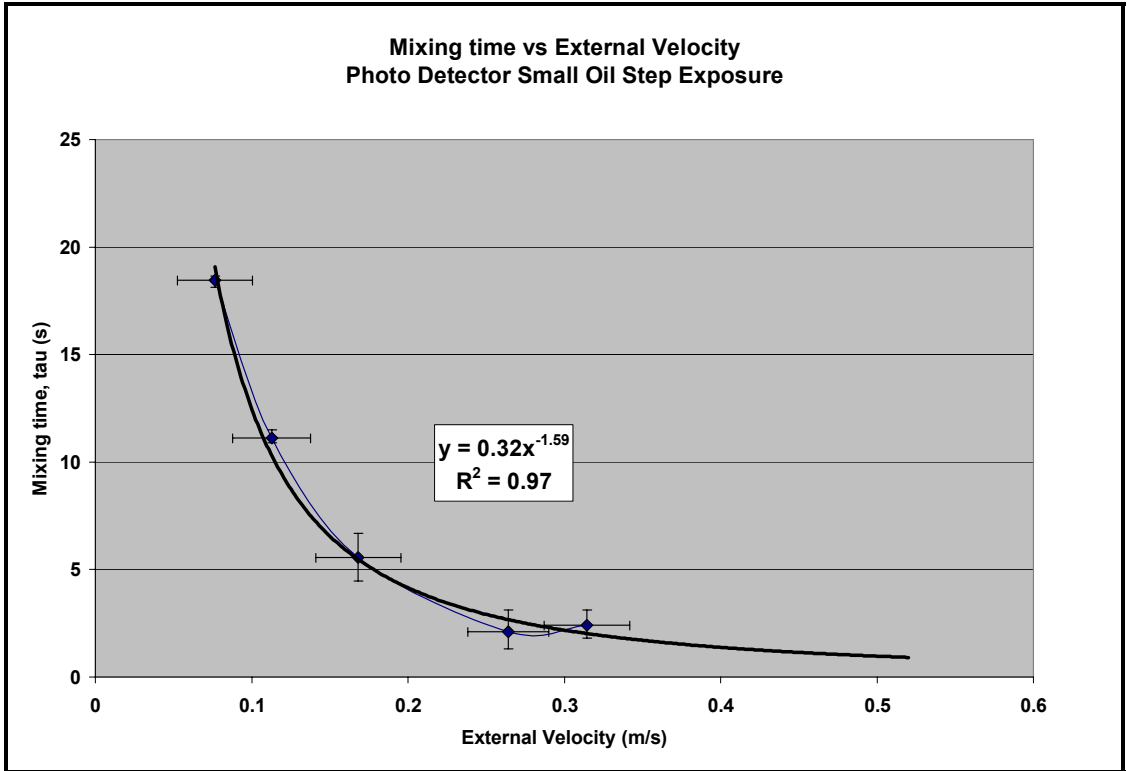
Figure 115 -- Mixing time versus external velocity for photo detector and small oil exposure.
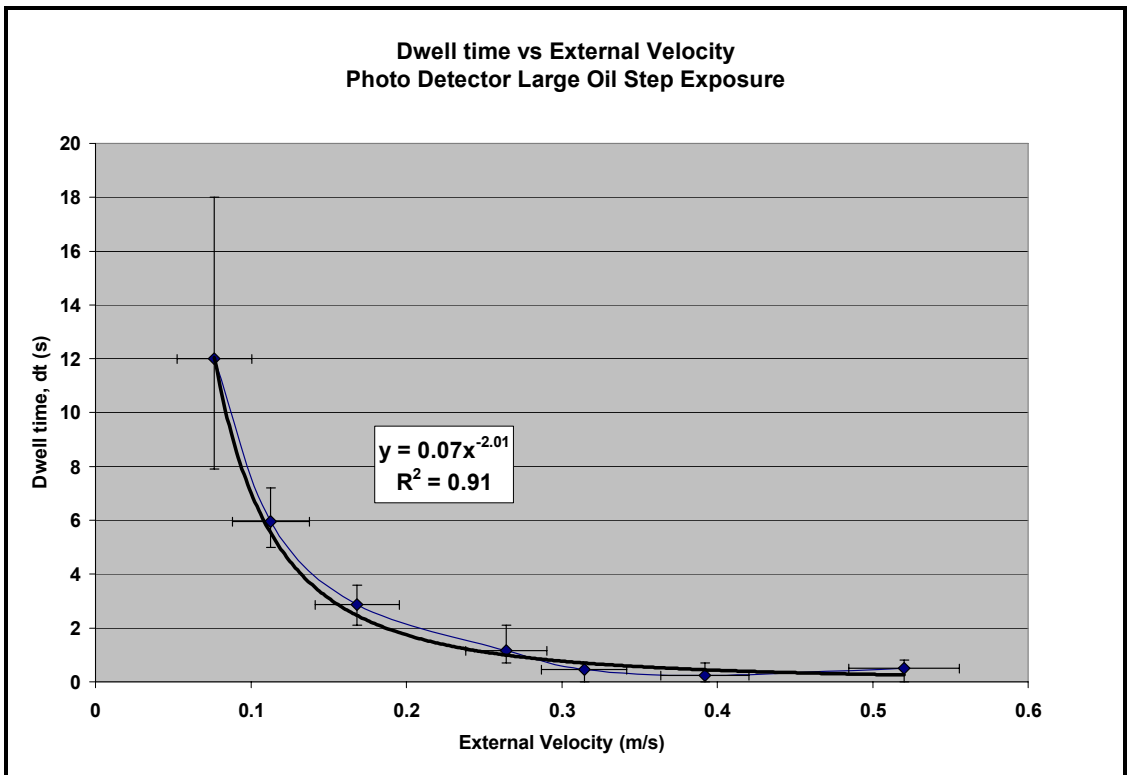
Figure 116 -- Dwell time versus external velocity for photo detector and large oil exposure.
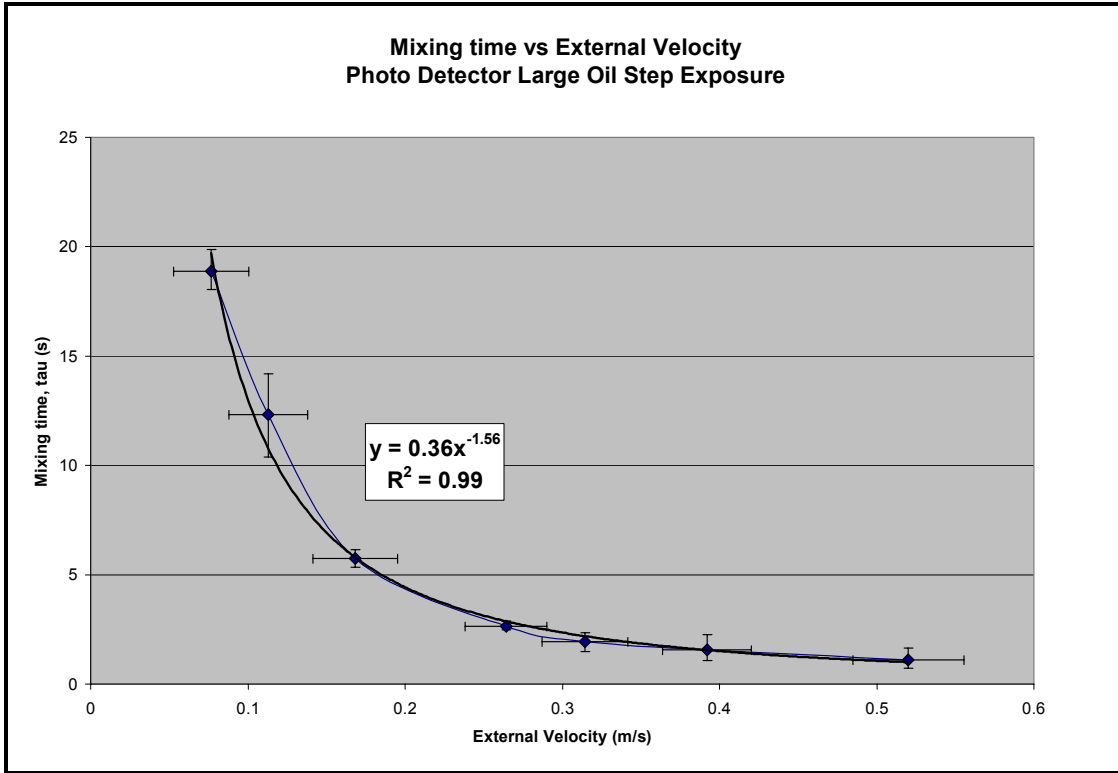
Figure 117 -- Mixing time versus external velocity for photo detector and large oil exposure.

The dwell time and mixing time coefficients for all four aerosol types used in the "step" exposure tests are summarized in Table 53.

Table 53 -- Dwell time and mixing time summary for photo detector used in "step" exposure tests.

Aerosol	Dwell time δt (s)	R^2	Mixing time τ (s)	R^2
Cotton Wick	$0.14*V^{-2.01}$	0.97	$0.51*V^{-1.27}$	0.92
Propene Soot	$0.37*V^{-1.38}$	0.97	$0.63*V^{-1.12}$	0.93
Small Oil	$0.25*V^{-1.73}$	0.88	$0.32*V^{-1.59}$	0.97
Large Oil	$0.07*V^{-2.01}$	0.91	$0.36*V^{-1.56}$	0.99

Cleary *et al* (1998) report the following values for two different photoelectric detectors (which are also different from the detector used in the current study).

Table 54 -- Dwell time and mixing time summary for photo detector in Cleary et al (1998).

Detector	Aerosol	Dwell time δt (s)	R^2	Mixing time τ (s)	R^2
Photo (P1)	Propene Soot	$1.8*V^{-1.0}$	0.88	$0.97*V^{-0.76}$	0.79
Photo (P2)	Propene Soot	$1.8*V^{-0.80}$	0.77	$0.80*V^{-0.75}$	0.82

Cleary *et al* (1998) suggest that the relative size of the plug flow length to mixing volume can be determined by dividing the dwell time by the mixing time. The results of this analysis for the work by Cleary *et al* as well as the current study are as follows:

Table 55 -- Summary of dwell time divided by mixing time for photo detectors.

Detector	Aerosol	Dwell Time /Mixing Time
Cleary P1	Propene Soot	$1.86*V^{-0.24}$
Cleary P2	Propene Soot	$2.25*V^{-0.05}$
Photo (current study)	Cotton Wick	$0.27*V^{-0.74}$
Photo (current study)	Propene Soot	$0.59*V^{-0.26}$
Photo (current study)	Small Oil	$0.78*V^{-0.14}$
Photo (current study)	Large Oil	$0.19*V^{-0.45}$

Appendix C.12: Brozovsky Model Determination

The detector response data collected in this study was used to determine the critical velocity value in accordance with the method proposed by Brozovsky, *et al* (1995). The critical velocity method utilizes lag time data plotted as a function of external velocity. The lag time is the delay from when aerosol reaches the leading edge of the detector until when an alarm point is reached. An exponential polynomial curve fit is applied to the data set in order to describe the data set a continuous function of external velocity. The maximum external velocity tested is used as one of the two values for determining the critical velocity. The velocity that corresponds to two times the lag time associated with the maximum external velocity is used as the second value for determining the critical velocity. These two velocity values are averaged together to produce the critical velocity for the particular detector and aerosol combination.

$$u_{cr} = \frac{u_{max} + u\left(\Delta t_{lag} = 2\Delta t_{lag}\big|_{u_{max}}\right)}{2}$$

(460)

The "step" exposure tests conducted as part of the current study were used to determine the model parameters in accordance with the method of Brozovsky *et al*.

Formatting Data

The procedures used to determine the variables associated with each term are described in the sections that follow. This is followed by plots of the data and the determination of the model parameters via a power law curve fitting procedure.

Velocity

The velocity term was based on the time-averaged exterior velocity measured with the LDV for the particular steady state test condition. The values were determined as part of the velocity characterization presented previously.

Response Lag Time

The response lag time was determined from the detector output signal and was measured from the start of the aerosol exposure until the alarm threshold was reached.

Data Plots

The natural logarithm of the response lag time for each aerosol type was plotted as a function of external velocity. The x direction error bars for external velocity represent the statistical standard deviation in the data which has been used as an estimate of the measurement uncertainty. The y direction error bars represent the maximum and minimum variation in the mean response time data point from the three repeated tests. A third order polynomial curve fit was applied to the log-normal plot. The plots that follow illustrate the polynomial curve fitting procedure that was used for each data set in order to determine the coefficients for the polynomial terms.
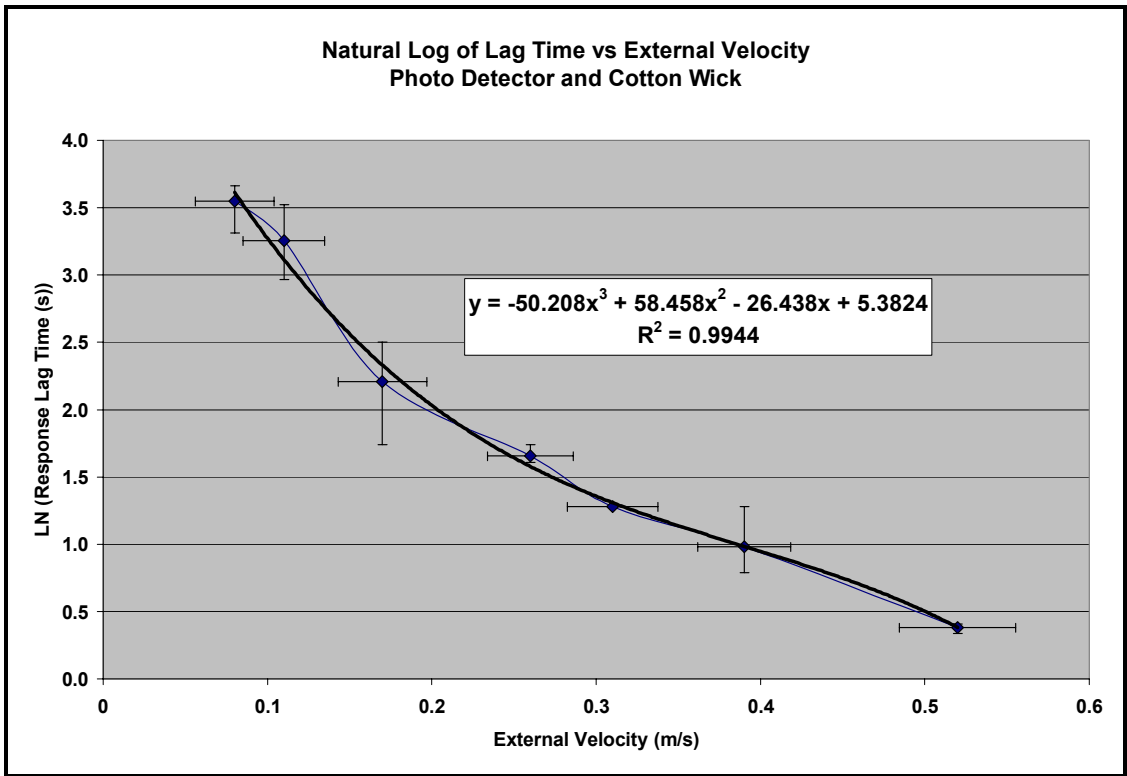
Figure 118 -- Polynomial curve fit for log-normal plot of photo detector and cotton wick.
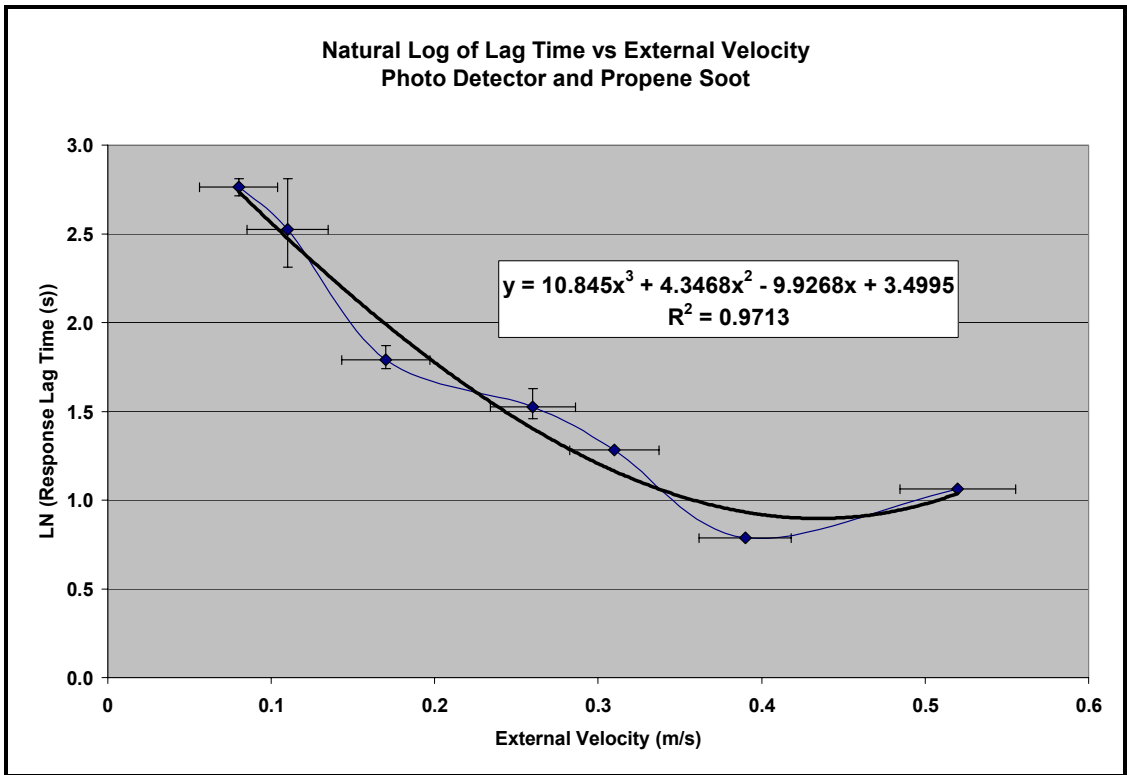
Figure 119 -- Polynomial curve fit for log-normal plot of photo detector and propene soot.
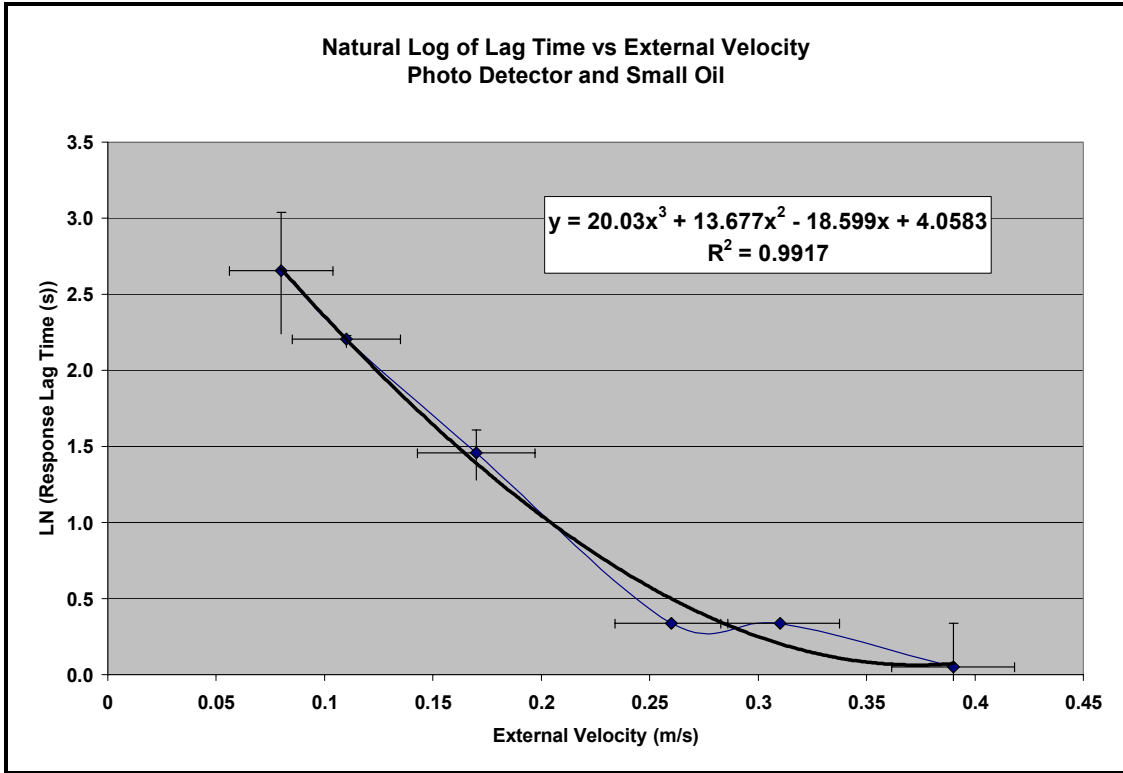
Figure 120 -- Polynomial curve fit for log-normal plot of photo detector and small oil.
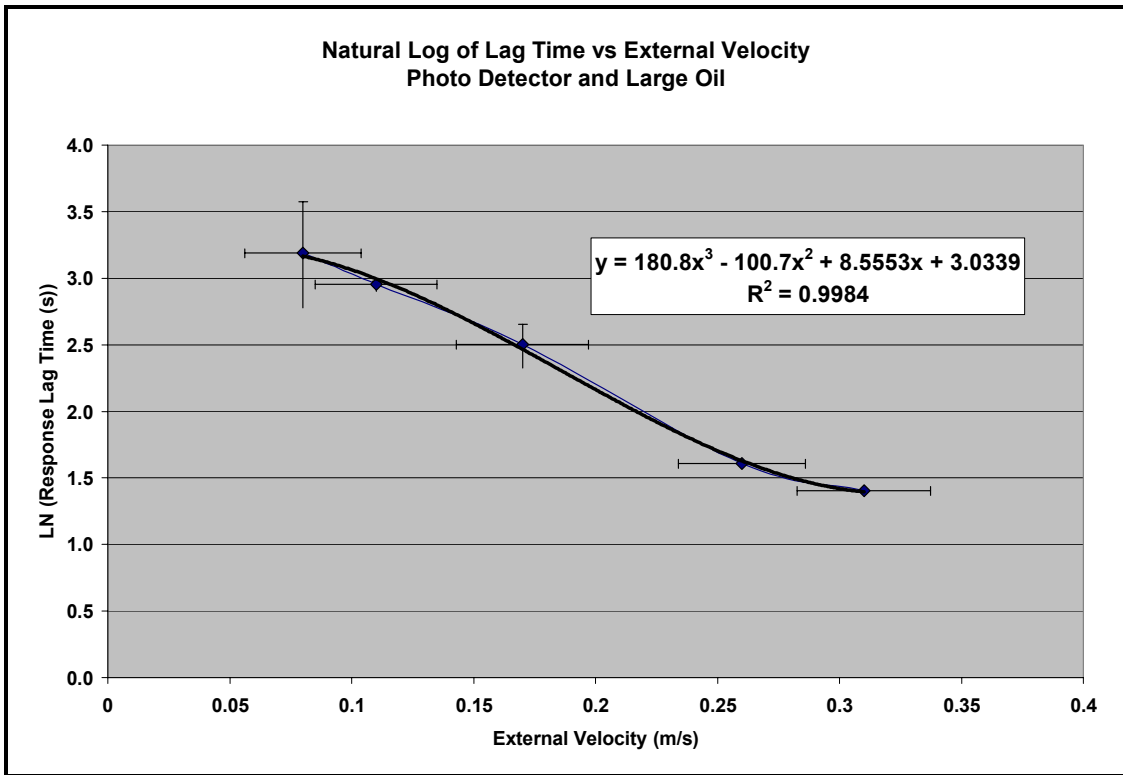
Figure 121 -- Polynomial curve fit for log-normal plot of photo detector and large oil.

The polynomial curve fits for the work of Brozovsky *et al* (1995) as well as the current study are summarized in Table 56.

Table 56 – Lag time curve fits for Brozovksy *et al* and current study.

Detector / Aerosol	Curve Fit	R^2
Ion / "Artificial" (Brozovsky)	$\Delta t_{r,lag} = \exp\left(1527u^3 + 918.1u^2 - 187.7u + 14.84\right)$	--
Photo / Cotton Wick	$\Delta t_{r,lag} = \exp\left(\text{-}50.208u^3 + 58.458u^2 \text{-}26.438u + 5.3824\right)$	0.99
Photo / Propene Soot	$\Delta t_{r,lag} = \exp\left(10.845u^3 + 4.3468u^2 - 9.9268u + 3.4995\right)$	0.97
Photo / Small Oil	$\Delta t_{r,lag} = \exp\left(20.03u^3 + 13.677u^2 - 18.599u + 4.0583\right)$	0.99
Photo / Large Oil	$\Delta t_{r,lag} = \exp\left(180.8u^3 \text{-}100.7u^2 + 8.5553u + 3.0339\right)$	0.99

The critical velocity was determined in accordance with the method suggested by Brozovsky *et al* and is summarized in the table that follows. The method is based on the average of the highest velocity tested and the velocity corresponding to twice the lag time at the maximum velocity. The results of this analysis are summarized in Table 57.

Table 57 – Critical velocity determination for photo detector.

Detector / Aerosol	Max Velocity Tested (m/s)	Lag Time (s)	2*Lag Time (s)	Velocity @ 2*Lag Time (m/s)	U_{cr} (m/s)
Photo / Cotton Wick	0.52	1.46	2.93	0.37	0.44
Photo / Propene Soot	0.52	2.82	5.65	0.21	0.36
Photo / Small Oil	0.52	2.46	4.93	0.15	0.34
Photo / Large Oil	0.31	4.04	8.07	0.21	0.26

The critical velocity values determined in Table 57 are well above the 0.15 m/s value suggested by Brozovsky *et al*. However, this trend is due primarily to the fact that a larger upper bound of velocity was used in the current study (0.31 and 0.52 m/s) as

416

opposed to the 0.2 m/s upper bound from Brozovsky *et al*. Therefore, the critical velocity

for this data set was also determined by forcing the upper bound to be 0.2 m/s in order to

be consistent with the original work by Brozovsky *et al*. The results of this particular

analysis are summarized in Table 58.

Table 58 – Summary of critical velocity for photo detector and "forcing" 0.20 m/s upper bound.

Detector / Aerosol	"Forced" Max Velocity (m/s)	Lag Time (s)	2*Lag Time (s)	Velocity @ 2*Lag Time (m/s)	U_{cr} (m/s)
Photo / Cotton Wick	0.20	7.63	15.25	0.14	0.17
Photo / Propene Soot	0.20	5.90	11.80	0.11	0.16
Photo / Small Oil	0.20	2.84	5.69	0.14	0.17
Photo / Large Oil	0.20	8.70	17.40	0.13	0.16

The results for critical velocity for this situation are consistent with the reported critical

velocity of 0.15 m/s reported by Brozovsky *et al*. However, this result can be attributed

to the forced upper bound of 0.20 m/s used in the averaging process. It should be noted

that the detectors used in the current study did in fact go into alarm at velocities well

below this "critical velocity" as was the case in the original study by Brozovksy *et al*

which had a lower limit of approximately 0.06 m/s. In addition, experimental results

recently reported by Cleary *et al* from NIST also confirm that alarm conditions have been

achieved at velocities below 0.15 m/s.

Appendix C.13: Uncertainty Analysis

The standard error propagation equation was used to determine the uncertainty in certain measured and calculated quantities in this study. The discussion that follows outlines the development of the standard error propagation equations relevant to the current study. Example calculations are provided which demonstrate the uncertainty estimates for specific quantities.

The development of the standard error equation begins considers a function y

$$y = y(x, w, z, ...)$$

(461)

The standard error of the function y, s_y, is (Ku, 1966)

$$s_y = \sqrt{\left(\frac{\partial y}{\partial x}\right)^2 s_x^2 + \left(\frac{\partial y}{\partial w}\right)^2 s_w^2 + \left(\frac{\partial y}{\partial z}\right)^2 s_z^2 + ... + 2\left(\frac{\partial y}{\partial x}\right)\left(\frac{\partial y}{\partial w}\right) s_{xw}^2 + ...}$$

(462)

The expression shown in Equation 462 simplifies to the following with the assumption that the variables x, w, z, etc are independent of each other, therefore, the covariance terms such as s_{xw} are zero.

$$s_y = \sqrt{\left(\frac{\partial y}{\partial x}\right)^2 s_x^2 + \left(\frac{\partial y}{\partial w}\right)^2 s_w^2 + \left(\frac{\partial y}{\partial z}\right)^2 s_z^2 + ...}$$

(463)

Some quantities developed as part of this study, such as the characteristic length and resistance factor of the detector were determined by linear curve fitting procedures. This

situation represents a specific condition where the variables are multiplied and/or divided by each other.

The function y for the product of two variables is represented as

$$y = x \cdot w$$

(464)

The associated partial derivative terms are

$$\frac{\partial y}{\partial x} = w$$

(465)

$$\frac{\partial y}{\partial w} = x$$

(466)

The partial derivative terms shown in Equations 465 and 466 can be recast in the following form using Equation 464.

$$\frac{\partial y}{\partial x} = w = \frac{y}{x}$$

(467)

$$\frac{\partial y}{\partial w} = x = \frac{y}{w}$$

(468)

Substituting the recast form the partial derivatives shown in Equations 467 and 468 into the standard error equation yields

$$s_y = \sqrt{\left(\frac{y}{x}\right)^2 s_x^2 + \left(\frac{y}{w}\right)^2 s_w^2}$$

(469)

The common variable y can be factored out for the final result for the special case of the error propagation for the product of two variables.

$$s_y = y\sqrt{\frac{s_x^2}{x^2} + \frac{s_w^2}{w^2}}$$

(470)

The standard error functions shown in Equations 463 and 470 were used to estimate the uncertainty in the following quantities.

The uncertainty in the resistance factor was estimated from the uncertainty in screen porosity and the screen Reynolds number. However, in order to estimate the uncertainty in these quantities, it was first necessary to estimate the uncertainty in the associated variables for screen porosity and screen Reynolds number.

Screen Diameter

The staggered arrangement of regular hexagons in the insect screen material were idealized as square openings as shown in Appendix C.3. The relevant dimensions of the regular hexagons were determined by scaling from an enlarged digital image of the insect screen. The side of a regular hexagon, s, was determined to be 0.442mm by scaling. The side of a regular hexagon, s, was demonstrated to be related to the side of an area-equivalent square, x, as $x = 1.61186s$ (Appendix C.3). Therefore, the scaled value of 0.442mm for the exterior of the regular hexagon was determined to have an external dimension of 0.7124mm for an area-equivalent square. The screen contained 12 regular hexagons over a measured distance of 9 mm. This would correspond to squares having a nominal exterior dimension of 0.75mm. This 9mm dimension was measured with a ruler with readings to the nearest 0.1mm. The corresponding uncertainty in this measurement,

420

therefore, would be +/- 0.05mm. This uncertainty in the overall dimension would result in external dimension of an individual square in the range of 0.7458mm to 0.7542mm (8.95mm/12 and 9.05mm/12, respectively). The uncertainty in the scaling methodology was estimated by comparing the scaled dimension of the area-equivalent square to the value obtained by dividing the overall measurement of 9mm by the 12 regular hexagons spanning this measurement. This uncertainty estimate was performed for the nominal as well as the upper and lower bounds of the measurement uncertainty for the ruler. The magnitude of the uncertainty in the screen diameter (based on the area-equivalent square) was approximated as the scaled value relative to the measured value. The percentage of the uncertainty in the screen diameter was also computed. This process is summarized as follows:

Screen Diameter

	Variable	Value	+/-		x (mm)	+	-
Measured	L (mm)	9	0.05	==>	0.75	0.754167	0.745833
Scaled	s (mm)	0.442		==>	0.712442	0.712442	0.712442

		+	-
Mag error	-0.037558	-0.041725	-0.033391
%error	-5.007717	-5.532537	-4.477034

The worst case scenario of the scaled screen diameter was used to estimate the uncertainty in the scaling methodology. Therefore, the screen diameter is reported as

$$d_{screen} = 0.7124 \pm 0.0417 \ mm$$

Screen Reynolds Number

The screen Reynolds number is a function of external velocity, screen diameter, and the kinematic viscosity of air.

$$Re = \frac{v_{ext} d_{screen}}{v}$$

421

The partial derivatives for the screen Reynolds number are as follows:

$$\frac{\partial \mathrm{Re}}{\partial v_{ext}} = \frac{d_{screen}}{v}$$

$$\frac{\partial \mathrm{Re}}{\partial d_{screen}} = \frac{v_{ext}}{v}$$

$$\frac{\partial \mathrm{Re}}{\partial v} = \frac{-v_{ext}d_{screen}}{v^2}$$

The corresponding standard error propagation equation for the screen Reynolds number is

$$s_{\mathrm{Re}} = \sqrt{\left(\frac{d_{screen}}{v}\right)^2 s_{v_{ext}}^2 + \left(\frac{v_{ext}}{v}\right)^2 s_{d_{screen}}^2 + \left(\frac{-v_{ext}d_{screen}}{v^2}\right)^2 s_v^2}$$

The screen diameter nominal value and associated uncertainty were determined in the preceding section and subsequently converted into units of meters for consistency with the Reynolds number determination. As demonstrated in the Model Paper, the ambient air temperature was nominally constant within 1 degree Celsius during testing. The corresponding uncertainty in the kinematic viscosity was calculated as 0.6% of the nominal value of 1.684E-05 m^2/s, or 1.0104E-07 m^2/s, via linear interpolation of kinematic viscosity values. The external velocity was based on the average approach velocity determined by integrating the velocity profile over the entry portion of the

detector as demonstrated in Appendix C.3. The estimated uncertainty in the external approach velocity value was taken as the statistical standard deviation in the LDV measurement. The uncertainty analysis for the screen Reynolds number was conducted over the range of external approach velocities as this uncertainty value is expected to vary as function of velocity. The uncertainty estimate for the screen Reynolds number, s_{Re}, was determined in accordance with the error propagation equation and is summarized below with the results of screen Reynolds number along with the magnitude of the estimated uncertainty in this value and as a percentage of the nominal screen Reynolds number.

Screen Reynolds Number

Variable	Value	Uncertainty		Re	s,Re	%(s,Re)
d,screen (m)	0.000712	0.000042				
nu (m^2/s)	1.68E-05	1.01E-07		Re	s,Re	%(s,Re)
V,ext (m/s)	0.500	0.034	==>	21.14	1.90	9.00
	0.377	0.027	==>	15.93	1.48	9.30
	0.302	0.026	==>	12.78	1.34	10.51
	0.254	0.025	==>	10.74	1.23	11.47
	0.162	0.026	==>	6.84	1.17	17.11
	0.108	0.024	==>	4.59	1.05	22.84
	0.074	0.023	==>	3.11	0.99	31.82

As shown in the percentages above, the estimated uncertainty in the screen Reynolds number is a function of external velocity. Therefore, the uncertainty results will need to be applied over this range of external velocity in for any estimate of uncertainty in additional quantities that are a function of screen Reynolds number.

Screen Porosity

The screen porosity, as shown in Appendix C.3, is a function of the external dimension of the screen opening, m, and the thickness of the wire mesh, d. The screen porosity expression for a square opening is based on the ratio of open area to total area:

$$\alpha = \frac{(m-d)^2}{m^2}$$

(476)

The expression above can be expanded to the following

$$\alpha = \frac{(m-d)^2}{m^2} = \frac{m^2 - 2md + d^2}{m^2} = 1 - \frac{2d}{m} + \frac{d^2}{m^2}$$

(477)

The partial derivatives for the screen porosity are:

$$\frac{\partial \alpha}{\partial m} = \frac{2d}{m^2} - \frac{2d^2}{m^3}$$

(478)

$$\frac{\partial \alpha}{\partial d} = \frac{-2}{m} - \frac{2d}{m^2}$$

(479)

The corresponding standard error propagation equation for the screen porosity is

$$s_\alpha = \sqrt{\left(\frac{2d}{m^2} - \frac{2d^2}{m^3}\right)^2 s_m^2 + \left(\frac{-2}{m} - \frac{2d}{m^2}\right)^2 s_d^2}$$

(480)

The screen external dimension and wire mesh thickness values were determined to be 0.7124 mm and 0.1321 mm, respectively in Appendix C.3. These values are both subject

to the same uncertainty from the scaling methodology used. The uncertainty in the external screen dimension was determined previously. The uncertainty in the wire mesh thickness value was determined by applying the same percentage (5.8%) of the screen external dimension. This corresponds to an estimated uncertainty in the wire mesh thickness of 0.00766 mm. The analysis for determining the estimated uncertainty in the screen porosity is summarized as

Screen Porosity

Variable	Value	Uncertainty		alpha	s,alpha	%(s,alpha)
m = d,screen (m)	0.000712	0.000042	==>	0.664	0.031	4.70
d = mesh (m)	0.000132	0.000008	==>			

Therefore, the screen porosity is reported as

$$\alpha = 0.664 \pm 0.031$$

Screen Porosity Function

The screen porosity function used to determine the resistance factor, as shown in Appendix C.3, is

$$f(\alpha) = \frac{(1-\alpha^2)}{\alpha^2}$$

(481)

This expression can be expanded to the following form

$$f(\alpha) = \frac{1}{\alpha^2} - 1$$

(482)

The partial derivative of the screen porosity function with respect to the screen porosity is

$$\frac{\partial f(\alpha)}{\partial \alpha} = \frac{-2}{\alpha^3}$$

(483)

425

The standard error propagation equation for the screen porosity function is

$$s_{f(\alpha)} = \sqrt{\left(\frac{-2}{\alpha^3}\right)^2 s_\alpha^2}$$

(484)

The analysis for determining the estimated uncertainty in the screen porosity function is summarized as

Screen Porosity Function

Variable	Value	Uncertainty		f(alpha)	s,f(alpha)	%(s,f(alpha))
alpha	0.664	0.031	==>	1.268	0.213	16.83

Therefore, the screen porosity function is reported as

$$\frac{\left(1-\alpha^2\right)}{\alpha^2} = 1.268 \pm 0.213$$

Resistance Factor

The resistance factor developed in Appendix C.3 is a function of the screen porosity and screen Reynolds number. The resistance factor for the photoelectric detector used to demonstrate various aspects of the analysis in the current study is

$$R = 0.0034\left[\left(\frac{1-\alpha^2}{\alpha^2}\right)\mathrm{Re}_d\right]$$

(485)

The corresponding partial derivatives for the resistance factor are as follows:

$$\frac{\partial R}{\partial\left(\frac{1-\alpha^2}{\alpha^2}\right)} = 0.0034\left[\mathrm{Re}_d\right]$$

(486)

426

$$\frac{\partial R}{\partial \mathrm{Re}_d} = 0.0034 \left[\left(\frac{1-\alpha^2}{\alpha^2} \right) \right]$$

<div align="right">(487)</div>

The standard error propagation equation for the resistance factor is

$$s_R = \sqrt{\left(0.0034 \left[\mathrm{Re}_d \right] \right)^2 s_{f(\alpha)}^2 + \left(0.0034 \left[\left(\frac{1-\alpha^2}{\alpha^2} \right) \right] \right)^2 s_{\mathrm{Re}}^2}$$

<div align="right">(488)</div>

The analysis for determining the estimated uncertainty in the resistance factor is summarized as

Resistance Factor (Photo Detector)

Variable	Value	Uncertainty		R	s,R	%(s,R)
f(alpha)	1.268	0.213				
Re	21.14	1.90	==>	0.0911	0.0174	19.08
	15.93	1.48	==>	0.0687	0.0132	19.23
	12.78	1.34	==>	0.0551	0.0109	19.84
	10.74	1.23	==>	0.0463	0.0094	20.37
	6.84	1.17	==>	0.0295	0.0071	24.00
	4.59	1.05	==>	0.0198	0.0056	28.37
	3.11	0.99	==>	0.0134	0.0048	36.00

As shown in the percentages above, the estimated uncertainty in the resistance factor is a function of screen Reynolds number and varies from 20 to 36% of the nominal value. This Reynolds number dependence will be used in determining the estimated uncertainty in subsequent variables that are a function of the resistance factor.

Internal Velocity (determined via resistance factor)

The internal velocity can be determined by using the external velocity and the resistance factor as an inlet velocity boundary condition as shown in Appendix C.3. The internal velocity can be expressed as

$$v_{int} = Rv_{ext}$$

<div align="right">(489)</div>

The corresponding partial derivatives for the internal velocity are as follows:

$$\frac{\partial v_{int}}{\partial R} = v_{ext}$$

<div align="right">(490)</div>

$$\frac{\partial v_{int}}{\partial v_{ext}} = R$$

<div align="right">(491)</div>

The standard error propagation equation for the internal velocity is

$$s_{v_{int}} = \sqrt{\left(v_{ext}\right)^2 s_R^2 + \left(R\right)^2 s_{v_{ext}}^2}$$

<div align="right">(492)</div>

The analysis for determining the estimated uncertainty in the internal velocity is summarized as

Internal Velocity (Photo Detector)

V,ext (m/s)	s,V,ext (m/s)	R	s,R		v,int	s,v,int	%(s,v,int)
0.500	0.034	0.091	0.017	==>	0.04554	0.00923	20.26
0.377	0.027	0.069	0.013	==>	0.02587	0.00531	20.53
0.302	0.026	0.055	0.011	==>	0.01664	0.00361	21.67
0.254	0.025	0.046	0.009	==>	0.01175	0.00266	22.62
0.162	0.026	0.029	0.007	==>	0.00477	0.00138	28.89
0.108	0.024	0.020	0.006	==>	0.00214	0.00077	35.94
0.074	0.023	0.013	0.005	==>	0.00099	0.00047	47.69

As shown in the percentages above, the estimated uncertainty in the internal velocity is a function of external velocity and resistance factor. The estimated uncertainty values vary from 20 to 48% of the nominal value. This velocity dependence will be used in determining the estimated uncertainty in subsequent variables that are a function of the internal velocity.

Characteristic Response Time

The characteristic response time developed in the lumped mass transport model analysis is a function of physical length of the detector and internal velocity.

$$t_c = \frac{L_p}{v_{int}}$$

(493)

The corresponding partial derivatives for the characteristic response time are as follows:

$$\frac{\partial t_c}{\partial L_p} = \frac{1}{v_{int}}$$

(494)

$$\frac{\partial t_c}{\partial v_{int} L_p} = \frac{-L_p}{v_{int}^2}$$

(495)

The standard error propagation equation for the characteristic response time is

$$s_{t_c} = \sqrt{\left(\frac{1}{v_{int}}\right)^2 s_{L_p}^2 + \left(\frac{-L_p}{v_{int}^2}\right)^2 s_{v_{int}}^2}$$

(496)

The physical length of the detector used to determine the characteristic response time is the diameter of the sensing chamber which is consistent with the development of the mass transport model in the current study. The sensing chamber diameter of the photoelectric detector was 48 mm and was measured with a ruler with gradations to the nearest millimeter. Therefore, the uncertainty in this measurement was estimated to be

0.5 mm. The analysis for determining the estimated uncertainty in the characteristic response time is summarized as

Characteristic Response Time (Photo Detector)

Variable	Value	Uncertainty		t,c	s,t,c	%(s,t,c)
L,p (m)	0.0480	0.0005				
v,int (m/s)	0.04554	0.00923	==>	1.054086	0.213871	20.29
	0.02587	0.00531	==>	1.8552218	0.381421	20.56
	0.01664	0.00361	==>	2.8840467	0.62557	21.69
	0.01175	0.00266	==>	4.0850865	0.925008	22.64
	0.00477	0.00138	==>	10.072779	2.911414	28.90
	0.00214	0.00077	==>	22.393939	8.052286	35.96
	0.00099	0.00047	==>	48.698178	23.22762	47.70

The values summarized in the preceding table indicate that on a percentage basis, the uncertainty in the characteristic response time are primarily due to the uncertainty in the internal velocity.

Smoke Concentration (via laser transmittance)

The external smoke concentration was determined from laser transmittance over the measurement pathlength by rearranging Equation 378 shown in Appendix C.7 into the following format.

$$C = -\frac{\ln(\tau)}{kL}$$

(497)

The corresponding partial derivatives for the smoke concentration via laser transmittance are as follows:

$$\frac{\partial C}{\partial \tau} = \frac{-1}{kL\tau}$$

(498)

430

$$\frac{\partial C}{\partial k} = \frac{\ln(\tau)}{k^2 L}$$

(499)

$$\frac{\partial C}{\partial L} = \frac{\ln(\tau)}{kL^2}$$

(500)

The standard error propagation equation for the smoke concentration via laser transmittance is

$$s_{C,L} = \sqrt{\left(\frac{-1}{kL\tau}\right)^2 s_\tau^2 + \left(\frac{\ln(\tau)}{k^2 L}\right)^2 s_k^2 + \left(\frac{\ln(\tau)}{kL^2}\right)^2 s_L^2}$$

(501)

The standard error propagation for the smoke concentration via laser transmittance was computed over the range of external velocities for each of the four aerosol types evaluated in the current study. At each external velocity the nominal steady state laser transmittance value and associated standard deviation were based on a 30 second average for each of three repeated tests. The 30 second average steady state laser transmittance and associated standard deviation for the three repeated tests were averaged. These averaged values were used in the uncertainty analysis. The estimated uncertainty for all four aerosol types is summarized in the following:

Species Concentration (via laser for Cotton Wick)

Variable	Value	Uncertainty		C (g/m^3)	s,C	%(s,C)
sigma (m^2/g)	8	1.1				
L (m)	1.52	0.01				
tau	0.9839	0.0008	==>	0.00133	0.00020	14.68
	0.9829	0.0013	==>	0.00142	0.00023	15.86
	0.9773	0.0015	==>	0.00189	0.00029	15.36
	0.9780	0.0014	==>	0.00183	0.00028	15.22
	0.9785	0.0013	==>	0.00179	0.00027	15.08
	0.9812	0.0012	==>	0.00156	0.00024	15.21
	0.9790	0.0012	==>	0.00175	0.00026	14.87

Species Concentration (via laser for Propylene)

Variable	Value	Uncertainty		C (g/m^3)	s,C	%(s,C)
sigma (m^2/g)	8	1.1				
L (m)	1.52	0.01				
tau	0.8941	0.0038	==>	0.00921	0.00132	14.28
	0.9069	0.0052	==>	0.00803	0.00120	14.95
	0.9270	0.0060	==>	0.00623	0.00101	16.21
	0.9460	0.0089	==>	0.00456	0.00100	21.84
	0.9335	0.0154	==>	0.00566	0.00157	27.68

Species Concentration (via laser for Small Oil)

Variable	Value	Uncertainty		C (g/m^3)	s,C	%(s,C)
sigma (m^2/g)	8	1.1				
L (m)	1.52	0.01				
tau	0.9743	0.0007	==>	0.00215	0.00030	14.03
	0.9782	0.0017	==>	0.00181	0.00029	15.78
	0.9831	0.0009	==>	0.00141	0.00021	14.78
	0.9883	0.0007	==>	0.00097	0.00015	15.03
	0.9894	0.0007	==>	0.00088	0.00013	15.24

Species Concentration (via laser for Large Oil)

Variable	Value	Uncertainty		C (g/m^3)	s,C	%(s,C)
sigma (m^2/g)	8	1.1				
L (m)	1.52	0.01				
tau	0.9332	0.0053	==>	0.00569	0.00091	16.00
	0.9432	0.0066	==>	0.00481	0.00088	18.25
	0.9422	0.0050	==>	0.00489	0.00080	16.36
	0.9494	0.0069	==>	0.00427	0.00084	19.67
	0.9485	0.0063	==>	0.00435	0.00081	18.68
	0.9460	0.0047	==>	0.00457	0.00075	16.45
	0.9525	0.0043	==>	0.00400	0.00067	16.65

For all four aerosol types and over the range of external velocities, the uncertainty in the smoke concentration via laser transmittance is generally 14 to 16% the nominal smoke concentration value with a few exceptions that include maximums of 20 to 28% the

nominal value. These values will be used for comparisons of model predictions to the appropriate experimental data set.

Smoke Concentration (via detector output)

The internal smoke concentration was determined from the detector output using Equation 385 in Appendix C.7.

$$C = \frac{-\ln\left(1 - \frac{\%O_u}{100}\right)}{k}$$

(502)

The corresponding partial derivatives for the smoke concentration via detector output are as follows:

$$\frac{\partial C}{\partial \%O_u} = \frac{-1}{\left(1 - \frac{\%O_u}{100}\right)k}$$

(503)

$$\frac{\partial C}{\partial k} = \frac{\ln\left(1 - \frac{\%O_u}{100}\right)}{k^2}$$

(504)

The standard error propagation equation for the smoke concentration via detector output is

$$s_{C,D} = \sqrt{\left(\frac{-1}{\left(1-\dfrac{\%O_u}{100}\right)k}\right)^2 s_{\%O_u}^2 + \left(\frac{\ln\left(1-\dfrac{\%O_u}{100}\right)}{k^2}\right)^2 s_k^2}$$

<div align="right">(505)</div>

The standard error propagation for the smoke concentration via detector output was computed over the range of external velocities for each of the four aerosol types evaluated in the current study. The uncertainty in the %obscuration correlated to the detector output is based on standard deviation in the clean air baseline value of 1 based on preliminary measurements of the detector output. The uncertainty in the %obscuration based on this baseline fluctuation for the two alarm points (0.2%/ft and 0.5%/ft) was 0.643 +/- 0.092%/m and 1.622 +/- 0.092%/m.